Philipps Universität Marburg

Localized states in the transition to turbulence in plane Poiseuille flow and thermal boundary layers

Dissertation

zur Erlangung des Doktorgrades der Naturwissenschaften (Dr. rer. nat.)

dem Fachbereich Physik der Philipps-Universität Marburg

vorgelegt von

Stefan Zammert

aus Herborn

Marburg, August 2015

Vom Fachbereich Physik der

Philipps-Universität Marburg (Hochschulkennziffer 1180)

als Dissertation angenommen am: 02.10.2015

Tag der mündlichen Prüfung: 06.10.2015

Erstgutachter: Prof. Dr. Bruno Eckhardt Fachbereich Physik
Philipps-Universität Marburg

Zweitgutachter: Prof. Dr. Marc Avila Lehrstuhl für Strömungsmechanik
Friedrich-Alexander-Universität Erlangen-Nürnberg

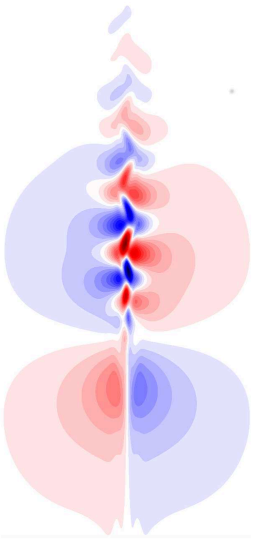

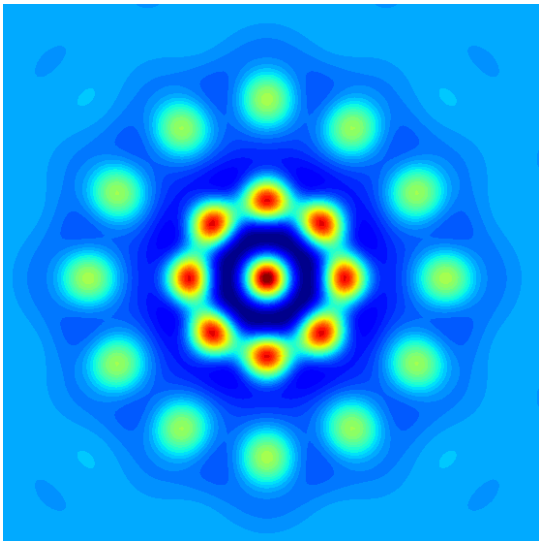

Localized states in the transition to turbulence in plane Poiseuille flow and thermal boundary layers

Stefan Zammert

Zusammenfassung

Die vorliegende Arbeit befasst sich mit der numerischen Untersuchung des Turbulenzübergangs und auftretender lokalisierter Strukturen in der ebenen Poiseuille-Strömung und dem asymptotischen Ansaugprofil über einer geheizten Platte. Die laminaren Profile beider Strömungen zeigen eine lineare Instabilität und im sogenannten subkritischen Bereich, wo das laminare Profil stabil ist, kann man jeweils überdauernde, aber dennoch transiente Turbulenz beobachten.

In beiden Strömungen können eine Vielzahl von exakten Lösungen der Navier-Stokes-Gleichungen mit speziellen numerischen Verfahren aufgespürt werden. Eine genauere Analyse zeigt, dass in beiden Systemen der Ursprung der subkritischen Turbulenz auf eine Bifurkationskaskade zurückgeführt werden kann, welche ihren Ausgangspunkt in einer solchen exakten Lösung hat. Die Bifurkationskaskade erzeugt einen chaotischen Attraktor, der durch eine äußere Krisenbifurkation (*Boundary crisis bifuration*) in einen chaotischen Sattel mit exponentiell verteilten Lebenszeiten umgewandelt wird. Eine zweite Art von Krisenbifurkationen, sogenannte innere Krisenbifurkationen (*Interior crisis bifurcation*), tragen zur Vergrößerung des Attraktors bei und werden für die ebene Poiseuille-Strömung genauer untersucht.

Während der Ausgangszustand für die Bifukationskaskade im Falle des asymptotischen Ansaugprofils über einer geheizten Platte mit der Instabilität des laminaren Profils verbunden ist, haben die relevanten Zustände in der ebenen Poiseuille-Strömung keine Verbindung zum laminaren Zustand. Dies führt zu zwei koexistierenden Übergangsmechanismen zur Turbulenz. Die beiden Mechanismen sind der *Bypass-Übergang* und der *Tollmien-Schlichting-Übergang*.

Die Phasenraumstruktur, die der Koexistenz dieser beiden Übergangsmechanismen zugrunde liegt, wird in dieser Arbeit untersucht. Zweidimensionale Projektionen, die exakte Lösungen nutzen, zeigen, dass es unterhalb der kritischen Reynoldszahl drei verschiedene Bereiche im Zustandsraum gibt. In einem dieser Bereiche liegt Bypass-Übergang vor, im zweiten beobachtet man ein rasches Zulaufen auf den laminaren Zustand und im dritten Bereich, welcher sehr klein ist und mit steigender Reynoldszahl wächst, kommt es zu einem Tollmien-Schlichting-Übergang. Die drei Bereiche liegen im Phasenraum teilweise sehr dicht beieinander und unterscheiden sich deutlich in der Zeit, die eine darin befindliche Anfangsbedingung benötigt um einen turbulenten Zustand zu erreichen. Oberhalb der kritischen Reynoldszahl gibt es nur noch die Bereiche mit Bypass- und Tollmien-Schlichting-Übergang, welche durch die stabile Mannigfaltigkeit einer besonderen exakten Lösung des Systems, des *Bypass-Edgestates*, getrennt werden.

In beiden Strömungen existieren verschiedene räumlich lokalisierte exakte Lösungen. In der ebenen Poiseuille Strömung können durch Analyse der Instabilitäten räumlich ausgedehnter

Tollmien-Schlichting-Wellen, periodische Bahnen gefunden werden, welche aus in Strömungsrichtung lokalisierten Paketen von Tollmien-Schlichting-Wellen bestehen. Des Weiteren kann eine in Strömungsrichtung lokalisierte, dreidimensionale, relativ periodische Bahn mittels der sogenannten *Edge-Tracking* Technik, die es erlaubt Trajektorien auf der Grenze zwischen laminarem und turbulentem Attraktionsgebiet zu verfolgen, gefunden werden. Die räumliche Länge dieser periodischen Bahn wächst annähernd linear mit der Reynoldszahl. Die Ergebnisse zeigen, dass die lokalisierte periodische Bahn bei hohen Reynoldszahlen in einer subkritischen, langwelligen Bifurkation einer räumlich ausgedehnten laufenden Welle erzeugt wird. Durch eine Verfolgung dieser Bahn in der Breite der simulierten numerischen Domäne kann eine relativ periodische Bahn identifiziert werden, die in beide Richtungen parallel zu den Platten lokalisiert ist. Die in Strömungsrichtung lokalisierten Zustände zeigen einen Abfall der Geschwindigkeitskomponenten, der über eine größere Distanz gut mit einem exponentiellen Abfall übereinstimmt. Die Erkenntnisse durch die doppelt-lokalisierte periodische Bahn und die Simulationen turbulenter Flecken, zeigen jedoch, dass in der ebenen Poiseuille-Strömung im großen Abstand um eine lokalisierte Struktur der Abfall der Geschwindigkeitskomponenten einem Potenzgesetz folgt.

Für das asymptotische Ansaugprofil über einer geheizten Platte können verschiedene einfach- und auch doppelt-lokalisierte Fixpunkte gefunden werden. Einer der doppelt-lokalisierten Zustände wird, ähnlich wie in der ebenen Poiseuille Strömung, durch zwei parallel stattfindende, langwellige Bifurkationen einer räumlich ausgedehnten Lösung erzeugt. Studiert man die Instabilitäten der lokalisierten Lösungen, so stellt man fest, dass entlang deren instabiler Richtungen Plume-artige Dynamik auftritt. Plumes im studierten System können also als eine Bewegung entlang der instabilen Mannigfaltigkeit einer exakten Lösung interpretiert werden. Ausgehend von den exakten Lösungen ist es möglich, diese Dynamik systematisch zu studieren. Die Resultate zeigen, dass sich die Plumes über einen längeren Zeitraum mit einer konstanten Geschwindigkeit ausbreiten, wobei die Ausbreitungsgeschwindigkeit mit der Rayleighzahl zunimmt.

Um das asymptotische Ansaugprofil über einer geheizten Platte und dessen exakte Lösungen zu studieren, wurde der *Channelflow*-Code (www.channelflow.org) erweitert. Der entwickelte Code ermöglicht außerdem die Simulation von Rayleigh-Bénard-, Poiseuille-Rayleigh-Bénard- und Couette-Rayleigh-Bénard-Strömung.

Abstract

This dissertation numerically investigates the transition to turbulence and occurring localized structures in plane Poiseuille flow and the asymptotic suction boundary layer over a heated plate. Calculations show that the laminar profiles of both flows are linearly unstable. Nevertheless, in both cases long-living, but transient turbulence can be observed in the subcritical range.

In the two systems a multitude of exact solutions of the Navier-Stokes equations is identified using specially tailored numerical methods. A detailed analysis shows that for both systems the origin of subcritical turbulence can be traced back to a bifurcation cascade that starts at one of those exact solutions. The bifurcation cascade creates a chaotic attractor which is transformed into a chaotic saddle by a so-called *boundary crisis bifurcation*. This chaotic saddle shows exponentially distributed lifetimes. A second type of crisis bifurcations, so-called *interior crisis bifurcations*, which are studied in detail for plane Poiseuille flow, contributes to an increase of the attractor and its temporal complexity.

For the asymptotic suction boundary layer over a heated plate, the exact solution that is the starting point for the bifurcation cascade is directly connected to the instability of the laminar state. For plane Poiseuille flow there is no such connection causing the coexistence of two transition mechanisms to turbulence. These are the *bypass transition* and the *Tollmien-Schlichting transition*.

The state space structure underlying the coexistence of the two transition scenarios is explored by two-dimensional projections of the state space that use exact solutions. The slices show that below the critical Reynolds number the state space consists of three parts. In one of these parts, bypass transition is located and in a second one a immediate return to the laminar states can be observed. In the third part, which is quite small and grows with increasing Reynolds number, initial conditions undergo Tollmien-Schichting transition to turbulence. In the state space, all three regions lie close to each other and can be distinguished by the time needed to reach the turbulent state. Above the critical Reynolds number, only the regions containing bypass and Tollmine-Schlichting transition can be found. There, both regions are separated by the stable manifold of a special exact solution of the system, the bypass *edge state*.

In both studied systems, various spatially localized exact solutions exist. For plane Poiseuille flow, the instabilities of the spatially extended Tollmien-Schlichting wave are analyzed. This allows to identify periodic orbits that consist of streamwise localized packages of Tollmien-Schlichting waves. Furthermore, by using the technique of *edge-tracking*, which allows to follow

trajectories on the boundary between the laminar and the transient turbulent part of the state space, a streamwise localized three-dimensional periodic orbit can be found. The streamwise length of this periodic orbit grows approximately linear with the Reynolds number. The result show further that the orbit is created at high Reynolds number in an subcritical long-wavelength instability of a streamwise extended traveling wave. By tacking the orbit to wider computational domains, a relative periodic orbit that is localized in both direction parallel to the plates can be found.

The streamwise localized state shows a decay of the velocity components that over a wider range is in a good agreement with an exponential decay. However, the results from the doubly-localized states, as well as simulations of turbulent spots, show that for large distances the decay of the velocity components follows a power law.

For the asymptotic suction boundary layer over a heated plate, it is also possible to identify different exact solutions that are localized in one or two directions parallel to the plate. For one of the doubly-localized states it is shown that it is created in two simultaneous long-wavelength instabilities of a spatially extended equilibrium solution. By studying the instabilities of these localized exact solutions one recognizes that plume-like dynamics appear along their unstable directions. Thus, plume motion in this flow can be interpreted as moving along the unstable direction of an exact solution. A systematic analysis of the plume shows that for a long time its tip moves with a constant speed that increases with the Rayleigh number.

To study the asymptotic suction boundary layer over a heated plate numerically, the *Channelflow*-code (www.channelflow.org) was enhanced. In addition to the parallel thermal boundary layer, the developed code allows to simulate Rayleigh-Bénard-, Poiseuille-Rayleigh-Bénard- and Couette-Rayleigh-Bénard flow.

Contents

Zusammenfassung **V**

Abstract **VII**

Contents **IX**

1 Introduction **1**

I Plane Poiseuille flow **5**

2 An introduction to plane Poiseuille flow **7**

3 Edge states and exact solutions in short domains **13**
3.1 Introduction . . . 13
3.2 Traveling waves edge states . . . 15
3.3 Periodically bursting edge states . . . 20
3.4 Three-dimensional traveling wave bifurcating from Tollmien-Schlichting-waves . 30

4 The origin of subcritical turbulence **35**
4.1 Introduction . . . 35
4.2 Enlargement of the attractor in an interior crisis bifurcation . . . 36
4.3 Destruction of the chaotic attractor in a boundary crisis bifurcation . . . 38
4.4 Embedded attractors and increasing lifetimes . . . 40
4.5 Attractors and saddles with different spatial wavelength . . . 43
4.6 Dependence on the operating condition . . . 44

5 Exact solutions for Bypass and Tollmien-Schlichting transition **47**
5.1 Introduction . . . 47
5.2 Two-dimensional slices of the state space . . . 48
5.3 TS transition and Bypass transition . . . 49

6 Streamwise and doubly-localized states **57**
6.1 Introduction . . . 57
6.2 Streamwise localized periodic orbits and edge states . . . 58
6.3 A doubly-localized periodic orbit . . . 65

6.4 Doubly-localized chaotic edge states . . . 70
6.5 Localized Tollmien-Schlichting waves . . . 72
6.6 Extracting different velocity scales using the method of comoving frames . . . 78
6.7 Streamwise localized turbulence . . . 81

7 Tails of localized structures **87**
7.1 Introduction . . . 87
7.2 The Brand & Gibson-model for plane Poiseuille flow . . . 88
7.3 Algebraic decay in the tails of turbulent spots . . . 92

8 Summary of the results for plane Poiseuille flow **95**
8.1 Critical Reynolds numbers for plane Poiseuille flow . . . 95
8.2 Summary and outlook . . . 96

II The asymptotic suction boundary layer over a heated plate **99**

9 Introduction to the system **101**

10 Stability and secondary solutions **105**
10.1 Introduction . . . 105
10.2 Stability analysis for $Ra = 0$ . . . 105
10.3 Stability Analysis for $Re = 0$ . . . 106
10.4 Stability Analysis for $Re \neq 0$ and $Ra \neq 0$ . . . 110
10.5 Nusselt numbers for secondary solutions . . . 113

11 Tertiary solutions and turbulence **115**
11.1 Introduction . . . 115
11.2 Superharmonic instabilities and transient chaos . . . 115
11.3 Subharmonic instabilities and localization . . . 117
11.4 Plume-like motion along unstable directions . . . 120
11.5 Fully localized solutions . . . 123
11.6 Mean turbulent profiles . . . 127
11.7 The edge-of-chaos for finite Re . . . 129

12 Summary of the results for the asymptotic suction boundary layer **131**

13 Comparison of the systems and concluding remarks **135**

A Numerical methods **137**
A.1 Channelflow and temperature . . . 137
A.2 Stability analysis . . . 140
A.3 Finding exact solutions . . . 141

Bibliography **143**

Danksagungen **153**

Chapter 1

Introduction

Many flows show two distinct kinds of dynamical states. The first, the so-called laminar state, is dynamically simple, often independent of time and shows only smooth variations of the velocities. The second one is the turbulent state that is erratic and shows large and complex spatial and temporal variations. In experiments the laminar state is often replaced by the turbulent one if the Reynolds number is increased[1]. This observations cause the long standing turbulence problem which in a definition by Noether (1921) for pipe flow reads as follows:

> *"Unter Turbulenzproblem versteht man, allgemein gesprochen, die Frage, warum der grundsätzlich immer mögliche Poiseuillesche Zustand nur begrenzt realisiert ist und dem hydraulischen Zustand Platz macht."*

Thus, the turbulence problem is the question why the laminar state ("Poiseuillescher Zustand") that does always exist is not always realized and at some point replaced by the turbulent state ("hydraulischer Zustand" using Noether's words). For many years, it was tried to solve this question by an analysis of the stability of the laminar state of a flow (see Eckert (2010, 2014) for reviews on the historical development of the turbulence problem and hydrodynamic stability theory). However, it turned out that quite often linear stability theory fails to explain the onset of turbulence. For plane Poiseuille flow, the pressure driven flow between two parallel plates, turbulence is observed in experiments for Reynolds numbers far below the one predicted by linear stability theory. For pipe Poiseuille flow (the pressure driven flow through a cylindrical pipe) and plane Couette flow (the flow between two plates moving in opposite directions), experiments and also numerical simulations show long-living turbulence although the laminar state is stable for all Reynolds numbers according to linear stability theory. It should be remarked that the fact that the critical Reynolds numbers predicted by stability theory are higher than those where turbulence can be observed does not imply that the stability of the laminar state is not relevant. While for Reynolds numbers below the linear instability turbulence in general is transient, above the critical Reynolds number a return to the laminar state is not possible.

[1] If the geometric parameters and the viscosity are fixed, an increase of Re is equivalent to an increase of the velocity.

Since about half a century there are approaches to understand turbulence using dynamical systems theory. Especially, different roads to turbulent dynamics have been proposed, e.g. the Ruelle-Takens scenario (Ruelle and Takens, 1971) and the period doubling scenario (Feigenbaum, 1978). For some systems that show turbulent dynamics evidences for the different scenarios exist (see e.g Eckmann, 1981, for a classical review). In general, the experimental evidences were found for systems that show *supercritical turbulence* (turbulence for parameter values were the base state is unstable) as e.g. Rayleigh-Bénard convection.

In recent times dynamical system theory has also contributed to an improved understanding of turbulence in systems where turbulence is observed although the laminar state is stable. Such *subcritical turbulence* can be found e.g. in pipe flow, plane Couette or plane Poiseuille flow. Numerical simulations (Brosa, 1989; Schmiegel and Eckhardt, 1997; Faisst and Eckhardt, 2004; Willis and Kerswell, 2007; Schneider and Eckhardt, 2008) and experiments (Bottin and Chate, 1998; Peixinho and Mullin, 2006; Hof et al., 2006, 2008) provided evidences that turbulence in subcritical systems is transient and thus it corresponds to a chaotic saddle rather than an attractor. This saddle is formed by three-dimensional exact solutions of the Navier-Stokes equations and homoclinic and hetereoclinic connections between them. Exact solutions, which appear in form of equilibria, traveling waves, or periodic orbits, can be found by using special-tailored numerical methods. Up to now a multitude of exact solutions has been found for different subcritical systems as plane Couette flow (e.g. Nagata, 1990; Clever and Busse, 1992; Schmiegel, 1999; Gibson et al., 2009), pipe flow (e.g. Faisst and Eckhardt, 2003b; Wedin and Kerswell, 2004; Pringle and Kerswell, 2007; Pringle et al., 2009), plane Poiseuille flow (Ehrenstein and Koch, 1991; Waleffe, 2001; Zammert, 2011; Gibson and Brand, 2014) or counter-rotating Taylor-Couette flow (Deguchi et al., 2014). In addition to their numerical identification, it was also possible to find evidences for exact solutions in experiments (Hof et al., 2004).

Recently, it was shown how a bifurcation cascade starting at an exact solution can form a chaotic saddle (Kreilos and Eckhardt, 2012; Avila et al., 2013) which was a large step towards the understanding of subcritical turbulence.

The majority of the exact solutions identified up to now are spatially extended. However, it is known since the experiments of Osbourne Reynolds (Reynolds, 1883), that in many systems subcritical turbulence is localized or spatially intermittent close to its onset. Turbulence can appear in localized form as puffs or slugs in pipe flow (Wygnanski and Champagne, 1973; Wygnanski et al., 1975) or as spots in plane Couette and plane Poiseuille flow (Carlson et al., 1982; Henningson et al., 1987; Lemoult et al., 2013). Furthermore, the formation of complex patterns of laminar and turbulent regions can be observed (Barkley and Tuckerman, 2005; Tuckerman et al., 2014; Duguet et al., 2010a; Brethouwer et al., 2012; Avila and Hof, 2013). In order to understand this observations using the framework of dynamical systems theory, there is a need to find localized exact solutions because they are expected to form a skeleton for spatially localized turbulence.

Some of the known exact solutions show spatial localization. For plane Couette flow, several spanwise localized solutions have been found (Schneider et al., 2010b,a; Gibson and Brand, 2014) and one doubly-localized equilibrium solution is known (Brand and Gibson, 2014). Localized solutions of plane Poiseuille and pipe flow were found by Jiménez (1990), Avila et al. (2013), Chantry et al. (2014) and Gibson and Brand (2014). For the localized periodic orbit in pipe flow found by Avila et al. (2013), it was even possible to show that a bifurcation cascade starting at its upper branch creates a chaotic saddle. However, despite the large progress within the last years, the way towards an extensive understanding of the spatio-temporal structures

of subcritical turbulence is still long.

By studying plane Poiseuille flow this thesis contributes to the progress in understanding of subcritical turbulence in the framework of dynamical systems theory. As already mentioned, plane Poiseuille flow shows turbulence for Reynolds numbers far below the one where its laminar state becomes unstable. Various exact solutions are identified for this flow that are related to the transition to subcritical turbulence. The formation of the chaotic saddle is investigated and a mechanism leading to a denser coverage of the state space is identified. Furthermore, it is investigated how the subcritical turbulence and its corresponding exact solutions are connected to the instability of the laminar state. With the distant goal to understand the formation of localized turbulence, spatially localized exact solutions are studied.

The second system studied in this thesis is the asymptotic suction boundary layer over a heated plate. Motivated by the success of the application of methods from dynamical systems theory to the transition to turbulence in shear flows, it is a self-evident idea to apply the methods to related problems. In thermal boundary layers that appear in a flow over a heated surface, special flow patterns, so-called plumes, are of accentuated importance for the dynamics and the heat transport. To study the dynamics inside of thermal boundary layers as well as the thermal plumes that appear therein, the asymptotic suction boundary layer over a heated plate is studied in this thesis as a model system for a real thermal boundary layer. For this system, the stability of the base flow and, analogous to plane Poiseuille flow, the origin of subcritical turbulence is studied. Furthermore, as for plane Poiseuille flow, localized exact solutions and mechanisms leading to their formation are investigated.

Part I

Plane Poiseuille flow

Chapter 2

An introduction to plane Poiseuille flow

Plane Poiseuille flow (PPF) is the pressure driven flow between two infinitely extended parallel plates. The study of PPF is of interest because of its analogy to pipe and duct flows, which have an enormous technical relevance. The flow is governed by the Navier-Stokes equations

$$\partial_t \vec{\tilde{u}}_{tot} + (\vec{\tilde{u}}_{tot} \cdot \nabla)\vec{\tilde{u}}_{tot} = -\nabla \tilde{p}_{tot} + \nu \Delta \vec{\tilde{u}}_{tot} \tag{2.1}$$

together with the continuity equation

$$\nabla \cdot \vec{\tilde{u}}_{tot} = 0. \tag{2.2}$$

In these equations $\vec{\tilde{u}}_{tot}$ is the velocity field, $\tilde{p}_{tot}$ is the pressure modified by density and ν is the kinematic viscosity.

Using the kinematic viscosity, the half domain width d and a characteristic velocity scale, for which most appropriately the maximum of the laminar profile U_0 is chosen, a Reynolds number,

$$Re = \frac{U_0 d}{\nu}, \tag{2.3}$$

can be defined and the equation can be made dimensionless:

$$\partial_t \vec{u}_{tot} + (\vec{u}_{tot} \cdot \nabla)\vec{u}_{tot} = -\nabla p_{tot} + \frac{1}{Re}\Delta \vec{u}_{tot}, \tag{2.4}$$

$$\nabla \cdot \vec{u}_{tot} = 0. \tag{2.5}$$

If the used velocity scales is the one of the laminar profile, this profile becomes

$$\vec{u}_0 = (U(y), 0, 0) \text{ with } U(y) = (1 - y^2). \tag{2.6}$$

The full flow field $\vec{u}_{tot}$ can be decomposed into the laminar flow and deviations from it

$$\vec{u}_{tot} = \vec{u}_0 + \vec{u}. \tag{2.7}$$

In the following, when visualizations of flow fields are shown or energies of a flow field are plotted, only the flow field $\vec{u} = (u, v, w)$ of deviations from the laminar profile is used. A coordinate system is chosen in which x points in streamwise, y in wall-normal and z in spanwise direction. A sketch of the geometry that also shows the relevant length scales and the convention used for the coordinate system is given in figure 2.1a.

The flow can be driven in different ways. In most cases it is driven by a constant pressure gradient or a constant flow rate, but in principle other constraints, e.g. constant energy input (Yosuke et al., 2014), are possible. In case of constant flow rate the bulk velocity

$$U_B = \frac{1}{2L_z} \int_{-1}^{1} \int_{0}^{L_z} \int_{0}^{L_x} u \; dxdydz$$

must be fixed at $2/3$ to obtain a laminar profile with a center-line velocity of 1. If the pressure gradient is fixed this center-line velocity is obtained with a pressure gradient of $-2/Re$.

If we have a solution of the Navier-Stokes equations for PPF (not necessarily an equilibrium solution), it has a characteristic bulk velocity and a characteristic pressure gradient. By comparing its bulk velocity with a laminar profile with the same value of U_B, a Reynolds number Re_B can be assigned to this solution. On the other hand, by comparing the pressure gradient to the one corresponding to a laminar profile, a pressure based Reynolds number Re_P can be assigned. The pressure Reynolds number can also be obtained by simply making the pressure gradient dimensionless. For the laminar solution, Re_B and Re_P are identical, but in all other cases they differ. Since Re_B and Re_P are based on the bulk velocity and the pressure gradient, Re_B is fixed in the case of constant flow rate and Re_P is constant if the pressure gradient is fixed.

Today it is a well known fact that the laminar plane Poiseuille profile becomes unstable near $Re_{crit} = 5772.22$ (Orszag, 1971), but for a long time stability of the PPF profile and especially the exact value of the critical Reynolds number and wavelengths had been unclear and subject of many studies (see e.g. Heisenberg, 1924; Lin, 1944; Thomas, 1953).

However, the results from linear stability theory fail to predict the onset of turbulence in PPF. Experimental observations as well as numerical studies show that the onset of turbulence lies somewhere around $Re_B = 1000$ (see e.g. Carlson et al., 1982; Tuckerman et al., 2014) and therefore far below the critical Reynolds number for the linear instability of the laminar profile.

Already Heisenberg, who investigated the stability of the laminar plane Poiseuille profile in 1924, doubted that the linear stability of the laminar state is able to explain the turbulence observed in PPF. He remarked (Heisenberg, 1924):

> *"Vom Standpunkt der Theorie aus müssen wir also darauf gefaßt sein, unter Umständen zwei kritische Reynoldssche Zahlen zu finden, die eine entsprechend dem Beginn der Turbulenz, die andere entsprechend dem Niederbrechen der Laminarbewegung."*

He distinguishes two different critical Reynolds numbers for the flow. The first is the Reynolds number for the onset of turbulence and the second is the one where the laminar flow becomes unstable. Indeed, the results of the stability analysis confirmed his conjecture that the critical Reynolds number for linear instability is not the one for the onset of turbulence.

Since the bifurcation of the laminar profile is subcritical, an idea how to obtain the second critical Reynolds number could be to follow the bifurcating solution to its turning point. However, the two-dimensional solution that bifurcates from the laminar flow does not extend down

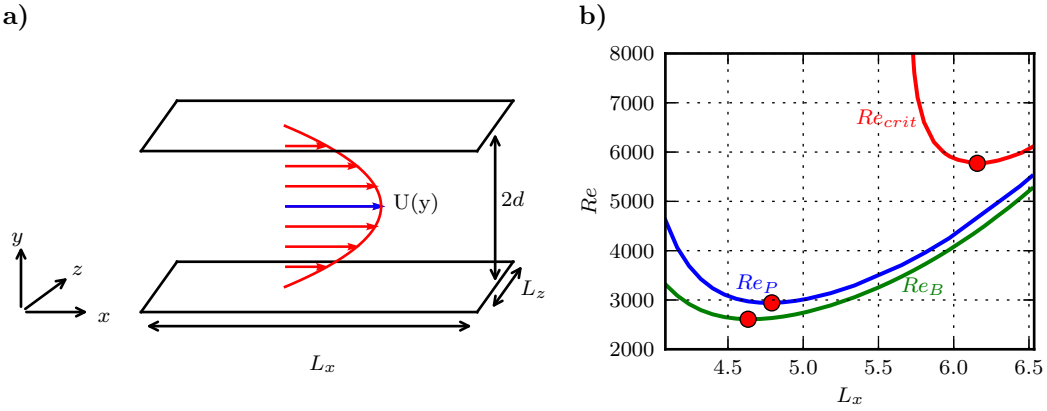

Figure 2.1: Panel a) shows a sketch of the geometry of the PPF geometry. In panel b) the critical Reynolds number of the laminar PPF profile is shown in dependence on the streamwise wavelength L_x (red). Furthermore, the bulk- and pressure Reynolds number Re_B and Re_P of the turning points of the bifurcating two-dimensional TS-wave are shown in green and blue, respectively.

to such low Reynolds numbers. In figure 2.1b the Reynolds numbers of the turning points of the two-dimensional waves are shown in dependence on the streamwise wavelength L_x. The plot illustrates that the minimal values of Re_B and Re_P as well as the corresponding wavelengths differ slightly. However, the lowest value of Re_B for which these two-dimensional waves exist is about 2610 and the lowest value of Re_P is about 2940. This is still far above the experimentally observed onset of turbulence.

Aside from the exact solutions that are created in the bifurcation of the laminar state there are other exact solutions of the Navier-Stokes equations for PPF. A couple of them have been identified during the last years (Waleffe, 2001; Nagata and Deguchi, 2013; Gibson and Brand, 2014; Rawat et al., 2014). Some of these structures exist for Reynolds numbers below the observed onset of turbulence. Chapter 3 is devoted to the identification of three-dimensional exact coherent structures. A more detailed introduction to this active topic of research will be given in this chapter and several new exact coherent structures and different strategies to find them will be presented. Moreover, the minimal Reynolds numbers for which such solutions exist will be determined.

In chapter 4 we will make a step towards the critical Reynolds number for the onset of turbulence, the second critical Reynolds number mentioned by Heisenberg. Starting with an exact coherent structure it will be shown how a sequence of bifurcations creates a chaotic saddle. A special class of bifurcations relevant in this context are crisis bifurcations that transform a chaotic attractor into a saddle. The Reynolds number at which the chaotic saddle appears can be seen as a critical Reynolds number for the appearance of transient subcritical turbulence.

In chapter 5 the connection between the exact coherent structures related to the origin of subcritical turbulence and those bifurcating from the laminar state is explored. The two known transition paths to turbulence, the bypass- and the TS-transition (see e.g. Schmid and Henningson, 2001) will be discussed and related to the different exact coherent structures. Furthermore, it is shown that in the state space different areas can be distinguished, where the two transition paths are present.

The turbulence in PPF appears at low Reynolds number in spatially inhomogeneous form. One observable phenomenon are turbulent spots (see e.g. Carlson et al., 1982; Alavyoon et al., 1986; Lemoult et al., 2013). The term turbulent spot means that the turbulence is localized in two directions parallel to the channel walls. A visualization of a turbulent spot observed in an experiment by Carlson et al. (1982) is shown in figure 2.2a.

Another manifestation of spatially inhomogeneous turbulence are laminar-turbulent bands or stripes (Aida et al., 2014; Tuckerman et al., 2014; Xiong et al., 2015) where strongly turbulent and weakly turbulent or almost laminar regions alternate in a relatively regular pattern. A visualization of a stripe pattern in PPF obtained in a numerical simulation is shown in figure 2.2b. The occurrence of laminar-turbulent bands is no peculiarity of PPF. These structures have also been found and studied in plane and Taylor-Couette flow (Prigent et al., 2002, 2003; Barkley and Tuckerman, 2005; Duguet et al., 2010a). Brethouwer et al. (2012) showed that the patterns also exist under the influence of Coriolis, buoyancy or Lorentz force but are shifted to higher Reynolds numbers. For the case of pipe flow this laminar-turbulent intermittency was already reported by Reynolds (1883) in his famous paper. Despite of the fact that laminar-turbulent patterns are a quite universal phenomenon, the underlying mechanism leading to their formation is still unclear.

A strategy that potentially might help to understand this widespread phenomenon is to explore the connection between localized exact solutions and localized turbulence. Therefore, as a step towards the distant goal to explain localized turbulence, chapter 6 is devoted to localized exact solutions of the Navier-Stokes equations for PPF. It will be shown how these structures appear and their properties will be discussed. Especially, the minimal Reynolds numbers for which they exist will be determined. Furthermore, we will explore how localized turbulent structures develop out of these solutions.

At the end of this chapter the main results will be summarized and especially all important threshold Reynolds numbers for PPF that have been found will be collected.

All performed numerical simulations of PPF use the *Channelflow*-code that was developed by J.F. Gibson (Gibson, 2012). For details on the code we refer to the channelflow manual available on www.channelflow.org. Together with T. Kreilos and M. Salewski code was adapted to work with parallel FFTW (OpenMP) and the *Octave*-library used for the linear algebra routines was replaced by the *Eigen*-package (Guennebaud et al., 2010).

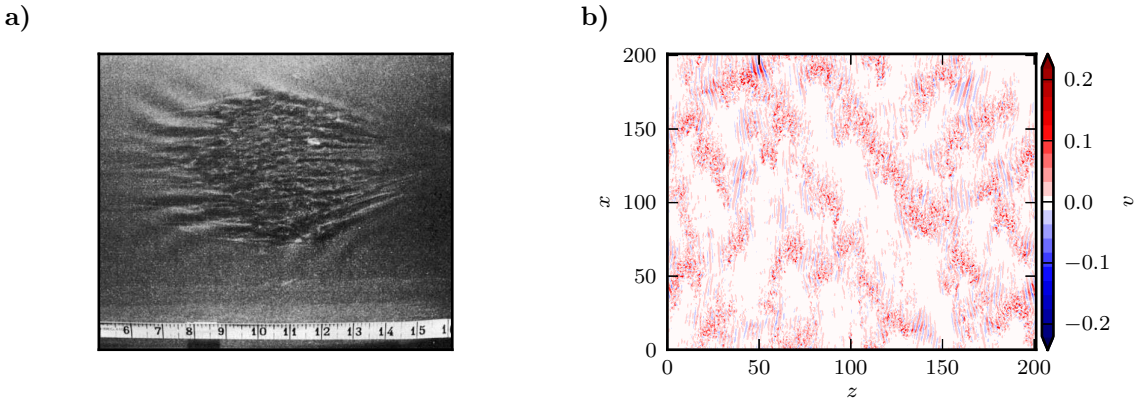

Figure 2.2: In a) a visualization of a turbulent spot observed in a channelflow experiment is shown. The picture is taken and adapted from (Carlson et al., 1982). In panel b) a visualization of laminar-turbulent pattern obtained in a numerical simulation is shown. In the visualization the wall-normal velocity component in the center-plane is color-coded. The simulation enforces a constant bulk velocity and a Reynolds number Re_B of 1100.

Chapter 3

Edge states and exact solutions in short domains

Parts of the results presented in this chapter have been published in
"Periodically bursting edge states in plane Poiseuille flow" , Stefan Zammert and Bruno Eckhardt, Fluid Dynamics Research 46 041419 (2014)
"Streamwise and doubly-localized periodic orbits in Plane Poiseuille flow" , Stefan Zammert and Bruno Eckhardt, Journal of Fluid Mechanics 761 348-359 (2014)

3.1 Introduction

For many flows in addition to the simple laminar solution other exact solutions of the Navier-Stokes equations, also called exact coherent structures (ECS), have been found. The simplest case are equilibrium solutions that do not depend on time and fulfill:

$$\vec{u}(x,y,z,t) = \vec{u}(x,y,z).$$

Various such solutions have been found for plane Couette flow (e.g. Nagata, 1990; Schmiegel, 1999; Itano and Generalis, 2009; Gibson et al., 2009). Another type of ECS are relative equilibria or traveling waves that move with a constant wave speed c and satisfy

$$\vec{u}(x,y,z,t+t_0) = \vec{u}(x-ct_0,y,z,t)$$

for all t_0. Traveling waves have been found and studied for pipe (Faisst and Eckhardt, 2003b; Wedin and Kerswell, 2004), plane Poiseuille (Waleffe, 2001; Nagata and Deguchi, 2013; Gibson and Brand, 2014), square duct flow (Wedin et al., 2009; Okino et al., 2010) and plane Couette flow (Gibson et al., 2009). The third type of ECS are (relative) periodic orbits satisfying

$$\vec{u}(x,y,z,t+T) = \vec{u}(x-cT,y,z,t)$$

for some period T. In a frame that is comoving with the constant speed c these states are periodic.

ECS play a major role for turbulent dynamics in shear flows. In the dynamical systems view of turbulence a turbulent trajectory is build up by the following two phases in an infinite loop:

1. Trajectory gets attracted by an exact coherent structure along one of its stable directions

2. Trajectory gets repelled by an exact coherent structure along one of its unstable directions

Up to now only a few exact coherent structures have been identified that are indeed embedded in the turbulent dynamics and support the above hypothesis. Most of the work has been done for plane Couette flow. For this flow homoclinic orbits embedded in the turbulent dynamics have been identified in minimal flow units (Kawahara and Kida, 2001; van Veen and Kawahara, 2011). Quite recently periodic obits that are similarly embedded in the turbulent dynamics of pipe flow have been identified by Altmeyer et al. (2014). Heteroclinic connections between exact coherent solutions (trajectories connecting two ECS) have been studied by Halcrow et al. (2009). In principle it should be possible to obtain mean quantities of a turbulent flow by using a sufficient number of periodic orbits, e.g time dependent exact coherent structures. The theory behind is the so-called periodic orbit theory (Cvitanović, 2013). An attempt to use periodic orbit theory to a hydrodynamic problem was recently made by Chandler and Kerswell (2013) for a Kolmogorov flow. However, up to now there are no successful applications to other hydrodynamic systems such as pipe or plane Poiseuille flow.

Another reason to study ECS is their proven relevance for the creation of subcritical turbulence. Recently, in plane Couette (Kreilos and Eckhardt, 2012) and pipe flow (Avila et al., 2013) simple exact coherent structures (e.g an equilibrium solution and a relative periodic orbit) have been found that are starting points of a bifurcation cascade creating a huge number of exact coherent structures and ultimately a chaotic attractor. This attractor is transformed into a chaotic saddle in a boundary crisis bifurcation. The identification of the described scenario impressively proves that exact solutions play a major role for the birth of turbulence. In chapter 4 it will be shown that the scenario is also present in plane Poiseuille flow.

Thus, because of their crucial role for the understanding of turbulent flows and the transition process this section is devoted to the identification of ECS in plane Poiseuille flow.

A powerful technique to identify exact coherent structures is *edge tracking* (Skufca et al., 2006). The state space of a subcritical flow can be divided into two parts according to the lifetimes which usually show strong fluctuations (Schmiegel and Eckhardt, 1997). Initial conditions in the one part show transient chaos with long lifetimes while such in the other part immediately return to the laminar state. Edge tracking uses this distinction to approximate a trajectory on the boundary between the two regions of state space.

For many cases this technique has been used to find attractors, so-called *edge states*, on the laminar-turbulent boundary. Edge states have been studied in plane Couette flow (Schneider et al., 2008; Duguet et al., 2009; Schneider et al., 2010b), pipe flow (see e.g Schneider et al., 2007; Duguet et al., 2008), square duct flow (Biau and Bottaro, 2009), parallel (Kreilos et al., 2013; Khapko et al., 2013) and even spatially developing boundary layers (Cherubini et al., 2011; Duguet et al., 2012). However, the edge state does not necessarily be an exact coherent structure. In many cases, especially in spatially extended domains, the edge state turns out to be chaotic (e.g. Duguet et al., 2009; Mellibovsky et al., 2009). The technique of edge

tracking will be used in section 3.2 and 3.3 to identify exact coherent structures in rather small computational domains.

Another strategy to search for ECS is to study the bifurcations of a known solution. In section 3.4 this strategy will be applied to the traveling wave bifurcating subcritically from the laminar plane Poiseuille profile.

A third successful strategy is the use of homotopies between different flows (e.g Nagata, 1990; Waleffe, 2003; Kreilos et al., 2013; Gibson and Brand, 2014; Deguchi et al., 2014). This method uses a so-called homotopy parameter to interpolate between two flow systems. A known solution of one flow (e.g. Taylor-Couette flow) can then be transfered to the another system (e.g Plane Couette flow) by a continuation in the homotopy parameter. For example, this method was used by Nagata (1990) who discovered the first three-dimensional exact solution in plane Couette flow (today often referred to as NBC-solution because Clever and Busse (1992) obtained the same exact solution using Rayleigh-Bénard-Couette flow) by tracking a three-dimensional exact solution from Taylor-Couette flow to plane Couette flow. In the context of the asymptotic suction boundary layer flow with and without temperature gradient this strategy is used in section 11.7.

3.2 Traveling waves edge states

Through extensive usage of edge tracking in different computational domains and with imposed symmetries, it was possible to find four different travelling wave.

In a short and narrow computational domain with a streamwise and spanwise extend of 0.75π, edge tracking quickly converges to a state with constant energy density,

$$E(\vec{u}) = \frac{1}{2L_xL_yL_z}\int_{-1}^{1}\int_{0}^{L_x}\int_{0}^{L_z}\vec{u}^2\ dxdydz. \tag{3.1}$$

We use a Newtons method (Viswanath, 2007) to converge to an exact solution. The method is briefly summarized in section A.3. Newtons method converges to a traveling wave that is localized to one side of the channel. We will refer to this traveling wave as TW_{Ew}. It obeys the symmetry

$$s_z\tau_x(\lambda_x/2) : [u,v,w](x,y,z) = [u,v,-w](x+\lambda_x/2,y,-z)$$

where λ_x is the streamwise wavelength of the traveling wave.

In a computational domain with a streamwise length of 2π and a width of 2π the edge state is a traveling wave (see Zammert, 2011; Zammert and Eckhardt, 2014c) that is symmetric to the center-plane,

$$s_y : [u,v,w](x,y,z) = [u,-v,w](x,-y,z)$$

and additionally obeys a shift-and reflect symmetry

$$s_z\tau_x(\lambda_x/2) : [u,v,w](x,y,z) = [u,v,-w](x+\lambda_x/2,y,-z).$$

The traveling wave shows a weak spanwise localization for $L_z = 2\pi$. If the width of the domain is increased the wave remains an edge state with the mentioned symmetries, but it becomes localized in spanwise direction.

In a short but wide domain with $L_x = 0.5\pi$ and $L_z = 2\pi$, the edge state is another traveling wave, referred to as TW_{Ew2}. This traveling wave is also localized to one side of the channel but

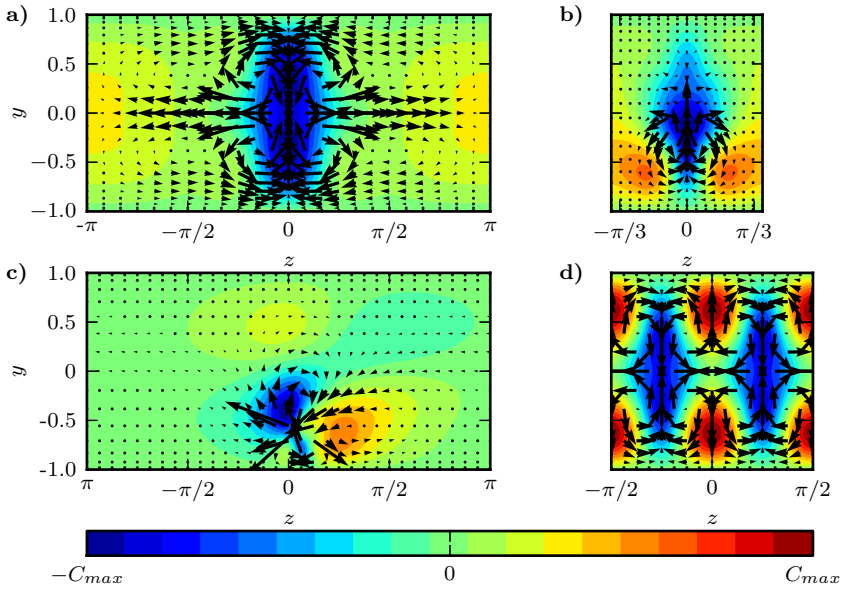

Figure 3.1: Streamwise averaged flow in the spanwise wall-normal plane for the traveling waves TW_E (a) , TW_{Ew} (b), TW_{Ew2} (c), and TW_{Eyz} (d). The values of C_{max} used in a) - d) are 0.089, 0.182, 0.225 and 0.166, respectively. The streamwise wavelength used in a) and d) is 2π. For b) and c) the wavelength is 0.75π and 0.5π, respectively.

additionally it is localized in the spanwise direction. TW_{Ew2} travels in streamwise direction and also slowly in spanwise direction.

For a domain with $L_x = 2\pi$ and $L_z = \pi$ and a symmetry restriction to a subspace with the discrete symmetries s_y and s_z (wall-normal and spanwise reflections), the edge state is a highly symmetric traveling wave (TW_{Eyz}). In section 3.2 the bifurcations of the upper branch of this traveling wave will be studied.

For all four traveling waves visualizations of the average flow in the streamwise wall-normal plane are given in figure 3.1. The figures reveal that TW_{Ew2} has the smallest structures. Furthermore, it shows the spanwise localization of TW_E and TW_{Ew2}.

The traveling wave TW_E is of accentuated importance for the system. In wide but short ($L_z \leq 2\pi$ and $L_x \approx 2\pi$) the wave localizes in spanwise direction and is the edge state of the system. In large computational domains exact solutions that bifurcate from TW_E are found to be edge states. This will be discussed in detail in the sections 6.2 and 6.3. Since TW_E or bifurcating states seem to dominate the laminar-turbulent boundary, it is reasonable to ask which domain size is necessary for TW_E to exist. Therefore, the dependences of the Reynolds numbers (Re_B and Re_P) of the bifurcation point of TW_E on the spanwise and streamwise wavelength are investigated. The results are shown in figure 3.3. In wide domains TW_E localizes in spanwise direction. Therefore, the position of the turning point does only change weakly if L_z is increased above 3π. The lowest bulk Reynolds number for the bifurcation point is 316.8 and is achieved for $L_z = 2.8\pi$ and $L_x = 2.95\pi$ (for the sampling of the parameter space steps of 0.05π in L_x and of 0.1π in L_z are used). Figure 3.3 shows impressively that for a wide range of spatial wavelengths the traveling wave appears at Reynolds numbers far below those for the onset of subcritical turbulence ($Re_B \approx 1000$). In quite narrow or short domains

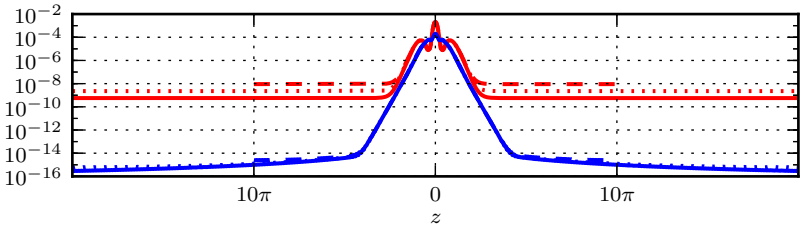

Figure 3.2: The spanwise variation of the full energy density $E_{\parallel}(z)$ (red) and the cross-flow energy density $E_{cf,\parallel}(z)$ (blue) for the edge state TW_E in domains of different width is shown. In each case the Reynolds number is 3000 and the streamwise wavelength is 2π. The domains widths L_z are 20π (dashed), 40π (dotted) and 80π (solid).

TW_E does either not exist, or it appears at Reynolds numbers much higher than the minimal one. Since the usual edge state of PPF does not exist or appears at high Reynolds numbers the features of transitional and turbulent flows in these small domains should be expected to be different from the one in large domains and in the actual physical system. E.g. the onset of sustaining turbulence lies at higher Reynolds number. In section 3.3 the edge states that replace TW_E in these short computational domains are discussed. Good measures for the localization of TW_E are the spanwise variation of the full energy density,

$$E_{\parallel}(z) = \frac{1}{4L_x} \int_0^{L_x} \int_{-1}^{1} \vec{u}^2 \, dxdy, \tag{3.2}$$

and the cross-flow energy density

$$E_{cf,\parallel}(z) = \frac{1}{4L_x} \int_0^{L_x} \int_{-1}^{1} (v^2 + w^2) \, dxdy. \tag{3.3}$$

Both densities are shown in figure 3.2 for $Re_B = 3000$ and different values of L_z. The maximum of the energy densities lies at the position of the low speed streak. With increasing distance to the maximum both densities decrease exponentially over several orders of magnitude. After this phase both densities remain at nearly constant finite values. The fact that these values decrease with increasing size of the computational domains suggest that there is an influence of the periodic boundary conditions on the localization.

For the other three traveling waves the minimal Reynolds number for the turning point is higher than for TW_E. The lowest Re_B for TW_{Eyz} is 410 while for TW_{Ew1} and TW_{Ew2} the lowest Re_B lies between 1000 and 2000. Depending on the traveling wave the minimal values of Re_B and Re_P might be far apart from each other. This phenomenon is illustrated in figure 3.4 where the pressure Reynolds number is plotted vs. the bulk Reynolds number for several traveling waves. For TW_{Eyz}, which is plotted for $L_x = 2\pi$ and $L_z = 1\pi$, the minimal values of Re_B (642.2) and Re_P (924.8) differ by almost 300. For TW_E the figure shows the solution curves for $L_x = 2.2\pi$ and $L_z = 2\pi$ (solid greed) and for $L_x = 3\pi$ and $L_z = 4\pi$ (dashed green). The minimal values of Re_B and Re_P are close to each other for this traveling wave. In the narrow domain with $L_z = 2\pi$ the difference is 26.7 and in the wide domain with $L_z = 4\pi$, where TW_E is already strongly localized, the difference is only 13.8. The increasing localization of TW_E with increasing L_z makes the solutions branch sharper and pushes it towards the diagonal of the diagram which corresponds to the laminar solution). Using the illustration in figure 3.4

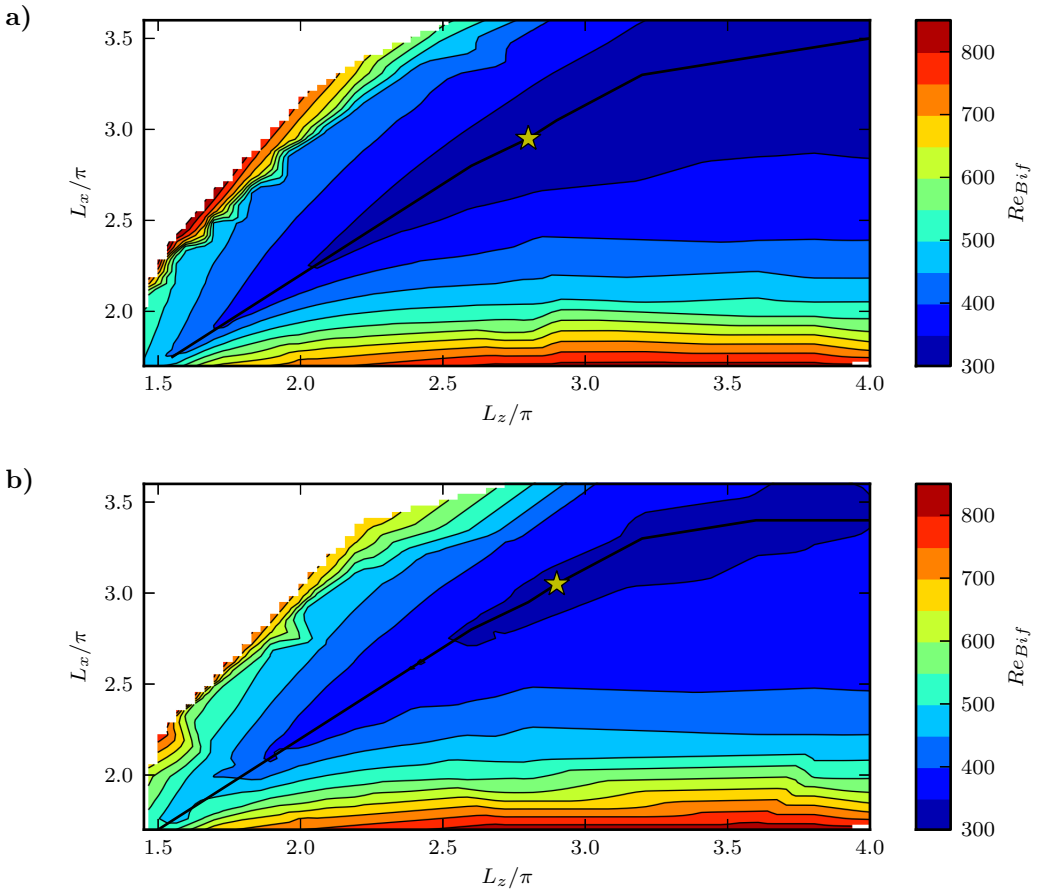

Figure 3.3: Panel a) and b) show the bulk Reynolds number Re_B and the pressure Reynolds number Re_P of the bifurcation point for the traveling waves TW_E in dependence on the streamwise and spanwise wavelengths. The black line shows the streamwise wavelength for the minimum Reynold number vs. spanwise wavelength. The point of the minimal Reynolds number for the bifurcation point is marked by a yellow star.

differences between the two most common operating conditions for PPF can be explained. If PPF is driven by a constant pressure gradient, this corresponds to a horizontal line while driving with constant mass flux corresponds to a vertical line. If the flow is laminar, there is no difference between a system with a fixed $Re_B = 700$ and another one with a fixed $Re_P = 700$, but if they depart from the laminar state the systems are different. They have to be different as their state space contains different exact coherent states. The gray line in the figure shows that thus having the same laminar state the intersections with the solution branches of the ECS are different for constant pressure gradient and constant bulk velocity. While for some ECS the intersections are close to each other (e.g. the lower branches of TW_E and its upper branch in the wide domain), for other ECS the intersections have a large distance. In particular, for the example case of constant bulk velocity shown in the figure using a gray vertical line there are intersections with the solutions branch of TW_{Eyz}. For the system operating at constant pressure gradient, there are no intersection with this solution branch of TW_{Eyz}.

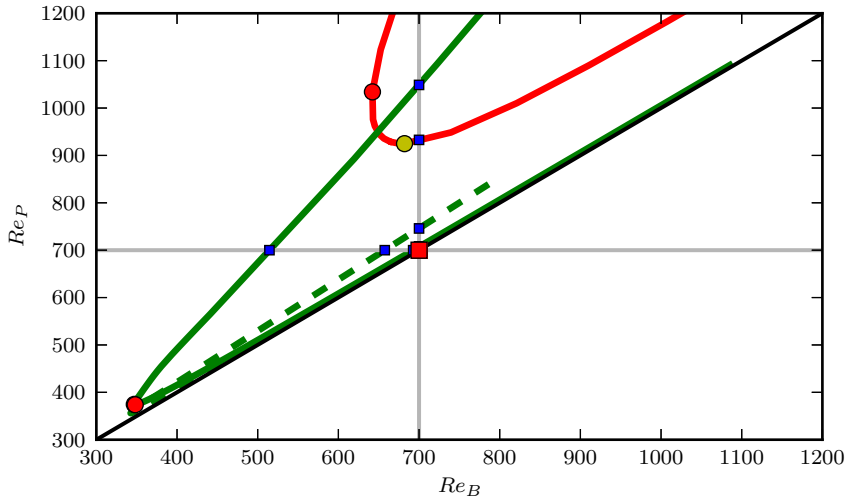

Figure 3.4: Pressure Reynolds number Re_P vs. bulk Reynolds number Re_B for selected travelling wave edge states. The red line shows the solution branch for TW_{Eyz} with $L_x = 2\pi$ and $L_z = \pi$. The green lines show the solution branches of TW_E for $L_x = 2.2\pi$ and $L_z = 2\pi$ (solid) and for $L_x = 3\pi$ and $L_z = 4\pi$ (dashed). The lowest values of Re_P and Re_B are marked on each branch by yellow and red cicles, respectively. The diagonal represents the laminar solution. The horizontal and vertical lines illustrate systems operating at constant pressure gradient and constant bulk velocity that have a common laminar solution (red square) but different intersections with the solution branches (blue squares).

By regarding the Re_P vs. Re_B representation it becomes evident that the common classification in terms of lower and upper branch solutions is not natural because the position of the bifurcation or turning point depends on the operating condition. Therefore, a state that is on the so-called upper branch for the case of constant bulk velocity can be on the lower branch if the system operates at constant pressure gradient.

Nevertheless, the influence of the operating condition on the Reynolds number for the onset of subcritical turbulence is most-likely small. Because the solution branch of TW_E, the edge state of the system without symmetry restriction, is very sharp and quite close to the diagonal, the intersections with this solution branch are close to each other for the two operating conditions.

The travelling waves TW_E and TW_{Eyz} exist down to very low Reynolds numbers far below the observed onset of turbulence. Since there is a large range in Reynolds number where no sustained turbulence can be observed despite existing three-dimensional ECS, the appearance of ECS is no good predictor for the onset of subcritical turbulence in PPF. This is also true for the case of pipe flow as pointed out by Pringle and Kerswell (2007). A more reliable way to find a critical Reynolds number starting from an exact coherent structure will be presented in section 4 where the bifurcations of TW_{Eyz} are explored.

3.3 Periodically bursting edge states

This section is devoted to a special class of edge states with a complex temporal dynamics that can be found in PPF. For short computational domains ($L_x < 2\pi$) and appropriate choices of L_z and Re_B, edge states in PPF are relative periodic orbits. These orbits have large periods and consist of a quiet phase during which the internal dynamics is only weak, and a dynamically very active bursting phase. The states have a huge similarity to the edge states in the asymptotic suction boundary layer (Kreilos et al., 2013; Khapko et al., 2013, 2014). A first orbit of this kind was found for an isolated value of Re_B by Toh and Itano (2003). For a fixed computational domain and $Re_B = 3000$ they found a periodic orbit by an edge-tracking method. In this section the results by Toh and Itano (2003) will be reproduced and extended to other domains and Reynolds numbers.

Narrow domains

In their pioneer work Toh and Itano (2003) showed that for $Re_B = 3000$ in small domains with a streamwise extent of π and a spanwise extent of 0.4π a trajectory on the edge of chaos shows periodic behavior. For long times the edge trajectory is nearly constant in energy and then a sudden burst appears. In their preceding publication (Itano and Toh, 2001), they speculate on base of the long quiet phases that the edge state is a traveling wave but finally they were able to prove that the state is periodic. However, they used specially shaped initial conditions and not arbitrary turbulent fields as initial conditions for their edge tracking. We use the same domain size and perform edge tracking starting from arbitrary turbulent fields. A numerical resolution of $N_x \times N_y \times N_z = 32 \times 65 \times 32$ is used and a constant mass-flux is imposed. In this section the term Reynolds number does always refer to the bulk Reynolds number Re_B. A typical edge trajectory is shown in figure 3.5 where on the y-axis the energy density,

$$E(\vec{u}) = \frac{1}{2L_xL_yL_z}\int \vec{u}^2 dxdydz, \tag{3.4}$$

is shown. The edge trajectory quickly reaches a state that looks periodic. The energy density E of this periodic orbit that we will in the following refer to as PO_1 repeats after a period T of 1508 advective time units.

This is a large time scale for this system, because a structure travelling with the mean speed of the flow $u_{mean} = 2/3U_0$ only needs about 4.7 time units to traverse the domain. The orbit

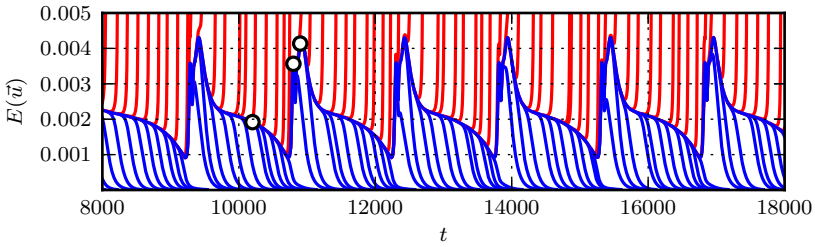

Figure 3.5: Edge tracking at $Re_B = 3000$ in a domain with size $L_x = \pi$ and $L_z = 0.4\pi$. For each refinement step the energies of the final turbulent and laminar trajectories are shown. The flow in the streamwise wall-normal plane is shown in figure 3.6 for the times marked by the black circles.

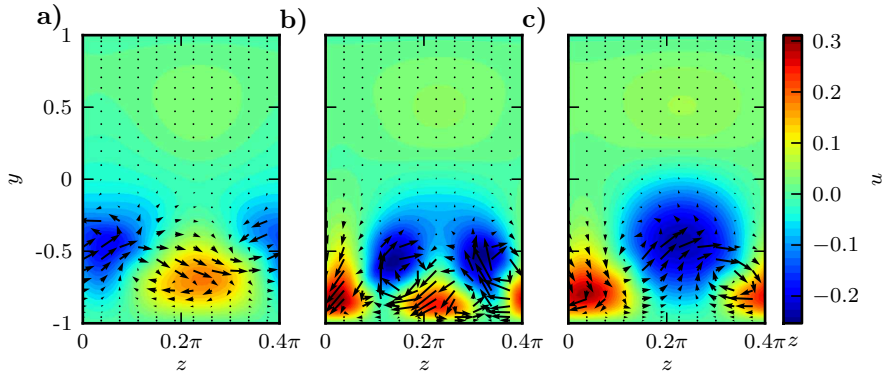

Figure 3.6: Flow in the streamwise wall-normal plane at $x = 0$ for the times marked by the black circles in figure 3.5. The streamwise velocity (deviation from the laminar profile) is color coded and the velocity in the plane is visualized by the arrows.

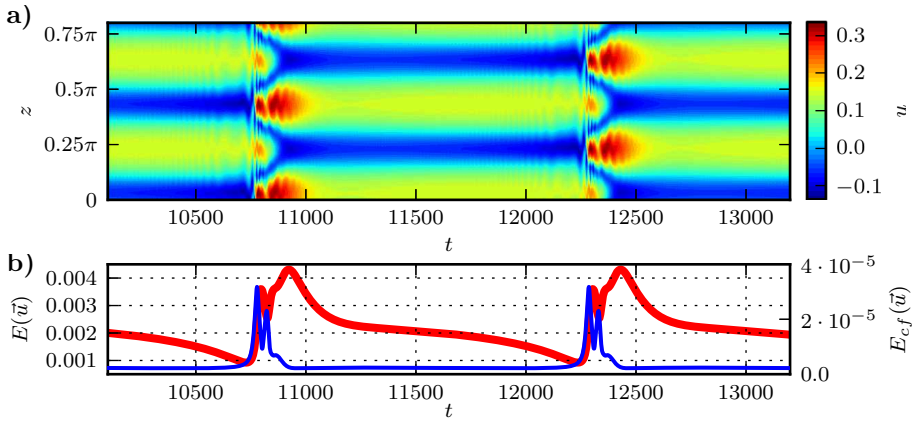

Figure 3.7: Time evolution of the periodic edge state PO_1. a) shows the streamwise velocity at the position $y = 0.223$ and $x = 0$ vs. time and reveals the spanwise dislocation by half a box width. b) shows the total (thick red line) and cross-flow energy (thin blue line) for the same time interval and the massive increase during the burst events.

consists of long phases during which the flow structure only varies slightly. These long quiet phases are separated by "bursting" phases with very active dynamics. Visualizations of the flow structure for different positions on the orbit are shown in figure 3.6. The positions of the visualizations on the orbit are marked by black circles in figure 3.5. During the quiet phases the flow structure shows a pair of streaks that is localized on one side of the channel. In the bursting phase the pair of streaks splits into two pairs (see figure 3.7b), the flow reorganizes and one pair of streaks is formed that is shifted by $L_z/2$ compared to the initial one. Periodic obits with comparable dynamics were found in the asymptotic suction boundary layer (ASBL) by Kreilos et al. (2013). To visualize the evolution of the streak pair during the orbit in figure 3.7a the time-variation of the streamwise velocity at fixed x-coordinate and at a distance of 0.233 from the lower plate is shown. Additionally, in figure 3.7b the corresponding full energy

$E(\vec{u})$ and cross-flow energy,

$$E_{cf}(\vec{u}) = \frac{1}{2L_xL_yL_z}\int (v^2+w^2)dxdydz, \tag{3.5}$$

are plotted. The cross-flow energy is a more reliable indicator of persistent dynamics than the full energy E since the flow will relaminarize if its value is too low, while even flow structures with a large value of E can immediately decay if there is no cross-flow motion. The fact that the orbit shifts in spanwise direction by one half of the domain width means that after two periods in energy we re-obtain the initial state up to advection in streamwise direction.

The periodic orbit shows many of the features described in the self-sustaining process of Waleffe (1997). The pair of streaks that exists during the quiet phase decays slowly, resulting in a slow decrease of total energy. At a certain point in time the streaks undergo an instability, new vortices form and the cross-flow energy content increases dramatically. Due to the cross-flow motion, energy is transfered into the streamwise component and strong streaks are formed. These streaks than undergo instabilities that nucleate further vortices and the cycle starts again.

As already mentioned, the orbit is remarkably similar to the edge states in the ASBL. This similarity can be explained by the fact that the ASBL profile close to the wall is similar to the Poiseuille profile from the wall to the mid-plane. Both profiles have a strong gradient in the velocity profile close to the wall which becomes smaller with increasing distance to the wall. It can be conjectured that this curse of the derivative of the laminar profile is crucial for the existence of this kind of bursting states. The theory is supported by the fact that for plane Couette flow, where the derivative of the base flow is constant, such bursting orbits have not been found yet while they appear if the laminar state is deformed towards the ASBL profile (Kreilos et al., 2013).

We want to track the orbit that was found at $Re_B = 3000$ to other Reynolds numbers. Since the period of the orbit is too long to achieve convergence with a Newton-method, we use edge tracking to continue the orbit in Re_B. This is done by using a flow field of one Reynolds number as initial condition for an edge tracking at a neighboring Reynolds number. For some values of Re_B it is checked if the tracked state is still an attracting edge state by performing an independent edge tracking starting from a random turbulent initial condition. It is possible to track the orbit down in Reynolds number to about 2100. The attracting states on the edge are similar to PO_1 in that they all show bursts in energy. However, there are differences in detail, and for some Re_B the sequence of bursts is not periodic but chaotic. In figure 3.8a a bifurcation diagram of the edge states is shown using the time between two bursts along the ordinate. For Reynolds numbers where the attracting edge state is periodic, the distance between two bursts becomes constant after an initial, possibly very long, transient, resulting in a single square entry in figure 3.8a. For period-doubled states two squares and in case of a aperiodic chaotic state small dots are plotted. Figure 3.8b shows the bifurcation diagram using the maximum of energy on the ordinate. Blue symbols are used for states that are similar to PO_1 in the sense that they shift by half a domain width between two bursts or that they bifurcate from these states. An example bifurcation is shown in the inset in figure 3.8b, where a period-2 state is created in a forward bifurcation at $Re_B \approx 2950$ and disappears again in an inverse pitchfork bifurcation at $Re_B \approx 2987$.

Another periodic orbit, referred to as PO_2, is found for $3200 < Re_B < 3300$ (green circles in figure 3.8). The states have relatively low periods between 400 and 500 time units and differ from PO_1 in that the structures do not shift by half a wavelength in spanwise direction over one period in energy. Specifically, after one period in energy the flow field equals the original

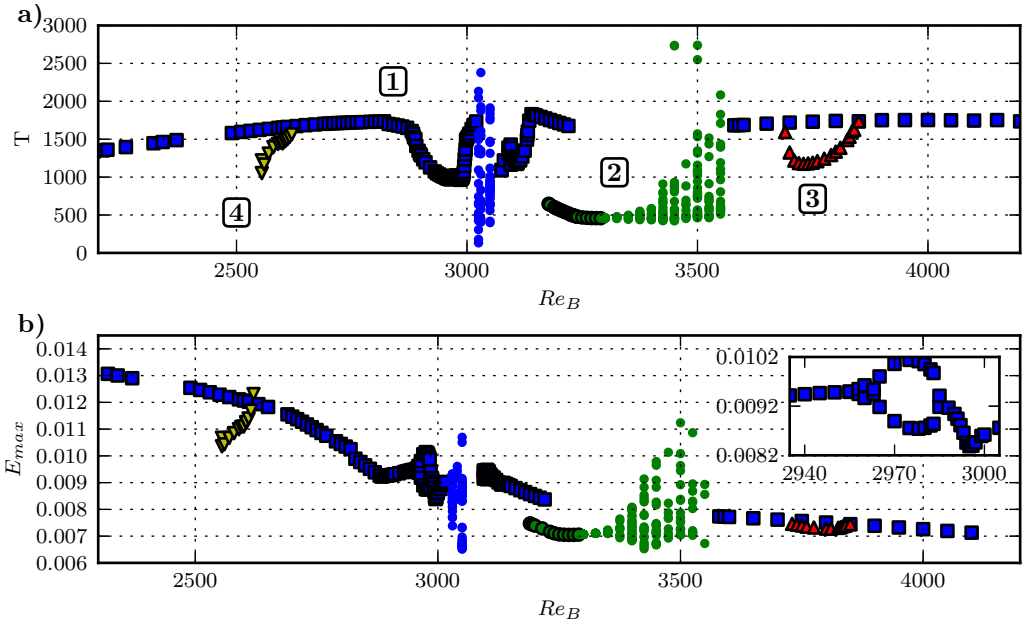

Figure 3.8: Bifurcation diagram for the edge states as a function of Reynolds number. The labels 1, 2, 3 and 4 indicate where the periodic orbits PO_1, PO_2, PO_3 and PO_4 are located. Panel a) shows the times between two bursts. If the identified edge state is a periodic state, the values are shown as squares, if it is aperiodic small dots are shown. In panel b) the maximum energy during the burst is used on the ordinate. The inset shows a small window where, with increasing Reynolds number, the PO_1 first undergoes a period-doubling, which then is reversed.

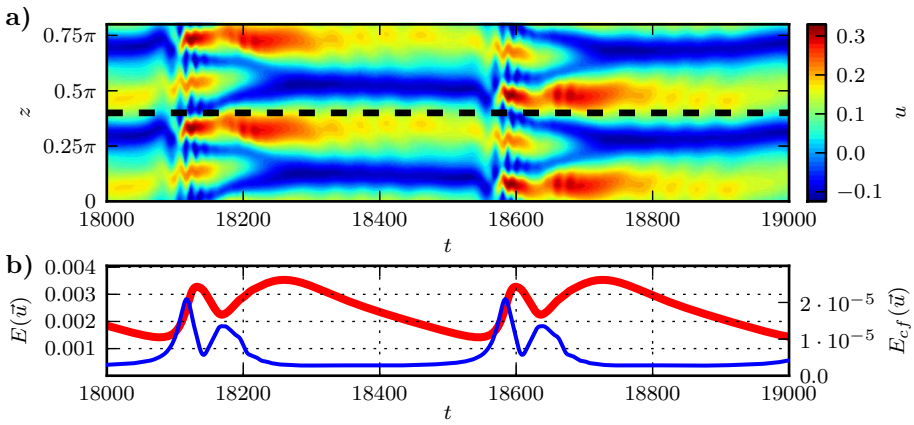

Figure 3.9: Time evolution of the periodic edge state PO_2 at $Re_B = 3250$. Panel a) shows the streamwise velocity at the position $y = 0.223$ and $x = 0$ vs. time and reveals the spanwise dislocation by half a box width. Panel b) shows the total (thick red line) and cross-flow energy (thin blue line) for the same time interval and the massive increase during the burst events.

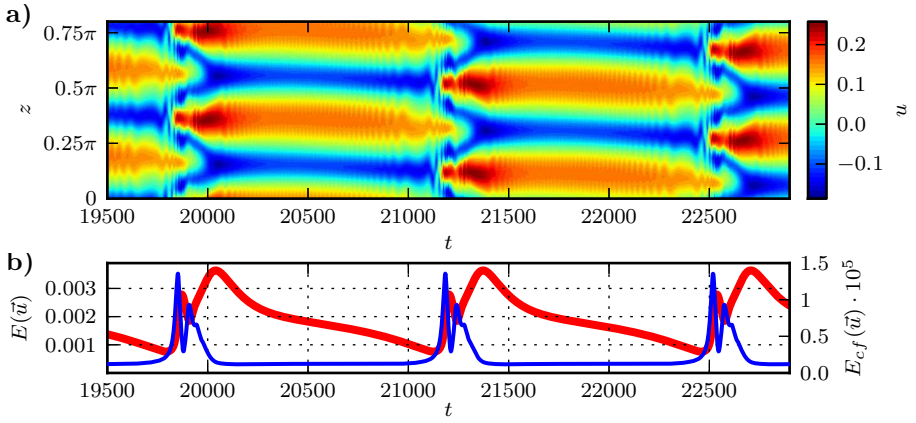

Figure 3.10: Time evolution of the periodic edge state PO_3 at $Re_B = 3800$. The visualizations are the same as in figure 3.7.

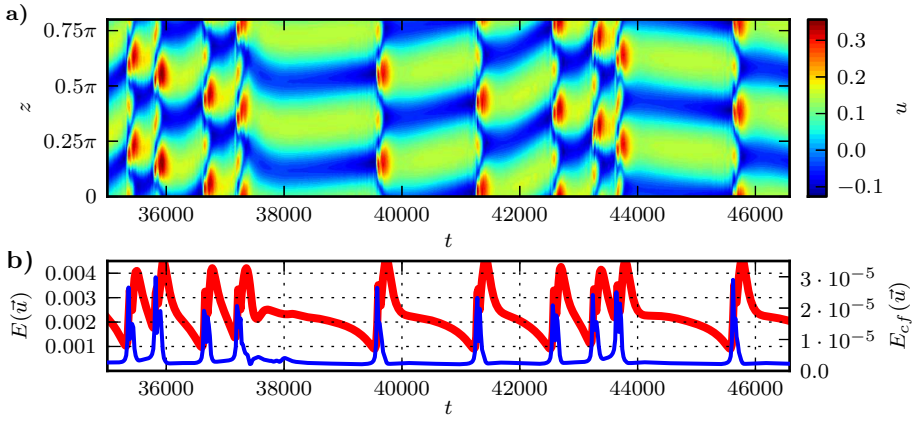

Figure 3.11: Space-time dynamics for a chaotic edge state at $Re_B = 3030$. The visualisations are the same as in figure 3.7.

one except for a spanwise reflection ($s_z : [u, v, w](x, y, z) = [u, v, -w](x, y, -z)$). The dynamics of the PO_2-state is visualized in figure 3.9 where also the axis for the reflection is shown. PO_2 undergoes a Neimark-Sacker bifurcation close to $Re_B = 3300$ which is followed by further bifurcations as Re_B increases. The orbit finally disappears close to $Re_B = 3600$.

Yet another periodic orbit, PO_3, is found for Re_B around 3800 (red triangles in figure 3.8). It differs from the above orbits in the displacement following the burst, which is only $0.385L_z$ (see figure 3.10). It seems to exist in a small range in Re_B only. The deviation of the shift from half a domain width is a precursor to the behavior in wider domains, where the sideways displacement becomes a consequence of the intrinsic dynamics and is not correlated with the width of the domain (a phenomenon also seen in the ASBL).

Between $Re_B = 2500$ and 2600 a fourth orbit (PO_4) exists. After one period in energy the state returns up to a spanwise reflection $s_z : [u, v, w](x, y, z) = [u, v, -w](x, y, -z)$. Therefore, the orbit has the same symmetry properties as PO_2 but larger periods.

In addition to the four orbits PO_1-PO_4 highlighted above there are also more complicated relative attractors in the edge. In particular, in the region between $Re_B = 3000$ and $Re_B =$

3100, many different states can be found. Among them are period doubled states, e.g. near $Re_B = 2960$ and 3095. States with higher periods exist as well: for instance, at $Re_B = 3090$ the relative attractor shows six different maxima in energy and hence corresponds to a period 6 state. For $Re_B = 3035$ the edge trajectories are chaotic but show intermittent behavior: the trajectories stay near a periodic state with essentially constant inter-burst periods for several 1000 time units before they enter a chaotic phase. For the slightly smaller Reynolds number of $Re_B = 3030$, the attracting state in the edge is chaotic without any intermittency, but the flow structure and the dynamics is quite similar to the periodic orbits at slightly higher Re_B, as is evident from the visualization of the edge trajectory shown in figure 3.11.

In order to demonstrate the periodicity of the orbits, we consider the orbit PO_1 at $Re_B = 3000$. In figure 3.12a we show the energy of the difference between the initial velocity field and a symmetry related one at a later time, $\vec{u}(t_0) - S(\vec{u}(t_0 + t))$. The symmetry operation S consists of the shifts in spanwise and streamwise direction that gives the minimal difference for a given value of t. The time between the two peaks with minimal energy is 1508 and corresponds to one period T in energy. After applying the symmetry operation S the energy of the difference of two flow fields after a time T is of order 10^{-7}, demonstrating that the orbit is closed. The same check of convergence was done for PO_2 at $Re_B = 3250$, where the symmetry operation S consists of a reflection in spanwise direction at the axis shown in figure 3.9 and the streamwise shift that minimizes the difference for a given value of t. In figure 3.12b the course of the energy difference for this orbit is shown. For PO_2 the time between the two peaks with minimal energy is 934.05 and corresponds to two periods T in energy. Therefore, the energy period of PO_2 is approximately $T = 467.025$ for this Reynolds number. After applying the appropriate symmetry operations the energy of the difference of two flow fields after a time T is of order 10^{-8}. The same analysis for PO_3 at $Re_B = 3800$ yields an error of $1 \cdot 10^{-7}$ and a period $T = 1333.5$.

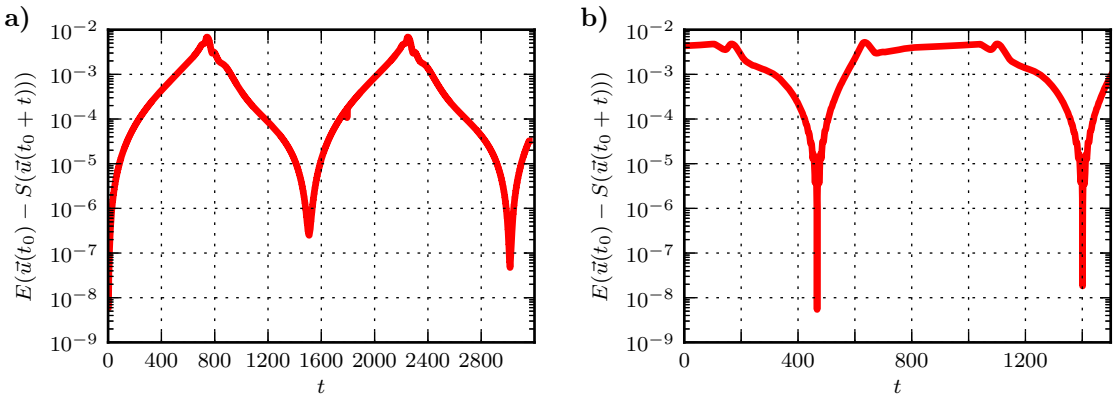

Figure 3.12: Energy of the difference flow field $\vec{u}(t_0) - S(\vec{u}(t_0 + t))$ as a function of t for $t_0 = 17964$. The symmetry operation S consists of a reflection in spanwise direction s_z (at the axis shown in figure 3.9) and the streamwise shift that gives the minimal difference for the value of t. The energy of the difference field has minima for $t = T$ and $t = 3T$.

Wide domains - Spanwise localized states

The edge states in narrow computational domains are quite similar to those found in the ASBL. Since for ASBL in wide domains the edge states become localized in spanwise direction while retaining the bursting and shifting features (Khapko et al., 2013, 2014), the question rises if this phenomenon can also be found in PPF. Because the bursting behavior in PPF can be observed for a domain width that is smaller by a factor of 5 than for the spatially extended states in ASBL, localization should also occur for narrower domains than in the ASBL. Khapko et al. (2013) use a domain with a width of 50 where the states they obtain are already strongly localized in spanwise direction. Thus, one can expect localized states in PPF for a width of 10. Nevertheless, it turns out that already a width of 2π is sufficient to obtain states showing spanwise localization.

We investigate the edge state in a computational domain with a spanwise width of 2π for various streamwise wavelengths. For a streamwise wavelength of 1.5π with resolution $N_x \times N_y \times N_z = 32 \times 65 \times 96$ a periodic edge state was identified. For this orbit the initial flow structure is obtained after one period in energy, but it is advected in streamwise and shifted in spanwise direction. In figure 3.13 a space-time plot of the orbit using the same visualizations as for the states in the narrow domains is shown. The figure reveals that the state continuously shifts to the right during the bursting phase and that it is weakly localized in the spanwise direction. We will refer to this orbit as $PO_{E,R}$ in the following. If the state is reflected in spanwise direction, an orbit continuously shifting to the left ($PO_{E,L}$) is obtained. The two orbits are reminiscent of the L- and R-states found by Khapko et al. (2013) in the ASBL. Since, the periods of the orbits, as in the narrow domains, are quite long, it is not possible to converge the orbits with a Newton-method. Furthermore, we are not able to analyze their stability by calculating the eigenvalues. A way to determine the stability of $PO_{E,R}$ inside the laminar-turbulent boundary is to use first return maps (Khapko et al., 2014). The maxima of $\sqrt{E(\vec{u})}$ on an edge trajectory converging towards $PO_{E,R}$ are collected. Then, the $(i+1)$-th maximum is plotted versus the i-th maximum. By calculating the slope β of the points close to the diagonal it is possible to receive information about the stability of the orbit. If $|\beta| < 1$ the orbit is stable inside the edge

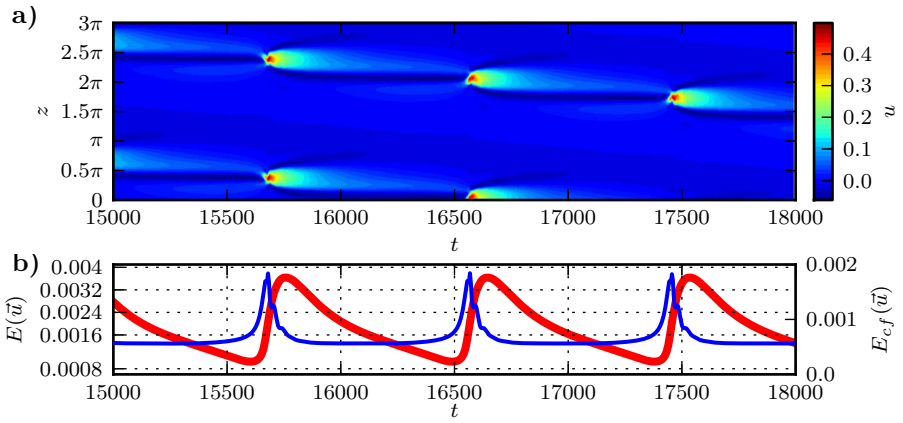

Figure 3.13: Time evolution of the periodic edge state $PO_{E,R}$. Panel a) shows the streamwise velocity at the position $y = 0.223$ and $x = 0$ vs. time and reveals the spanwise dislocation of the state. Panel b) shows the total (thick red line) and cross-flow energy density (thin blue line) for the same time interval and the massive increase during the burst events.

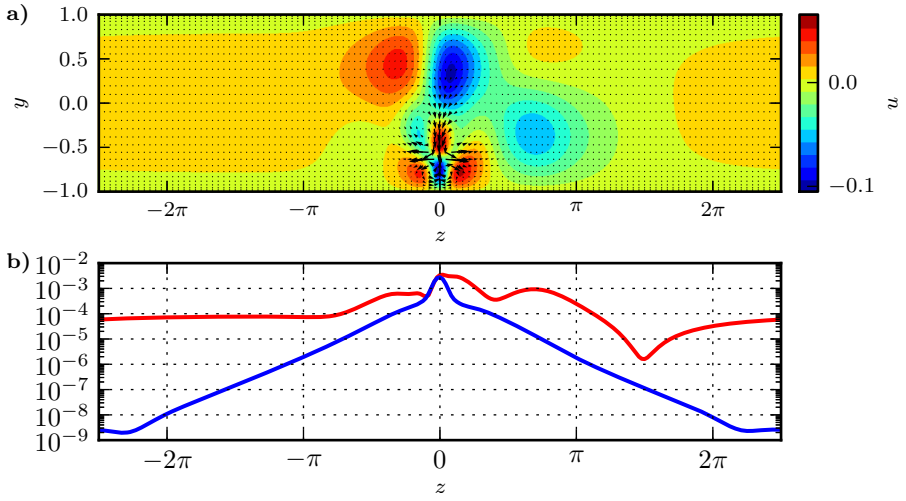

Figure 3.14: Periodic orbit $PO_{E,R}$ in a domain with $L_z = 5\pi$ at the time of minimal energy E. In a) the mean flow in the spanwise wall-normal plane is shown. Panel b) shows the total $E_{\|}(z)$ (red line) and cross flow energy density $E_{cf,\|}(z)$ (blue line) vs. spanwise coordinate z

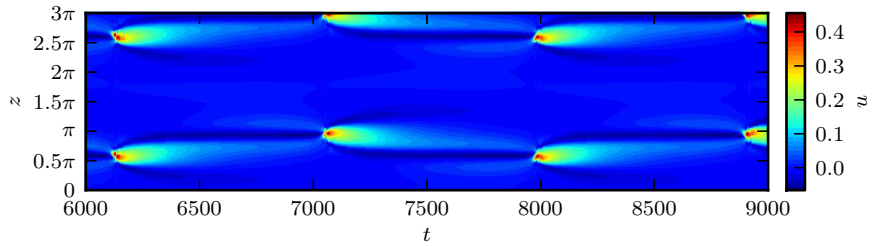

Figure 3.15: Space-time representation of the periodic orbit $PO_{E,LR}$. Shown is the streamwise velocity at $y = -0.858$ and $x = 0$ versus time. The Reynolds number is 3000 and the length and width of the domain are 1.15π and 2π, respectively.

and for $|\beta| > 1$ it is unstable. For $PO_{E,R}$ at $Re_B = 3000$ we obtain $\beta = -0.63$ what indicates that the orbit is indeed a stable attractor inside the laminar-turbulent boundary.

To study the localization of $PO_{E,R}$ which is already present for $L_z = 2\pi$, the orbit is transferred to a computational domain with $L_z = 5\pi$. Edge tracking is used to converge to the orbit. For the time of minimal energy the streamwise averaged flow in the spanwise wall-normal plane is shown in figure 3.14a. The strong part of the flow structure is restricted to a small part of the domain with a width of approximately 1.5π.

As in section 3.2 the spanwise variation of the full energy density $E_{\|}(z)$ and the cross-flow energy density $E_{cf,\|}(z)$ of the deviation from the laminar flow are used as measures for the localization. In figure 3.14b both densities are plotted for the time of minimal energy. The plot reveals a high asymmetry of the state, especially for the streamwise velocity component. To the right of the dynamically active structure in the middle of the domain the decrease of $E_{\|}$ is rather slow while on the other side the quantity quickly drops almost four powers of ten. In contrast to the full energy density, the cross-flow component is almost symmetric and shows a nice exponential decay over several orders of magnitude on each side. Despite of the L- and

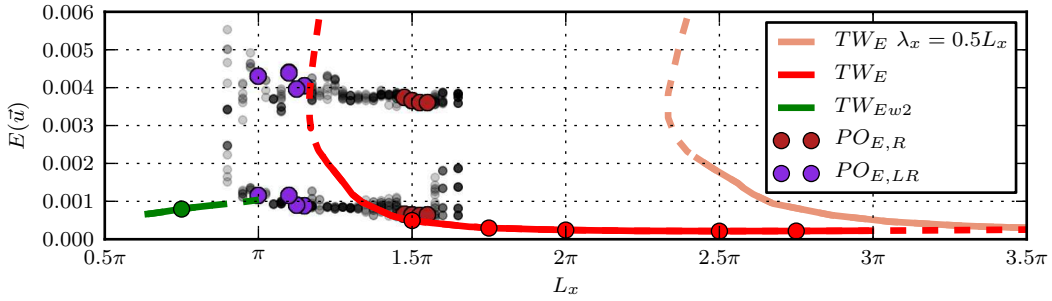

Figure 3.16: Bifurcation diagram showing the edge states in a domain with spanwise wavelength 2π at $Re_B = 3000$. For states $PO_{E,R}$ and $PO_{E,LR}$ large circles are used while for bifurcated states and aperiodic ones small dots are shown. Red lines are drawn for the traveling wave TW_E with a wavelength equal to the domain length. Light red is used for TW_E with a wavelength that is half the domain length. TW_{Ew2} is shown by a green line. If the traveling waves have only one unstable eigenvalue, a solid line is used. If there are more unstable eigenvalues, a dashed line is drawn.

R-states in the ASBL, edge states were identified that alter the shifting direction between left and right. In the domain with a streamwise extend of 1.5π where the $PO_{E,R}$ and $PO_{E,L}$ were identified we fail to find an orbit with an alternating shifting behavior using edge tracking. But for a slightly shorter computational domain with $L_x = 1.15\pi$, a periodic orbit that alternates between a shift to the left and a shift to the right can be identified. A space-time plot of the orbit is shown in figure 3.15. The plot reveals the jumping behavior of the state. In the following the orbit that is reminiscent of the LR-state of Khapko et al. (2013) is referred to as $PO_{E,LR}$.

The fact that $PO_{E,LR}$ seems to be no edge state in the domain with a streamwise extend of 1.5π raises the question how the edge state of the system changes in dependence on L_x with a fixed spanwise width of L_z. To answer this question independent edge trackings for various values of L_x are performed. For $0.9\pi < L_x < 1.7\pi$ it is possible to find edge states that are dynamically similar to the localized jumping states $PO_{E,L}$, $PO_{E,R}$ and $PO_{E,LR}$. For larger values of L_x edge tracking converges to the traveling wave TW_E after eventually showing a transient phase with bursting behavior. For smaller values of L_x the traveling wave TW_{Ew2} is found. In figure 3.16 a bifurcation diagram showing the maxima in energy of the edge states on the y-axis is shown. In case of a simple periodic state a large circle is drawn. For bifurcated states, e.g. period doubled orbits, or chaotic edge states small black dots are drawn for each maximum on the edge trajectory after a transient phase of about 10^4 time units. Despite of the three already mentioned orbits there are other bursting edge states that exist for slightly different values of L_x. For example for $L_x = 1.65\pi$ a period-four state is an attracting edge state. Because the orbits have long periods and can not be tracked by a standard continuation method, a detailed analysis of the present bifurcations is difficult and computationally very expensive. In addition to the bursting orbits, the bifurcation diagram contains the traveling wave TW_E (see section 3.2) that for a small range in L_x below 1.7π is an edge state that coexists with the bursting edge states. For larger values of L_x, e.g. $L_x = 2.75\pi$, we also observe a coexistence of edge states, because TW_E with a wavelength of 2.75π and TW_E with wavelength 1.375π, which fits two times in the domain, have one unstable eigenvalue (for details on the calculation of the eigenvalues of ECS see appendix A.2).

The fact that the PPF edge states presented in this section share much of their features with the edge states found in the ASBL impressively demonstrates that the near-wall coherent structures in PPF and boundary layers are quite similar. Therefore, it is expectable that also other results on exact coherent structures found in PPF can be transferred to boundary layers.

3.4 Three-dimensional traveling wave bifurcating from Tollmien-Schlichting-waves

Apart from edge tracking there is a second strategy for the search for exact coherent structures in PPF. The two-dimensional Tollmien-Schlichting traveling wave, henceforth referred to as TW_{TS}, that bifurcates from the laminar flow has a large number of three-dimensional instabilities. An analysis of these instabilities provides a systematic method to identify exact coherent structures. As a first step a stability analysis of TW_{TS} for a streamwise and spanwise wavelength of 2π is performed. For details on the method used to calculate the stability of this ECS we refer to appendix A.2. Figure 3.17 shows the number of unstable eigenvalues for $Re_B \geq 5600$ in a bar diagram. With increasing distance to the point where it connects to the laminar state, the TS-waves becomes more unstable which results in 73 unstable eigenvalues for $Re_B = 5320$ and 352 for $Re_B = 4690$ in a computational domain with streamwise and spanwise wavelength of 2π. If between two Reynolds numbers the number of unstable eigenvalues changes, at least

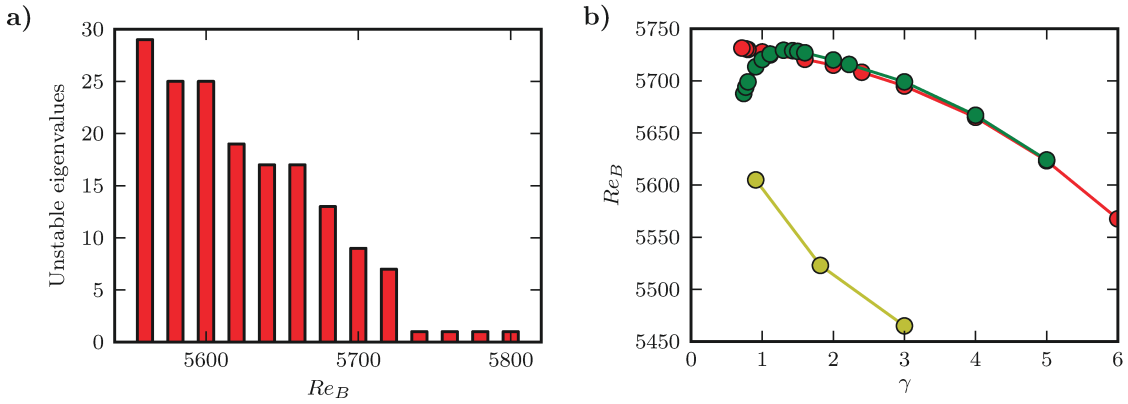

Figure 3.17: a) Unstable eigenvalues of the traveling wave TW_{TS} with a streamwise length of 2π in dependence on the Reynolds number. In spanwise and streamwise direction only disturbances with wave numbers of integer value are considered. In panel b) the bifurcation curves of the identified traveling waves TW_A, TW_B and TW_C are shown. The Reynolds number where the waves bifurcate from TW_{TS} with streamwise wavelength 2π is shown in dependence on the spanwise wavenumber $\gamma = 2\pi/\lambda_z$.

one bifurcation lies between these Reynolds numbers. A fine resolution in Reynolds number allows to identify the eigenvalues whose stability changes. By perturbing TW_{TS} in the direction of an eigenvector corresponding to an eigenvalue that changes its stability it is possible to obtain initial guesses for ECS. Using this guesses we are able to identify different types of traveling wave solutions with a Newton-method. The traveling waves are found using a numerical resolution of $N_x \times N_y \times N_z = 32 \times 81 \times 64$ for $L_x \times L_y \times L_z = 2\pi \times 2 \times 2\pi$. To check convergence a higher resolution is used. One class of solutions (TW_A) that can be identified is invariant under the symmetries

$$s_z : [u, v, w](x, y, z) = [u, v, -w](x, y, -z) \tag{3.6}$$

and

$$s_y \tau_x(\lambda_x/2) : [u, v, w](x, y, z) = [u, -v, w](x + \lambda_x/2, -y, z). \tag{3.7}$$

The second class of solutions (TW_B) also obeys the symmetry s_z and additionally it is invariant under

$$s_y\tau_x(\lambda_x/2)\tau_z(\lambda_z/2) : [u,v,w](x,y,z) = [u,-v,w][x+\lambda_x/2,-y,z+\lambda_z/2]. \tag{3.8}$$

In both cases λ_x and λ_z are the streamwise and the spanwise wavelengths, respectively.

A third type of traveling waves (TW_C) obeys the symmetry $s_y\tau_x(\lambda_x/2)$ and travels in streamwise and spanwise direction.

In figure 3.17b the Reynolds number of the bifurcation point is shown vs. the spanwise wavenumber for the different traveling waves. Interestingly, traveling waves with very low spanwise wavelengths can be found at quite low Re_B while such with moderate spanwise wavelengths do only exist at high Reynolds numbers. This is in contrast to the traveling waves in section 3.2 which have the property that for small spanwise or streamwise wavelengths they are shifted to higher values of Re_B.

Visualizations of some selected traveling waves are shown in figure 3.18. The pictures reveal that all of the traveling waves are characterized by strong streaks and vortices close to the walls. TW_A and TW_B are quite similar up to the difference in the symmetry. TW_C differs strongly from the other waves. The streak and vortex structures are more prolate than for TW_A and TW_B.

The traveling waves of type A, B and C bifurcate from the TS-wave TW_{TS} and incorporate one pair of rolls of the TS-waves. If we allow for bifurcations the incorporate two pairs of rolls the number of unstable eigenvalues of the TS-wave and also the number of bifurcating solutions increases dramatically.

Especially, a fourth class of traveling waves (type D) can be identified. The waves obey s_z symmetry and additionally

$$s_y\tau_x(\lambda_x/4)\tau_z(-\lambda_z/4) : [u,v,w](x,y,z) = [u,-v,w][x+\lambda_x/4,-y,z-\lambda_z/4] \tag{3.9}$$

and

$$\tau_x(\lambda_x/2)\tau_z(\lambda_z/2) : [u,v,w](x,y,z) = [u,v,w][x+\lambda_x/2,y,z+\lambda_z/2]. \tag{3.10}$$

For this traveling wave the wavelength λ_x is twice the wavelength λ_0 of the original TS-wave TW_{TS}.

In figure 3.19 the bifurcation diagram containing the traveling waves A-D for selected spanwise wavelengths is shown. It can be seen that in all cases the bifurcating branch extends to higher Reynolds numbers. It was not possible to identify traveling waves that extend to Reynolds numbers as low as those found by Ehrenstein and Koch (1991).

The identified traveling waves even exist for very small spanwise length-scales, e.g solutions of type A can be found for spanwise wavelengths down to about 0.5.

The visualizations of ECS using the wall-normal flow close to the plate, as shown in figure 3.20, reveal a huge similarity to the patterns of aligned and staggered Lambda-vortices which are characteristic for K- and H-type instabilities of TS-waves (Herbert, 1988; Saiki et al., 1993), respectively However, the structures that are visible in the figure can not be interpreted as Lambda-vortices because the direction of the flow is from bottom to top.

Anyhow, if trajectories undergoing K- or H-type TS-transition in supercritical PPF come at some point close to one of the unstable traveling waves (TW_A or TW_B for K-type and TW_D for H-type) can possibly investigated using projections of state space as used by Gibson et al. (2008). If the traveling waves are visited during K- and H-type transition, this would allow for a dynamical system interpretation of these transitions.

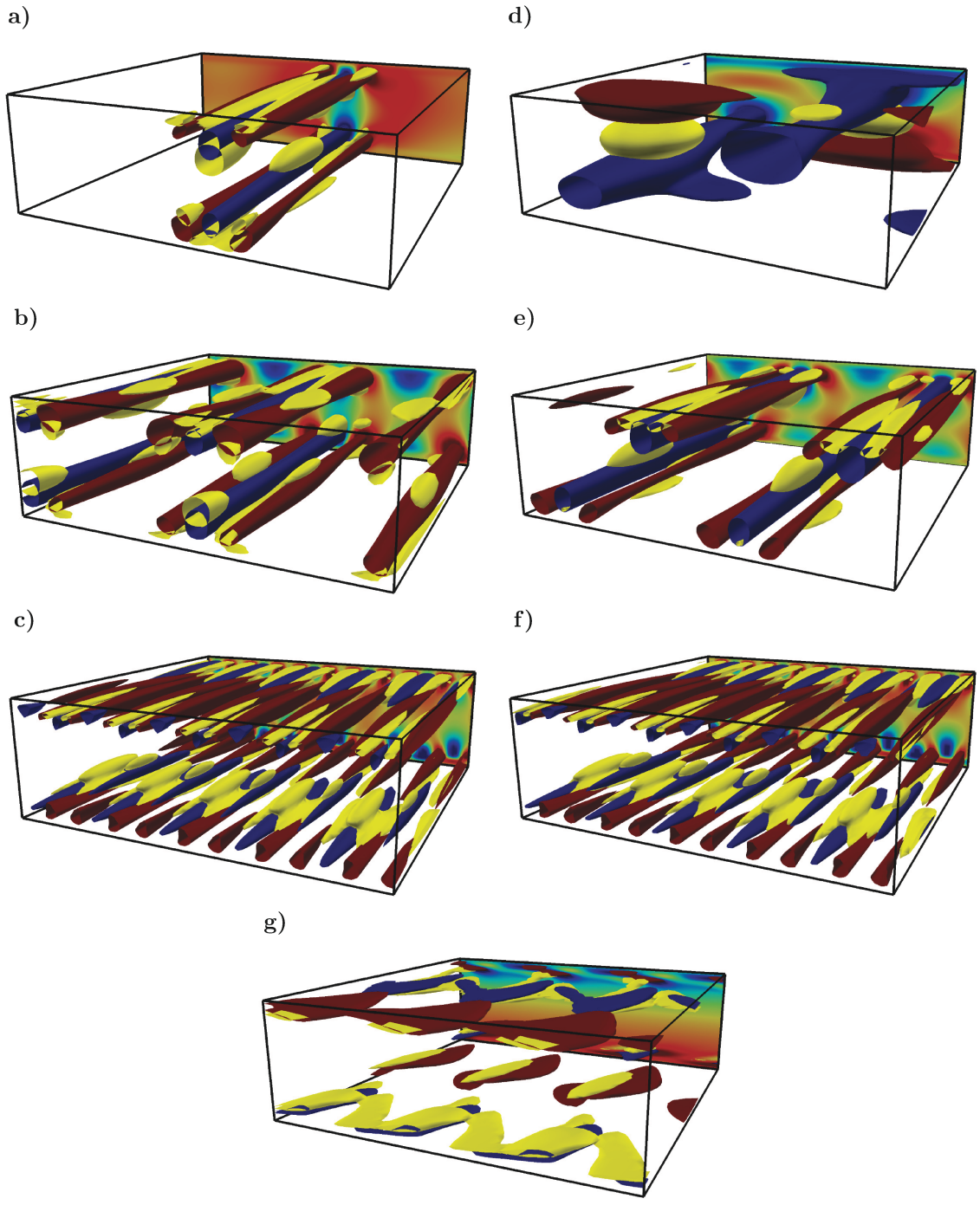

Figure 3.18: Visualizations of $TW_{A,2\pi}$ a), $TW_{A,1\pi}$ b), $TW_{A,2\pi/5}$ c), $TW_{B,2\pi}$ d), $TW_{B,1\pi}$ e), $TW_{B,2\pi/5}$ f) and $TW_{C,2\pi/3}$ g). The plots show iso-contours of positive and negative streamwise velocity in red and blue, respectively. Iso-contours of the Q-vortex-criterion are shown in yellow. In each case, except for d) where it is 5770, the Reynolds number is 8200. On the back plane of the box, the streamwise velocity is color-coded from the minimum value (dark blue) to the maximum values (red). The direction of the flow is perpendicular to back plane.

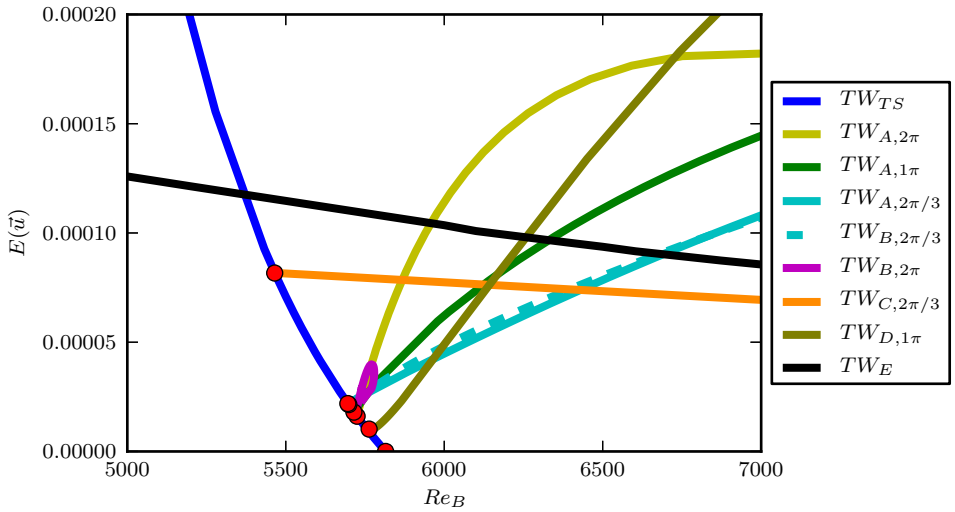

Figure 3.19: Bifurcation diagram for three-dimensional traveling waves bifurcating from the TS-wave TW_{TS} with streamwise wavelength $\lambda_0 = 2\pi$ (blue line). On the ordinate the energy density of the states is used. The point where the bifurcate from TW_{TS} are marked with circles. Additionally, the edge state TW_E with spanwise and streamwise wavelength 2π is shown by a black line.

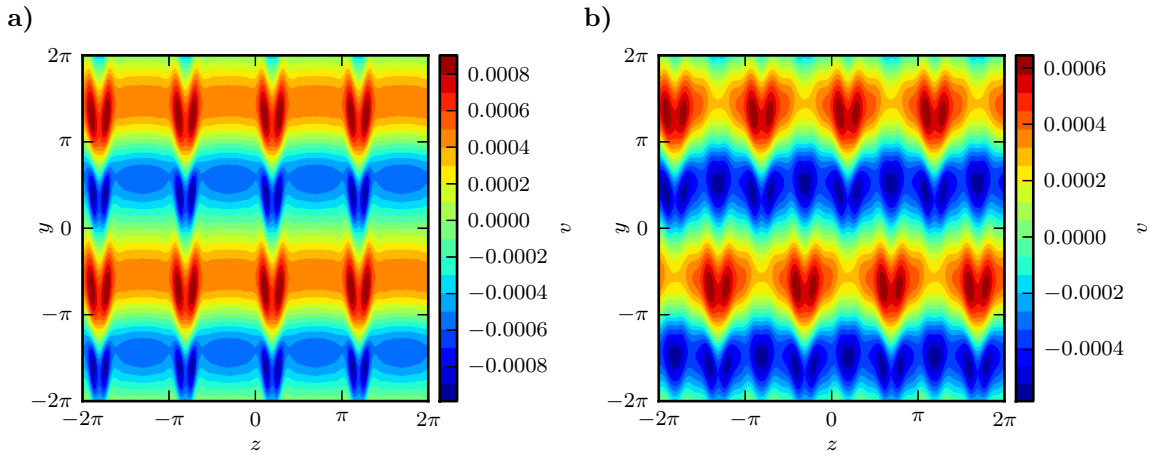

Figure 3.20: Wall-normal flow in a plane parallel to the plates in a distance of 0.10 from the lower plate for the travelling waves TW_A and TW_D with spanwise wavelength π and $Re_B = 8200$. The streamwise wavelengths are 2π and 4π, respectively. The direction of the flow is from bottom to top.

Chapter 4

The origin of subcritical turbulence

Parts of the results presented in this section have been published in
"Crisis bifurcations in plane Poiseuille flow" , Stefan Zammert and Bruno Eckhardt, Physical Review E 91 041003(R) 2015
"Bypass transition and subcritical turbulence in plane Poiseuille flow" , Stefan Zammert and Bruno Eckhardt, Proceedings of TSFP-9, arXiv:1506.04370

4.1 Introduction

As explained in the beginning of chapter 2 the linear instability of the laminar state and solutions branching from the laminar profile cannot explain the subcritical turbulence that can be observed for Reynolds numbers as low as 1000 (e.g Carlson et al., 1982; Tuckerman et al., 2014).

The results of the previous section show that the pure existence of exact coherent structures is not sufficient to explain the onset of transient turbulence. Nevertheless, they play an important role for its existence. For the case of plane Couette flow Kreilos and Eckhardt (2012) found an equilibrium solution whose upper branch is the starting point for a bifurcation cascade that leads to a chaotic attractor. This chaotic attractor is destroyed in a boundary crisis bifurcation. Following the boundary crisis bifurcation the system shows turbulence lifetimes that are exponentially distributed. A similar scenario has been shown to exist in pipe flow (Avila et al., 2013).

In the following it will be shown that for the case of plane Poiseuille flow the onset of subcritical turbulence can be linked to a traveling wave that is not connected to the linear instability of the laminar state. Thus, we will demonstrate that despite of the linear instability of PPF the mechanism leading to subcritical turbulence is the same as for pipe and plane Couette flow that lack a linear instability.

For plane Poiseuille flow without symmetry restriction it was not possible to identify an edge state whose upper branch is stable right after its bifurcation point, which is necessary to

study a possible subsequent bifurcation to a chaotic state. In order to reduce the size of the state space and to stabilize ECS, the system is restricted to a subspace with the following two discrete symmetries:

$$s_y : [u, v, w](x, y, z) = [u, -v, w](x, -y, z), \tag{4.1}$$
$$s_z : [u, v, w](x, y, z) = [u, v, -w](x, y, -z). \tag{4.2}$$

The edge state in this subspace is the traveling wave TW_{Eyz}, which we already encountered in section 3.2. Using a continuation method (Dijkstra et al., 2014) it is possible to track this edge state down in Reynolds number and around its bifurcation point. (If in this chapter, except for section 4.6, the term Reynolds number is used, the Reynolds number Re_B basing on the bulk velocity is meant.) A stability analysis in the symmetric subspace shows that the lower branch has one unstable eigenvalue for a large range in Reynolds number starting at the bifurcation point at $Re_B = 641$. In the symmetric subspace the upper branch is stable right after its appearance, but it has 25 unstable eigenvalues (for $Re_B = 652$) in the full system. Visualizations of the flow field of the upper and the lower branch are shown in figure 4.1. At $Re_B \approx 707$ the upper branch undergoes a Hopf bifurcation which creates a stable relative periodic orbit that is referred to as PO_{yz} in the following. PO_{yz} undergoes a Neimark-Sacker bifurcation at $Re_B \approx 761.5$ that creates a stable torus. With increasing Reynolds number this torus undergoes further bifurcations and a chaotic attractor is created. The bifurcation diagram in figure 4.2a shows TW_{Eyz} and the attractor that is created in the bifurcation cascade starting at its upper branch and henceforth referred to as A_1. To draw the bifurcation diagram of the attractor the minima of the amplitude

$$a(\vec{u}) \equiv \mathcal{L}^2(\vec{u}) = \sqrt{\frac{1}{L_x L_y L_z} \int \vec{u}^2 dV} \tag{4.3}$$

of flow fields on trajectories on the attractor are plotted. In figure 4.2b a magnification of the attractor is shown and two major changes of the attractor are marked using a blue and a red line, respectively. At $Re_{IC} \approx 785.1$, marked by the blue line, an interior crisis bifurcation causes a sudden expansion of the attractor and at $Re_{XC} \approx 786.5$, marked by the red line, an exterior or boundary crisis bifurcation destroys the attractor.

In the following two subsections these two phenomena will be discussed in detail. In section 4.4 it will be shown that beside the attractor formed by the bifurcations of TW_{Eyz}, other attractors exist for some values of Re_B . Especially, we will show that inside of the basin of A_1 another attractor exists. Furthermore, the influence of the streamwise wavelength and of the operating condition on the attractor will be explored in section 4.5 and 4.6.

4.2 Enlargement of the attractor in an interior crisis bifurcation

In the magnification of the attractor in figure 4.2b one can see that below $Re_B = 785.1$ the attractor is restricted to an interval in $a(\vec{u})$ between 0.18 and 0.205. Above this Reynolds number the attractor extends over a much wider interval in $a(\vec{u})$. In the bifurcation diagram the newly occupied area is much brighter than the rest of the attractor. This is because the points in this region are less dense since it is only visited occasionally. A bifurcation that leads to a spreading of an attractor into a region which slightly after the bifurcation is only seldom

visited was first described by Grebogi et al. (1982) and is called *interior crisis bifurcation*. In an interior crisis bifurcation the attractor collides with an unstable orbit in its basin of attraction. For trajectories on the attractor two phases with different dynamics can be distinguished. The first phase is 'quiet' and the trajectories stay in the region of the old attractor. Below the Reynolds number of the crisis bifurcation only the quiet phase can be observed. Above Re_{IC}, the quiet phases are interrupted by 'bursting' phases. In a bursting phase the trajectories visit the new parts of the attractor. Quiet phases with very different durations can be observed. However, if Re_B is further increases above Re_{IC}, bursting phases appear more often and the typical length of the quiet phases decreases. To illustrate the phenomenon, trajectories on the attractor for Reynolds numbers slightly above and below the interior crisis are shown in figure 4.3. According to Grebogi et al. (1987) for an interior crisis the lengths of the quiet phases are exponentially distributed and the characteristic times τ_q follow a power law $\tau_q \propto (Re - Re_{IC})^{-\gamma}$. To analyze this, the lengths of the quiet phases are calculated using a threshold in energy. We assume that during a quiet phase the amplitude $a(\vec{u})$ never drops below $a_t = 0.176$. If the amplitude of the trajectory drops below a_t, it enters a bursting phase. A requirement for a bursting phase is the repeated occurrence of excursions to values below a_t. Accordingly, if no excursions are noted for more than 250 time units, we conclude that the system has returned to a quiet phase.

Thus, we obtain distributions of the durations of quiet phases. These distributions are shown for different values of Re_B in figure 4.4a where it becomes evident that the distribution is exponential. By fitting the distribution for $t > t_{trans} = 10^4$ to an exponential decay,

$$p(t) = A \cdot e^{-(t - t_{trans})/\tau_q}, \tag{4.4}$$

we obtain the characteristic times τ_q trajectories spend in the quiet phases. These characteristic times are shown versus Re_B in figure 4.4b. The double logarithmic plot in the inset reveals that the lifetimes follow a power-law. Therefore, we fit a power law,

$$\tau_q(Re_B) = A(Re_B - Re_{IC})^{-\gamma}, \tag{4.5}$$

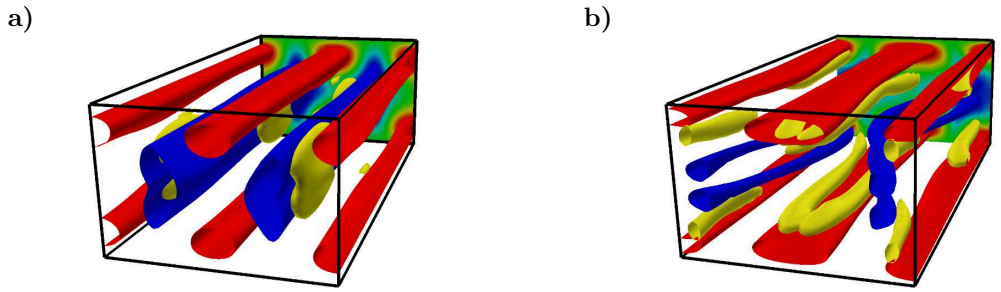

Figure 4.1: Visualizations of the lower (a) and upper branch (b) of the travelling wave TW_{Eyz} at $Re_B = 850$. The red and blue surfaces show iso-surfaces of $u = \pm 0.15$ for the lower and $u = \pm 0.30$ for the upper branch. The yellow surfaces show iso-surfaces of the Q-vortex criterion. The iso-values are 0.008 and 0.08, respectively. On the back side of the box the streamwise velocity (deviation from laminar) is color coded.

to the data. We use $Re_{IC} = 785.1$ because this is the lowest values for which we observe excursions to the bursting phase. The best fit is obtained for $\gamma = 0.8$ which is shown in the figure by a solid red line.

Typical turbulent trajectories show an enormous complexity that is difficult to create in a sequence of simple Neimarck-Sacker or period-doubling bifurcations. Interior crisis bifurcations possibly play an important role for the emergence of complexity. The trajectory in figure 4.3a is, albeit not periodic, rather regular. The interior crisis dramatically increases the complexity of the trajectories on the attractor (see figure 4.3a-d). Moreover, since interior crisis bifurcations contribute to a more dense coverage of the state space with parts of the attractor, they can pave the way for boundary crisis bifurcations in which the attractor collides with its boundary.

4.3 Destruction of the chaotic attractor in a boundary crisis bifurcation

To visualize the basin of attraction of the attractor, two-dimensional slices of the state space are considered. It is appropriate to choose a slice that contains the upper and lower branch of TW_{Eyz}. Since the upper branch lies inside the basin of attraction and the lower branch lies on the boundary of the basin, this choice ensures that the slice cuts the basin of attraction. Using two parameters, α and A, and the flow fields of the lower and upper branch of TW_{Eyz}, a slice of the state space can be defined by:

$$\vec{u}(\alpha, A) = A\frac{(1-\alpha)\vec{u}_1 + \alpha\vec{u}_2}{||(1-\alpha)\vec{u}_1 + \alpha\vec{u}_2||_{L2}}. \tag{4.6}$$

The parameter α allows for interpolation between the upper and the lower branch and A is the amplitude of the flow field.

Examples of slices following this definition that use the lower branch and the upper branch of the traveling wave as $\vec{u}_1$ and $\vec{u}_2$, respectively, are shown in figure 4.5. In these figures the

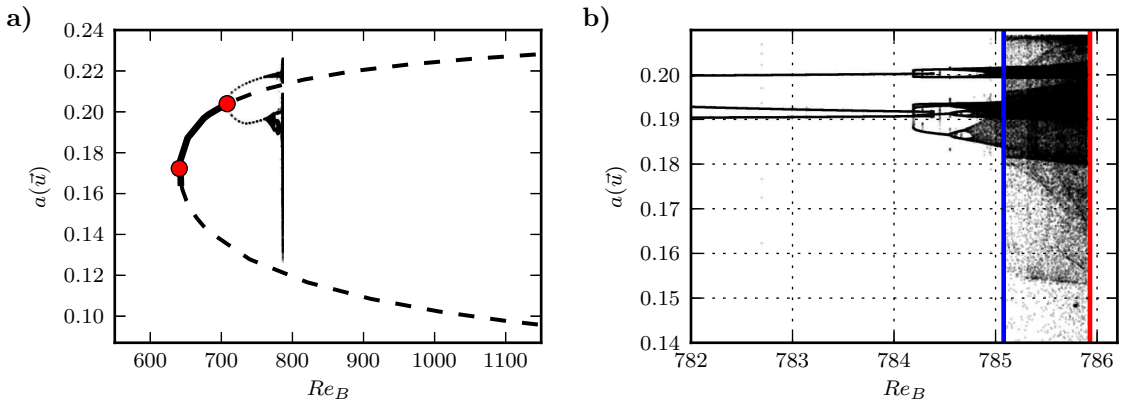

Figure 4.2: In a) the solution branch of TW_{Eyz} and the bifurcation cascade that starts at the upper branch of TW_{Eyz} are shown. The solution branch of TW_{Eyz} is shown by black solid (stable) and dashed (unstable) lines, respectively. Time-dependent states are shown by plotting minima and maxima of $a(\vec{u})$. In panel b) a magnification of the chaotic attractor is shown.

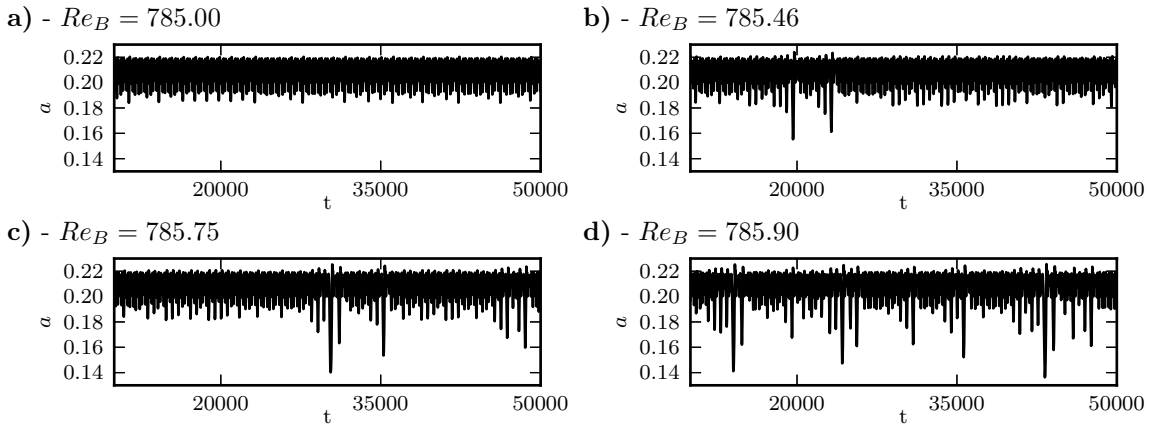

Figure 4.3: Amplitudes $a(\vec{u})$ of trajectories below and above the Reynolds number of the interior crisis. The Reynolds number in a) is 785.0 which is slightly below the crisis. In b), c) and d) trajectories after the crisis at Re_B=785.46, 785.75 and 785.9 showing typical intermittent burst are plotted.

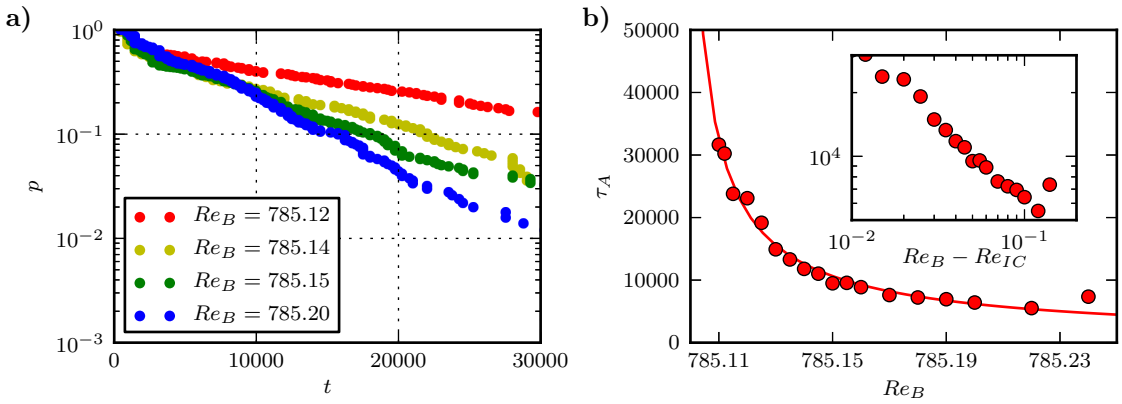

Figure 4.4: Probability to stay in the phase with the small amplitude oscillations for t time units. The lengths of the quiet phases are clearly exponentially distributed and the characteristic timescale τ_q increases with decreasing distance to Re_{IC}. The double logarithmic plot in the inset of b) reveals the algebraic decrease of the times τ.

initial conditions are colored according to the time they need to fall below a certain threshold a_l in amplitude. The value of this threshold is chosen such that a trajectory falling below it directly relaminarizes. The slice at $Re_B = 780$ shows a red region corresponding to initial conditions in the basin of the attractor. As it is visible in figure 4.2, the attractor disappears at $Re_{XC} \approx 785.95$. For $Re > Re_{XC}$ in the state space region that was formerly occupied by the basin of the attractor, the lifetime (the time an initial condition needs to fall below a_l in amplitude) fluctuates randomly, which is also found in other subcritical flows (Schmiegel and Eckhardt, 1997; Faisst and Eckhardt, 2003a) and low-dimensional models (Eckhardt and Mersmann, 1999; Moehlis et al., 2004a,b). For these Reynolds numbers no stable attractors exist beside the laminar one. Any initial condition returns to the laminar state for a sufficiently large observation time. The phenomenon that destroys the stable attractor and generates the randomly distributed lifetimes is a so-called boundary or exterior crisis bifurcation (Grebogi et al., 1982). The object that is created in this bifurcation is referred to as chaotic saddle.

A typical feature of a chaotic saddle is that the survival times are exponentially distributed,

$$p(t) \propto C \cdot e^{-t/\tau}.$$

In figure 4.6a the lifetime distributions for Reynolds numbers slightly above the boundary crisis are shown. Indeed, they show an exponential decay for $t > t_{trans} = 10^2$. The characteristic lifetimes τ which are estimated using the method described by Avila et al. (2010) are shown in figure 4.6b.

Similar to the case of the interior crisis, the characteristic lifetimes τ follow a power-law with distance of the Reynolds number to that of the exterior crisis Re_{XC} . We use $Re_{XC} = 785.95$ what is the lowest Reynolds number for which we observe relaminarization and fit the function

$$\tau(Re) = B(Re - Re_{XC})^{-\delta} \tag{4.7}$$

to the data. The best fits to the data is obtained for $\delta = 1.5$ and shown in figure 4.6b.

The boundary crisis happens in a symmetric subspace of the full system. Since this subspace is of measure zero if the full state space is considered, it is justified to ask if it is possible to see an effect of the boundary crisis on the lifetimes of the full system. To answer this question, the characteristic lifetimes for the same computational domain without symmetry restriction are calculated. In figure 4.7a the distributions of the survival probabilities for Reynolds numbers close to Re_{BC} are shown. The characteristic lifetimes are shown in figure 4.7b. The simulations show that lifetimes in the full system are exponentially distributed but typically with a characteristic lifetime much shorter than in the symmetric subspace. The boundary crisis in the symmetric subspace, whose position is marked in the figure by the red line, has no visible influence on the lifetimes of the full system.

4.4 Embedded attractors and increasing lifetimes

In addition to the attractor A_1 discussed in detail in the previous two sections, it is possible to identify further attractors in the same mirror-symmetric subspace.

Inside of A_1 another stable attractor A_{1b} exists between $Re_B \approx 778.3$ and $Re_B \approx 780.6$. A visualization of A_{1b} is shown in figure 4.8a. At $Re_B \approx 780.6$ this attractor is destroyed. Above this Reynolds number trajectories exist that show features of trajectories on A_{1b} for a transient time. This behavior is illustrated in figure 4.8c which shows a trajectory with transient A_{1b}-like

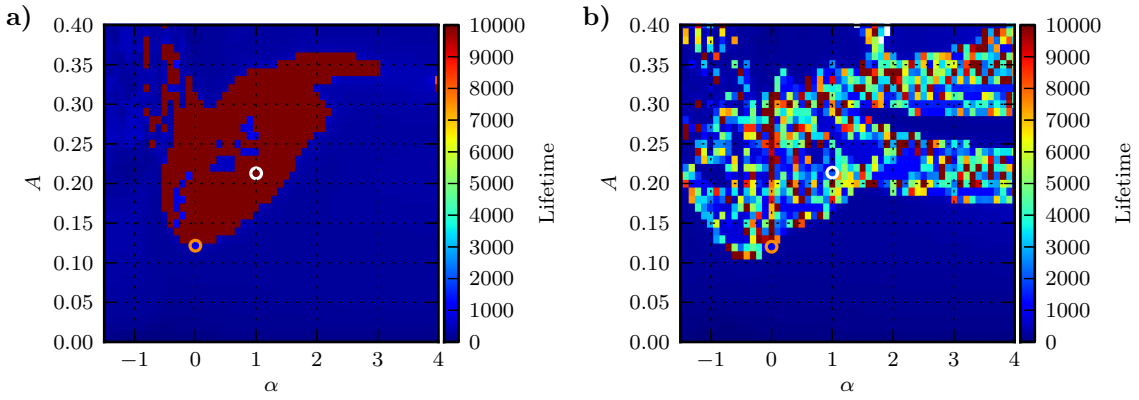

Figure 4.5: State space slices for different Reynolds numbers. The initial conditions are color coded according to their lifetime, that is the time they need to fall below 0.005 in amplitude a. Initial conditions that do not fall below this value within the observation time of 10^4 time units are shown with this value as lifetime. In panels a) and b) the Reynolds numbers are 780 and 790, respectively. The positions of the upper and lower branch of TW_{Eyz} are marked with white and orange circles, respectively.

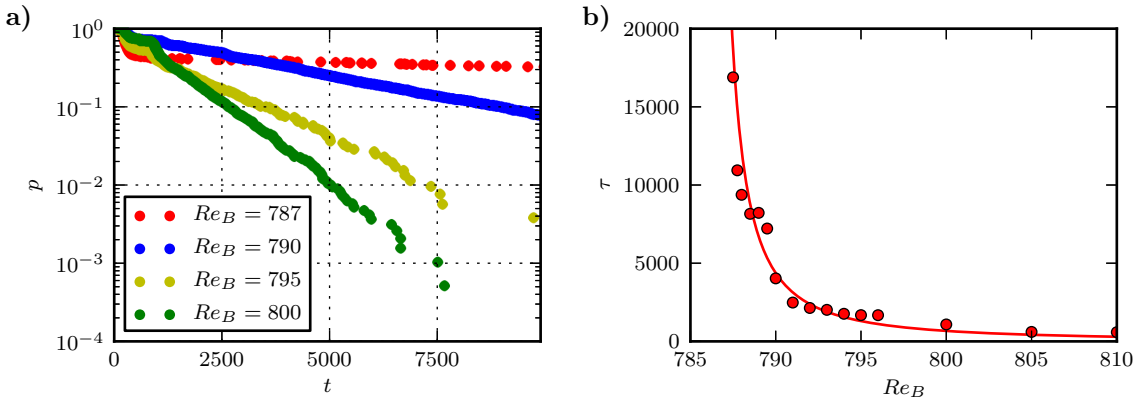

Figure 4.6: In panel a) the survival probabilities for Re_B=787 (red), 790 (blue) and 800 (green) in the symmetric subspace are shown. Panel b) shows the characteristic lifetimes τ in dependence on the Reynolds number.

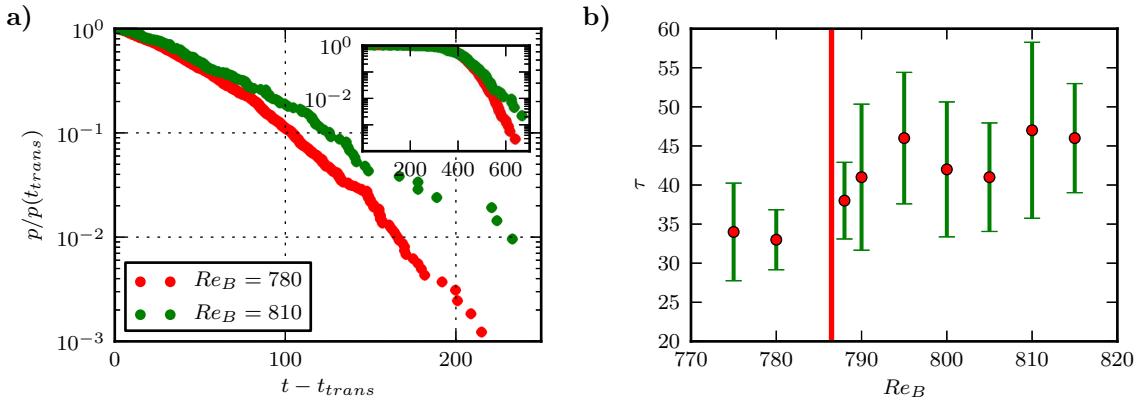

Figure 4.7: In panel a) the survival probabilities for $Re_B = 780$ (red) and 810 (green) in the unrestricted system are shown. For the plot a transient phase of 400 time units is removed ($t_{trans} = 400$). The threshold for laminarization is an amplitude $a(\vec{u})$ of 0.008. The complete distribution is shown in the inset. In b) the characteristic lifetimes in dependence on the Reynolds number are shown. The red line marks the position of the boundary crisis in the symmetric subspace.

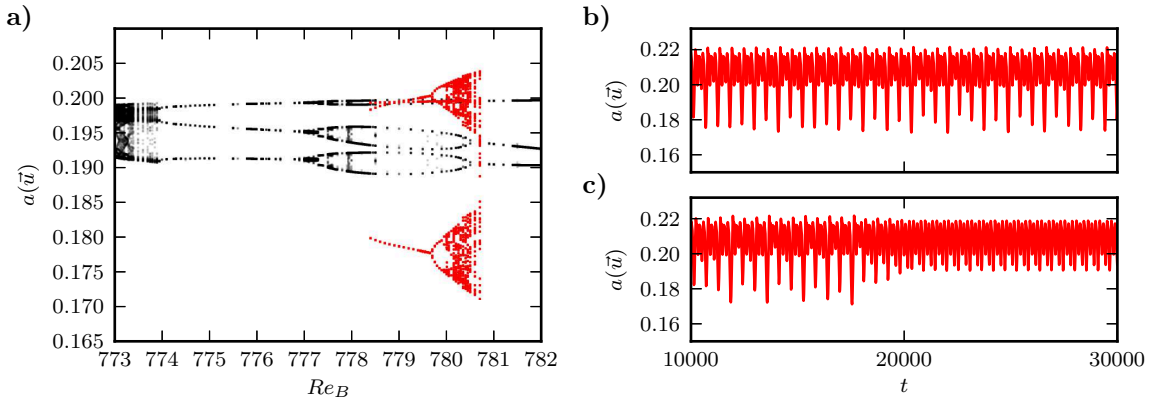

Figure 4.8: In a) the attractor A_{1b} (red) is shown together with A_1 (black). For the visualization the minima of $a(\vec{u})$ for trajectories on the attractors are used. In b) the amplitudes $a(\vec{u})$ of a trajectory on the attractor A_{1b} for $Re_B = 780.4$ is shown. Panel c) shows a trajectory for $Re_B = 780.7$. The trajectory stays on the chaotic saddle left by A_{1b} for about 18000 time units before it suddenly switches to the stable attractor A_1.

behavior and a trajectory on A_1 for $Re_B = 780.7$. It was not possible to find trajectories that relaminarize after showing transient A_{1b}-like behavior. This is a strong evidence that A_{1b} is indeed inside of the basin of attraction of A_1. Therefore, the destruction of A_{1b} leaves a chaotic saddle inside of the basin of A_1. In principle, the saddle left by the crisis of A_{1b} can be the unstable object which A_1 within the interior crisis collides with, but it is difficult to give a proof for this claim.

At $Re \approx 828$ a relative periodic orbit with a period of $T \approx 390$ appears. The periodic orbit

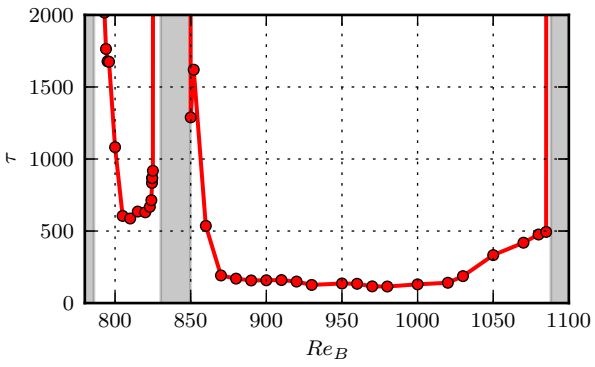

Figure 4.9: Characteristic lifetime in dependence on the Reynolds number. Regions where stable attractors exist are shaded gray.

is the starting point for a bifurcation cascade that creates another chaotic attractor (A_2). This attractor is destroyed at $Re \approx 837.5$. A third attractor (A_3) that appears at $Re = 841.8$ and disappears at $Re = 841.8$ is coexisting with A_2 for an interval in Re. After A_3 disappeared we did not find another stable attractor for a large interval in Re. However, there might exist other ones which are difficult to find because of tiny basins of attraction. Finally, at $Re \approx 1087$ a fourth attractor (A_4) appears. The attractors A_2-A_4 appear in regions of the state space occupied by the large saddle created in the boundary crisis of A_1 which was checked using slices of the state space. Thus, it was shown that analogous to the case of Couette flow (Kreilos et al., 2014a) (and in all likelihood also pipe flow (Altmeyer et al., 2014)) smaller chaotic saddles can exist embedded in a larger outer saddle. This can contribute to an increase of the characteristic lifetimes.

In figure 4.9 the characteristic lifetimes are shown for a range in Reynolds number that contains four stable attractors. For Reynolds numbers, where a stable attractor exists, the characteristic lifetimes are plotted as infinite. Of course, for $Re_B > Re_{XC}$ there is a large set of initial conditions that show exponentially distributed lifetimes even if the other attractors are stable. However, if a stable attractor exists, initial conditions in its basin have an infinite lifetime which sets the largest time scale for relaminarization.

4.5 Attractors and saddles with different spatial wavelength

The attractors shown in the previous section show a complicated temporal dynamics, but their spatial dynamics remains rather simple. In particular, they all have a streamwise wavelength of 2π. A third kind of crisis bifurcations, so-called merging crisis bifurcations (Grebogi et al., 1987), could provide a way to increase the spatial complexity of the attractor and also of trajectories on the subsequently created chaotic saddle. Necessary for a merging crisis that increases the spatial complexity is the existence of attractors or saddles with different spatial wavelengths. Such attractors with different wavelengths can be found by tracking the traveling wave TW_{Eyz} in L_x and L_z and following the bifurcations of its upper branch. In figure 4.10a attractors with streamwise wavelengths 1.5π (blue) and 3π (red) are shown in addition to the one with $L_x = 2\pi$ (black). Although possibly unstable, in a computational domain with a streamwise extend of 6π all three attractors co-exist. Thus, a merging of the attractors (or the

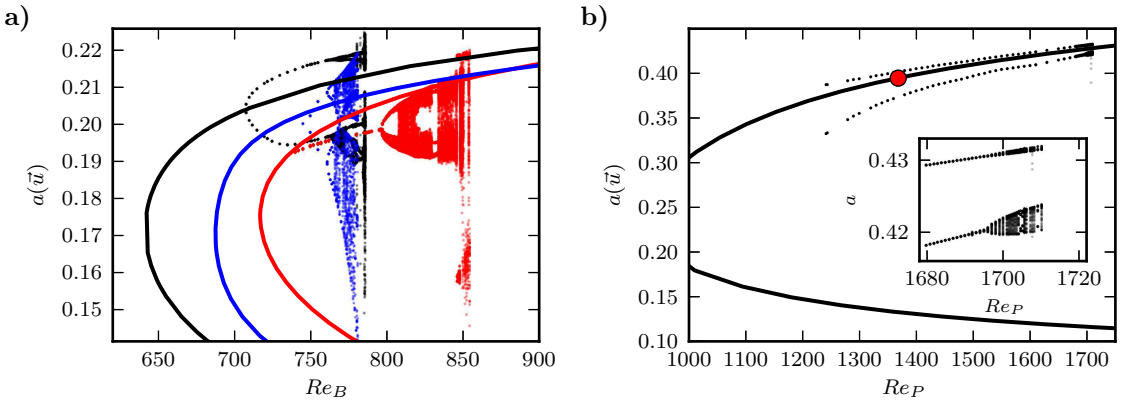

Figure 4.10: In a) the bifurcation diagrams for attractors with different streamwise wavelengths L_x are shown. The values of L_x are 2.0π (black), 1.5π (blue) and 3.0π (red). For the solution branches of TW_{Eyz} solid lines ares used. Time-dependent states are shown by plotting minima and maxima of $a(\vec{u})$. Panel b) shows a bifurcation diagram for the system operating at constant pressure gradient. The solutions branch of TW_{Eyz} is shown by a black solid line. The red dot marks a Hopf bifurcation that destabilizes the upper branch. The inset shows a zoom of the attractor.

saddles) can in principle generate an attractor or saddle that has a higher spatial complexity in streamwise direction.

4.6 Dependence on the operating condition

Up to this point, the discussion of the bifurcation was for systems operating at constant mass flux with Re_B as the bifurcation parameter. For systems operating at constant pressure gradient it is also possible to find a bifurcation cascade leading to a chaotic attractor that is destroyed in a boundary crisis at $Re_P \approx 1710$. However, the details of the bifurcation cascade differ strongly from the case of constant bulk velocity. In figure 4.10b the bifurcation diagram of the system operating at constant pressure gradient ($L_x = 2\pi$ and $L_z = 1\pi$) is shown. The upper branch of TW_{Eyz} is stable for $Re_P < 1368$ where a time periodic state is created. The time periodic state can also be found for $Re_P < 1368$ and if the upper branch of TW_{Eyz} is perturbed slightly for $Re_P > 1368$, it jumps to a periodic state in finite distance. This suggest that, in contrast to the case of constant bulk velocity, the bifurcation of the upper branch is subcritical. The periodic state is stable for a large range in Re_P. Slightly below $Re_P = 1700$ it becomes unstable and a bifurcation cascade starts (see inset in figure 4.10b). Eventually, at $Re_P \approx 1710$, the attractor that has been created by this cascade is destroyed.

It was shown that the origin of transient subcritical turbulence in plane Poiseuille flow is related to a bifurcation cascade that starts with a simple traveling wave. Ultimately, the transient turbulence is created by a boundary crisis bifurcation as it has been found for pipe and plane Couette flow before. As in these cases, our study is in a symmetry restricted subspace. Nevertheless, as all solutions of the symmetry restricted system do also exist in the full system, the results are also valid for the full system. The fact that the exact coherent structures are not connected to the laminar state or its bifurcations does finally prove that the instability of

the laminar state is completely irrelevant for the subcritical turbulence in PPF.

Finally, I want to pick up the quote by Heisenberg at the beginning of chapter 2. While the Reynolds number for the breakdown of the laminar motion is known to high precision since the 1970s, the results of this section are a step towards the other critical Reynolds number mentioned by Heisenberg, the Reynolds number of the onset of turbulence.

Chapter 5

Exact solutions for Bypass and Tollmien-Schlichting transition

5.1 Introduction

In PPF as well as in boundary layers different routes to turbulence are known (Kachanov, 1994; Schmid and Henningson, 2001). For Reynolds numbers for which the laminar state is unstable, any small perturbation will lead to the formation of two-dimensional Tollmien-Schlichting waves (TS-waves). These waves grow (slowly) in amplitude and because they are unstable to three-dimensional disturbances (*secondary instability*) (Saiki et al., 1993), they finally break down and a three-dimensional turbulent state is reached. Apart from this Tollmien-Schlichting transition to turbulence, there is another route to turbulence in which no two-dimensional TS-waves appear. Because the TS-mechanism described above is somehow bypassed on this route to turbulence, this second kind of transition to turbulence was named *Bypass transition* (Morkovin, 1969; Henningson et al., 1993). This transition mechanism is most important in the subcritical range but it does also exist above the linear instability.

In this section it will be shown how the two transition scenarios are connected to ECS. Furthermore, we will explore the state space structure close to the linear instability, where the ECS related to both transition scenarios are coexisting edge states. It will also be shown that TS-transition is of minor importance in the subcritical range and that both transition scenarios coexist close to each other in the state space.

For the investigations in this section a computational domain with a streamwise length of 2π and a spanwise width of 2π is used. For this computational domain the Reynolds number of the linear instability is 5815. The simulations use a resolution of $N_x \times N_y \times N_z = 32 \times 65 \times 32$ and constant bulk velocity. As already mentioned in section 3.2 (see also Zammert, 2011; Zammert and Eckhardt, 2014c) the edge state for this domain-size is the traveling wave TW_E. This traveling wave has one unstable eigenvalue for $510 < Re_B < 5850$. At Reynolds number 5815 a two-dimensional traveling wave TW_{TS} bifurcates subcritically from the laminar profile. For $5727 < Re_B < 5815$ this traveling wave also has only one unstable direction. Its stable manifold therefore is also of co-dimension one and separates the state space into two parts. TW_{TS} is a

second edge state for this range in Re_B. For lower Re_B, there are lots of secondary bifurcations (see section 3.4) that add more and more unstable directions to the state. Specifically, near the turning point at $Re_B = 4690$, the lower branch has about 352 unstable directions (in a computational domain with $L_x = L_z = 2\pi$). A bifurcation diagram containing both traveling waves is shown in figure 5.1.

5.2 Two-dimensional slices of the state space

The coexistence of two different edge states and different transition paths rises the question how they are connected to each other and how the state space looks like. To investigate the state space structure, we want to use the two-dimensional slices of the state space that we already encountered in section 4.3. The slice of the state space should contain two given flow fields $\mathbf{u}_1$ and $\mathbf{u}_2$ which can be achieved by parameterizing the velocity fields of the slice with a mixing parameter α and an amplitude A, i.e.,

$$\mathbf{u}(\alpha, A) = A\frac{(1-\alpha)\mathbf{u}_1 + \alpha\mathbf{u}_2}{||(1-\alpha)\mathbf{u}_1 + \alpha\mathbf{u}_2||_{L2}} \tag{5.1}$$

As a first step the slices are used to explore the appearance of TW_E at low Reynolds numbers. Therefore, we construct slices of the state space using the lower and upper branch of TW_E for u_1 and u_2, respectively. The resulting slices are visualized using the lifetime of the initial conditions (the time they need to fall below 0.002 in amplitude $a(\vec{u})$).

In figure 5.2 slices for different values of Re_B close to the bifurcation point of TW_E are shown. When TW_E appears at low values of Re_B it has more than one unstable direction. Thus, no stable attractor forms, but even where TW_E has more than one unstable direction (e.g. $Re_B = 500$ in figure 5.2a), the stable manifold of TW_E is visible in the slices. With increasing Re_B the lower branch stabilizes and the stable manifold separates a bubble filled with transient chaos from a region where initial conditions immediately relaminarize (figure 5.2b). The phenomenon is quite similar to plane Couette flow (Kreilos and Eckhardt, 2012) and the symmetry restricted subspace of PPF studied in section 4. As can be seen in figure

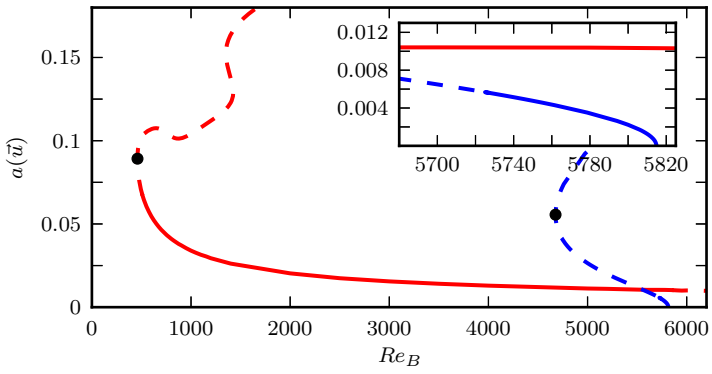

Figure 5.1: Bifurcation diagrams of TW_E (red) and TW_{TS} (blue). A solid line is used if the traveling wave has just one unstable eigenvalue, while a dashed line is used if the wave has further unstable eigenvalues. In the inset a zoom of the region is shown where both waves have only one unstable eigenvalue. The bifurcation points of the waves are marked with black dots.

5.2c, the chaotic region in the state space grows with increasing Reynolds number and the lifetimes increase. Inside the region of transient chaos there exist holes which contain initial conditions that relaminarize quickly.

To investigate the relation between the two traveling waves TW_E and TW_{TS} in the region where they coexist, slices of the state space are regarded that use the lower branches of TW_E and TW_{TS} for u_1 and u_2, respectively. For the visualization of the slices we use the transition time, because for high Re_B the lifetimes are very long. Because the chaotic state space part grows with the Reynolds number, at $Re_B = 4685$ where the traveling wave TW_{TS} appears, a huge part of the state space is occupied by chaotic transients. Therefore, since the energy of TW_{TS} is very high at the bifurcation point, the state, most likely, appears in some of the tiny holes of the chaotic region. Right after its appearance TW_{TS} is less relevant for the dynamics of the system due to its high number of unstable eigenvalues. In the state space slice for $Re_B = 5720$ shown in figure 5.3a, it is possible to see the large turbulent basin and that the lower branch of TW_{TS} lies below the laminar turbulent border. As the Reynolds number increases, more and more of the unstable directions become stable, until finally, between 5727 and 5815, the lower branch of TW_{TS} has a stable manifold of co-dimension one that allows to divide the state space. Thus, for $Re_B > 5727$ the traveling wave TW_{TS} is much more important for the dynamics than below. In state space slices for $Re_B > 5727$ it is possible to see a laminar-turbulent boundary connected to TW_{TS}. This boundary can be distinguished from the one connected to TW_E, since close to the boundary connected to TW_{TS} the transition times are significantly higher and even exceed $4 \cdot 10^4$ time units. The question how the two boundaries are actually connected is difficult to answer. For Reynolds number 5780 (inset in figure 5.3d) it seems that the borders do not cross but rather form a spiral down to very small scales.

Even for $Re_B = 5855 > Re_{crit}$ (figure 5.3f) where TW_{TS} already collided with the laminar state, a sharp border between regions with short and long transition times is visible.

However, another key feature that becomes apparent in this visualization is that no separated turbulent bubble related to TW_{TS} exists at these Reynolds numbers. There is also no difference in statistical properties of the turbulence reached by trajectories starting close to the TW_{TS} boundary and such starting close to the TW_E boundary. Therefore, there is only one kind of turbulence, but there are two different ways and in particular different time scales on which the transition takes place.

5.3 TS transition and Bypass transition

The huge differences in the timescales for transition, that become obvious in the slices of the state space, suggest the existence of different mechanisms for the transition to turbulence. A close inspection of trajectories becoming turbulent on the slower path shows that they undergo what is usually called a Tollmien-Schichting (TS) transition. Starting with a three-dimensional flow field, the flow structure becomes more and more two-dimensional and the two-dimensional roll structure of TW_{TS} is reached. After approaching TW_{TS} along its stable directions, the trajectory is repelled in the unstable direction of TW_{TS} leading to an increase in amplitude. Finally, a three-dimensional instability destroys the two-dimensional roll-solution and a turbulent state is reached.

Trajectories becoming turbulent on the fast path do not approach a two-dimensional roll structure at any time. Therefore, they undergo what is classically called a bypass transition

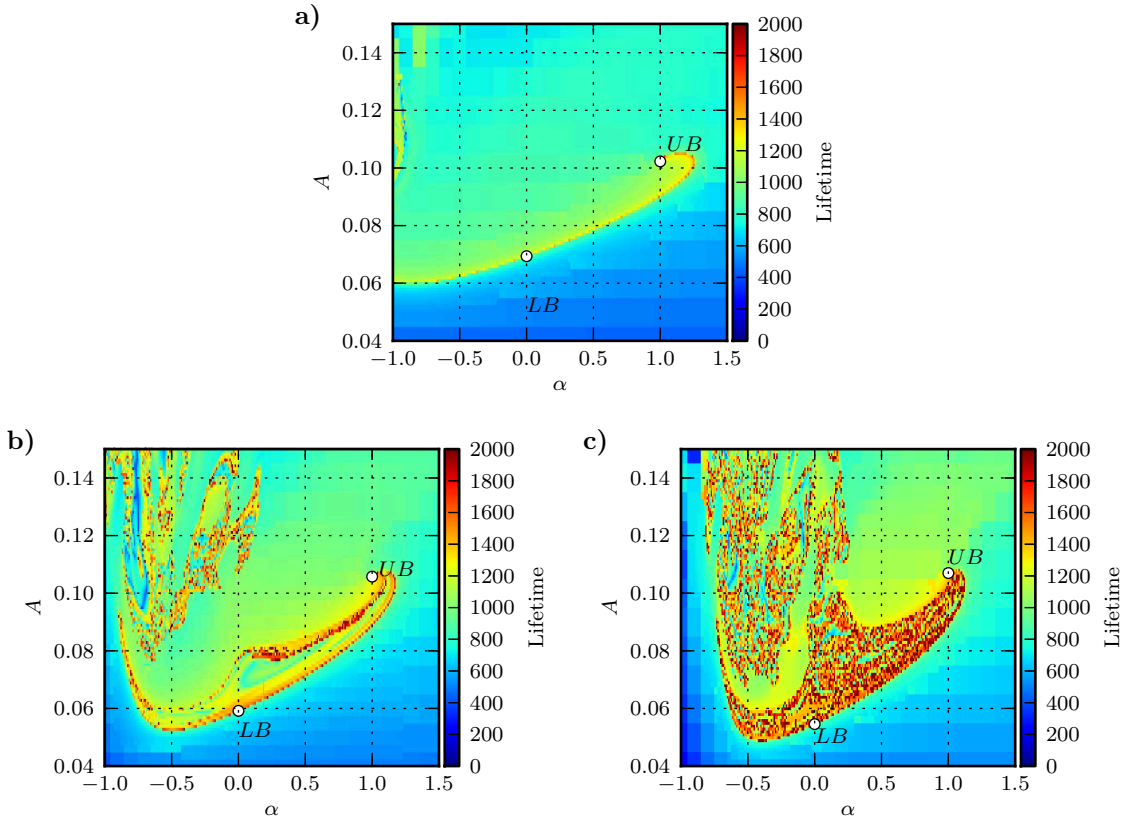

Figure 5.2: State space slices for different Reynolds numbers. The initial conditions are color coded according to their lifetime, the time they need to fall below 0.002 in amplitude $a(\vec{u})$. Initial conditions that do not fall below this value within the observation time of 2000 time units are shown with this value as lifetime. For a), b) and c) the Reynolds numbers are 500, 560 and 600, respectively. The positions of the upper and lower branch of TW_E are marked with white dots.

(Schmid and Henningson, 2001).

In figure 5.4 some trajectories starting at an initial condition taken from the slice in figure 5.3 are shown. The green and blue lines are typical representatives of TS transition and the solid yellow trajectory is a typical bypass transition trajectory. The trajectory shown with a dashed yellow line is of an intermediate type. It takes several thousand time units until the trajectory becomes turbulent and it comes a little bit closer to the roll structure of TW_{TS}, but it always stays three-dimensional.

The comparison of the trajectories suggests the following interpretation of subcritical TS transition. Actually, trajectories that undergo TS transition are on the way to decay but this is prevented by the stable manifold of TW_{TS}. They then depart from this manifold in the unstable direction of TW_{TS}, which is a slow process because the growth rate corresponding to this direction (the real part of the unstable eigenvalues) is very small. The scenario is comparable to the one described by Kreilos et al. (2014a), but the other way around. In their study on plane Couette flow they found new chaotic saddles emerging inside of an existing one. In the present case an existing chaotic saddle is enclosed (at least in part) by an new one.

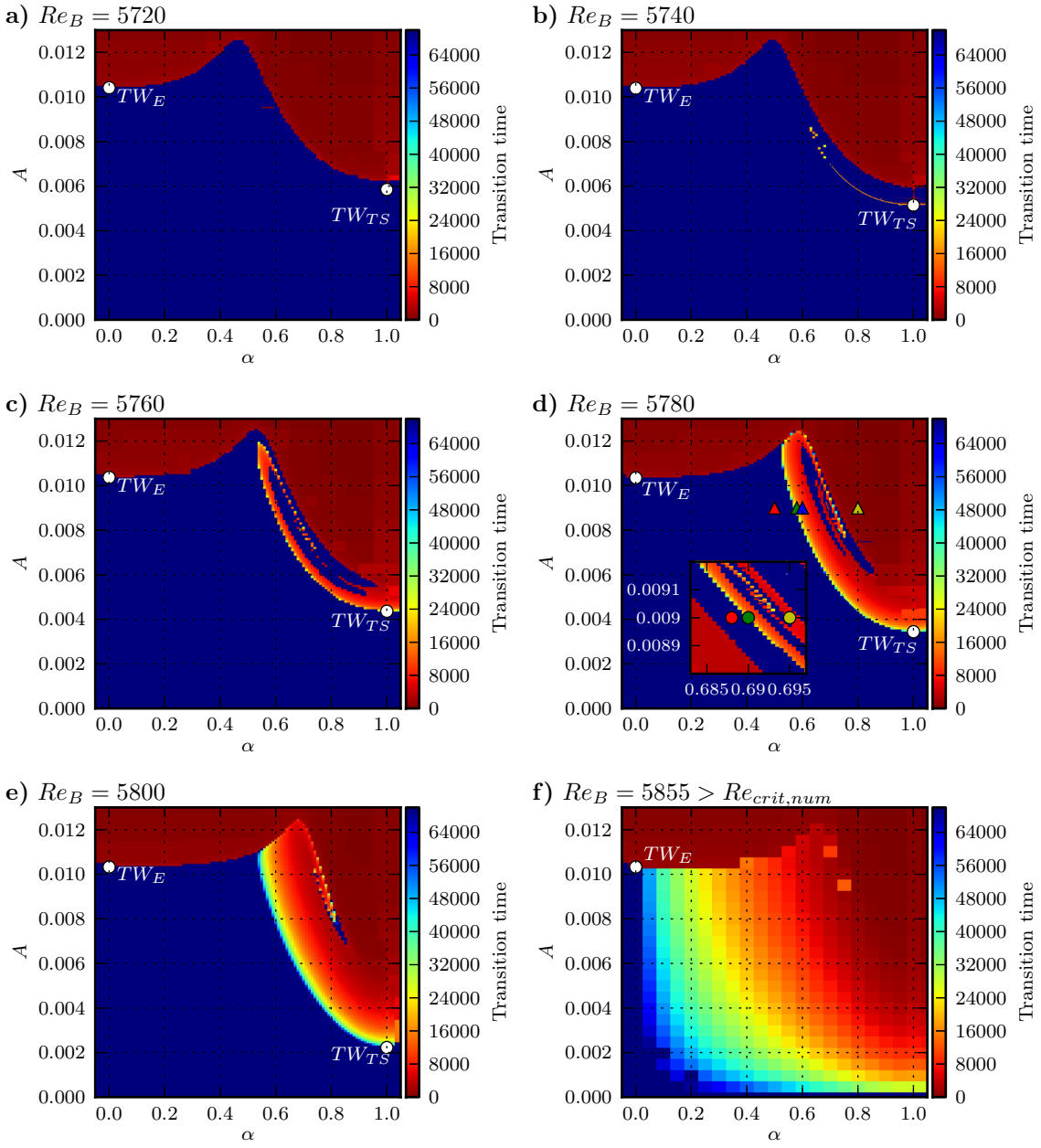

Figure 5.3: 2D-slices of the state space for various Reynolds numbers. For $Re_B < Re_{crit,num}$ the parameter α interpolates between the flow fields of both traveling waves. For $Re_B > Re_{crit,num}$ the interpolation on the x-axis is between the flow field of TW_E and the unstable mode of the laminar state. The transition time of the initial condition is color coded. The maximum integration time is 70000 time units, therefore for $Re_B < Re_{crit}$ initial conditions becoming laminar are plotted with the max. integration time. Even for $Re_B = 5855 > Re_{crit}$ (f) a sharp change from the rather slow TS transition to the rather quick bypass transition is visible.

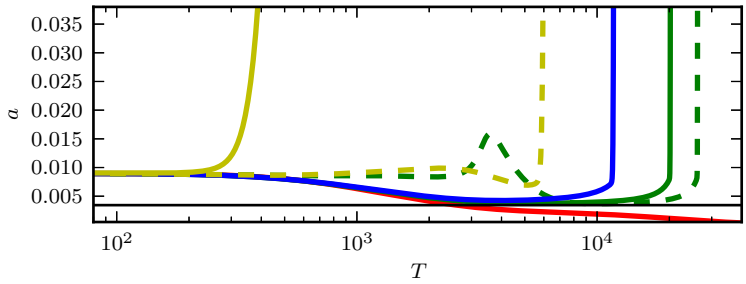

Figure 5.4: Amplitude a of the flow field vs. time for selected initial conditions at $Re_B = 5780$. The initial conditions for the trajectories drawn with solid and dashed lines are marked in figure 5.3d with triangles and circles, respectively. The black line corresponds to the amplitude of the lower branch of TW_{TS} at $Re_B = 5780$. The green and blue lines are typical representatives of TS transition and the solid yellow trajectory is a typical bypass transition trajectory. The trajectory shown with a dashed yellow line is of an intermediate type.

Major differences in the mechanism of the transition can be identified by a closer inspection of the flow structures in the late stages of the transition. In the figures 5.5 and 5.6 the vortex structures that appear in typical bypass and TS transitions are visualized by the Q-vortex criterion (Jeong and Hussain, 1995). The initial conditions are the slightly disturbed traveling waves TW_E and TW_{TS}. In both simulations the Reynolds number is 5780, the domain length is 2π, the width is 2π, and the resolution is $N_x \times N_y \times N_z = 192 \times 177 \times 192$. For the TS transition the visualizations show the secondary instability of the TS-waves which starts after a long phase during that the TS-wave grows in magnitude. The spanwise rolls of the TS-wave have a very low positive value of Q that is below the values used for the iso-surfaces. The iso-surfaces of the Q-criterion show that streamwise vortices appear close to the wall. These vortices develop a Lambda-like shape (figure 5.5c) and then form a hairpin vortex (figure 5.5d). The heads of the hairpin vortices move towards the center-plane until the upper and the lower vortex structures touch and the large hairpin structures are destroyed leaving a turbulent band. The turbulent band quickly spreads in spanwise direction resulting in an uniformly turbulent state at $t \approx 1885$.

For the case of bypass transition apparently the strongest vortex structures are close to the center. The strength of the vortices grows as time elapses and a strong streamwise modulation (right panel in figure 5.6d) of the vortex structures develops that is not present in the TS transition. The vortex structures spread towards the wall (compare figure 5.6 d and e) and also in spanwise direction. Finally, the domain is uniformly turbulent.

Additional simulations at $Re_B = 6000$ show that the course of both transitions is qualitatively the same in the supercritical range.

The main difference of the transition types is the region where the vortex structures appear and develop. While TS transition starts with vortices close to the wall that develop into hairpin vortices, bypass transition is dominated by streamwise vortices close to the mid-plane. However, the two cases visualized in figure 5.5 and 5.6 are somehow limit cases and especially not all cases of bypass transition show that pronounced vortex structure close to the center-plane.

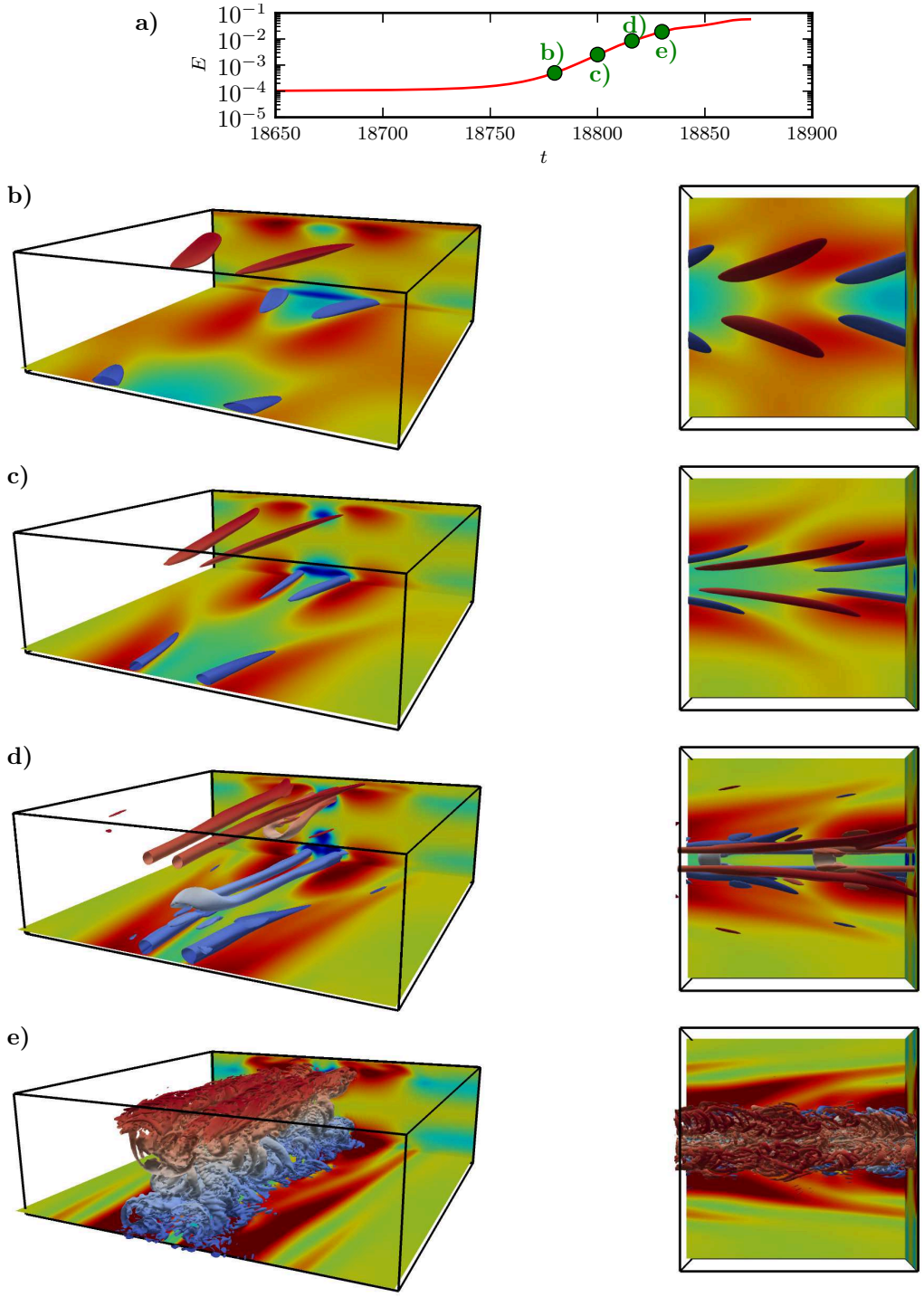

Figure 5.5: Tollmien-Schlichting transition visualized by iso-surfaces of the Q-vortex criterion. The initial condition is the laminar profile with a small random perturbation. The Reynolds number of the simulation is 5780. The energy versus time is shown in a). The circles in a) mark the positions of the visualizations b)-e). The values of the iso-contours are 0.0005 for b), 0.05 for c) and d) and 0.5 in e). The iso-surfaces are colored according to their wall-normal position ranging form -1 (blue) to 1 (red). The streamwise velocity, color coded from blue (minimum value) to red (maximum value), is shown in the back side and in a plane parallel to the plates in a distance of 0.1 to the lower plate.

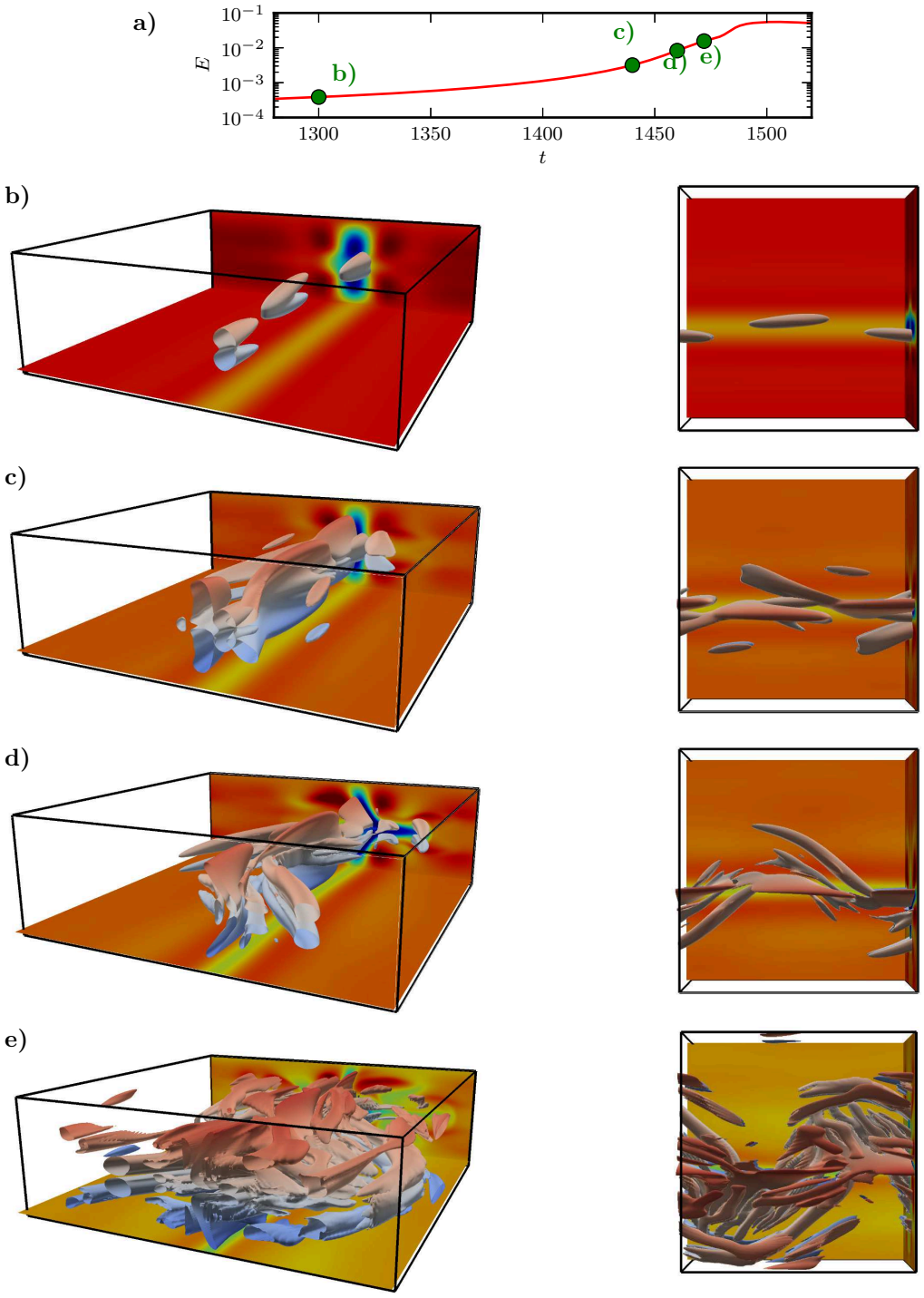

Figure 5.6: Bypass transition visualized by iso-surfaces of the Q-vortex criterion. The initial condition is the laminar profile with a small random perturbation. The Reynolds number of the simulation is 5780. The energy versus time is shown in a). The circles in a) mark the positions of the visualizations b)-e). The values of the iso-contours are 0.0005 for b), 0.05 for c) and d) and 0.5 in e). The iso-surfaces are colored according to their wall-normal position ranging form -1 (blue) to 1 (red). The streamwise velocity, color coded from blue (minimum value) to red (maximum value), is shown in the back side and in a plane parallel to the plates in a distance of 0.1 to the lower plate.

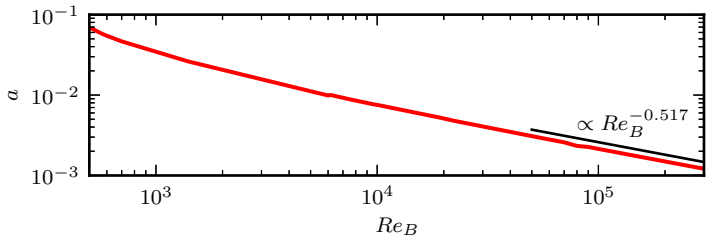

Figure 5.7: Double logarithmic plot of the amplitude a of TW_E vs. Re_B. For high Reynolds numbers $a(\vec{u})$ (red) scales as $Re_B^{-0.517}$ (black).

The fact that bypass transition is related to the exact coherent structure TW_E offers an opportunity to calculate an upper bound for the scaling of the minimal threshold for bypass transition. TW_E can easily be tracked to high values of Re_B. With increasing Re_B its variation with streamwise coordinate becomes weaker. This allows to reduce streamwise resolution with increasing Re_B while increasing the wall-normal resolution to proper resolve the developing critical layer (Maslowe, 1986). It was possible to track TW_E up to $Re_B = 3 \cdot 10^5$ where a wall-normal resolution of $N_y = 225$ was used. In figure 5.7 the amplitude a of the traveling wave is shown vs. Re_B in a double logarithmic plot. The plot shows that TW_E asymptotically approaches the laminar state. Previous studies by Itano et al. (2013) and Wang et al. (2007) for plane Couette flow showed that ECS can scale differently with increasing Reynolds number. Some of them approach the laminar state, while others keep a finite distance to it. For TW_E, the decrease of the amplitude $a(\vec{u})$ is in agreement with a $Re_B^{-0.517}$ scaling. The actual threshold for bypass transition can decrease faster than $Re_B^{-0.517}$ but not slower. For boundary layers Fransson et al. (2005) found that the threshold for inducing bypass transition by free-stream turbulence scales as $Re^{-0.5}$ what is quite close to the scaling obtained from TW_E.

In this section the existence of different routes to turbulence was investigated by methods of dynamical systems theory. The existence of two different edge states in the subcritical range allows for two different paths to turbulence. Since the edge state TW_E which is responsible for bypass transition exists for subcritical and supercritical values of Re_B, bypass transition is always possible. TS transition is relatively unimportant for $Re_B < Re_{crit}$. Especially, for Reynolds numbers where TW_{TS} does not exist or has multiple unstable eigenvalues the amount of initial conditions undergoing TS-transition is of measure zero. Since also the Blasius and the asymptotic suction boundary layer show two paths to turbulence and have a base flow that is linearly unstable above a critical Reynolds number (see section 10.2 for a stability analysis of the asymptotic suction boundary layer), the phenomenon investigated in this section is also present in these flows. As for PPF, a state for bypass transition can be found in these flows (see Kreilos et al., 2013; Khapko et al., 2013 for ASBL and Duguet et al., 2012 for the Blasius boundary layer) which most likely also exists in the supercritical regime. Therefore, coexisting transition paths are present in the supercritical regime, while for subcritical Reynolds numbers bypass transition dominates and TS transition is possible but unlikely.

Chapter 6

Streamwise and doubly-localized states

Parts of the results presented in section 6.2, 6.3 and 6.7 have been published in "Streamwise and doubly-localized periodic orbits in plane Poiseuille flow" , S. Zammert and B. Eckhardt, Journal of Fluid Mechanics , vol. 761, pp. 348-359, 2014
"A spotlike edge state in plane Poiseuille flow", S. Zammert and B. Eckhardt, Proceedings in Applied Mathematics and Mechanics , vol. 14, pp. 591-592, 2014

6.1 Introduction

Within the last decade the study of coherent structures in small periodic domains contributed enormously to our understanding of the origin of turbulence, the state space structure, and the understanding of the transition in subcritical flows. For the case of PPF the previous sections explained the origin subcritical turbulence and the existence of two transition paths using exact coherent states. For plane Couette and pipe flow similar progress has been achieved (e.g. Gibson et al., 2008; Mellibovsky and Eckhardt, 2012; Kreilos and Eckhardt, 2012) for small computational domains. But because of the complex spatio-temporal dynamics of subcritical flow close to the onset of turbulence (Moxey and Barkley, 2010; Duguet et al., 2010a; Tuckerman et al., 2014) and the existence of turbulent spots (e.g. Carlson et al., 1982; Henningson et al., 1987; Lemoult et al., 2013), the study of small periodic computational domains is not able to provide a complete picture of the physical processes and phenomena related to subcritical turbulence. Therefore, the investigation of large system sizes is necessary.

With the intent to understand the dynamics in these spatially extended systems and rendered possible by the increase of computational power, in recent times some exact coherent structures in such large computational domains were identified for the case of plane Couette and pipe flow (Schneider et al., 2010a; Brand and Gibson, 2014; Avila et al., 2013). For PPF we already encountered spanwise localized ECS in the previous sections.

In this section different spatially localized, in particular streamwise and doubly-localized, structures of plane Poiseuille flow are studied in detail. To identify localized ECS, the technique

of edge tracking, bifurcation analysis of known spatially extended ECS, and continuation in the geometric parameters are used. In addition to the investigation of ECS, localized turbulence in PPF is studied and compared to the dynamics that exists in pipe flow.

6.2 Streamwise localized periodic orbits and edge states

In a small computational domain with $L_x = L_z = 2\pi$ edge tracking converges to the traveling wave TW_E (see section 3.2). We fix the streamwise wavelength of the wave to $L_x = 2\pi$ and analyze its stability with respect to disturbances with wavelengths that are multiples of its wavelength. The results show that TW_E is unstable to disturbances with long wavelengths. For $Re_B = 1400$ the basic wave shows an instability to disturbances with $L_x = 4\pi$. In particular, the wave has an additional pair of complex conjugated eigenvalues for $Re_B < 1785$ indicating a Hopf bifurcation. It is possible to identify the bifurcating periodic state (referred to as $PO_{E,short}$ in what follows) using edge tracking in a domain with $L_x = 4\pi$. For this domain length and at $Re_B = 1400$, edge tracking quickly converges to a time-periodic state with a period of about 580. If the periodic orbit is tracked to higher Reynolds numbers, it turns out that it indeed connects to TW_E at $Re_B \approx 1785$. The spanwise flow in the mid-plane of the orbit and the traveling wave is shown for $Re_B = 1400$ in figure 6.1. The plot reveals that the bifurcating orbit is quite similar to the spatially extended traveling wave, but it is overlain by a modulation with a wavelength of 4π. The modulation becomes stronger with decreasing Reynolds number, and therefore with increasing distance to the bifurcation point.

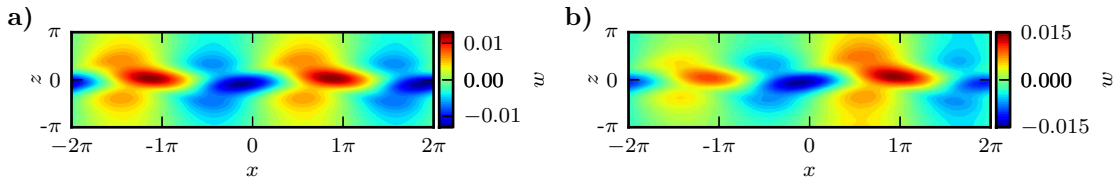

Figure 6.1: In panel a) and b) visualizations of the spanwise velocity in the center-plane for the traveling wave TW_E and the periodic orbit $PO_{E,short}$ that bifurcates from TW_E are shown. For both plots the Reynolds number Re_B is 1400.

Despite of this instability with a wavelength of 4π, TW_E has further instabilities corresponding to larger wavelengths. Therefore, the traveling wave cannot be the edge state in a spatially extended computational domain. To identify the real edge state, an edge tracking in a longer domain of length 32π but for the same width 2π and Reynolds number $Re_B = 1400$ is performed. For this calculation a resolution of $N_x \times N_y \times N_z = 512 \times 49 \times 32$ is used. The edge tracking converges quite quickly to a state that at first glance looks like a state of constant energy density,

$$E(\vec{u}) = \frac{1}{4L_xL_z} \int_0^{L_x} \int_{-1}^{1} \int_0^{L_z} \vec{u}^2 dxdydz. \tag{6.1}$$

However, as the closer inspection of the edge trajectory in figure 6.2 reveals, the energy density is not constant but shows a regular oscillation with an amplitude of order 10^{-8}.

Although the initial velocity field fills the entire domain in streamwise direction, the flow structure of the state obtained by edge tracking is localized in streamwise direction. Using this state as an initial condition in a Newton search, we quickly converged to a streamwise

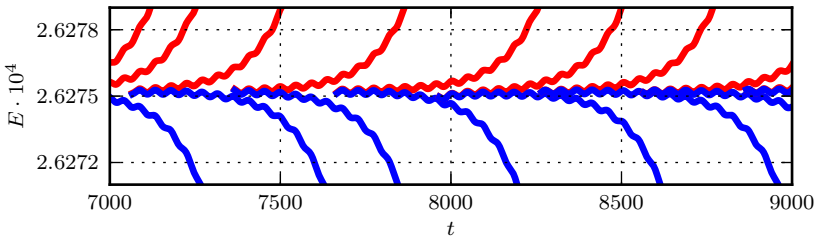

Figure 6.2: Edge tracking in a computational domain of length $L_x = 32\pi$ and width $L_z = 2\pi$ at $Re_B = 1400$. Shown are the energy densities $E(\vec{u})$ of the trajectories on both sides of the laminar-turbulent boundary. For the trajectories on the turbulent and laminar side red and blue color is used, respectively. The edge trajectory bracketed by these trajectories oscillates periodically in energy.

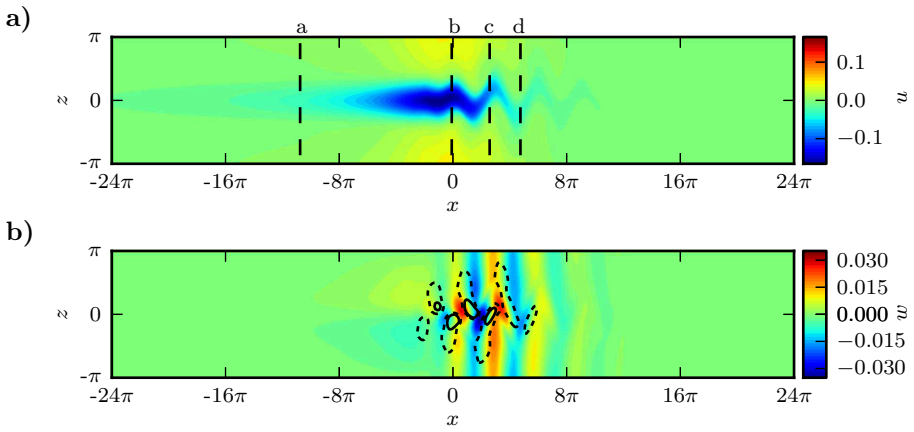

Figure 6.3: Velocities in the mid-plane for the edge state PO_E at $Re_B = 1400$. Panels a) and b) show the streamwise and spanwise velocities, respectively. The black lines in a) mark the positions of the spanwise wall-normal cross-sections in 6.4 a)-d). The solid and dashed lines in b) are iso-contours of the Q-vortex criterion (Jeong and Hussain (1995)) at levels of 0.001 and 0.0001, respectively. The direction of the flow is from left to right.

localized relative periodic orbit, henceforth refered to as PO_E. The localization at $Re_B = 1400$ is already quite strong what allows to transfer the state to a computational domain of length 64π for further study. In the computational domain with $L_x = 64\pi$, $L_z = 2\pi$ and $L_y = 2$ a resolution of $768 \times 65 \times 48$ is used. The results are checked with a higher spanwise resolution of $N_z = 80$. The streamwise and the spanwise velocity components in the mid-plane are shown in figure 6.3. Cross-sections for $Re_B = 1400$ for different streamwise positions are shown in figure 6.4a - d and the streamwise averaged velocity is shown in figure 6.4e. These visualizations show that the orbit has a mirror symmetry,

$$s_y : [u, v, w](x, y, z) = [u, -v, w](x, -y, z), \tag{6.2}$$

and is dominated by a strong narrow low speed streak and a weak and extended high speed streak. It is therefore very similar to the traveling wave TW_E. A comparison of the streamwise averaged flow for TW_E shown in figure 3.1 in section 3.2 and of the average flow for PO_E shown in figure 6.4e also reveals this similarity.

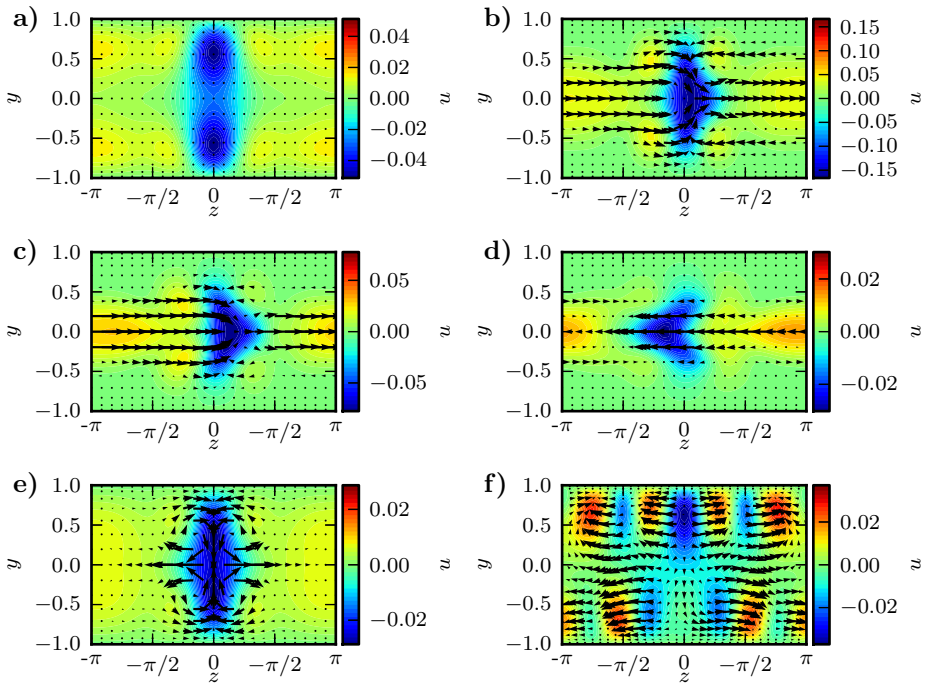

Figure 6.4: a) - d) Cross-sections of the edge state PO_E at $Re_B = 1400$ at the streamwise positions indicated in figure 6.3a). The in-plane components of the velocity are visualized by arrows and the streamwise velocity component is color coded. Panels e) and f) show the streamwise-average flow of PO_E at $Re_B = 1400$ and of the orbit that bifurcates from it, PO_{asy}, at $Re_B = 1625$, respectively.

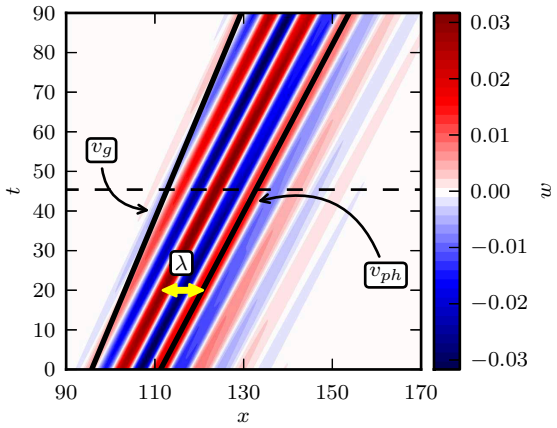

Figure 6.5: Visualization of the dynamics of PO_E by a space-time-display of the spanwise velocity in the mid-plane $y = 0$ at at $z = 0$ for $Re_B = 1400$. The solid black lines indicate the group velocity v_g and the phase velocity v_{ph} for one of the maxima. The wavelength λ of the internal modulations varies along the state. The dashed black lines marks one period in energy, which is only half a period of the state.

The complex spatial propagation pattern of the wave can be seen in plots of the spanwise velocity in the mid-plane at $z = 0$ vs. time in figure 6.5. After two periods in energy, the state returns except for a downstream shift. After one period in energy it returns up to a symmetry operation,

$$s_z : [u, v, w](x, y, z) = [u, v, -w](x, y, -z), \tag{6.3}$$

and a shift that is half the one after two periods. The figure clearly shows a group velocity v_g for the envelope of the state and a phase velocity v_{ph} for the underlying structure. The group velocity v_g can be read off from the period in energy, as distance traveled over two periods divided by the two periods. The corresponding line in the figure shows that this follows the envelope rather well. The structures underneath the envelope move with a different velocity that can be read off from the slope of the maxima. However, the wavelength λ of the spanwise modulations varies slightly with position and is slightly larger at the front than in the center and towards the end of the state. Therefore, also the velocity of each maximum varies slightly, so that the phase velocity depends on the position within the state.

We use a continuation method (see e.g. Dijkstra et al., 2014) to track the state in Reynolds number. It turns out that the periodic orbit exists down to $Re_B \approx 1038$, where it is created in a saddle node bifurcation. Furthermore, it is also possible to identify the upper branch of the periodic orbit. Bifurcation diagrams using the minimum of the energy and the period of the orbit on the ordinate are shown in figure 6.6.

A stability analysis of the state shows that for $Re_B > 1100$ the lower branch has one unstable direction. Therefore, for these Reynolds numbers the state is an edge state whose stable manifold can separate the state space into two parts. For other values of Re_B the periodic orbit has more than one unstable direction. The bifurcation at $Re_B = 1100$ is a Sacker-Neimark bifurcation that breaks the s_y-symmetry. This bifurcation is followed by further bifurcations, resulting in eight unstable directions for the lower branch. One of the bifurcations of the lower branch is a pitchfork bifurcation that breaks the s_y-symmetry and creates an asymmetric periodic orbit (PO_{asy}). The image of the state in figure 6.4f shows that its flow structure is more complex than those of PO_E. The solution branch of PO_{asy} is also shown in figure 6.6.

Length of the orbit and decay in the tails

Since PO_E is streamwise localized, an interesting quantity to study is its streamwise length. For an investigation of the length, we study the total energy density of the deviation from the laminar flow as a function of the streamwise position,

$$E_\perp(x) = \frac{1}{4L_z} \int_0^{L_z} \int_{-1}^{1} \mathbf{u}^2 \, dydz, \tag{6.4}$$

and the density of the cross-flow energy,

$$E_{\perp,c}(x) = \frac{1}{4L_z} \int_0^{L_z} \int_{-1}^{1} v^2 + w^2 \, dydz. \tag{6.5}$$

The energy densities for the periodic orbit at $Re_B = 2010$ (at the time of minimum energy) are shown in figure 6.7a. One can identify a small area with relatively high cross-flow energy at the front of the state. In this region the cross-flow motion draws energy from the laminar profile and transfers it into streamwise velocity which then drives streaks and causes a steep increase of the total energy density at the front of the state. The energy in the streamwise

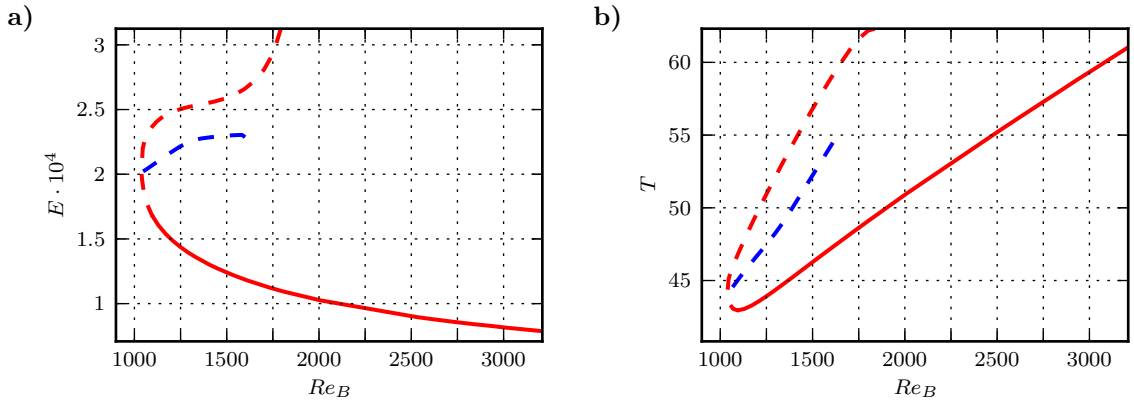

Figure 6.6: Bifurcation diagrams for the coherent structures. In panel a) the minimum energy of the localized periodic orbit (red) and the asymmetric orbit (blue) are shown in dependence on Re_B. In both cases the minimum in energy over the period is shown. The stability of the orbit is indicated by the line type, solid for a single unstable direction, and dashed for more than one. Panel b) shows the variation of the periods in energy vs. Re_B.

velocity has its maximum at a streamwise position where the cross-flow energy is already very low again. In the absence of cross-flow motion the streaks decay viscously, which results in the long upstream tail of the state.

Based on the energy density one can introduce two characteristic length scales for PO_E, defined as the distances from the maximum of the energy density to the points upstream (l_t) and downstream (l_h) where the energy has dropped to half the maximum value. These length scales vs. Reynolds number are shown in figure 6.7b. On the downstream side, the energy drops off quickly, on a length scale that varies very little with the Reynolds number. On the upstream side, the energy drops off more slowly, on a length scale that increases linearly with Re_B. The reason for this scaling is the viscous decay of the streaks on a time scale proportional to Re_B. This translates into a spatial scale proportional to Re_B due to the almost constant advection velocity. Although the structure becomes longer with increasing Reynolds number, the total energy density of the lower branch and also the maximum of the energy density decrease with increasing Re_B as can be seen in figure 6.6.

To study the decay of the flow structure in its front and tail, we regard the infinity-norms

$$\mathcal{L}^\infty(u)(x) = \max_{z,y}|u(x,y,z)|, \tag{6.6}$$

here given for the streamwise component u of the velocity components along the streamwise position x. For $Re_B = 1100$ the course of the infinity-norms in dependence on the streamwise coordinates x is shown in figure 6.8. Especially in the tail, the decay of all three components is in good agreement with an exponential decay. By using exponential fits $\exp(x - x_0)/\lambda_x$ to the data, we obtain length scales λ_x for the decays in the tail. For the streamwise and spanwise velocity components these length scales are 20.37 (1) and 21.84 (2), respectively. The wall-normal velocity component which is necessary for streak generation decays on a length scale of only 7.92 (3) and thus it decays much faster than the other components.

In the head of the structures, deviations from an exponential decay appear especially for the spanwise velocity component w. A more general discussion of the decay in the head and

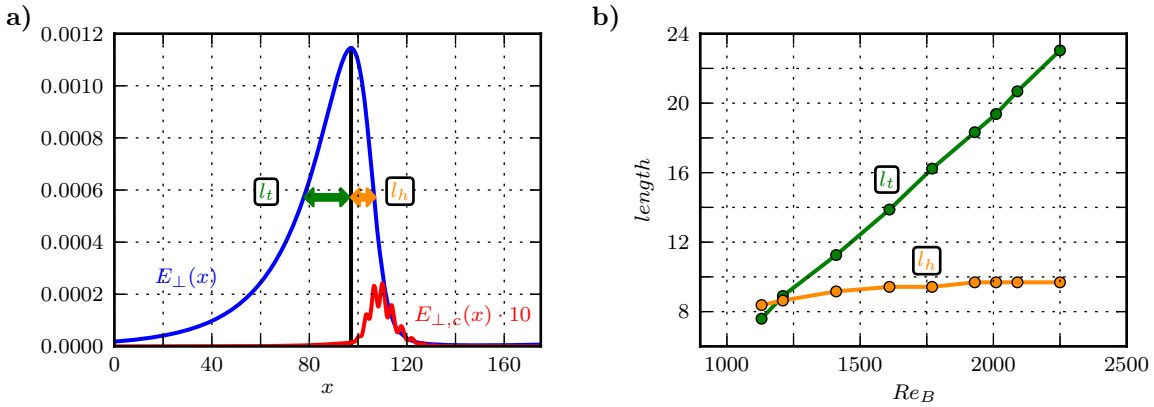

Figure 6.7: Energy profiles of the localized state PO_E. In panel a) the total (red) and the cross-flow (blue) energy densities at $Re_B = 2010$ are shown along the flow direction, which is from left to right. The cross-flow energy density is multiplied by a factor of 10. Panel b) shows the upstream l_h (orange) and downstream l_t (green) distances from the maximum to half the maximal values in energy *vs.* Reynolds number.

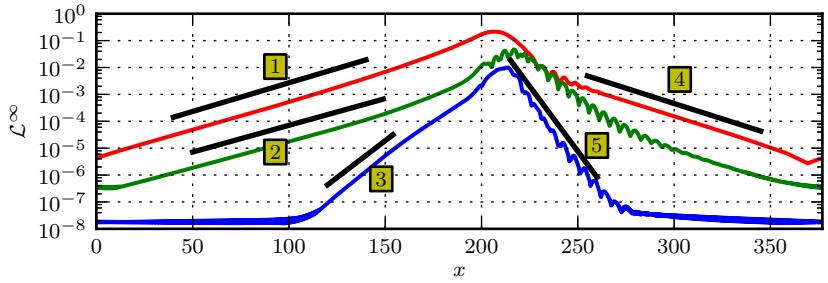

Figure 6.8: $\mathcal{L}^\infty$-norm (maximum over y and z) of the streamwise u (red), the spanwise w (green) and wall-normal v (blue) velocity component versus streamwise coordinate x. The Reynolds number is 1100 and the length of the computational domain is 120π. The black lines marked by the labels $1-5$ show exponential decays with slopes obtained by fitting the decay of the velocity components.

tail of localized states can be found in section 7. Exponential fits to v and u, which decay approximately exponential, yield length scales of 19.05 (4) and 4.49 (5), respectively.

In principal, the length scales obtained by the exponential fits to the tails of the state could be used as a measure for the length of the state. But since exponential scaling might be visible only where the amplitudes of the velocities are already quite small, this definition can be less meaningful than the one used above. A further problem is that in some case there is a complete lack of an exponential scaling (compare section 7.3).

Long-wavelength instability

In finite domains with periodic boundary conditions the increasing length of the structures will at some point cause interferences between head and tail and a loss of localization. If

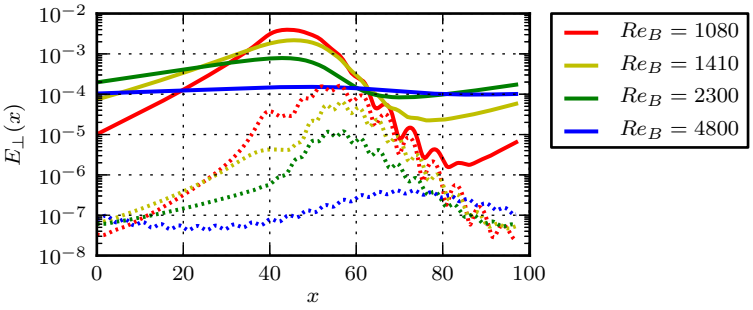

Figure 6.9: Profiles of PO_E for increasing Reynolds numbers. The solid lines show the total and the dashed lines the cross-flow energy densities. Consistent with the increase in l_d, the states become more and more delocalized with increasing Reynolds number, until they merge into a spatially extended state near $Re_B = 5385$. The streamwise length of the computational domain is 32π.

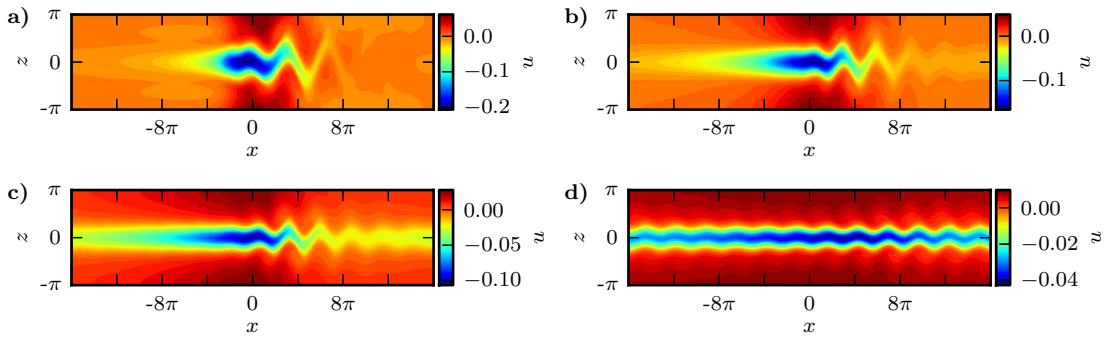

Figure 6.10: Streamwise velocity in the center-plane for the periodic orbit PO_E. The panels a)-d) correspond to the Reynolds numbers $Re_B = 1080, 1410, 2300$ and 4900, respectively.

the streamwise length L_x of the computational domains is fixed at 32π and the orbit PO_E is continued to high Reynolds numbers, the orbit connects to the streamwise extended traveling wave TW_E with a wavelength of 2.66π at $Re_B \approx 5385$. This is documented in figure 6.9 in a plot of the energy densities vs. Re_B. For low Re_B there is a pronounced maximum in the densities, but for increasing Re_B the differences decrease and finally at $Re_B \approx 5385$ the uniform energy density corresponding to the traveling wave is obtained. The approach of the traveling wave is also visible in the flow structures which are visualized in figure 6.10 using the streamwise velocity in the mid-plane.

Turned the other way round, the localized state arises out of a streamwise long-wavelength instability of a traveling wave. These long-wavelength instabilities apparently are a widespread mechanism for the generation of localized states. They were also discussed for the generation of localized states in plane Couette flow (Melnikov et al., 2014) or in pipe flow (Chantry et al., 2014). As we will see later in this section, the Tollmien-Schlichting waves of PPF also show long-wavelength instabilities leading to localized states.

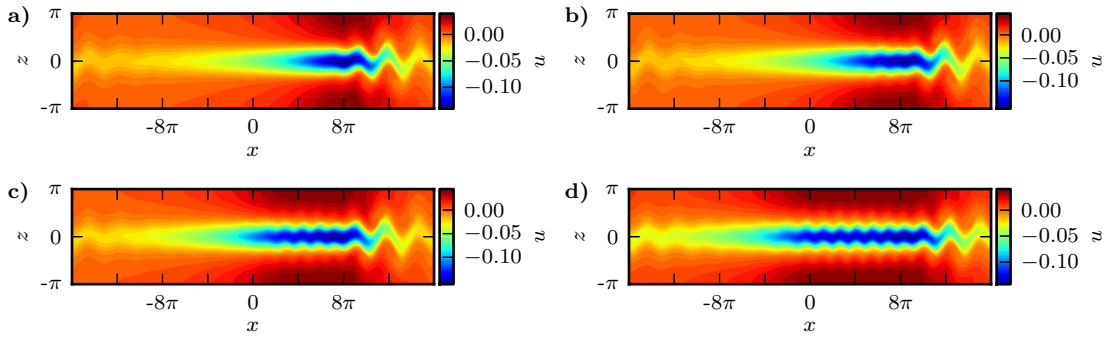

Figure 6.11: Streamwise velocity in the center-plane for relative periodic orbits of different length. The orbit shown in panel a) is PO_E at $Re_B = 1700$. In b) - d) other relative periodic orbits at the same Reynolds number are visualized.

Periodic orbits of different spatial length

Since in spatially intermittent flows laminar regions and turbulent patches could have different length and spread in streamwise direction (see Avila and Hof 2013 and section 6.7), the existence of ECS of different length for the same values of Re_B is essential. Indeed, it is possible to find further relative periodic orbits related to PO_E that show a streamwise localization but differ from PO_E in their length.

The orbits, that were found in a computational domain with a streamwise length of 32π using a resolution of $N_x \times N_y \times N_z = 256 \times 33 \times 48$, have flow structures quite similar to PO_E. They are also symmetric to reflections at the center-plane and have a dominant low-speed streak. The point in which they differ from PO_E at the same value of Re_B is the streamwise length of the low-speed streak. In these structures the low-speed streak is longer and has additional wiggles. Visualizations of those states at $Re_B = 1700$ using the streamwise velocity in the center plane are shown in figure 6.11.

As for PO_E it is possible to continue these orbits to lower Reynolds numbers. In contrast to the case of PO_E, the localization does not become stronger with decreasing Reynolds number and transfers of the states into larger domains failed. Thus, the orbits are unfortunately strongly modulated rather than localized in streamwise direction.

6.3 A doubly-localized periodic orbit

The periodic orbit PO_E discussed in the previous section is spatially extended in the spanwise direction albeit the modulation with the spanwise coordinate z is quite strong which is an early sign for localization. For the traveling wave TW_E, from which PO_E bifurcates, it is known from section 3.2 that it localizes when the spanwise width of the computational domain is increased. Therefore, it is reasonable to assume that PO_E should behave similar if it is continued in L_z. We start with PO_E in a domain with $L_x = 64\pi$ and $L_z = 2\pi$. For the continuation a Reynolds number of $Re_B = 2180$ is fixed. As in section 3.2 we use the energy density $E_{\|}(z)$ (equation 3.2) as a measure of the localization. In figure 6.12 the quantity is shown for various widths L_z. For each value of L_z the maximum located at $z = 0$ corresponds to the position of the low-speed streak. For $L_z = 2\pi$ the second smaller maximum is the position of the weak high-speed

streak. Somewhere between 2π and 2.5π the lower maximum splits into two and for $L_z > 5\pi$ the energy density has a very low value over most of the domain indicating a spanwise localized flow structure.

Thus, the orbit PO_E and also the streamwise extended traveling wave TW_E (see section 3.2) that are not spanwise localized in narrow domains can be smoothly morphed into a spanwise localized solution. This mechanism for spanwise localization, which does not involve a long-wavelength modulation, was also recently described by Chantry and Kerswell (2015) for a 9-PDE model of plane Couette flow.

The largest value of L_z which is studied is 72π. For this domain a resolution of $N_x \times N_y \times N_z = 384 \times 49 \times 1728$ is used. The doubly-localized solution in this domain keeps the s_y-symmetry of PO_E. The period of the orbit changes slightly with increasing width. While the spanwise extended orbit for $L_z = 2\pi$ has a period of 52.47, the doubly-localized orbit for $L_z = 72\pi$ has a period T of 53.575. After this time the state returns in shape apart from a shift in streamwise direction and the symmetry operation s_z. The group speed v_g for the spanwise extended orbit at $Re_B = 2180$ is 0.9033 and for the doubly-localized orbit one finds $v_g = 0.8803$.

Discussion of the localization properties

An interesting question is how the localized solution decays in its peripheral region. In (Gibson and Brand, 2014) and (Brand and Gibson, 2014) the decay of spanwise localized and doubly-localized equilibrium solutions in plane Couette flow is analyzed. For solutions with pure spanwise localization an exponential decay, $u \propto \exp(-\alpha z)$, is found that depends on the streamwise wavenumber α of the structure. In streamwise direction they assume a similar scaling, $u \propto \exp(-\mu(\gamma)x/Re)$, that depends on the Reynolds number and the spanwise wavelength γ. They showed that for appropriately chosen γ, the streamwise decay of their doubly-localized equilibrium solution is in concordance with the assumed exponential scaling. For a transfer of this approach to PPF see section 7.2.

However, for the doubly-localized periodic orbit presented and discussed in this section the decay in the spanwise direction deviates from an exponential scaling as the plots of the energy density $E_{\|}(z)$ in figure 6.12 reveal. Since the integrated density $E_{\|}(z)$ increases with the length of the turbulent region, a much better measure is the infinity-norm,

$$\mathcal{L}^{\infty}(u)(z) = \max_{x,y}|u(x,y,z)|, \tag{6.7}$$

of the velocity components along the spanwise coordinate z which is here given for the streamwise component u. The use of this quantity has the additional advantage that it was also used by Brand and Gibson (2014) which simplifies comparison. The values of $\mathcal{L}^{\infty}(u)$ and $\mathcal{L}^{\infty}(w)$ are shown in figure 6.13 for $L_z = 72\pi$. The decay of $\mathcal{L}^{\infty}(u)$ is slower than exponential while $\mathcal{L}^{\infty}(w)$ drops off faster. The faster drop of the spanwise velocity component is hidden in $E_{\|}(z)$ because of the large contribution of the streamwise velocity component.

The boundary conditions clearly influence the the behavior near $z = L_z$. The streamwise velocity component is symmetric under reflection at the boundary whereas the spanwise component is antisymmetric and vanishes at the boundary. Taking this into account, we apply fits to the numerical data that respect these symmetries. The streamwise component is fitted to

$$u(z) = A(z^{-2} + (L_z - z)^{-2}) \tag{6.8}$$

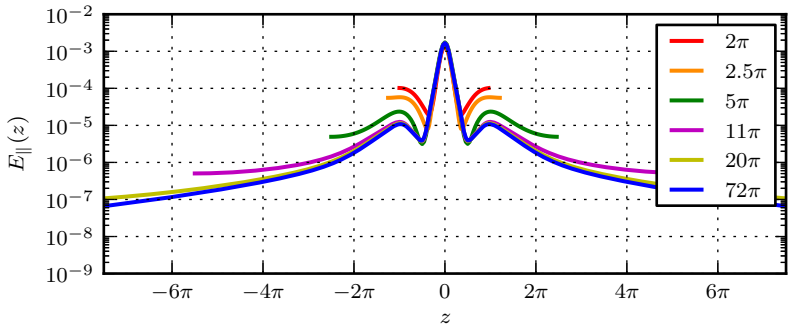

Figure 6.12: Spanwise profiles of the total energy density for PO_E at $Re_B = 2180$ for various spanwise widths L_z.

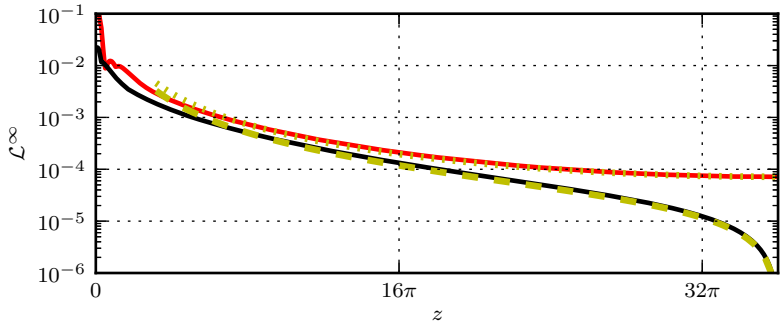

Figure 6.13: The $\mathcal{L}^\infty$-norms (maximum over y and x) of the streamwise u (solid red) and the spanwise w (solid black) velocity component are shown versus the spanwise coordinate z. The yellow lines show fits $A(z^{-2} + (L_z - z)^{-2})$ (solid) and $B(z^{-2} - (L_z - z)^{-2})$ (dashed).

while for the spanwise velocity component the fit function

$$w(z) = B(z^{-2} - (L_z - z)^{-2}) \tag{6.9}$$

is used. For both components we optimized the values of A and B using a least-squares method. The obtained fits are in amazing agreement with the numerical data as can be seen in figure 6.13. Therefore, the velocity field of the doubly-localized periodic orbits falls off like $1/z^2$ over the width of the domain. In the streamwise direction the decay is in concordance with an exponential decay. Since the structure is much longer than wide (see figure 6.14), the streamwise extend of the domain might by too small to reveal a possibly underlying algebraic decay.

The observed $1/z^2$ scaling in spanwise direction allows for an different view on the doubly-localized orbit. Analytically, it is possible to show that for the flow around a cylindrical obstacle, the velocities decay as $1/z^2$ in the direction perpendicular to the direction of the flow (Landau and Lifschitz, 1991). Therefore, in the far field the localized orbit can be interpreted as an obstacle for the laminar flow.

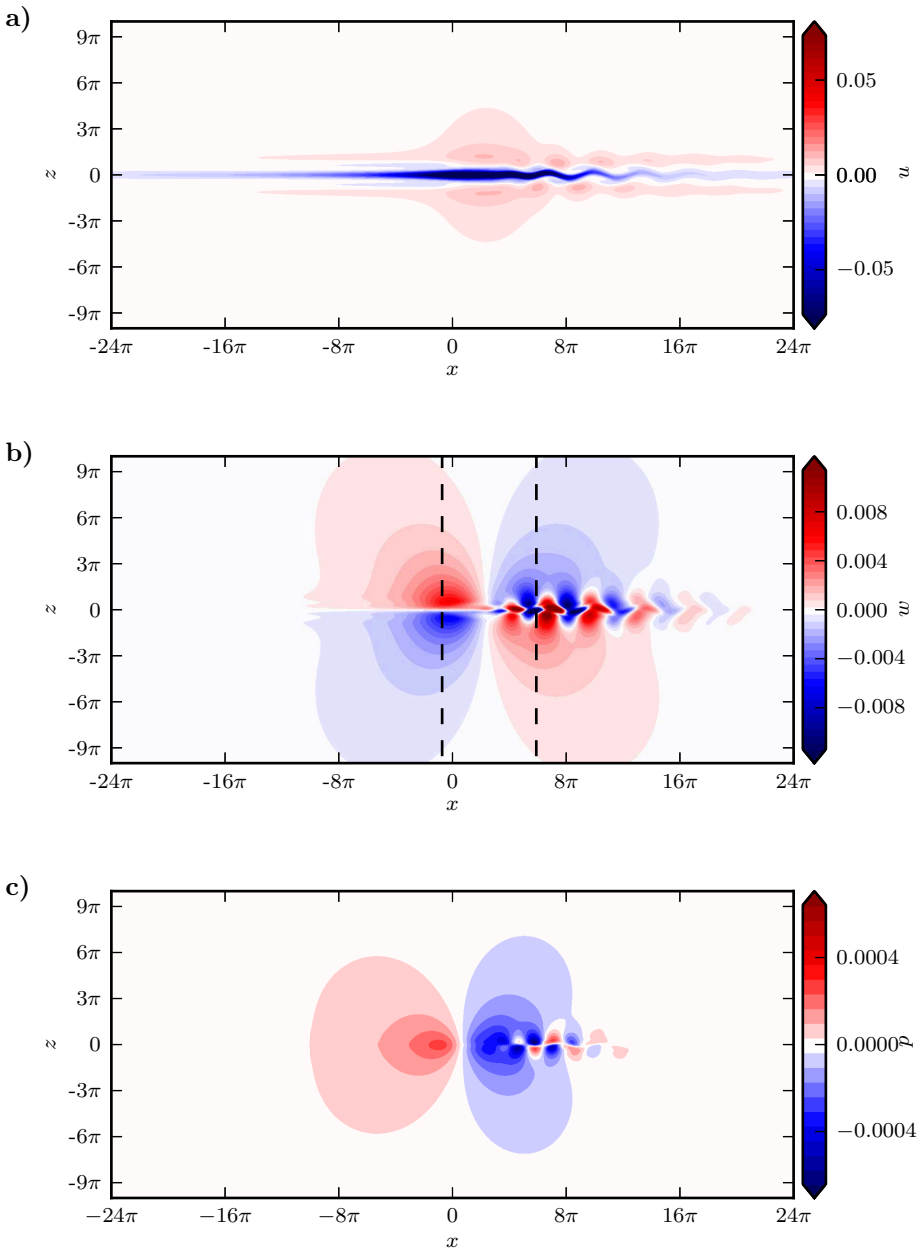

Figure 6.14: Panel a) and b) show the streamwise and spanwise velocity in the center-plane for the doubly-localized periodic orbit at $Re_B = 2180$, respectively. The dashed lines in b) mark the downstream positions of the maxima in the energy density. Panel c) shows the pressure fluctuations in the center-plane.

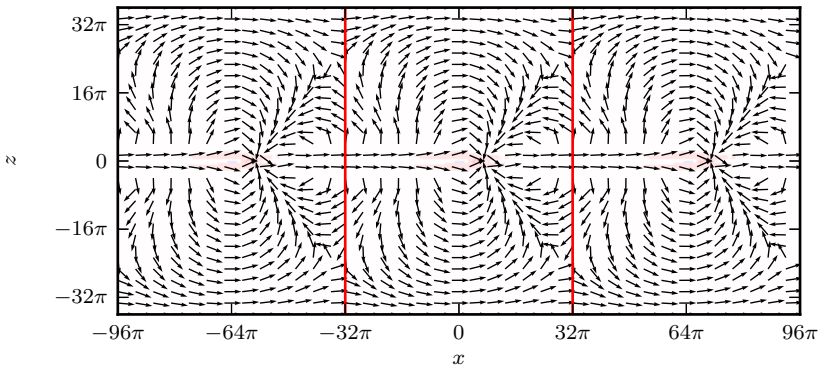

Figure 6.15: Vector plot of the y-averaged flow in the xz-plane. The arrows show $(\tilde{u}, \tilde{w})/\sqrt{\tilde{u}^2 + \tilde{w}^2}$, where $\tilde{u}$ and $\tilde{w}$ are the y-averaged streamwise and spanwise velocity, respectively.

Visualizations of the flow field and the large-scale flow

In figure 6.14 three visualizations of the periodic orbit are given. In figure 6.14a and b the streamwise and spanwise velocities in the center-plane are shown. The visualization of the spanwise velocity reveals a large-scale, quadrupolar-like flow field, where the centers of the left and the right pairs of lobes coincide with intensity maxima of $E_{\perp,c}(x)$. The quadrupolar shape of the spanwise velocity also exists in some distance to the mid-plane, but becomes less distinct close to the walls. Figure 6.14c shows the fluctuating pressure p in the center-plane. For this quantity the visualization reveals a dipolar-structure with the positive pole in the tail and the negative pole in the head of the structure. The positive pressure in the tail together with the negative pressure in the front lead to a locally increased pressure gradient at the position of the localized flow structure.

A plot of the direction of the y-averaged flow is shown in figure 6.15. For their equilibrium solution of plane Couette flow, Brand and Gibson (2014) found a perfect quadrupole flow field in direction of the y-averaged flow. The present solution is traveling in streamwise direction and does not have a symmetry with respect to x. This leads to a strong deformed quadrupole in the direction of the y-averaged flow. In particular, the inward and outward directions are not perpendicular. Large-scale quadrupole flows as they appear in the spanwise velocity component and the y-averaged flow have also been observed in turbulent spots in plane Couette (e.g. Schumacher and Eckhardt, 2001; Lagha and Manneville, 2007; Duguet and Schlatter, 2013; Gibson and Brand, 2014) and plane Poiseuille flow (Lemoult et al., 2013, 2014).

6.4 Doubly-localized chaotic edge states

At $Re_B = 2180$ a stability analysis in dependence on L_z of the localized state discussed in the last section is performed. It is found that the state has two unstable directions if the domain width is increased to values above 5.75π (for smaller values of L_z there is only one unstable eigenvalue). Thus, in a wide domain the doubly-localized state is not an attracting state in the laminar-turbulent boundary.

In the case of a supercritical bifurcation with increasing width, the bifurcating state should extend to larger values of L_z and at least for a small range in L_z it must have one unstable direction. Thus, within this range in L_z the state should be accessible by edge tracking. But an edge tracking starting at the slightly disturbed orbit PO_E in a computational domain with $L_z = 6\pi$ and $L_x = 64\pi$ with resolution $N_x \times N_y \times N_z = 1024 \times 65 \times 144$ does not converge towards an exact coherent structure. This is a strong evidence that the bifurcation of PO_E with increasing L_z is subcritical. A plot showing the edge trajectory approximated by the trajectories on the turbulent and the laminar side is shown in figure 6.16. The trajectory begins with a transient phase of about 1500 time units during which it departs slowly from PO_E. Afterwards, the trajectory shows aperiodic chaotic behavior. Although the trajectory leaves PO_E, the fluid structure stays localized. Visualizations of the flow field of the trajectory at $t = 2500$ and $t = 3500$ are shown in figure 6.17. They reveal that in addition to the localization the quadrupole-like structures of the spanwise velocity of PO_E is retained.

Further edge trackings in a large domain with $L_x = 32\pi$ and $L_z = 8\pi$ at $Re_B = 1400$ and $Re_B = 2000$ did also result in an aperiodic spanwise and streamwise localized structure.

The results of the simulations suggest that while in computational domains that are either short and wide or long and narrow the edge states is an exact coherent state, in large domains it is a localized chaotic state that is quite similar to a turbulent spot. This observation of a chaotic localized edge state in spatially extended domains is quite similar to the case of plane Couette flow (Schneider et al., 2008; Duguet et al., 2009) and pipe Poiseuille flow (Mellibovsky et al., 2009).

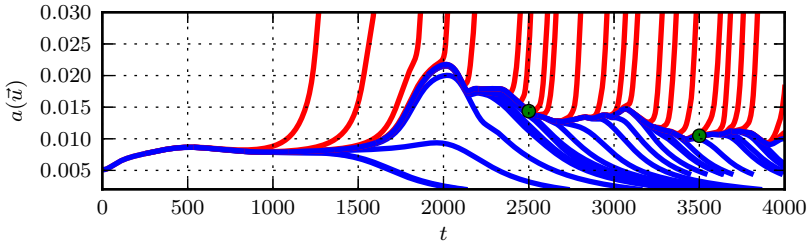

Figure 6.16: Edge tracking in a computational domain with $L_x = 64\pi$ and $L_z = 6\pi$ at $Re_B = 2180$. For each refinement step the energies of the final turbulent and laminar trajectories are shown. Initial condition is the slightly disturbed periodic orbit PO_E for this domain size. Visualizations of the flow fields for the times marked by the green dots are shown in figure 6.17.

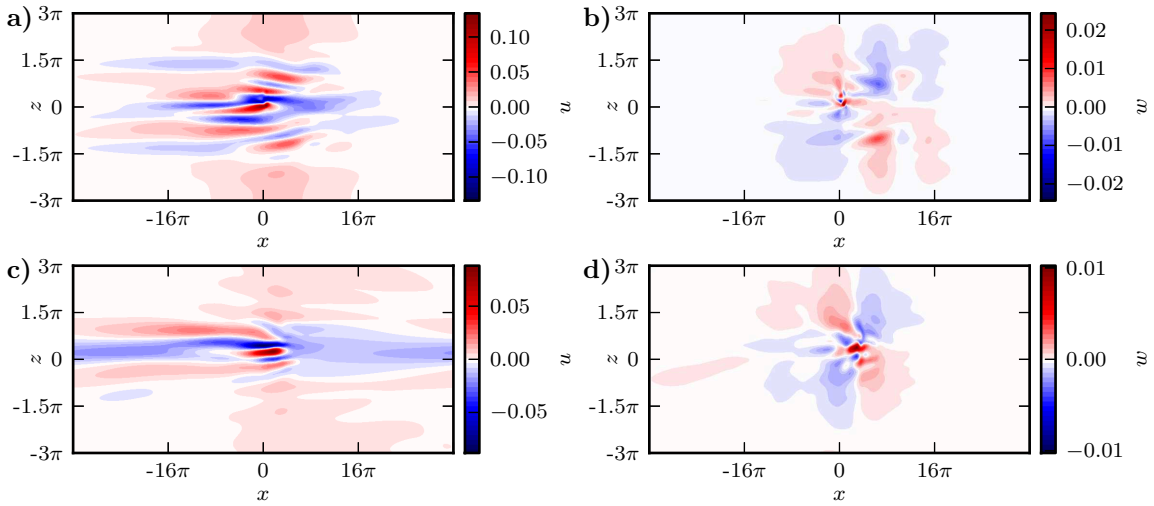

Figure 6.17: The panels a) and b) show the streamwise and spanwise velocity in a plane parallel to the plates in a distance of 0.29 for the flow field on the edge trajectory at $t = 2500$. Panel c) and d) show the same visualizations for $t = 3500$. The direction of the flow is from left to right.

6.5 Localized Tollmien-Schlichting waves

The streamwise localized solutions discussed in section 6.2 bifurcate from spatially extended exact coherent states within a long-wavelength instability. The Tollmien-Schlichting waves also show these kind of long-wavelength instability to modulated and localized states (Drissi et al., 1999). Localized TS-waves were first identified and studied by Jiménez (1990) and Price et al. (1993). They are relatively easy to identify in two-dimensional Poiseuille flow because for some parameter values they are stable and can be found by time integration. An example of a simulation of two-dimensional Poiseuille flow is shown in figure 6.18. The figure shows a spatio-temporal plot of the energy density $E_\perp(x)$ for a simulation at $Re_B = 2530$ with $L_x = 128\pi$ starting with a noisy initial condition. After some hundred time units a stationary pattern of four localized stable TS-waves forms. For fixed domain length the number of localized TS-waves in the final pattern depends on the initial condition. Other simulations for the same values of Re_B and L_x result in patterns that contain two or five localized TS-waves. Wang et al. (2015) calculated detailed statistics of the laminar gaps for these kind of simulation.

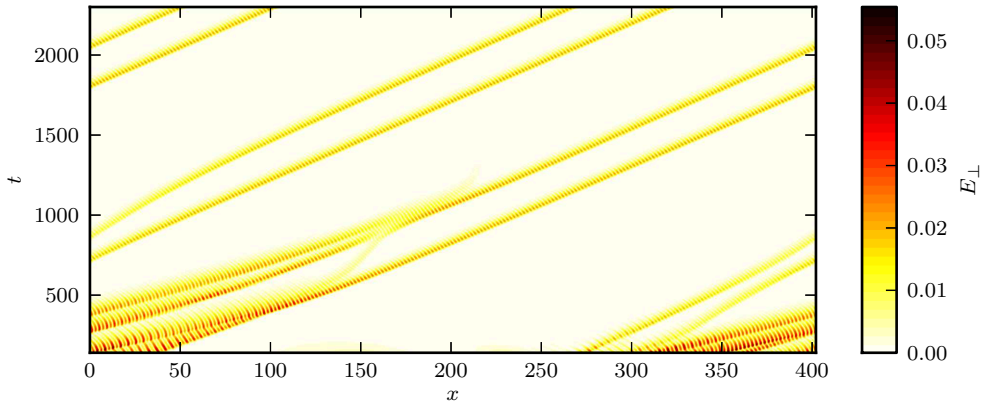

Figure 6.18: Spatio-temporal plot of the energy density $E_\perp(x)$ for a simulation of two-dimensional Poiseuille flow at $Re_B = 2530$. The simulation starts with random noise. After some time a stationary stable pattern of four localized TS-waves forms.

Price et al. (1993) were able to track the localized TS-wave to Reynolds numbers around 2330, which is much lower than the lowest Reynolds number where extended TS-waves exist.

In this section the long-wavelength instabilities of the spatially extended TS-waves are investigated. It will further be shown that in addition to the localized TS-waves that directly bifurcate from the spatially extended traveling wave, further localized TS-waves exist. In particular, for a fixed Reynolds number, localized TS-waves with different streamwise length can be found. Finally, examples of three-dimensional exact solutions that bifurcate from the localized TS-waves are presented.

Long-wavelength instabilities of TS-waves

We investigate the stability of the TS-wave TW_{TS} with a wavelength $\lambda_0 = 2\pi$ to two-dimensional disturbances with streamwise wavelengths that are multiples of this basic wavelength. The longest disturbance wavelength that is regarded is 32π. If the Reynolds number is decreased

from the point where the TS-wave bifurcates from the laminar profile, the first instabilities of the traveling wave are related to the longest wavelengths. At $Re_B \approx 5760$ the traveling wave undergoes a Hopf bifurcation that creates a relative periodic orbit with an streamwise wavelength of $\lambda = 32\pi$. At a lower Re_B of 5630 a Hopf bifurcation creating a orbit with wavelength 16π occurs. With further decreasing Reynolds number relative periodic orbits with decreasing streamwise wavelength are created in Hopf bifurcations. A bifurcation diagram that shows the spatially extended TS-waves and the bifurcating periodic orbit is given in figure 6.19. The solution branches of the obits with the longest λ extend down to the lowest values of Re_B. For $\lambda = 32\pi$ the turning point is at $Re_B = 2334$ that is quite close to the value found by Price et al. (1993).

If the modulated TS-waves are continued to lower Reynolds numbers, the modulation becomes stronger. To illustrated the increasing modulation, the energy densities of the streamwise velocity component of the relative periodic orbits with $\lambda = 4\pi$, 8π and 32π are shown in figure 6.20 for different Reynolds numbers. For the orbit with $L_x = 32\pi$ is is justified to say that it becomes localized with decreasing Re_B since minima and maxima of the energy density differ by more than two orders of magnitude. For the orbits with smaller wavelengths the modulation of the densities does also become stronger with decreasing Re_B, but especially for the relatively small wavelengths $\lambda = 4\pi$ (figure 6.20a and b) and 6π they do not become localized.

However, the relative periodic orbit with $\lambda = 32\pi$ shows a good streamwise localization if the Reynolds number is low. Two visualization of a flow field on the orbit at $Re_B = 4065$ are shown in figure 6.21. The orbit is easily transferable to larger domains to study the localization properties. In figure 6.22 a plot of the $\mathcal{L}^\infty$-norm of the streamwise velocity is shown for the localized TS-wave at $Re_B = 4065$ in a domain with $L_x = 112\pi$. The $\mathcal{L}^\infty$-norm decays exponentially in the head as well as in the tail of the structure, but the slopes are different. Just as for the streamwise localized three-dimensional orbit PO_E discussed in section 6.2, the decay in the head is steeper than in the tail. For a quantification an exponential decay, $A \exp(x/l_x)$, is fitted to the different decays in the head and the tail. The obtained values of l_x are characteristic length scales for the decay. At $Re_B = 4065$ the decay in the tail (1) is 10.8 for both velocity components. For the steep decay in the head (2) we find $l_x = -2.8$ and for the flat decays we obtain -48.2 and -46.4 for the wall-normal (4) and streamwise (3) velocity component, respectively. For the localized TS-wave, in contrast to the streamwise localized orbit PO_E, the decays for the streamwise and wall-normal velocity coincide almost perfectly. This is a consequence of the two-dimensional roll-structures forming the scaffold of the orbit which correlates the streamwise and wall-normal velocity.

A stability analysis with respect to two-dimensional disturbances of the localized relative periodic orbit in a domain with a streamwise length of 32π shows that the upper branch is stable to two-dimensional disturbances. Right after the turning point the lower branch has one unstable direction.

Packages of TS-waves

Apart from the localized TS-waves that bifurcated directly from the spatially extended traveling wave, it is possible to identify another kind of localized TS-waves. As a starting point the localized TS-wave at $Re_B = 4065$ was used. We double a roll-pair in the core region of this structure and thus we obtain a flow field with an additional pair of rolls. This flow field is used as an initial guess for a search for a relative periodic orbit. Indeed, using this approach it is possible to identify a streamwise localized periodic orbit with an additional roll-pair. By

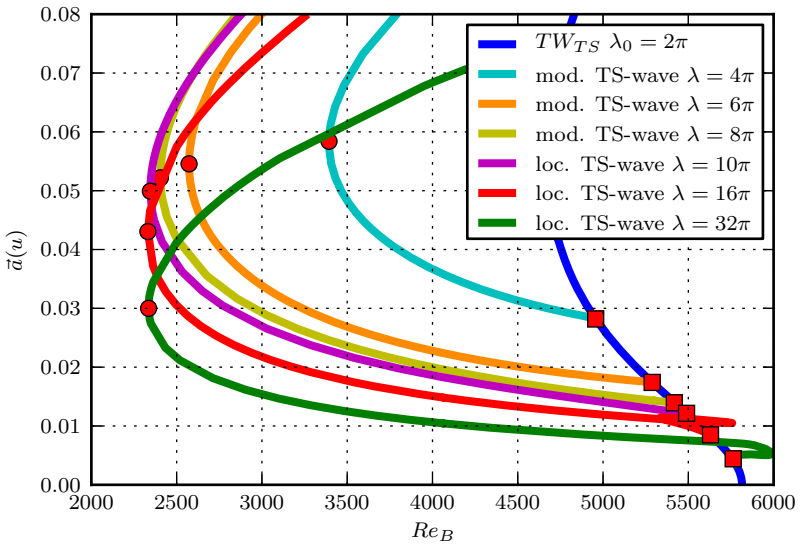

Figure 6.19: Bifurcation diagram showing modulated and localized TS-waves branching from the spatially extended TS-wave (blue). The turning points are marked by red circles and the points where the modulated states bifurcate from the spatially extended traveling wave are marked by red squares.

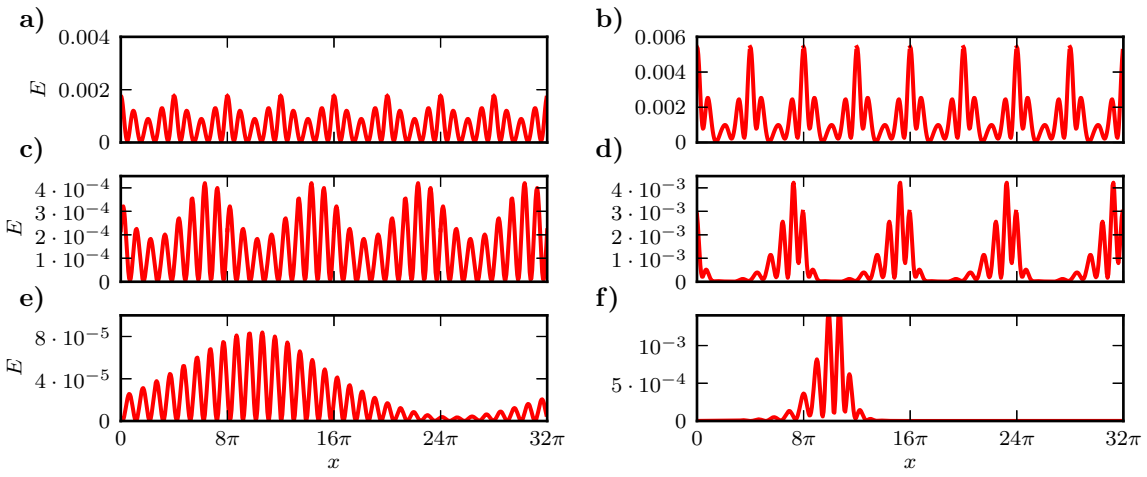

Figure 6.20: In a) and b) the energy densities $E_\perp(x)$ for the modulated TS-wave with wavelength $\lambda_x = 4\pi$ are shown for $Re_B = 3595$ and $Re_B = 4684$, respectively. For a modulated TS-wave with $\lambda_x = 8\pi$, the energy densities are shown for $Re_B = 2852$ and $Re_B = 5300$ in c) and d), respectively. For the modulated TS-wave with $\lambda_x = 32\pi$, which becomes localized at low Reynolds numbers, the densities are shown for $Re_B = 4065$ and $Re_B = 5802$ in e) and f), respectively.

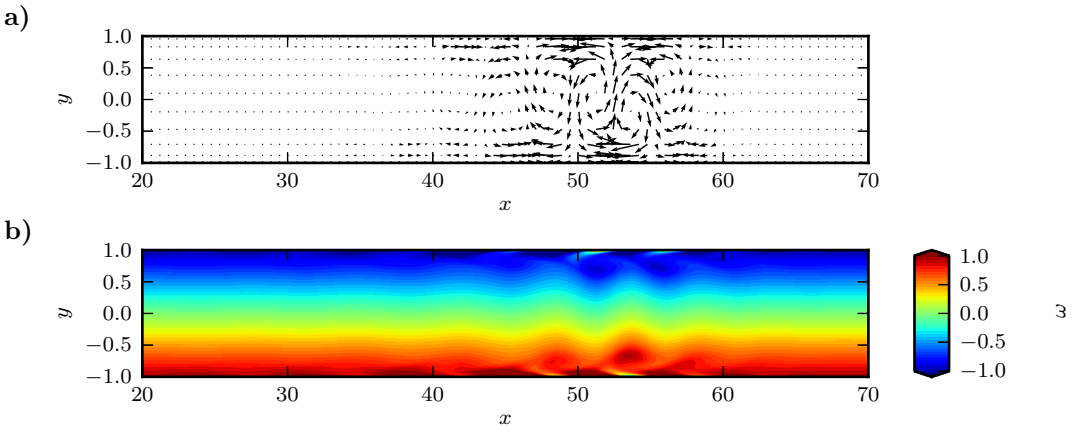

Figure 6.21: Visualizations of the localized TS-wave at $Re_B = 4065$. In a) the flow in the streamwise wall-normal plane is shown for the localized TS-wave at $Re_B = 4065$. For the same state, the streamwise vorticity $\omega_x = \partial_x w - \partial_y (U + u)$ of the full velocity field in the streamwise wall-normal plane is shown in b).

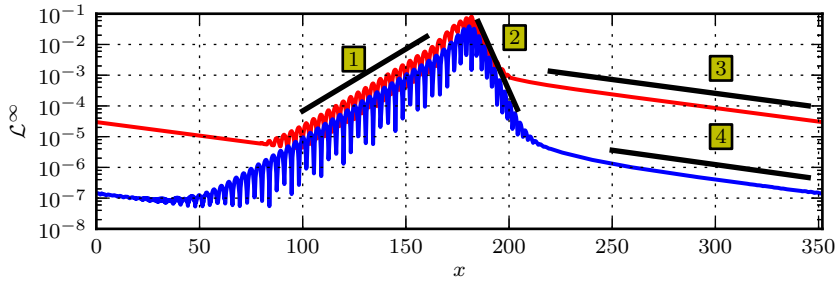

Figure 6.22: Course of the $\mathcal{L}^\infty$-norm of the streamwise (red) and the wall-normal (blue) velocity components for the lower branch of a localized TS-wave at $Re_B = 4065$. The black lines labeled $1 - 4$ show slopes obtained from exponential fits to numerical data. The corresponding decay constants l_x are 10.8, -2.8, -48.2 and -46.4.

repeating this procedure several times, periodic orbits with an arbitrary number of roll-pairs can be identified. In figure 6.23 the $\mathcal{L}^\infty$-norm of the streamwise and wall-normal velocity component is shown for orbits with one, two and three additional roll-pairs (all for $Re_B = 4065$). The figure reveals that the inner region of the orbit is not homogeneous but shows a modulation. Furthermore, as for the ordinary localized TS-wave, the decays of the velocity components in the head and the tail differ, but they do not depend on the length of the structure. If the states are tracked to lower values of Re_B the structures split and form 2, 3, and 4 localized TS-waves, respectively.

Three-dimensional streamwise localized solutions

As discussed in section 3.4 the two-dimensional, spatially extended TS-waves are highly unstable to three-dimensional disturbances. Their streamwise localized counter-parts share this property. With increasing distance to the bifurcation point the localized TS-wave develop many

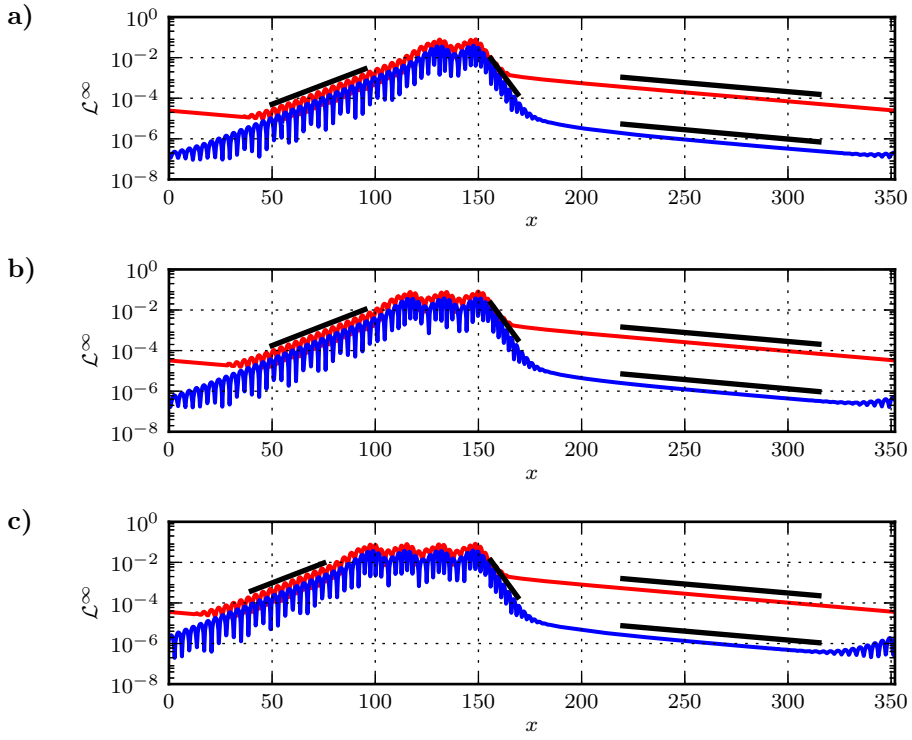

Figure 6.23: Course of the $\mathcal{L}^\infty$-norm of the streamwise (red) and the wall-normal (blue) velocity components for localized TS-waves of different length. For each wave the Reynolds number is 4065. The black lines show exponential fits to the decays.

instabilities. We identify the bifurcating states using the same procedure as in section 3.4. The bifurcating ECS are relative periodic orbits and can, analogous to the spatially extended solutions, be classified according to their symmetries. However, since the localized TS-wave is in contrast to the traveling wave TW_{TS} not periodic in streamwise direction, the symmetries of the classes of states are different.

In the bifurcation diagram in figure 6.24a the streamwise extended TS-waves with wavelength 2π and the localized orbit $PO_{TS,32\pi}$ bifurcating in an subharmonic instability with wavelength 32π (red) are shown. Additionally, the solution curves for two classes of bifurcating three-dimensional solutions are shown. The difference of the two solutions classes can be explained using the visualizations of the flow close to the wall shown in figure 6.24b and c. For both classes the wall-normal velocity is modulated in spanwise direction. But while for type A orbits the maxima of this modulation are at the same spanwise position for the upper and the lower plate, they are shifted by $0.5\lambda_z$ for type B orbits.

As figure 6.24 b and c show the spanwise modulation of the orbits becomes stronger with increasing Reynolds number. The streamwise localization of the state keeps quite strong even if the Reynolds number is increased to values above 7000.

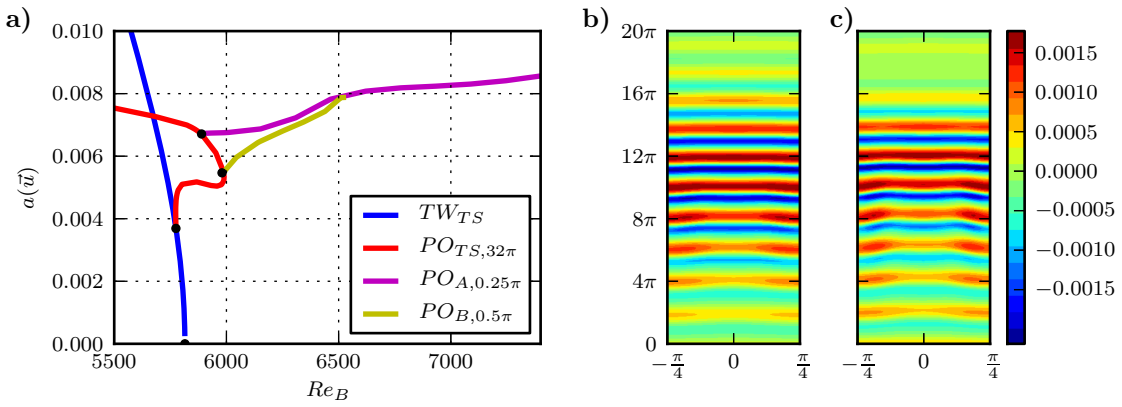

Figure 6.24: Bifurcation diagram showing spatially extended TS-waves ($\lambda_x = 2\pi$), localized TS-waves and three-dimensional streamwise localized periodic orbits bifurcating from the localized TS-waves. Panels b) and c) show visualizations of the wall-normal velocity component in a distance of 0.1 from the lower-wall orbit of class A with spanwise wavelength 0.5π ($PO_{A,0.5\pi}$) for $Re_B = 6140$ and $Re_B = 6520$. The direction of the flow is from bottom to top.

6.6 Extracting different velocity scales using the method of comoving frames

For the periodic orbits described in the sections 6.2 - 6.5 the inner structures (spanwise rolls for the TS-wave and modulation of the streaks for PO_E) move with a speed that is different from the speed of the envelope. If both velocities would coincide, the exact solution would have no time dependence and be a relative equilibrium. As also remarked by Chantry et al. (2014), there is nothing that forbids steamwise localized solutions to be relative equilibria. However, up to now all steamwise localized solutions in plane Poiseuille and pipe flow (Avila et al., 2013; Chantry et al., 2014) are relative periodic orbits. Therefore, there are obviously two important velocities in the flow structure. The method of *comoving frames* described by Kreilos et al. (2014b) provides a way to study the dynamics of flows in a frame of reference that moves with a (in general time-dependent) velocity extracted from the flow. In this section an adaption of the method of *comoving frames* will be presented that allows to choose one of the velocities of the orbit and thus to choose the comoving frame of the modulation envelope or of the inner structure.

The idea underlying the method of comoving frames is that any change of a velocity field has a component that points along the direction of pure advection while the remaining part is the actual change of the velocity field in the advected frame. Thus, the instantaneous streamwise advection velocity is defined by

$$c_x = \frac{\langle \partial_x \vec{u}(x,y,z,t) \cdot \partial_t \vec{u}(x,y,z,t) \rangle}{||\partial_x \vec{u}(x,y,z,t)||^2}. \tag{6.10}$$

The velocity of the comoving frame depends on the choice of the scalar product and associated norm. An obvious choice, also used by Kreilos et al. (2014b), is the usual Euclidean scalar product

$$\langle \vec{a}(x,y,z) \cdot \vec{b}(x,y,z) \rangle = \int (\vec{a}(x,y,z) \cdot \vec{b}(x,y,z)) dx\ dy\ dz. \tag{6.11}$$

Because this definition incorporates all scales of fluid motion, if more than one velocity scale is present the resulting advection velocity is a mixture of these velocities. To reduce this problem instead of using the full flowfield in equation 6.11, it is possible to use just one particular streamwise mode,

$$\vec{u}_{m_x}(x,y,z) = \sum_{m_y=0}^{M_y-1} \sum_{m_z=0}^{M_z-1} \tilde{u}_{m_x,m_y,m_z} T_{m_y}(y) e^{2\pi i (k_x/L_x + k_z/L_z)} + c.c., \tag{6.12}$$

of the velocity field. The result is not a scalar product on the vector space of all velocity fields anymore, since it is not positive definite. However, this definition is still usable in equation 6.10 to calculate an advection speed. The idea of using a single mode is to get the advection velocity of a flow structure with a certain wavelength. In any computational domain the envelope of localized structures has a large contribution from the streamwise mode number 1. Thus, using only the $m_x = 1$ to calculate the advection velocity should yield the speed of the envelope. If one is interested in the comoving frame of the inner structure of a localized state, a mode that has a large contribution to the structure should be used. Similar to the investigation here, Del Álamo and Jiménez (2009) calculated the phase velocity of individual modes in dependence on the wall-normal coordinate. But they did no wall-normal averages of c_x and they only regarded fully turbulent flows.

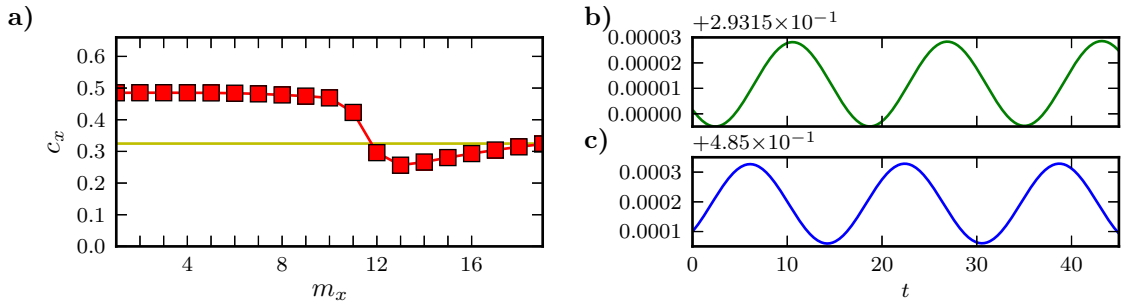

Figure 6.25: Advection velocities obtained by applying the method of comoving frames to the localized TS-wave at $Re_B = 4065$. In a) the average velocities are plotted vs. the mode number used to calculated the advection speed. The red line is to guide the eye only. As a reference the mean advection speed obtained by using the full Eulcidean scalar product is shown by a yellow line. In b) and c) the advection speed vs. times is shown for the case $m_x = 1$ and $m_x = 16$, respectively.

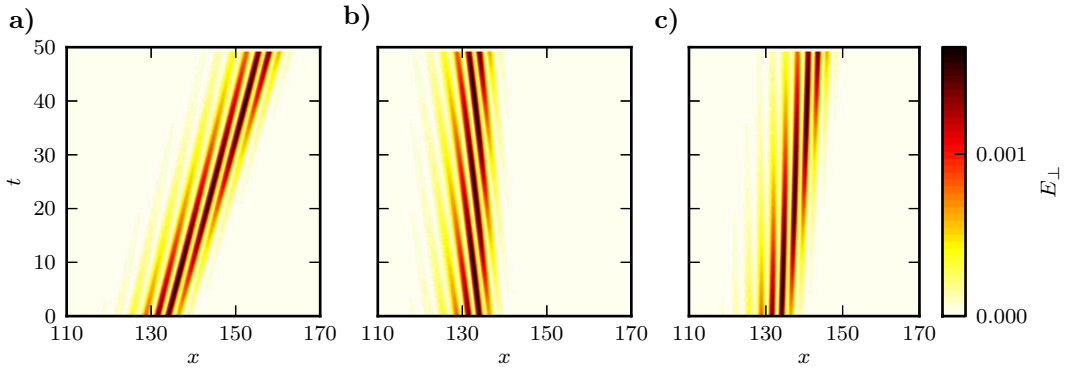

Figure 6.26: Spatio-temporal plot of the streamwise energy density of the localized TS-wave at $Re_B = 4065$. Panel a) shows the situation in the lab-frame. In b) and c) comoving frames obtained by using mode $m_x = 1$ and $m_x = 16$ are shown. In b) the envelope of the structure is stationary and the inner roll-structure is moving. In c) the rolls are stationary but the envelope keeps moving.

For the localized TS-waves discussed in section 6.5 the advection velocities calculated using only the contribution of one single mode are shown in figure 6.25 in dependence on the mode number. The figure reveals a drop of the advection speed at $m_x = 12$. This implies that the small-scale structures of the inner structure move with lower speed than the envelope.

To remove the motion of the envelope and the inner structure, appropriate choices are the modes 1 and 16, respectively. The mode 16 is the right choice to obtain the speed of the inner structure because in a computational domain with $L_x = 32\pi$ this mode number corresponds to a spatial wavelength of 2π which is almost the wavelength of the inner structure.

A zoom of the velocities obtained by using $m_x = 1$ and $m_x = 16$ is shown in figures 6.25b and c and reveals a small amplitude oscillation. However, the mean values of the advection velocities are quite different. The result for $m_x = 16$ is close to the advection speed obtained using the Euclidean scalar product calculation and yields an advection speed of about 0.325.

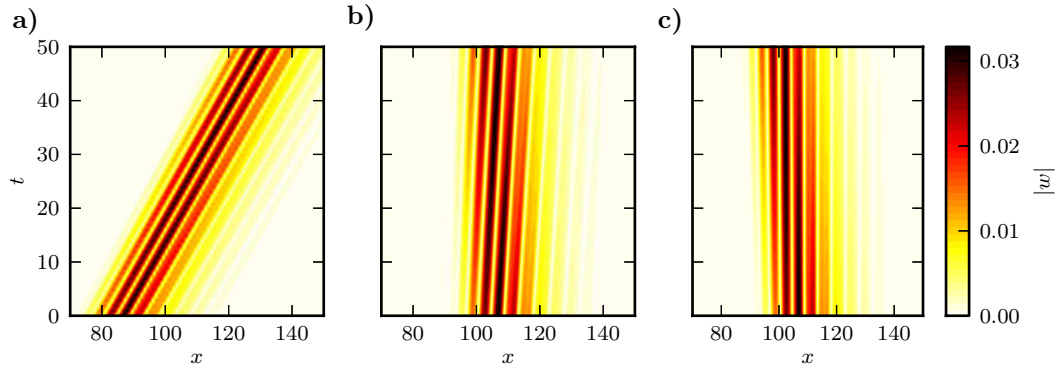

Figure 6.27: Spatio-temporal plot of the magnitude of the spanwise velocity $|w|$ for PO_E at $Re_B = 1410$. Panel a) shows the situation in the lab-frame. In b) and c) comoving frames obtained by using mode $m_x = 1$ and $m_x = 22$ are shown.

The advection speed for $m_x = 1$ is about 0.49 and therefore much larger. We want to check if the speeds obtained using the mode 1 and 16 do really yield a frame of reference that is comoving with the envelope and the inner structure, respectively. Therefore, spatio-temporal plots of the energy density $E_\perp(x)$ (see equation 6.4) are regarded. Figure 6.26a shows the situation in the lab frame. In this frame of reference the orbit is obviously travelling in streamwise direction. In figure 6.26b the frame of reference is moving with an advection velocity obtained by the streamwise mode $m_x = 1$. In this comoving frame the localized structure is obviously not advected. The inner structure is dynamically active and travelling through the envelope. The frame of reference in figure 6.26c is comoving with the advection velocity obtained by using mode $m_x = 16$. In this frame of reference the localized structure is still moving in streamwise direction albeit slower the in the lab-frame. However, the inner structure is almost stationary.

For the streamwise localized edge state PO_E discussed in section 6.2 it is also possible to find comoving frames for the envelope and the inner structure. In figure 6.27 spatio-temporal plots of the absolute value of the spanwise velocity are shown for the lab-frame and frames moving with the speed of the envelope and the inner structure, respectively. For this orbit we use mode number 22 to calculate the speed of the inner structure. This mode number corresponds to a wavelength of about 9.1 what is close to the wavelength of the inner structure (compare figure 6.5 in section 6.2). The figure reveals that also for PO_E the method captures the two different velocities of the orbit quite well.

In this subsection it was shown how the method of comoving frames can be adapted to obtain comoving frames that correspond to structures of different spatial extension. For localized exact coherent structures the method does well separate the dynamics of the inner structure and of the envelope. The method can easily be enhanced. For example, for a structure having more than one length scale in the inner structure more modes can be used to give a more accurate value for the advection speed. Possibly, the described approach can also be used to analyze localized spreading turbulence and the interaction between small and large scales within this process.

6.7 Streamwise localized turbulence

In this section streamwise localized turbulence in PPF is investigated. To trigger a localized turbulent structure the streamwise localized periodic orbit PO_E in a computational domain with $L_x = 64\pi$, $L_z = 2\pi$ and a resolution $N_x \times N_y \times N_z = 768 \times 65 \times 80$ is used. The width of the domain is chosen to be 2π to ensure that the turbulence is space filling in spanwise direction.

When the initial condition is integrated forward in time, a localized turbulent structure develops. Depending on the Reynolds number three different kinds of streamwise localized turbulence can be found. At Reynolds numbers around 1250 a localized turbulent structure develops that is short and does not grow in length. The energy densities, shown in figure 6.28a, have a maximum in the tail of the structure. Furthermore, the decrease rather steep in the tail and flat in the head of the structure. According to these properties, the localized turbulent structures are comparable to puffs in pipe flow (Wygnanski et al., 1975).

For higher Reynolds numbers it is only possible to find localized turbulent structures that increase in length and none that keep their size. For this manifestation of localized turbulence, the energy density does also show a maximum close to the tail together with an steep decrease in the tail and a slow decrease in the head. A snapshot of the energy densities for these kind of structure at $Re_B = 1410$ is shown in figure 6.28b.

At even higher values of Re_B, e.g at $Re_B = 1890$, the turbulent region grows faster in length and the energy densities now also have a maximum in the head of the structure. In figure 6.28c the instantaneous energy densities for these kind of structure at $Re_B = 1890$ are shown.

The two growing structures are comparable to the turbulent slugs in pipe flow. The observation of two different kinds of slugs is in concordance with the case of pipe flow where this has also been reported (e.g. Duguet et al., 2010b). Henceforth, the nomenclature used by Song (2014) is taken over and the two slug like structures are called *slug I* and *slug II*. For the three manifestations of localized turbulence in figure 6.29, spatio-temporal plots of the streamwise energy densities of the velocity components,

$$E_{\perp,u}(x) = \frac{1}{4L_z} \int_0^{L_z} \int_{-1}^{1} u^2 \, dydz, \tag{6.13}$$

(here given for the streamwise component) are shown in a frame co-moving with the mean velocity U_B of the flow.

The puff (figure 6.29a) moves slightly slower than the mean flow. The tail of the puff shows a steep increase of $E_\perp(x)$ for all times. In contrast, in the head the decrease of the energy densities is rather flat for all times. The speed of the tail shows only weak fluctuations compared to the head.

For the slug I at $Re_B = 1410$ (figure 6.29b) in the tail the decay of $E_{\perp,u}(x)$ is similar to the decay of the puff. The leading edge is less well defined than the trailing edge due to the flatter decay of $E_{\perp,u}(x)$. The mean speeds of the leading and trailing edge are different. For the slug shown in the figure the speed of the leading edge is almost the mean fluid velocity which is not a generic feature of a slug I. For other values of Re_B, it is possible to find slugs of type I whose leading edge moves with a mean speed different from the bulk velocity.

For the slug II at $Re_B = 1810$ (figure 6.29c) the speeds of both edges show a strong deviation from the mean fluid velocity and therefore in the moving frame the structures spread in both the up- and the downstream direction. Furthermore, for this type of slugs the fluctuations of the leading edge velocity are smaller than for the type I slug.

In some rare cases a phenomenon comparable to the splitting of puffs in pipe flow can be observed. As in pipe flow (Nishi et al., 2008) the splitting appears in the front of the structure. A spatio-temporal visualization of a splitting event at $Re_B = 1270$ is shown in figure 6.30. The figure reveals that a small amount of cross-flow motion originating from the front edge triggers a new puff in some distance to the original one. The new generated puff has the same speed as the old one.

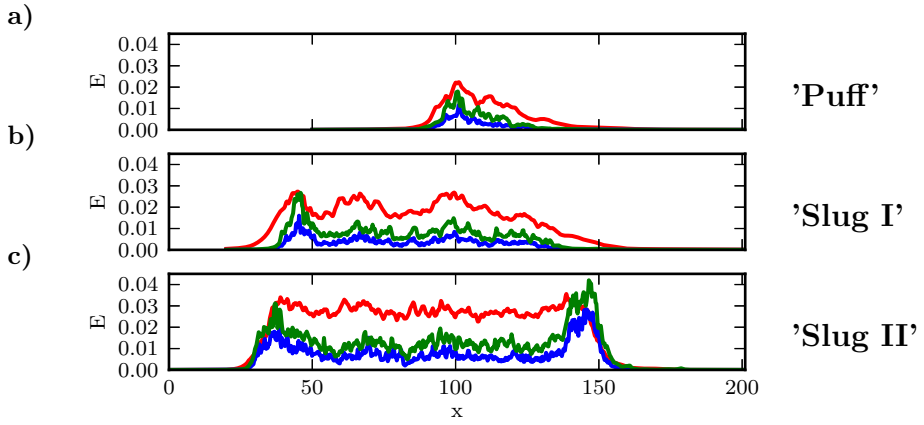

Figure 6.28: Energy densities $E_{\perp,u}$ (red), $E_{\perp,v}$ (blue) and $E_{\perp,w}$ (green) of localized turbulent structures. The densities of the spanwise and wall-normal velocity component are multiplied by a factor of ten. In dependence on the Reynolds number three different kinds of localized turbulence can be found. The Reynolds number for a) is 1250, for b) it is 1410, and for c) it is 1890. The structure in a) is puff-like. The structures in b) and c) are comparable to "slugs" and differ in the form of the leading edge.

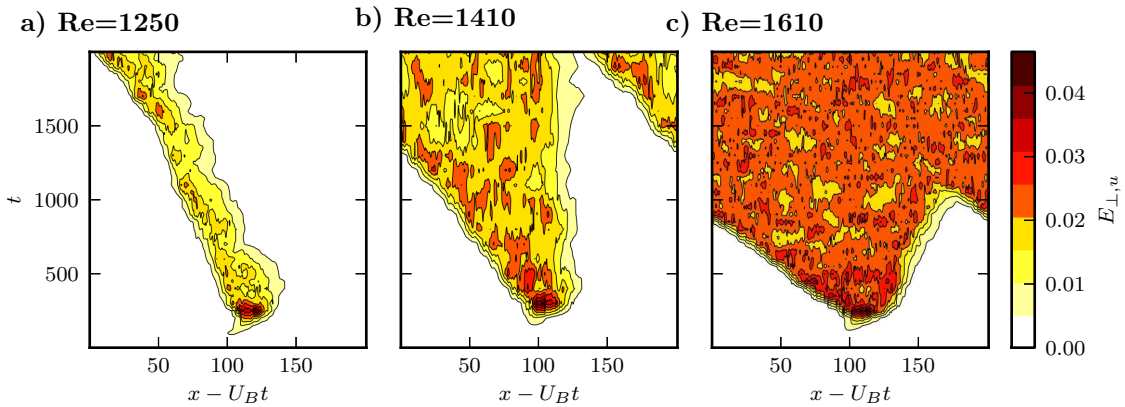

Figure 6.29: Spatio-temporal plot of the streamwise energy density for localized spreading turbulence for different values of Re_B.

Inspection of the flow structure of spreading turbulence reveals that at the interface between laminar and turbulent motion pronounced hairpin vortices are present. In figure 6.31 this

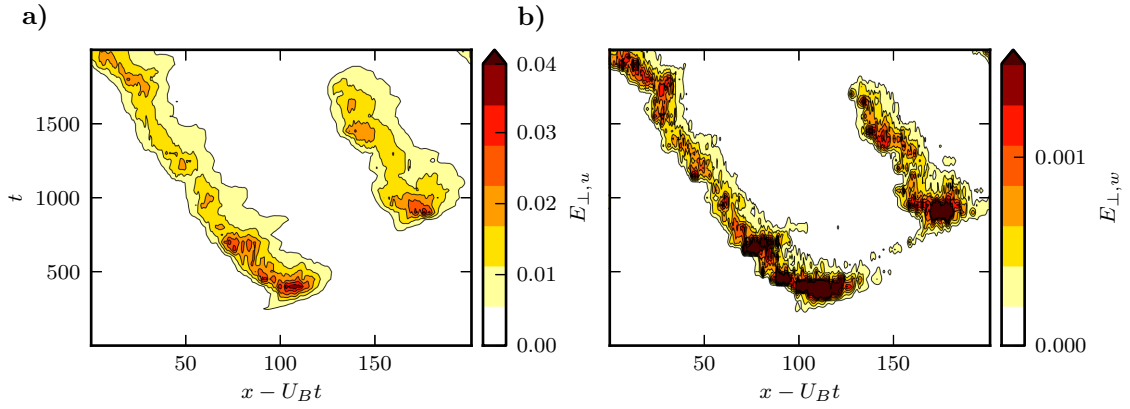

Figure 6.30: Spatio-temporal plot of the energy densities showing the splitting of a puff at $Re_B = 1270$.

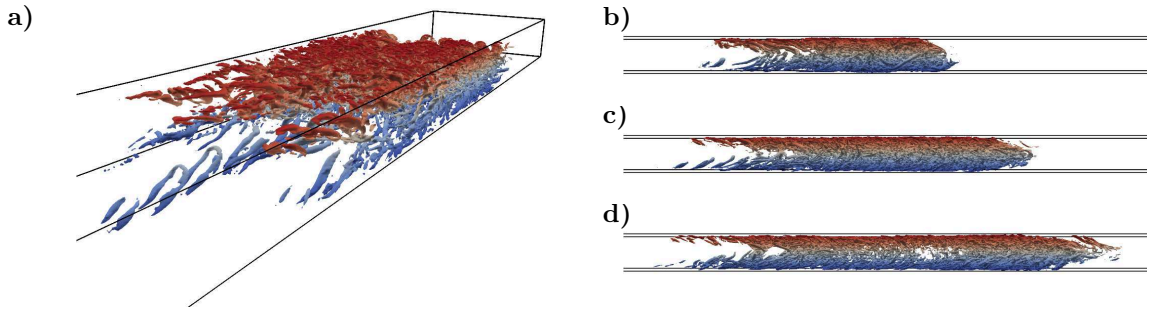

Figure 6.31: In panel a) a localized turbulent patch at $Re_B = 2519$ is visualized by iso-surfaces of the Q-vortex criterion. The value of Q used for the iso-surfaces is 0.9. The surfaces are color coded according to their wall-normal position form -1 (blue) to $+1$ (red). Panels b) - d) show side-views of a spreading turbulent slug in distances of 100 advective time units. The plots show iso-surfaces of the Q-criterion ($Q = 0.9$) which are color coded according to their wall-normal position.

phenomenon is illustrated for a spreading turbulent slug in a domain with $L_z = 2\pi$ at $Re_B = 2519$. In the left panel the visualizations of iso-contours of the Q-vortex criterion reveal a line of hairpin vortices at the trailing edge of the slug. The side views of the slug for different times shown in figure 6.31b-d demonstrate that the appearance of the hairpins at the tail is not a once-only but a recurring phenomenon. Evidences for this kind of continuous generation of hairpin vortices have also been observed in experiments on localized pipe flow turbulence (van Doorne and Westerweel, 2009).

A critical Reynolds number for spreading turbulence

With the goal to determine the Reynolds number where streamwise localized turbulence starts to spread, which marks the transition from puffs to slug I, the dependence of the front speeds is investigated quantitatively. For Reynolds number between 1200 and 2200, localized turbulence is triggered by the disturbed periodic orbit PO_E. Using a threshold E_{tr} in $E_\perp(x)$ of 0.006

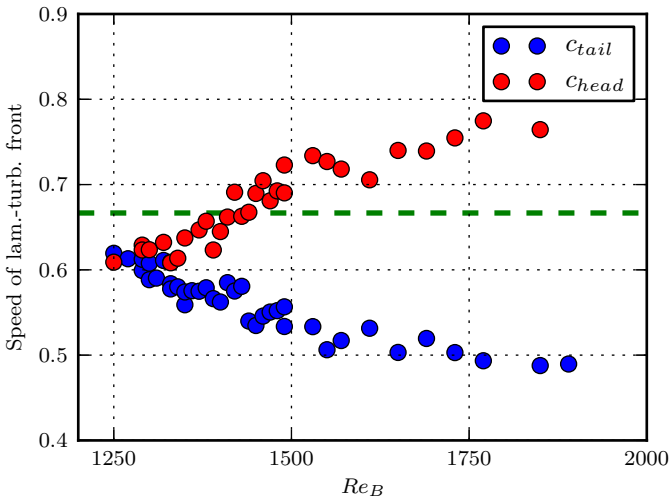

Figure 6.32: Speeds of laminar turbulent front vs. Reynolds number. The red and blue circles show the speed in the front and the tail of a localized structure, respectively. The dashed green line shows the value of the bulk velocity for comparison.

the positions of the leading and trailing edge are determined. By fitting these positions to a function linear in time the average speeds of both fronts are obtained.

If at some point the head and the tail of the structure connect due to the periodic boundary conditions, only fronts up to a distance of 200 time units to the connection are used for the fit. Furthermore, the first 100 time units after the transition (time where E_{tr} is exceeded for the first time) are ignored for the fit.

For each performed simulation the speeds of the front and the tail are plotted in figure 6.32. The exact value of the transition from puffs to slugs is difficult to determine. With the obtained data it is possible to limit the Reynolds number for this transition to an interval in Re_B between 1250 and 1350.

In an extensive study Song (2014) was able to determine the front speeds for pipe flow to high accuracy. Using the pipe flow model developed by Barkley (2011) they were able to model the occurrence of the two kinds of slugs and the transition from puff to slug motion.

Are there differences depending on the route to turbulence?

A question that arises is, if the properties of localized turbulent structures are the same regardless if the initial seed triggered a TS-like transition or a bypass transition. To answer this question, a localized turbulent state that developed out of the streamwise localized periodic orbit PO_E is compared to one developed out of a streamwise localized TS-wave. For both cases the spanwise energy density is shown in a spatio-temporal plot in figure 6.33. At this Reynolds number both transition scenarios result in a type II slug with a leading edge characterized by a high maximum of the spanwise energy density and a trailing edge with another but less high maximum of the spanwise energy density. Furthermore, for both cases above $t = 500$ a minimum of E exists in short distance to the leading edge. The energy densities of the remaining

two velocity components do not reveal any differences between the localized structures.

Although the exact process of the transition is different, the simulations suggest that the localized turbulent structures obtained by TS and bypass transition are the same.

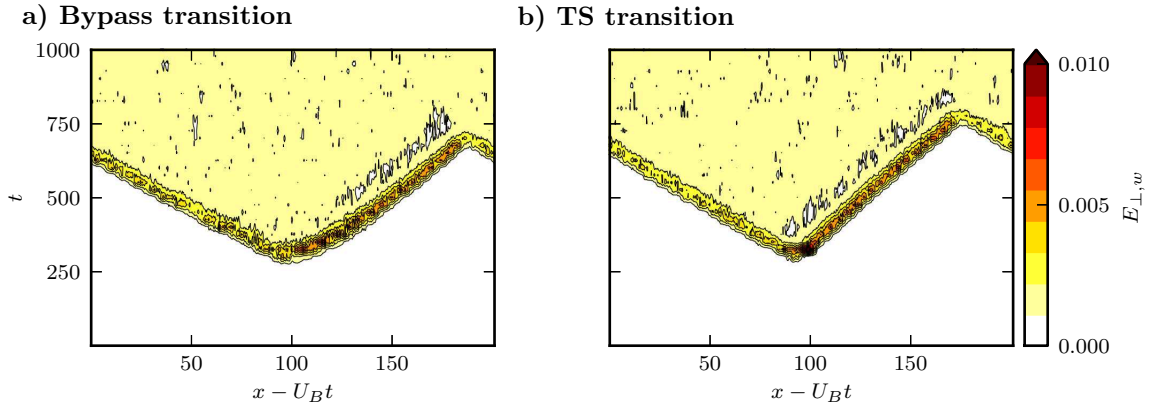

Figure 6.33: Spatio-temporal plot of the energy density of localized spreading turbulence initiated by a localized TS-waves (a) and the localized edge state PO_E (b). In both cases the Reynolds number is 2520.

Chapter 7

Tails of localized structures

7.1 Introduction

In the last chapter various localized structures were discussed. The findings on the decay in the streamwise and spanwise tails of the states were ambiguous. For states with pure streamwise localization (see section 6.2 for PO_E and 6.5 for the localized TS-waves) the results clearly indicate that the decays in the front and the tail are exponential over a large distance. Similarly, for ECS with pure spanwise localization (see section 3.2 for TW_E and 3.3 for the bursting periodic orbits) an exponential decay in the tails could be identified. However, the study of the doubly-localized solution in section 6.3 revealed that the decay in spanwise direction is better described by a power law. A detailed form of the tails of localized flow structures is crucial for the understanding of spatio-temporal intermittent flows since algebraic tails can allow flow structures to interact over larger distances than exponentially decaying tails.

There exist ideas to describe the spatially and temporally intermittent turbulence by a stochastic process named *directed percolation* (e.g. Pomeau, 1986; Moxey and Barkley, 2010; Allhoff and Eckhardt, 2012; Shi et al., 2015). in this context, a detailed knowledge of the tails could be important because a necessary condition for directed percolation to occur is the sole presence of short range interactions (Hinrichsen, 2000).

It is shown that in the tails of localized structures both kinds of decays can be found. Exponential decay can be observed for short distances, while a power law becomes visible for large distances.

In their recent paper Brand and Gibson (2014) reported a doubly-localized equilibrium solution for PCF that appears to be exponentially localized in the spanwise and streamwise direction. They proposed a model equation for the tails which allows to predict the decay rate and the profiles in the tails. An adaptation of this model for PPF is discussed in section 7.2. This model describes the tails of streak dominated localized states in PPF and shows that, at least for some range, the tails of streamwise localized states are well described by an exponential decay.

Using simulations of a turbulent spot in PPF, the localization of doubly-localized turbulent states in large domains is explored. The simulations show that in the far tails of localized states

the decay follows a power law.

7.2 The Brand & Gibson-model for plane Poiseuille flow

For plane Couette flow Brand and Gibson (2014) proposed an equation that models the streamwise velocity component u in the streamwise tails of their doubly-localized equilibrium solution. They analyzed the terms of the Navier-Stokes equation and found that only a few contribute in the tails of their localized equilibrium. For plane Couette flow these dominant terms are:

$$y\partial_x u = Re^{-1}(\partial_{yy}u + \partial_{zz}u). \tag{7.1}$$

For the case plane Poiseuille flow the term on the left side must be changed to $(1-y^2)\partial_x u$ due to the different base flow. Additionally, a term $\partial_t u$ has to be added on the left side because in contrast to PCF streamwise localized states in PPF are always advected. Thus, for PPF the equation modifies to:

$$\partial_t u + (1-y^2)\partial_x u = Re^{-1}(\partial_{yy}u + \partial_{zz}u). \tag{7.2}$$

As ansatz for the flow field we use

$$u(x,y,z,t) = u(y)\exp\left[i\gamma z - \mu(x-ct)/Re\right]. \tag{7.3}$$

This ansatz is periodic in spanwise direction with wavenumber γ, moves in streamwise direction with the constant wavespeed c, and decays exponentially in streamwise direction with a decay constant μ/Re. Substituting the ansatz in equation 7.2 we obtain:

$$u'' - (\gamma^2 - \mu(1-y^2-c))u = 0. \tag{7.4}$$

A general solution of this ODE that can be found using *Mathematica* is

$$u(y) = a \cdot D_{\frac{-\gamma^2-c\mu+\mu-\sqrt{\mu}}{2\sqrt{\mu}}}(\sqrt{2}\sqrt[4]{\mu}y) + b \cdot D_{\frac{-\gamma^2+(c-1)\mu-\sqrt{\mu}}{2\sqrt{\mu}}}(i\sqrt{2}\sqrt[4]{\mu}y), \tag{7.5}$$

where $D_n(z)$ are parabolic cylinder functions. The boundary conditions $u(\pm 1) = 0$ determine μ and the relative values of a and b as a function of γ and c. To find non-trivial solutions for this equation, we need to find roots of the function

$$\begin{aligned} f(\mu) = -D_{\frac{-\gamma^2-c\mu+\mu-\sqrt{\mu}}{2\sqrt{\mu}}}(\sqrt{2}\sqrt[4]{\mu}) \cdot D_{\frac{-\gamma^2+(c-1)\mu-\sqrt{\mu}}{2\sqrt{\mu}}}(-i\sqrt{2}\sqrt[4]{\mu}) \\ + D_{\frac{-\gamma^2-c\mu+\mu-\sqrt{\mu}}{2\sqrt{\mu}}}(-\sqrt{2}\sqrt[4]{\mu}) \cdot D_{\frac{-\gamma^2+(c-1)\mu-\sqrt{\mu}}{2\sqrt{\mu}}}(i\sqrt{2}\sqrt[4]{\mu}). \end{aligned} \tag{7.6}$$

Application to PO_E

As a first example we investigate the periodic orbit PO_E in a domains with a streamwise length of 116π and a spanwise width of 2π ($\gamma = 1.0$). At $Re_B = 1100$ the wavespeed of the structure is $c = 0.8499$. The function $f(\mu)$ for this value of c and $\gamma = 1$ is shown in figure 7.1. The profile for the root at $\mu = -54.93$ is asymmetric and therefore it does not fit to PO_E. The profile for $\mu = -49.00$ is a good approximation to the tail of PO_E and the profile for $\mu = 57.20$ fits to the head of the orbit. Plots of the profiles obtained by the theory for different γ and from the DNS data (at the $z-$position of the low-speed streak) are shown in figure 7.2a and b for the

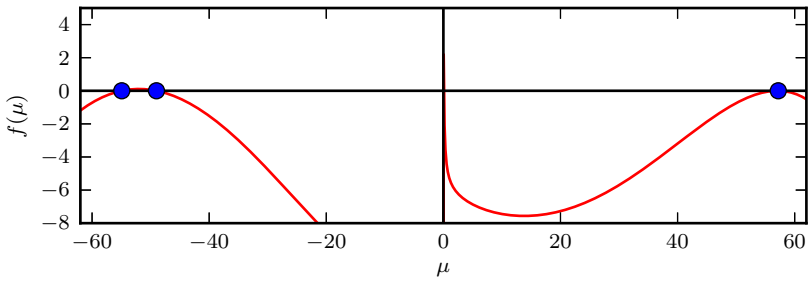

Figure 7.1: $f(\mu)$ vs. μ for $\gamma = 1.0$ and $c = 0.8499$

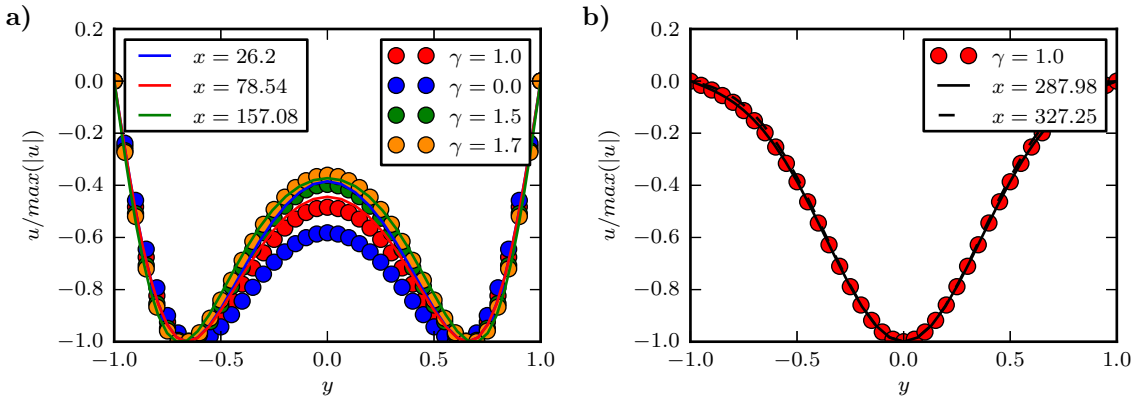

Figure 7.2: Normalized profiles in the tail of the orbit for various values of γ. The lines are the data for PO_E at $Re_B = 1100$ obtained by DNS for different streamwise positions. The profiles for $\gamma = 1.0$ and $\gamma = 1.5$ are good approximations of the DNS data.

tail and the front of the structure, respectively. The best agreement between the theoretical and the DNS profiles is obtained for wavenumbers between 1.5 and 1.7 which is a consequence of the fact that the low-speed streak has a width that is smaller than π.

In figure 7.3 the $\mathcal{L}_y^\infty$-norm of the streamwise velocity u (maximum of over y of $|u|$) is shown versus the streamwise coordinate x at the spanwise position of the low-speed streak. The red lines in the plots are the exponential decay with the decay constants obtained by the model. Exponential fits ($\exp \mu x/Re$) to $\mathcal{L}_y^\infty(u)$ yield $\mu = -53.93$ in the tail and $\mu = 58.03$ in the head of the structure. Thus, the real course of the decay and the predicted decay out of the model agree quite well, which shows that the adapted Brand&Gibson-model is able to describe the streak decay in the tails of localized structures in PPF.

Application to localized TS-waves

As a second example the implications for the case of a streamwise localized TS-wave (see section 6.5) are discussed. The wavespeed of a localized TS-wave at $Re_B = 3000$ is 0.54788. The slow decay in the head is well approximated by an exponential decay with $\mu/Re = -0.0355$ what yields $\mu_{DNS} = -106.50$. In the tail of the structure $\mathcal{L}_y^\infty(u)$ is modulated due to the underlying

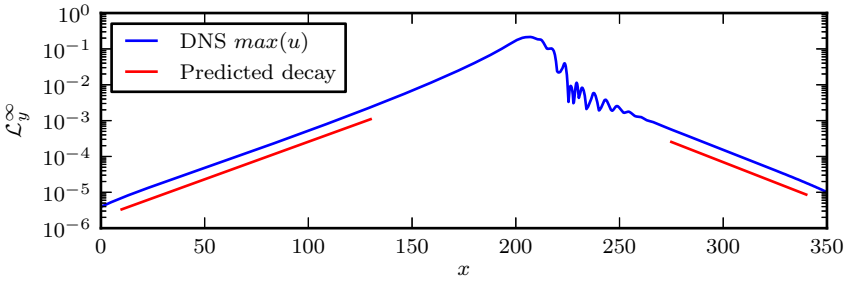

Figure 7.3: Maximum of the streamwise velocity component u at the spanwise position of the strong low-speed streak versus streamwise position x for the orbit PO_E at $Re_B = 1100$. The red solid lines show the exponential decay predicted by the theory.

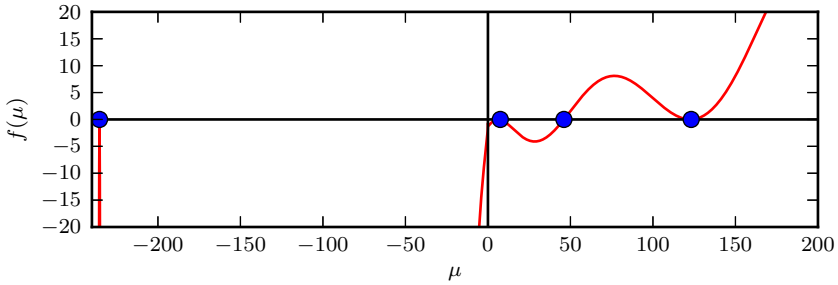

Figure 7.4: $f(\mu)$ vs. μ for $\gamma = 0.0$ and $c = 0.54788$

roll structures. A good exponential fit to $\mathcal{L}_y^\infty$ in the tail is obtained for $\mu/Re = 0.124$ yielding $\mu_{DNS} = 372.40$. The function $f(\mu)$ for $c = 0.54788$ and $\gamma = 0$ is shown in figure 7.4. The negative root that is closest to μ_{DNS} is $\mu = 235.40$. But even this value deviates strongly from the actual decay. For the front of the orbit the root at $\mu = 123.18$ is close to the real decay. The profile corresponding to this root is compared to the actual profile in figure 7.5. They match only qualitatively and deviate strongly in the positions of the minima.

The example of the localized TS-wave demonstrates that the model only describes the tails of localized states that are dominated by streaks. Because in the TS-wave no streaks are present the model has to fail. More precisely, for the localized TS-waves the terms $u\partial_x u$ and $v\partial_y u$, that contribute to the streamwise velocity, are of comparable strength. Thus, the neglect of $v\partial_y u$ is not justified which causes strong deviations between the DNS data and the model.

Dependence of the decay rate on the wavespeed

The examples of the localized TS-wave that has a quite low wavespeed of 0.54 showed that the root of $f(\mu)$ at negative values of μ moves to lower values with decreasing c. This raises the question on the dependence of the decay rate on the streamwise wavespeed of a state. For a fixed spanwise wavenumber $\gamma = 1.0$ the dependence of the relevant roots of $f(\mu)$ on c is studied. The roots corresponding to the slowest decays in the tail and at the front are shown in dependence on the wavespeed c in figure 7.6.

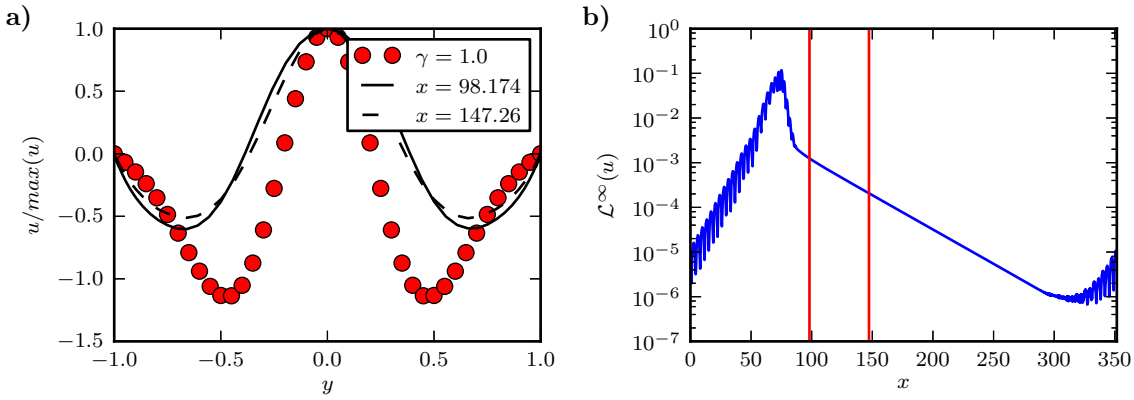

Figure 7.5: In a) normalized profiles of the streamwise velocity for two different positions in the head of the localized TS-wave are shown using solid and dashed black lines. The profile resulting from the model for $\gamma = 0$ is shown using red circles. In panel b) for the localized TS-wave at $Re_B = 3000$ the maximum of the streamwise velocity is shown dependent on the streamwise coordinated x. The positions of the profiles shown in a) are indicated by solid red lines.

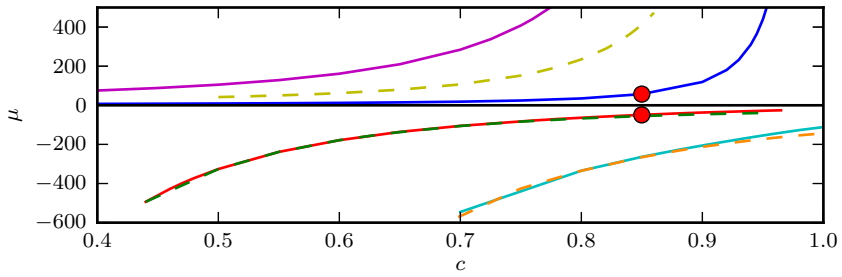

Figure 7.6: Positions of the roots of $f(\mu)$ in dependence on the wavespeed c. Solid and dashed lines are used when the corresponding profiles are symmetric and asymmetric, respectively. The roots which yield the best fits to TW_E at $Re = 1100$ are marked using red circles.

For low values of c the model predicts that streak dominated structures should show a steep exponential decay in their tails. The corresponding profiles are strongly localized near the walls can be expected for structures with low wavespeeds. For high values of c streak dominated states will show a steep decay in the front and a long tail.

Dependence of the decay rate on the wavenumber

The roots of $f(\mu)$ and thus the decay rates depend also on the spanwise wavenumber. For three different wavespeeds c the dependence of a root of $f(\mu)$ on the wavenumber γ is shown in figure 7.7. The root is the one at negative value of μ with a symmetric profile and the smallest absolute value of μ. For the investigated wavespeeds the absolute values of μ grow with increasing spanwise wavenumber or decreasing spanwise wavelength. Thus, for states with high spanwise wavenumbers, μ becomes large allowing for large decay constants μ/Re

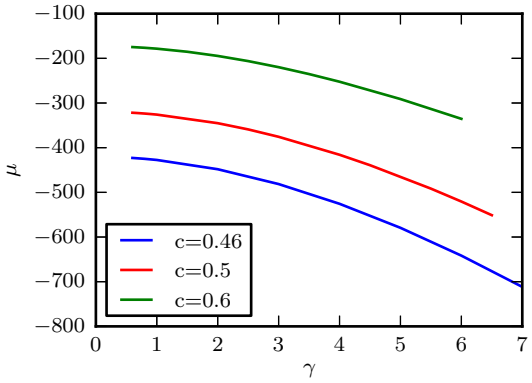

Figure 7.7: Dependence of the root of $f(\mu)$ at negative values of μ with a symmetric profile and smallest absolute value on the wavenumber γ.

and strong localization even at high values of Re. The three-dimensional streamwise localized orbits presented in section 6.5 are ECS where this effect is present.

7.3 Algebraic decay in the tails of turbulent spots

While there is no doubt that in the tails of exact solutions which are only localized in streamwise direction an exponential decay over a large range is visible (see sections 6.2 and 6.5), the situation is different in the spanwise tails of doubly-localized states. The results in section 6.3 show a good agreement with an algebraic decay in spanwise direction, but in streamwise direction the decay is still rather exponential.

The fact that for the doubly-localized state an algebraic decay is only visible in the spanwise direction might be due to a too small value of the streamwise domain length. Since further increasing the domain size for the doubly-localized orbit is difficult because of the computational cost and the poor convergence of the Newton-method, a different approach is used to investigate the localization in large domains. At $Re_B = 2000$ a small turbulent spot in a domain with $L_x = L_z = 112\pi$ and with a coarse resolution of $N_x \times N_y \times N_z = 1120 \times 33 \times 1456$ is simulated. We generate a random perturbation and overlay a window-function to obtain a localized perturbation. The resulting flow field is integrated forward in time. For different times the decay of the streamwise energy densities in the tails of the spot are shown in figure 7.8. The turbulent spot shows an algebraic decay in the tails in streamwise as well as in spanwise direction. As done in section 6.3 algebraic decays,

$$E(z) = A(z^{-\delta_1} + (L_z - z)^{-\delta_1}) \text{ and } E(x) = B(x^{-\delta_2} + (L_x - x)^{-\delta_2}), \tag{7.7}$$

are fitted to the data. The results are shown in the figure using black lines and agree well with the actual decay. The exponents obtained by the fit procedure vary between 1.6 and 2.1.

If the used computational domain is too small, the algebraic decay is masked by the exponential. The reason for the algebraic decay is that in the far tails the decay of the large-scale flow (Schumacher and Eckhardt, 2001; Lemoult et al., 2013; Duguet and Schlatter, 2013) around the turbulent spot is the dominant process. As already state in section 6.3 these large-scale

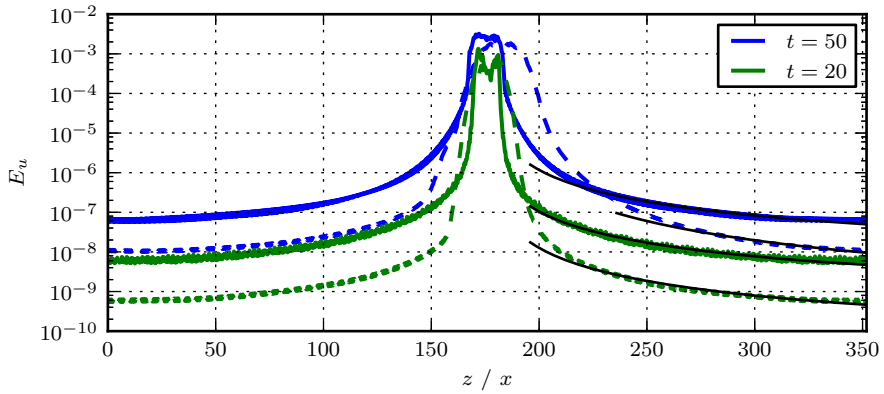

Figure 7.8: Decay of the streamwise energy density in the streamwise (solid) and spanwise (dashed) tails of a turbulent spot at $Re_B = 2000$ at $t = 20$ (green) and $t = 50$ (blue). The black lines show fits of $A(z^{-\delta_1} + (L_z - z)^{-\delta_1})$ and $B(x^{-\delta_2} + (L_x - x)^{-\delta_2})$ to the decays.

flows typically have a quadrupolar shape and as for their analogues in electrodynamics they decay algebraically.

The conjecture that the large-scale flow is responsible for the algebraic decay is supported by the fact that the localized TS-wave which due to its two-dimensionality does not allow for a large-scale flow, shows an exponential decay of the velocity components over five orders of magnitude (see figure 6.22). In the presence of shear, a three-dimensional state always includes a large-scale flow because it acts as an obstacle for the flow. Thus, the streamwise localized orbit PO_E shows deviations form pure exponential decay in the tail and the front (see figure 6.8).

As the magnitude of the flow in the algebraic tails is quite low, the interaction of localized flow structures over large distances is very weak. The algebraic decay becomes only visible where the energy density is three orders of magnitude lower than in the turbulent region. Therefore, the requirement of short range interactions necessary for the existence of directed percolation is fulfilled despite of algebraic tails.

Chapter 8

Summary of the results for plane Poiseuille flow

8.1 Critical Reynolds numbers for plane Poiseuille flow

As explained in chapter 2 there are different ways to define Reynolds numbers for PPF. The definition based on the bulk velocity (Re_B) is most suitable when simulations or experiments operate with a constant flow rate while the pressure gradient based formulation is advantageous if the pressure gradient (Re_P) is fixed while the flow rate might vary over time. For the laminar flow, Re_B and Re_P are identical, but for other exact solutions they differ in general. This is of particular importance for the transition process. If two systems operating at fixed flow rate and at fixed pressure gradient and whose Reynolds numbers coincide for the laminar state become turbulent due to finite amplitude disturbances, the behave subtly different since the state space structures are different. The differences of the state space are due to disparate sets of ECS (see section 3.2). In particular, the existence or non-existence of a particular ECS contributes to the different state space structures. For the ECS that were identified in this thesis, the critical Reynolds number for their appearance are arranged. In addition, we collect the relevant Reynolds numbers for states and effects that were not studied in dependence on the geometrical parameters but only for fixed values of L_x and L_z.

As already mentioned, for the laminar state the Reynolds numbers based on the pressure gradient and on the bulk flow are the same. Furthermore, the instability occurs in both case at a Reynolds number of 5772.2. The Tollmien-Schlichting waves that bifurcate subcritically from the base flow can be tracked down to $Re_B = 2610$ and $Re_P = 2941$. The study of the spatially extended, three-dimensional ECS in section 3.2 showed that they appear at a quite low values of Re_B and Re_P. The lowest critical Reynolds numbers for the appearance is achieved for TW_E where the values of Re_B and Re_P are 317 and 339, respectively.

For which Reynolds number the localized orbit PO_E appears depends on the spanwise width of the computational domain. The lowest value of Re_B is 1018.5 which is achieved for $L_z = 1.75\pi$. Localized TS-waves appear at higher values of Re_B and Re_P. The Reynolds numbers for their appearance are independent of L_z due to the two-dimensionality of the

localized TS-waves. The turning points of these orbits lie at $Re_B = 2334$ and $Re_P = 2373$.

An overview of all relevant Reynolds numbers for ECS is given in table 8.1. In addition the table contains the stability of the laminar flow, the critical Reynolds number (based on the bulk flow) for the streamwise spreading of localized turbulence that was found in section 6.7, the Reynolds numbers for the first boundary crisis in the symmetric subspace, and the lowest Reynolds number where the periodically bursting states discussed in section 3.3 were found.

	$Re_{B,min}$	L_x	L_z	$Re_{P,min}$	L_x	L_z
TW_{TS}	2610	1.48	-	2941	1.53	-
Loc. TS-waves	2334	-	-	2373	-	-
TW_E	316.8	2.8π	2.95π	339.1	2.9π	3.05π
PO_E	1018.5	-	1.75π	1023.18	-	1.75π
Instability of Lam. State	5772.22	1.96π	-	5722.22	1.96π	
Bursting edge states	~ 2100	π	0.4π	-	-	-
Spreading Turb.	1300 ± 50	-	2π	-	-	-
1st Crisis Bif.	785.95	2π	1π	1710	2π	1π

Table 8.1: Critical Re_B and Re_P for exact coherent structures and the laminar profile. In addition, the relevant Reynolds numbers for the first crisis bifurcation in the symmetric subspace, the onset of spreading turbulence, and the occurrence of periodically bursting edge states are given.

8.2 Summary and outlook

In the first part of this thesis subcritical turbulence in plane Poiseuille flow and occurring localized states were discussed. This chapter presents a brief synopsis of the main findings and an outlook including recommendations for future research.

Exact coherent states and minimal Reynolds number for their existence

Various exact coherent states of PPF were identified. Especially, it was shown that the edge state of this flow strongly depends on the geometrical parameters of the computational domain. In periodic domains with quite small streamwise and spanwise wavelengths the edge states are periodic orbits with complex temporal dynamics and long periods which are localized in wall-normal direction and which are quite reminiscent of those found in parallel boundary layers. Due to their long periods, it was not possible to track these orbits by standard continuation techniques. Thus, it was not possible to obtain the upper branch states which possibly are more relevant for the turbulent dynamics. Potentially, the upper branches of the bursting orbits can be identified in future work using multi-shooting methods (Sánchez and Net, 2010).

In addition to these periodic states, several relative equilibrium solutions were found using edge tracking and bifurcation analysis. The Reynolds numbers at which the ECS appear were studied in dependence on the geometrical parameters. It turned out that they can be found for Reynolds numbers as low as $Re_B = 317$ which is far below the onset of subcritical turbulence. However, it remains unknown if this is really the "maximal Reynolds number below which no coherent states can exist" (Eckhardt, 2008). It is not possible to determine this Reynolds number for a real physical system. Only for low-dimensional models, as the one introduced by

Moehlis et al. (2004b), it is possible to find all existing ECS and thus to determine the lowest Reynolds number for which ECS can exist (Pausch et al., 2014).

Unfortunately, up to now there are no simple physical arguments for the appearance of ECS in plane Poiseuille, plane Couette or pipe flow. It would be nice to find such a simple and elegant argument as for Rayleigh-Bénard convection where the mechanism behind the instability of the laminar state and the appearance of a secondary convection solution have a physical foundation in the fact that viscous forces are outbalanced by buoyancy forces if the Rayleigh number exceeds a certain value (e.g Bergé and Dubois, 2006).

Origin of subcritical turbulence

It was shown that a bifurcation cascade starting at an exact coherent structure not related to the instability of the laminar state creates a chaotic attractor in PPF. Crisis bifurcations contribute to the increase of the complexity of the attractor and transform the chaotic attractor into a saddle that shows characteristic exponentially distributed lifetimes. Thus, the same mechanism for the generation of subcritical turbulence formerly found for pipe and plane Couette flow could be identified for PPF.

Although the attractor is chaotic, its dynamics are less complex than those of genuine turbulence due to the symmetry constraint and the small size of the periodic domain. Possibly, the spatio-temporal complexity could be increased by a merging of different attractors. As it was shown this phenomenon is theoretically possible, because attractors with different spatial wavelength exist. However, a merging of two attractors with different spatial wavelength has not yet been observed. In large computational domains it might be possible to find a bifurcation cascade starting at a localized exact solution as it was found for the case of pipe flow (Avila et al., 2013).

Bypass and TS transition

In PPF two scenarios for the transition to turbulence coexist. Above the linear instability, the Tollmien-Schlichting transition (TS transition) dominates especially for small disturbances. Because the instability of the base flow is subcritical, TS transition can also occur below Re_{crit}. A second path to turbulence is provided by bypass transition which is predominant in the subcritical range but also exists above Re_{crit}. In this transition process no TS-waves appear. Using the relevant ECS for both transitions, the TS-waves and the edge state TW_E for bypass transition, it was possible to obtain an improved picture how both transition scenarios coexist in the state space. The state space investigation revealed that, though possible in the subcritical range, only a small amount of initial conditions becomes turbulent via TS transition. With increasing Reynolds number the transition becomes more important. In the supercritical range the TS transition is realized for all initial conditions with small amplitude. Bypass transition does always coexist with TS transition and is generally a much faster way to turbulence. Both scenarios can lie in close proximity in the state space. For Reynolds numbers above Re_{crit}, the stable manifold of the bypass edge state TW_E separates TS and bypass transition. This implies that tiny changes of the amplitude of an initial condition can change the type of transition which in turn changes the time required to reach the turbulent state drastically.

Furthermore, by using the bypass edge state TW_E it was possible to determine a scaling for the threshold required for bypass transition. It was found that the threshold amplitude decays at least as $Re^{-0.5}$.

The phenomenon of coexisting transition scenarios is no unique property of plane Poiseuille flow. It can be observed in other flows as the Blasius and the asymptotic suction boundary layer. In these flows the state space structure is presumably akin to plane Poiseuille. Analogous investigations of the state space of these flows could be used to support this conjecture.

Localized states

Different spatially localized exact solutions for PPF were found. Among these states the first doubly-localized relative periodic orbit for a plane shear flow should be emphasized. The orbit was identified by tracking a streamwise localized orbit that is an edge state in narrow domains to wider domains. During the tracking in domain width the state localized spontaneously without bifurcation. The doubly-localized state shows a quadrupolar structure of the large-scale flow. In its spanwise tails the decay of the velocity field is in agreement with a power law. In additional simulations of turbulent spots it was also observed that the decay in the tails follows a power law. The algebraic decay in the tail of doubly-localized states (turbulent states and exact solutions) might be related to the decay of the large-scale flow. The decay in the tails could be quantified by future investigations. An interesting question in this context is the dependence of the decay on the size of the localized state and how the decay differs between Couette and Poiseuille flow.

Because of the very high computational costs, the upper branch of the doubly-localized state has not yet been identified. In further computations the upper branch hopefully will be found which possibly can help to understand how localized turbulence is created.

A widespread mechanism for the creation of streamwise localized exact solutions seems to be the long-wavelength instability that was found to occur for the TS-wave and the traveling wave edge state TW_E. Given the multitude of known exact solutions for plane Poiseuille, plane Couette and pipe flow, this mechanism provides a systematic approach for finding further localized states.

Studying localized Tollmien-Schlichting waves, it was possible to find streamwise localized solutions of different length. Similarly, relative periodic orbits with different streamwise extend that resemble the localized edge state PO_E were found. Such states are relevant because they might contribute to the understanding of the spreading of localized turbulence. One could imagine that turbulence spreads along a scaffold formed by such exact solutions of different length. In particular, one question that arises in this context is, if a phenomenon similar to homoclinic snaking that was shown to exist in spanwise direction (Schneider et al., 2010a) also exists for solutions localized in the streamwise direction.

The study of streamwise localized turbulence in plane Poiseuille flow revealed that the system behaves quite similar to pipe flow if the domain is narrow. Structures analogous to turbulent puffs exist as well as two kinds of slugs. Furthermore, as in the case of pipe flow the splitting of puff-like structures can be observed. The existence of decaying and splitting puffs allows to define critical Reynolds numbers for the onset of turbulence based on the characteristic time scales of both processes as was done for pipe flow by Avila et al. (2011). The similarity to pipe flow diminishes in wide computational domains where stripe patterns can develop. An investigation how the stripe patterns appear if the domain width increases should be part of future research.

Part II

The asymptotic suction boundary layer over a heated plate

Chapter 9

Introduction to the system

Thermal boundary layers occur in case of a flow over a heated surface. They develop in simple model systems such as Rayleigh-Bénard convection at high Ra where they have been in the focus of many studies. They also appear in nature where the atmospheric boundary layer or the convection within the earth's mantle are examples.

The importance of thermal boundary layers arises from the fact that they have a large influence on the heat transfer (and thus the Nusselt number)(Ahlers et al., 2009). In particular, the coherent structures that appear in form of plumes inside of the boundary layer contribute to the heat flow (Grossmann and Lohse, 2004). For the geophysical application of thermal boundary layers, coherent structures are also of accentuated importance. For example, instabilities of the atmospheric boundary layer lead to the formation of convection rolls which can be observed in form of cloud streets (Etling and Brown, 1993). Inside of the earth's mantle coherent structures arise in the form of thermal plumes (Montelli et al., 2004) which are of special interest because of their contribution to the heat transport.

For the case of velocity boundary layers the study of parallel boundary layers such as the asymptotic suction boundary layer (ASBL) offers a possibility to investigate the coherent structures inside of a boundary layer, since, in contrast to the spatially developing Blasius boundary layer, the ASBL allows for the existence of exact coherent structures (ECS). It is easier to study and characterize these ECS than coherent structures that are not exact solutions. So far, several of these ECS of the ASBL, travelling waves and periodic orbits, have been identified and studied (Kreilos et al., 2013; Khapko et al., 2013, 2014; Deguchi and Hall, 2014; Jelli, 2014).

The studies of iso-thermal ASBL inspired the idea of using a parallel thermal boundary layer to improve our understanding of ECS and the dynamics inside of thermal boundary layers. A parallel thermal boundary layer is realized by the ASBL over a heated plate, henceforth referred to as TASBL. This is the flow over a heated plate at constant temperature through which fluid is homogeneously sucked with a speed $-V_s$. In infinite distance to the plate the fluid has the velocity U_∞ relative to the plate and the temperature difference of the plate and the fluid in infinite distance is T_0. A schematic sketch of the system is shown in figure 9.1.

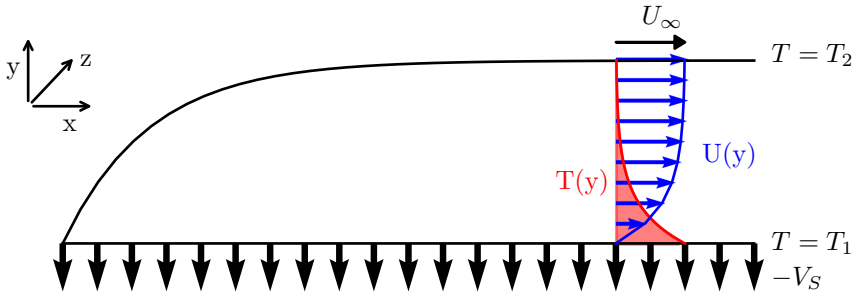

Figure 9.1: Sketch of the ASBL with heated plate. The temperature difference between the plate and the flow in infinite distance is $T_0 = T_1 - T_2$. In infinite distance to the plate the flow moves with U_0 in streamwise (x-) direction. In red an blue the shapes of the laminar profiles of the temperature and of the streamwise velocity are indicated, respectively.

The flow is governed by the Overbeck-Boussinesq equations (Landau and Lifschitz, 1991):

$$\partial_t \vec{\tilde{u}} + (\vec{\tilde{u}} \cdot \nabla)\vec{\tilde{u}} = -\nabla\tilde{p} + \nu\Delta\vec{\tilde{u}} + \beta g\tilde{\theta}\vec{e}_3, \tag{9.1}$$

$$\partial_t\tilde{\theta} + (\vec{\tilde{u}} \cdot \nabla)\tilde{\theta} = \kappa\Delta\tilde{\theta}, \tag{9.2}$$

$$\nabla\vec{\tilde{u}} = 0. \tag{9.3}$$

In these equations ν is the kinematic viscosity, κ is the thermal diffusivity, β is the thermal expansion coefficient, g is gravitational acceleration, and $\vec{\tilde{u}}$ and $\tilde{\theta}$ are the velocity and temperature fields, respectively. For the given boundary conditions of the system,

$$u(y = 0) = 0 \quad u(y = \infty) = U_\infty \tag{9.4}$$

$$v(y = 0) = -V_S \tag{9.5}$$

$$\theta(y = 0) = T_0 \quad \theta(y = \infty) = 0, \tag{9.6}$$

one easily derives the stationary laminar profiles for the velocity and temperature field

$$\vec{U}(x, y, z) = (U(y), -V_s, 0) \text{ with } U(y) = U_\infty(1 - e^{-V_s y/\nu}), \tag{9.7}$$

$$T(x, y, z) = T_0 \cdot e^{-V_s/\kappa}. \tag{9.8}$$

A characteristic length scale of the system is the displacement thickness (Schlichting and Gersten, 1997)

$$\delta = \int_0^\infty (1 - \frac{U(y)}{U_\infty})dy = \frac{\nu}{V_S}. \tag{9.9}$$

The dimensionless numbers characterizing the system are the Reynolds, Prandtl and Rayleigh number given by the following definitions:

$$Re = \frac{U_\infty\delta}{\nu} = \frac{U_\infty}{V_s}, \quad Pr = \frac{\nu}{\kappa}, \quad Ra = \frac{\beta g\delta^3 T_0}{\kappa\nu}. \tag{9.10}$$

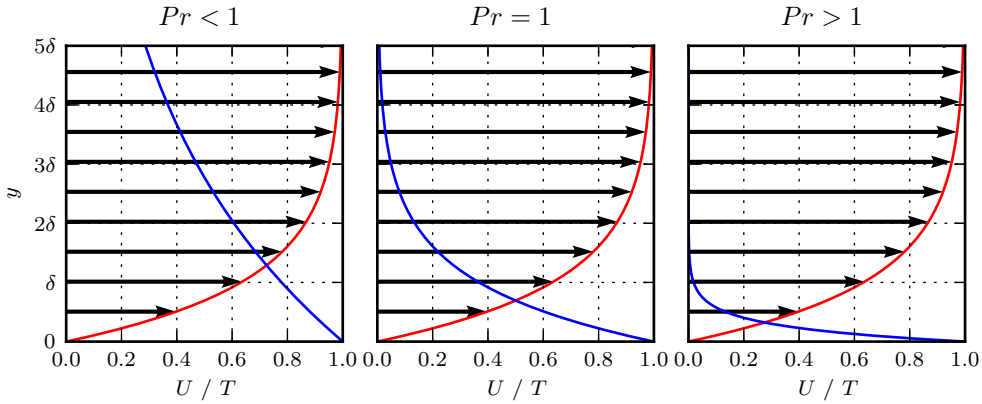

Figure 9.2: Illustration of the role of the Prandtl number for TASBL. The red lines show the streamwise component of the base flow U and the blue lines the temperature profile T, respectively. For $Pr = 1$ the thermal and the viscous boundary layer have equal thickness. For $Pr < 1$ the thickness of thermal boundary layer is larger than then the one of the velocity boundary layer. For $Pr > 1$ (e.g. water and oils) it is the other way around.

We make the equations dimensionless by measuring lengths in units of δ, time in units of δ^2/κ (what corresponds to measuring velocities in units of κ/δ) and temperature in units of T_0/Ra.

$$\partial_t \vec{u}_{tot} + (\vec{u}_{tot} \cdot \nabla)\vec{u}_{tot} = -\nabla p + Pr\Delta\vec{u}_{tot} + Pr\,Ra\theta_{tot}\vec{e}_3, \tag{9.11}$$

$$\partial_t \theta_{tot} + (\vec{u}_{tot} \cdot \nabla)\theta_{tot} = \Delta\theta_{tot}, \tag{9.12}$$

$$\nabla \cdot \vec{u}_{tot} = 0. \tag{9.13}$$

With the above choices for the dimensionless units the laminar profiles become:

$$\vec{U}(x, y, z) = (U(y), -Pr, 0) \text{ with } U(y) = Pr\,Re \cdot (1 - e^{-y}) \tag{9.14}$$

$$\text{and } T(x, y, z) = Ra \cdot e^{-Pr\ y}. \tag{9.15}$$

Regarding the dimensionless temperature profile it becomes evident that the thickness δ_{th} of the thermal boundary layer is inverse proportional to the Prandtl number.

$$\delta_{th} = \frac{1}{Pr} \tag{9.16}$$

Thus, the Prandtl number defines the ratio between the thickness of the velocity boundary layer and the thermal boundary layer. In figure 9.2 the effect of Pr is illustrated. For values of Pr smaller than one (e.g air and liquid metals) the thermal boundary layer is much thicker than the velocity boundary layer. For $Pr = 1$ both have the same thickness, while for $Pr > 1$ (e.g. water and oils) the thermal boundary layer is the thinner one.

Within this part of the thesis ASBL over a heated plate will be studied with a focus lying on the ECS of the flow. For the numerical simulations of the system the *Channelflow*-code was modified to handle suction through the walls and an additional temperature field. A description of the necessary modifications is given in appendix A.1. In the numerical simulations the wall-normal direction has to be truncated in some distance L_y. In this distance a plate at

temperature $T = 0$ moving with speed U_∞ is assumed and no-slip boundary conditions are used. Thus, the base profiles are modified to

$$U^*(y) = Re\,Pr\frac{1 - e^{-y}}{1 - e^{-L_y}} \tag{9.17}$$

and

$$T^*(y) = \frac{Ra}{1 - e^{-Pr\ L_y}}\left(e^{-Pr\ y} - e^{-Pr\ L_y}\right). \tag{9.18}$$

For L_y a value equal or larger than 20 is used in the simulations making the differences of the profile real profiles $U(y)$ and $T(y)$ and the profiles $U^*(y)$ and $T^*(y)$ used in the simulations negligible.

As for the case of PPF, the full velocity and temperature fields are decomposed in the base flow and fluctuation on top:

$$\theta_{tot} = T + \theta, \tag{9.19}$$

$$\vec{u}_{tot} = \vec{U} + \vec{u}. \tag{9.20}$$

If not explicitly stated differently, only the fluctuations θ and $\vec{u}$ are visualized or used in bifurcation diagrams.

The further outline of this second part of my thesis is as follows. First, in chapter 10 the stability of the system is analyzed and the solutions bifurcating from the laminar state are discussed. In chapter 11 the bifurcating tertiary solutions and their relation to the turbulent flow are explored. By analyzing the superharmonic instabilities of the secondary solution the origin of transient turbulence in the subcritical range is investigated in section 11.2. In section 11.3 equilibrium solutions of the system that are localized in one spatial direction are identified and discussed. It will be shown that long-wavelength instabilities are of particular importance for their generation. The relation of equilibrium solutions to plume-like dynamics in TASBL is discussed in section 11.4.

In section 11.5 various doubly-localized equilibrium solutions are presented and for one particular exact solution it is shown how it bifurcates from a spatially extended stationary pattern.

Mean profiles of turbulent TASBL at $Re = 0$ are discussed in section 11.6. In section 11.7 it will be shown that the edge states of iso-thermal ASBL can be connected to the thermal instability before I conclude in chapter 12 with a summary and an outlook.

Chapter 10

Stability and secondary solutions

10.1 Introduction

Although for many flows such as pipe flow, plane Couette flow or plane Poiseuille flow linear stability theory fails to predict or explain the occurrence of turbulent motion (e.g. Grossmann, 2000), an analysis of the stability of the base flow remains a reasonable starting point for the investigations of TASBL. Thus, in this section the stability properties of the base flow are calculated in dependence on the three dimensionless numbers Re, Pr and Ra and the streamwise and spanwise wavenumbers. For each case the secondary solutions bifurcating at the linear instability are analyzed.

10.2 Stability analysis for $Ra = 0$

For the case $Ra = 0$ the system reduces to isothermal ASBL. Hocking (1975) showed that the laminar profile of ASBL has a linear instability at $Re \approx 54370$ for a critical wavenumber $\alpha = 0.1555$. The fact that ASBL becomes unstable at such a high Reynolds number compared to the Blasius boundary layer which becomes unstable at $Re = 519.4$ (Schmid and Henningson, 2001) impressively shows the stabilizing effect of the suction. Milinazzo and Saffman (1985) tracked the traveling wave solutions that bifurcate from the laminar profile and found that they extend down to Reynolds numbers around 3000. We recompute the stability curve using *Channelflow's* Arnoldi-method, which is briefly described in appendix A.2. To obtain the stability curve the stability of the laminar state is calculated with a fine resolution in Re to ensure that the relative error of the critical Re is of order 10^{-2}. Squire's theorem (Schmid and Henningson, 2001) ensures that a two-dimensional streamwise mode is the first to become unstable which allows to restrict on two-dimensional disturbances that are independent of the spanwise coordinate z. The resulting critical Reynolds numbers that confirm the results of Hocking (1975) and the more recent ones by Fransson and Alfredsson (2003) are shown in dependence of the streamwise wavenumber in figure 10.1a.

The Tollmien-Schlichting-like traveling wave solution bifurcating subcritically from the laminar flow at the point of the linear instability is tracked in Re for various values of the streamwise

wavelength. The resulting solution curve is shown in 10.1b together with the bifurcation diagram for $k_x = 0.155$. The minimal Reynolds number of the turning point is 3168 which is achieved for $k_x = 0.203$. These results show that, as in the case of PPF, the two dimensional waves connected to the instability of the base flow appear at Reynolds numbers much higher than the observed onset of subcritical turbulence which was found to be at $Re \approx 270$ (Khapko, 2014).

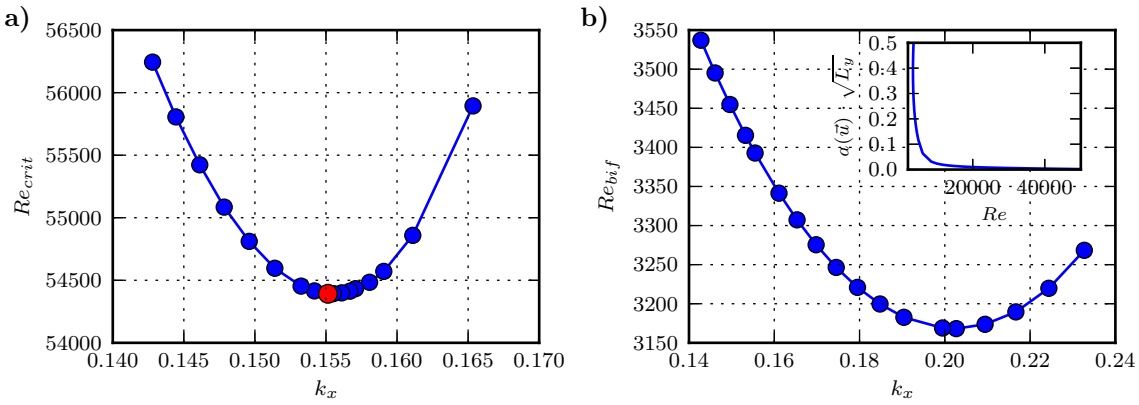

Figure 10.1: Panel a) shows the critical Reynolds number Re_{crit} for $Ra = 0$. The minimal critical Reynolds number that is achieved for $k = 0.155$ is marked by a red circle. In b) the Reynolds number Re_{bif} of the bifurcation point of the bifurcating Tollmien-Schlichting-wave is shown versus streamwise wavenumber k_x. The inset in panel b) shows the bifurcation diagram of the Tollmien-Schlichting-wave for $k_x = 0.157$ using the amplitude $a(\vec{u})$ multiplied by $\sqrt{L_y}$ on the abscissa.

Visualizations of the bifurcating two-dimensional solutions are given in figure 10.2 for different Reynolds numbers. Because in contrast to PPF the flow has no symmetry with respect to the wall-normal direction y, the clockwise and counter-clockwise rolls behave different in dependence on Re. Close to the bifurcation point at $Re = 50000$ (figure 10.2a) the rolls are almost symmetrical. When Re is decreased, the counter-clockwise roll disappears while the clockwise roll survives but becomes narrower (figure 10.2b).

10.3 Stability Analysis for $Re = 0$

We now want to investigate the stability for the case $Re = 0$. The obtained stability curves for various Prandtl numbers, including the physical relevant ones Pr=0.7 (air) and Pr=6 (water), are shown in figure 10.3. In contrast to the case of Rayleigh-Bénard convection, the results show a strong dependence on the Prandtl number and therefore on the relative size of the thermal to the viscous boundary layer. For the case $Pr = 1$ a critical Rayleigh number of 19.4705 and a critical wavenumber of 0.438 are obtained.

In figure 10.4 the critical Rayleigh and the critical wave number are shown depending on the Prandtl number. The dependence of the critical wavenumber on Pr is approximately linear while the dependence of the critical Rayleigh number almost follows a power law with an exponent of 3. At this point it is worth to remember the definition of Ra. In the definition given in equation 9.10 the velocity boundary layer thickness δ is used. As illustrated in figure

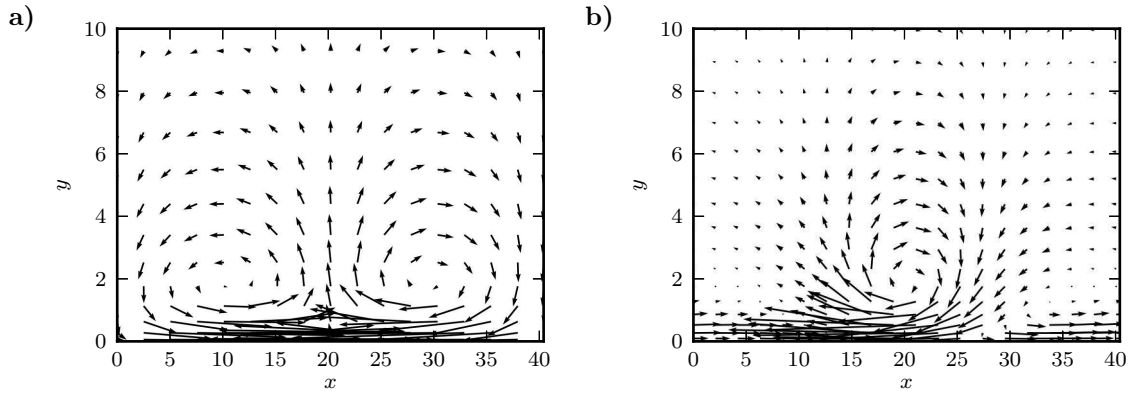

Figure 10.2: Visualizations of the TS-wave bifurcating from the base flow for $Re = 50000$ (a) and $Re = 8475$ (b). In both cases the streamwise wavenumber is 0.157. The direction of the flow is from left to right.

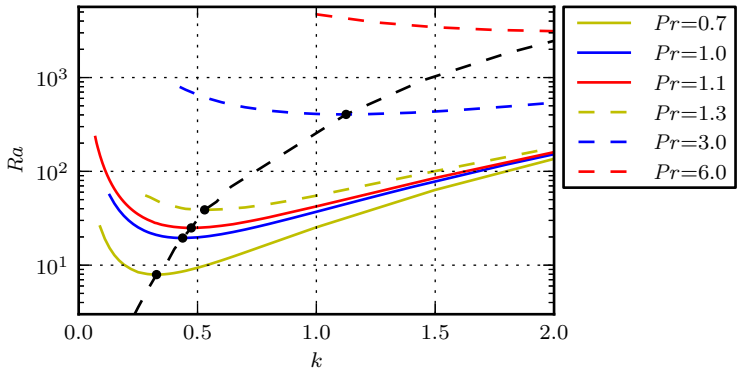

Figure 10.3: Stability boundary for Re=0 and different values of the Prandtl number. For each Prandtl number the lowest critical Rayleigh number is marked by a black circle.

9.2 for large values of Pr the thickness of the temperature boundary layer δ_{th} is much smaller than the one of the velocities. Therefore, the relevant length scale of the system is δ_{th}. We can derive a Rayleigh number based on δ_{th} by multiplication of Ra with $1/Pr^3$ because $Ra \propto \delta^3$ and $\delta/\delta_{th} = Pr$. Furthermore, we can obtain a wavenumber based on δ_{th} by dividing the wavenumber based on δ by Pr. The insets in figure 10.4 show the results of this change of the length scale. For the wavenumber as well as for Ra the change of the length scale leads to critical values that reach a constant value for large values of Pr. The critical wavenumber $k_{crit,th}$ and Rayleigh number Ra_{th} based on the thickness of the temperature boundary layer that are asymptotically reached for large Prandtl numbers are 0.363 and 14.3, respectively.

By using a Newton's-method (Viswanath, 2007) included in the channelflow package, it is possible to identify ECS bifurcating at the linear instability and to continue them in Rayleigh number. For a brief description of the used method see appendix A.3. It turns out that in contrast to the case of Rayleigh-Bénard convection the bifurcation is subcritical. The bifurcating exact solution is an equilibrium solution which we refer to as R_1 in the following. A bifurcation diagram of R_1 for the critical wave number k_{crit} and $Pr = 1$ is given in figure

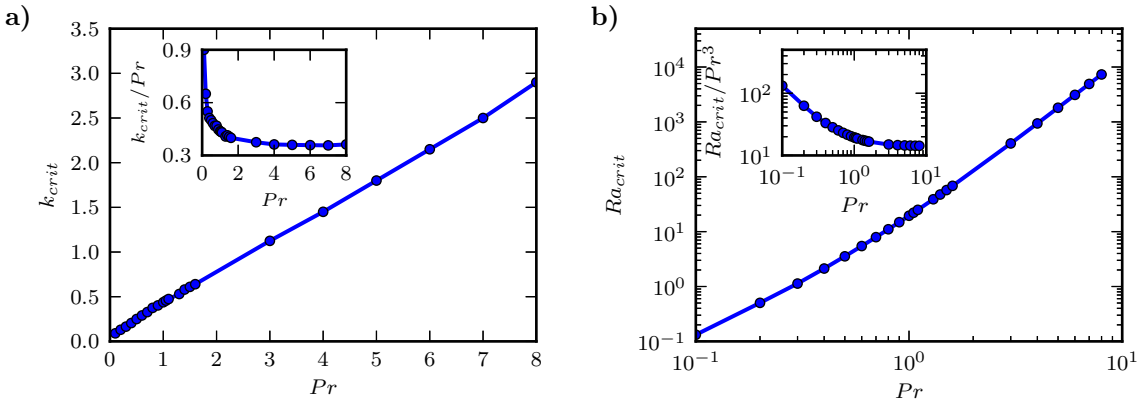

Figure 10.4: In a) the dependence of the critical wavenumber on the Prandtl number is shown. Panel b) shows the dependence of the critical Rayleigh number on the Prandtl number. The insets show the same quantities but based on the thermal boundary layer thickness δ_{th} instead of the viscous one.

10.5a. The Rayleigh numbers of the turning points of the bifurcating solutions depend on the wavenumber. In figure 10.5a this dependence of the turning point as well as the dependence of the critical Rayleigh number on the wavenumber is shown. With decreasing wave number the turning point moves to lower values of Ra and the subcriticality of the bifurcation becomes more distinct. For small wavenumbers it becomes difficult to determine the Rayleigh number of the turning point because the necessary domain size increases in spanwise and also in wall-normal direction. Furthermore, because of an increasing number of instabilities for low wavenumbers it becomes difficult to follow the correct solution branch. However, due to the decreasing slope of the turning point with increasing Ra, the simulations suggest that for zero wavenumber a finite Rayleigh number for the turning point is reached. Possibly, the Rayleigh number obtained for $k = 0$ is the Rayleigh number of the turning point of a localized state. A good candidate is the localized equilibrium we will discuss in section 11.3.

Visualizations of the flow and temperature fields of the lower and the upper branch of R_1 are shown in 10.6. The secondary solution consists of one pair of counter-rotating convection rolls. With increasing distance from the bifurcation point the height of these rolls grows and therefore they become stretched and their aspect ration (height/width) increases. To quantify the growth in height, a way to define a height of the structures is necessary. One possibility is to use the energy density of the velocity field $E_{u,xz}(y)$ (or of the temperature field $E_{\theta,xz}(y)$) depending on the wall distance

$$E_{u,xz}(y) = \frac{1}{2L_xL_z}\int_0^{Lx}\int_0^{L_z}\vec{u}^2 dxdz, \tag{10.1}$$

$$E_{\theta,xz}(y) = \frac{1}{2L_xL_z}\int_0^{Lx}\int_0^{L_z}\theta^2 dxdz. \tag{10.2}$$

In this equations $\vec{u}$ and θ are the deviations from the laminar profile. Examples for the resulting energy profiles of the flow field and the temperature field are shown in figure 10.7a. As the height of the structure we define the distance from the lower plate where the density falls below 1/50 of its maximum value. An illustration of the resulting height is shown in figure 10.7a by

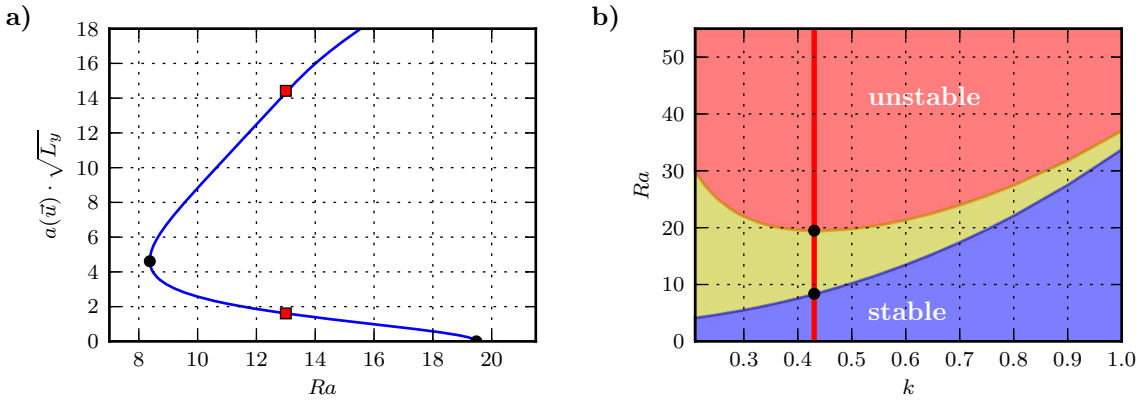

Figure 10.5: a) Bifurcation diagram of the roll-state bifurcating from the laminar flow. The Prandtl number is 1.0 and the wavelength is $k = k_{crit} = 0.4305$. The states marked by the red squares are shown in figure 10.6. b) Stability diagram for $Pr = 1$. In the red area the laminar profile is unstable. In the blue area the laminar flow is stable. In the yellow area the laminar flow is stable and the lower branch of the roll-solutions bifurcation from the laminar profile exists. The red line marks the critical wavelength k_{crit}. In both figures the black circles mark the point where the roll-solution bifurcates from the laminar flow and where it appears in a saddle node bifurcation for the critical wavenumber.

green arrows. Using this definition we obtain two different heights. One, h_u, resulting from the velocity field and another, h_t, resulting from the temperature field. In figure 10.7b both heights are plotted for the lower and the upper branch of the roll solution for different Rayleigh numbers and Prandtl numbers. The growth rate with Ra as well as the absolute values of the height depend strongly on the Prandtl number. For small values Pr the height and the growth rate are larger than for bigger values of Pr. In particular, the height of the upper branch solution grows linearly with Ra (for sufficient distance from the turning point). The slope increases with decreasing Prandtl number form about 0.4 for $Pr = 3$ to 8.1 for $Pr = 0.7$.

Altogether, the results show that for small Prandtl number the roll solutions become remarkably high. The increase of the height with Ra is larger for smaller values of the Prandtl number. Furthermore, independent of Pr the growth seems to be unbounded.

For high Rayleigh numbers a second two-dimensional eigenmode becomes unstable. The stability curve for this eigenmode is shown in figure 10.8a for $Pr = 1$. The critical wavenumber for this mode at $Pr = 1$ is about 0.612 and the critical Rayleigh number is about 173. For all Prandtl numbers this eigenmode is the second to become unstable. Where this mode becomes unstable an equilibrium solution, henceforth referred to as R_2, is created in a subcritical bifurcation. This equilibrium solution, as the second unstable mode, looks like the roll solution discussed above sitting on top of a pair of flat rolls. A visualization of the bifurcating exact solutions is shown in figure 10.8b. The second pairs of rolls of the R_2 solutions have their centers in a distance of about 5 from the plate where the temperature gradient is already quite low. This is reminiscent of the free-stream coherent structures of isothermal ASBL described by Deguchi and Hall (2014) which have vortex structures in distance to the plate where the shear gradient is quite low.

For even higher Rayleigh numbers further modes become unstable. Each further unstable

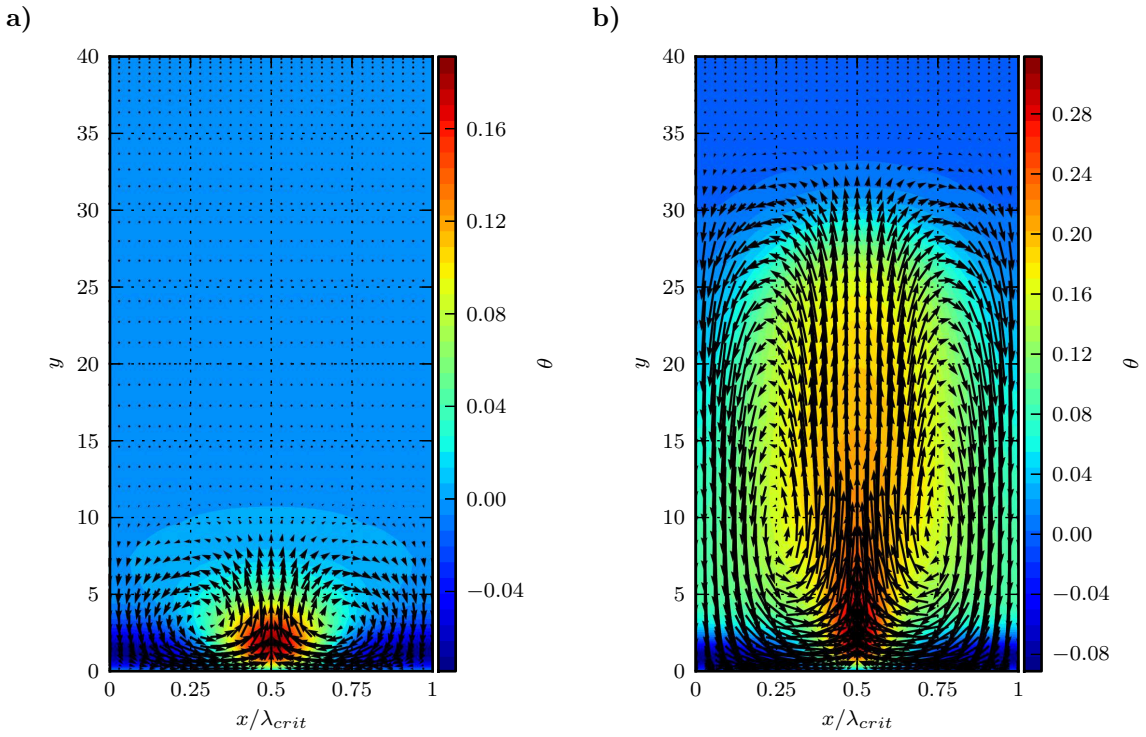

Figure 10.6: In panels a) and b) the flow- and temperature fields for the lower and upper branch of the bifurcation solution R_1 at Ra=13 are shown. The Prandtl number is 1.0 and the spanwise wavelength is $k = k_{crit} = 0.4305$. The velocity is visualized by the arrows. The temperature field (divided by Ra) is represented by the colors. For both fields only the deviation from the laminar profile is shown.

mode has one more layer of flat rolls. At the critical wavenumber the Rayleigh numbers where the second and the third mode become unstable are 179.1 and 934.2, respectively.

10.4 Stability Analysis for $Re \neq 0$ and $Ra \neq 0$

Since a relation comparable to Squire's theorem holds for the flow (Gage and Reid, 1968) it is sufficient to know the stability boundary for transversal and longitudinal modes to obtain a complete stability diagram.

A stability analysis of modes that depend only on the spanwise wavenumber and are invariant in the streamwise direction (longitudinal modes) yields the same critical Rayleigh number as in the case of vanishing Reynolds number.

The stability curve for spanwise invariant modes (transversal modes) shown in figure 10.9 reveals a stabilizing effect of the Reynolds number. The critical wavenumber moves to lower values and remains close to 0.2 for a wider range in Re.

This kind of stabilizing effect of the Reynolds number with respect to transversal disturbances was also found in thermal plane Poiseuille flow (Gage and Reid, 1968; Nicolas et al., 2000). Nevertheless, as follows from 10.2 for $Re > Re_{crit} = 54370$ the base flow becomes un-

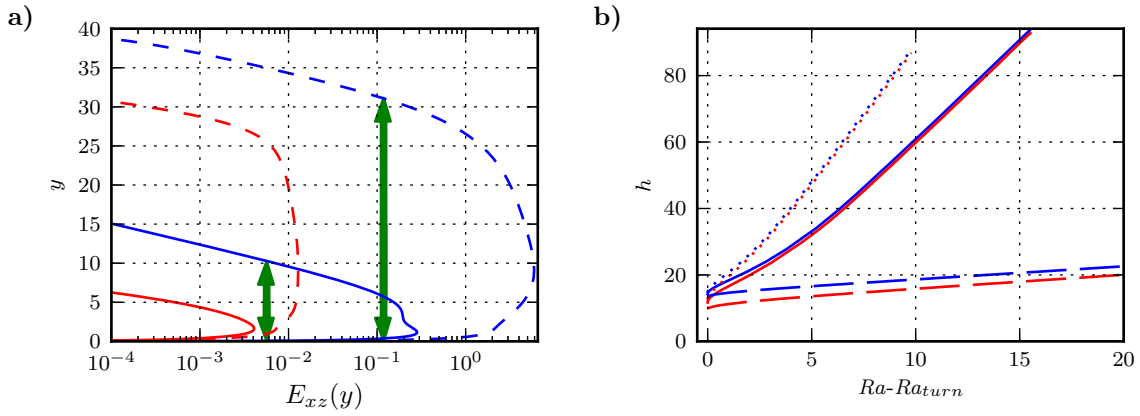

Figure 10.7: a) Energy density depending on wall-normal coordinate y for the upper (dashed) and the lower (solid) branch of the roll solution R_1 for Ra=13, Pr=1.0 and $k = k_{crit}$. The density for the flow field is drawn in blue and for the temperature field red is used. b) Calculated height of the upper branch roll solution depending on the distance to the tuning point for $Pr = 0.7, 1.0$ and 3 (dotted, solid and dashed lines). For the heights resulting from the temperature and the velocity field, red and blue color is used, respectively. In each case the height is defined as the distance from the lower plate, where the energy density is only 1/50 of the maximum of the energy density. The green arrows in a) illustrate the height following this definition for the profile resulting from the velocity field.

stable to a spanwise invariant Tollmien-Schlichting modes with wave number $k_{crit} = 0.157$ for $Ra = 0$.

The ECS bifurcating from the longitudinal instability are the equilibrium solutions found for $Re = 0$ in the previous section with an additional streamwise velocity component. Therefore, independent of Re the solutions curves have their turning points at the same values of Ra as these solutions (shown in figure 10.5b) and they grow in height in the same way.

The ECS that bifurcate from the transversal instability are transversal rolls or, more precisely transversal waves, because they are traveling wave solutions. Henceforth, these solutions are referred to as W_1. The solution branches of the waves depend strongly on the Reynolds number what can be seen in in figure 10.9 where solution curves are shown for some values of Re. Visualizations of the flow fields of the upper and lower branch of the W_1 solution at $Re = 5$ are shown in figure 10.10. The figure shows that the shearing at finite Re tilts the convection rolls in the direction of the the mean flow. Especially, the up-flow region of the roll is tilted while the down-flow region stays almost straight. In contrast to the case of the TS-waves in section 10.2 the roll turning counter-clockwise is the stronger one while the clockwise roll is small and deformed.

For systems that are thermally stratified and under the influence of shear an often used dimensionless number is the Richardson number,

$$Ri = \frac{g\beta T_0 \delta}{U_\infty^2} = \frac{Ra}{Re^2 Pr}, \tag{10.3}$$

that relates the buoyancy to the flow gradient. The value of Ri is a measure for the importance of natural convection compared to forced convection. If Ri is small, effects of natural convection

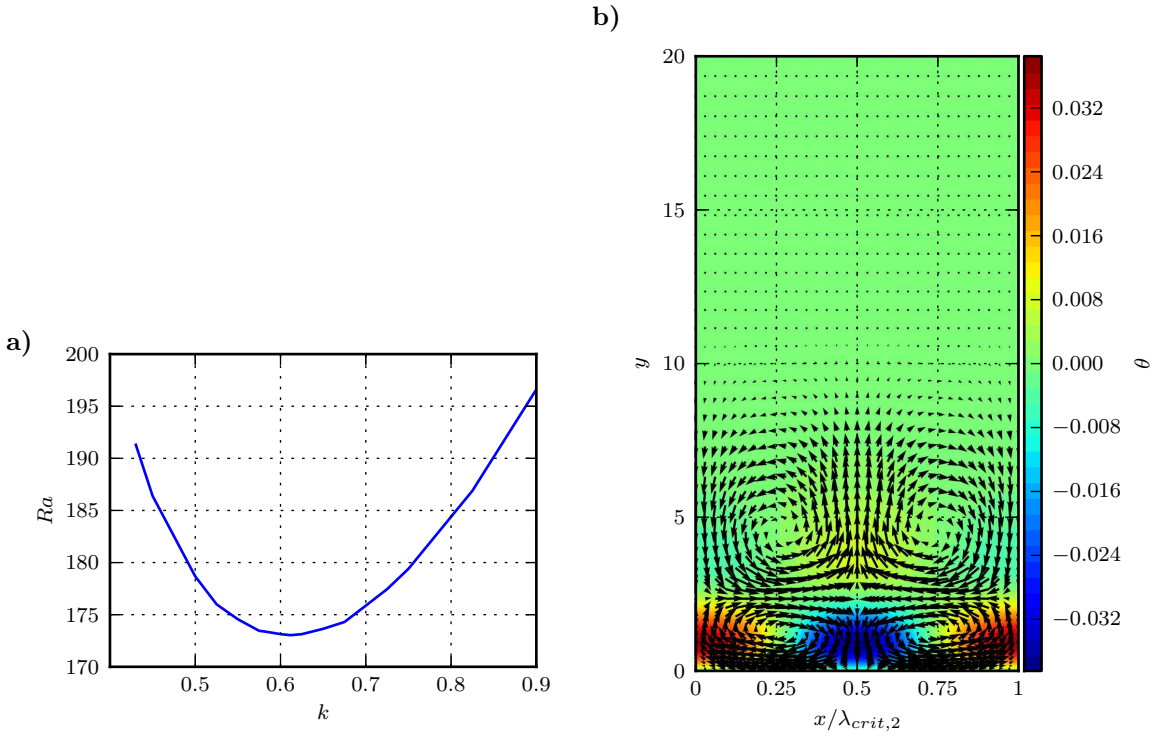

Figure 10.8: In panel a) the stability curve for the second two-dimensional unstable mode of the base flow is shown for $Pr = 0$. Panel b) shows a visualization of the equilibrium solution that bifurcates from the base flow where the second mode becomes unstable. The velocity is visualized by the arrows and the temperature field divided by Ra is represented by colors. For both fields only the deviation from the laminar profile is shown. The Rayleigh number and wavenumber for the solution are 167 and 0.61, respectively.

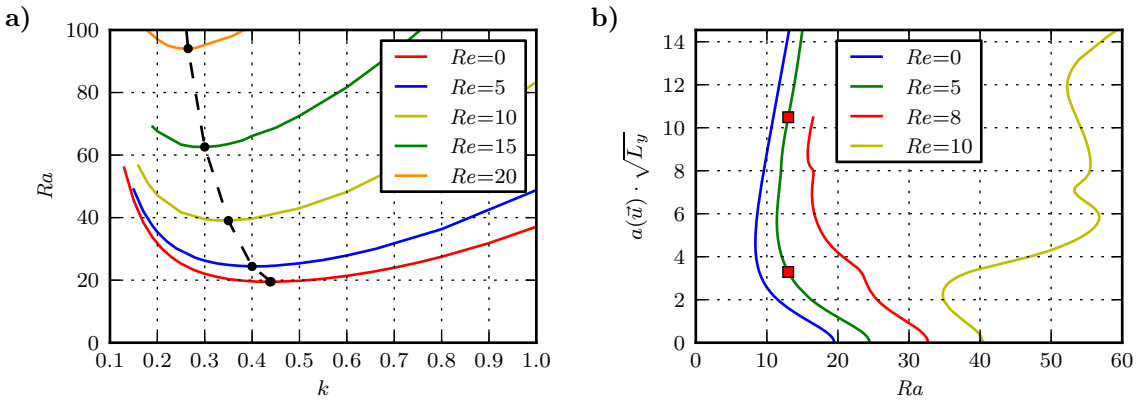

Figure 10.9: In panel a) stability boundaries for transversal rolls at Pr=1 are shown for different Reynolds numbers. In b) bifurcation diagrams for transversal roll solutions with $k_x = 0.4305$ are shown for various Reynolds numbers. For the positions marked by the red squares the flow fields are shown in figure 10.10.

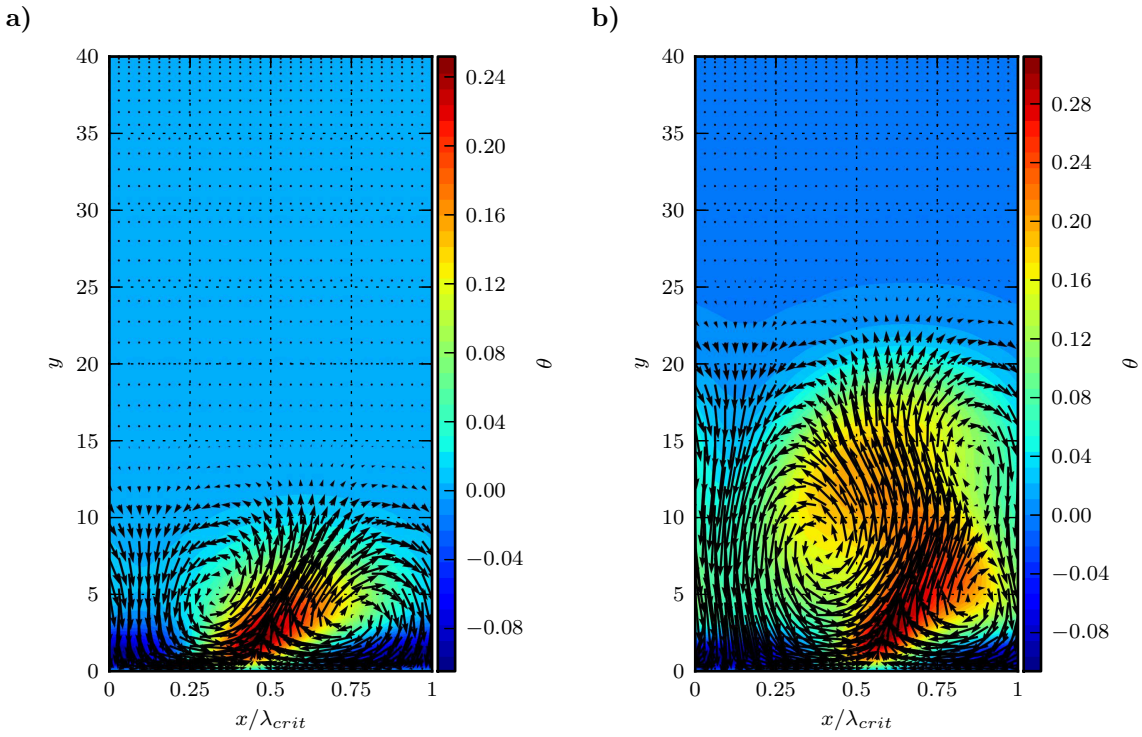

Figure 10.10: Flow and temperature fields for the bifurcation transversal roll solutions at $Re = 5$ and $Ra = 13$ for the lower (a) and the upper branch (b). The Prandtl number is 1.0 and the spanwise wave number is $k = k_{crit} = 0.4305$. The velocity is visualized by the arrows and the temperature field (divided by Ra) is represented by the colors. For both fields only the deviation from the laminar profile is shown.

are of minor important while if Ri is large, forced convection is negligible. As in the study of Gage and Reid (1968) for Rayleigh-Bénard-Poiseuille flow it is possible to give a critical value of the Richardson number which marks the transition from one kind of instability to the other. For ASBL over a heated plate we obtain a critical Richardson number (equation 10.3) of approximately $Ri^* = 19.47/(54000^2 \cdot 1.0) \approx 7 \cdot 10^{-9}$. For smaller Richardson numbers the system has an instability to transversal rolls or waves while for larger values of Ri the system has am instability to longitudinal rolls.

10.5 Nusselt numbers for secondary solutions

A common dimensionless number describing the heat flux is the Nusselt number,

$$Nu = \frac{\phi_{conv} + \phi_{cond}}{\phi_{cond}}, \tag{10.4}$$

which is usually defined as the ratio of the total heat flux $\phi_{conv} + \phi_{cond}$ to the conductive heat flux ϕ_{cond}. In the dimensionless form introduced above the covective heat flux of the base flow becomes

$$\phi_{conv} = \langle v \cdot T \rangle = -PrRa\ e^{-Pr\ y}. \tag{10.5}$$

For the conductive heat flux of the base flow of TASBL we obtain

$$\phi_{cond} = -\partial_y \langle T \rangle = PrRa\ e^{-Pr\ y}. \tag{10.6}$$

Thus, in contrast to Rayleigh-Bénard convection, the conductive heat flow of the base flow depends on the wall-normal coordinate y.

To obtain a dimensionless heat flux we will use the ratio of the total heat flux to the conductive heat flux of the base flow at the wall:

$$Nu(y) = \frac{\langle (-Pr + v)(\theta + T) \rangle - \partial_y \langle \theta + T \rangle}{PrRa}. \tag{10.7}$$

To get rid of the dependence on the wall-normal coordinate the quantity is integrated over y.

$$\tilde{Nu} = \int_0^\infty Nu(y)\ dy \tag{10.8}$$

Because for the laminar state the conductive heat flow is due to the suction compensated by conductive heat flow in the opposite direction, evaluating equation 10.7 for the base flow yields zero independent of the wall-normal position. However, for ECS as the secondary solution R_1

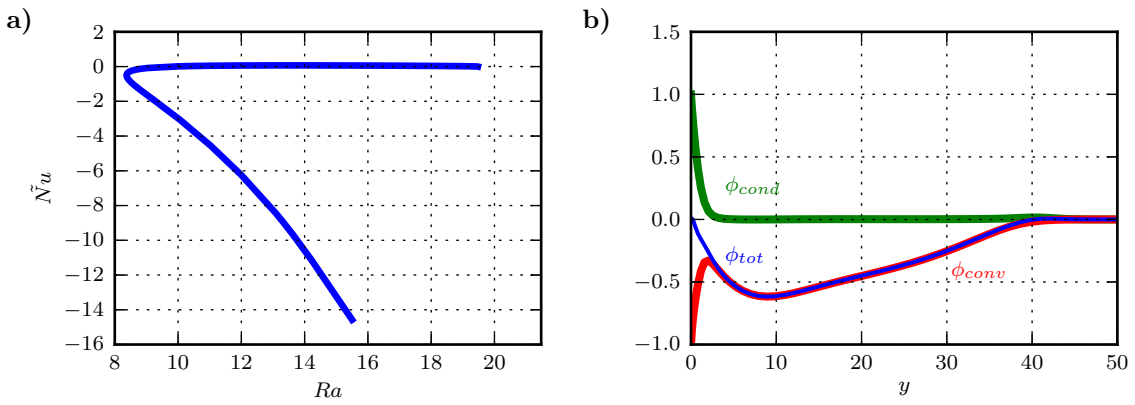

Figure 10.11: In a) the Nusselt number $\tilde{Nu}$ is shown as a function of the Rayleigh number for the secondary solution R_1 with $k = k_{crit}$ at $Re = 0$. In panel b) for the upper branch of R_1 at $Ra = 15.5$ the contributions of the conductive (green) and convective (red) heat flow are as functions of on the wall-normal coordinate y. The resulting total heat flow is shown by the thin blue line. The quantities are normalized with respect to the Rayleigh number.

the quantities $Nu(y)$ and $\tilde{Nu}$ are non-zero. In figure 10.11a the Nusselt number $\tilde{Nu}$ is shown in dependence on the Rayleigh number for the roll solution R_1 with $k = k_{crit}$ and $Pr = 1$. Especially for the upper branch, the heat transport due to convection has large negative values, leading to negative values of $\tilde{Nu}$ with large modulus. The contributions of the convective and the conductive heat transport for a state on the upper branch of R_1 are shown as function of y in figure 10.11b.

The figure shows that for the secondary solution R_1 the conductive heat transport is only relevant close to the wall and quickly drops to zero for larger values of y. Furthermore, the plot illustrates that indeed the convective heat transport causes the large negative values of $\tilde{Nu}$ (the integral over the blue curve). The reason for the negative convective heat transport is that due to the suction the wall-normal velocity is negative almost through the entire domain, while the total temperature is always positive.

Chapter 11

Tertiary solutions and turbulence

11.1 Introduction

Within the last chapter ECS bifurcating directly from the base flow were identified. In this chapter the stability of these secondary solutions is analyzed and bifurcating tertiary and quaternary solutions are tracked. Furthermore, in section 11.6 turbulent temperature profiles are computed and compared to those of the secondary solutions. In section 11.7 for non-zero Reynolds number the edge state of the system is investigated and it is shown that this state is connected to a tertiary solution of the system.

11.2 Superharmonic instabilities and transient chaos

The stability of R_1 at $Pr = 1$ and $Re = 0$ to two-dimensional, superharmonic disturbances is analyzed. The term 'superharmonic disturbances' means that the disturbances have wavelengths $\lambda = \lambda_0/N$ where λ_0 is the spatial wavelength of R_1 and N is an integer. On the practical side this is done by using *Channelflow's* Arnoldi algorithm to calculate the eigenvalues of R_1 in a computational domain with $L_x = 0.1$, $L_z = \lambda_0$ and $L_y = 40$. The resolution is $N_x \times N_y \times N_z = 4 \times 65 \times 32$.

The results show that the lower branch of R_1 is quite stable to superharmonic disturbances. For a wide range of spatial wavelengths it has only one unstable direction. This indicates that R_1 is an edge state (Skufca et al., 2006) for the two-dimensional system (at least for domain sizes that allow only for one spatial wavelength of R_1).

Slightly above the bifurcation point the upper branch of R_1 is stable. With increasing Ra the upper branch is destabilized by a supercritical Hopf bifurcation that creates a periodic orbit, PO_1. The dependence of the Rayleigh number of this Hopf bifurcation on the spatial wave number is shown in figure 11.1a. If the Rayleigh number is further increased the periodic orbit undergoes a Neimark-Sacker bifurcation which creates a stable torus. Further bifurcations then create a chaotic attractor. The bifurcation diagram, sampled by plotting maxima of $a(\vec{u}) \cdot \sqrt{L_y}$ for trajectories on the attractor, is shown in figure 11.1b. The chaotic attractor is eventually converted into a chaotic saddle by a boundary crisis bifurcation (e.g. Lai and Tél, 2011). For

$k = k_{crit}$ this happens at $Ra \approx 10.06$. Following the boundary crisis, for $Ra < Ra_{crit}$ initial conditions can be found that transiently show chaotic dynamic before they finally return to the base flow. The bifurcation cascade that eventually creates transient chaos is akin to the cases of PPF (see chapter 4), plane Couette flow (Kreilos and Eckhardt, 2012), and pipe flow (Avila et al., 2013). The main difference is that in the present case the ECS which is the starting point of the cascade originates from a bifurcation of the base flow.

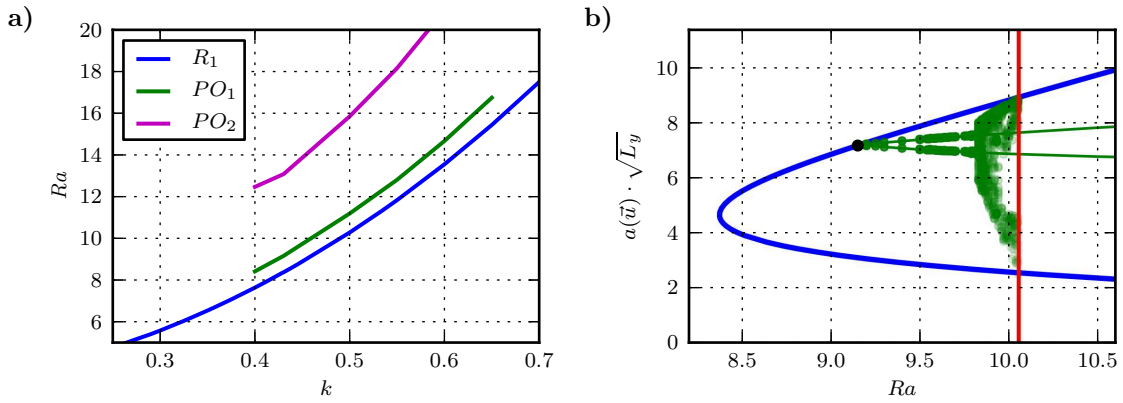

Figure 11.1: In panel a) the bifurcation curves for the periodic states PO_1 and PO_2 are shown together with a curve (blue) showing the turning point of R_1 vs. wavenumber. In panel b) the bifurcation diagram of R_1 with wavenumber $k = k_{crit}$ at $Pr = 1$ and $Re = 0$ is shown. The solution curve of R_1 is shown by a blue line. Chaotic and periodic states are indicated by green points representing minima and maxima of $a(\vec{u}) \cdot \sqrt{L_y}$ in the course of time. In addition the solid green lines show the minimum and maximum of $a(\vec{u}) \cdot \sqrt{L_y}$ for the orbit PO. The bifurcation points of R_1 and PO are marked by black circles.

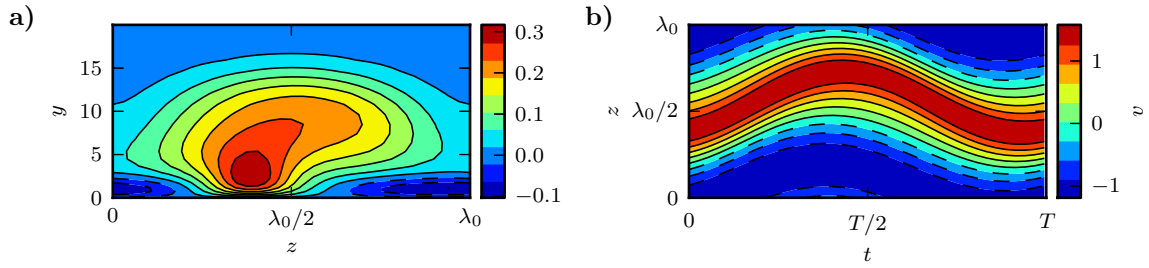

Figure 11.2: Visualization of the periodic orbit PO_1 at $Ra = 9.475$. The left panel shows the instantaneous temperature field (deviation from laminar divided by Ra) in the yz-plane. The right panel shows the wall-normal velocity in a distance of 2.7 from the lower plate in a spatio-temporal plot. The instantaneous temperature field in a) corresponds to the time $t = 0$ in b).

The orbit PO_1 is visualized in figure 11.2 using a plot of the temperature field in the yz-plane and a spatio-temporal plot of the wall-normal velocity in a distance of 2.7 from the lower plate. The temperature field reveals an asymmetry compared to the symmetric equilibrium

R_1. This asymmetry is caused by a tilt of the up-flow region compared to R_1 which varies periodically in time as the spatio-temporal plot in figure 11.2b shows.

With increasing Ra the upper branch of R_1 undergoes further Hopf-bifurcations that create further unstable periodic orbits. The stability line of a further periodic orbit PO_2 is also shown in figure 11.1a.

11.3 Subharmonic instabilities and localization

After the discussion of superharmonic instabilities of the roll solution R_1 we now analyze the stability to two-dimensional subharmonic disturbances. The term 'subharmonic disturbances' means that the disturbances have wavelengths $\lambda = N\lambda_0$ where λ_0 is the spatial wavelength of R_1 and N is an integer.

Subharmonic bifurcations involving two roll-pairs

As a first step subharmonic instabilities that incorporate two roll-pairs of R_1 are investigated. Thus, their spatial wavelength is $\lambda = 2\lambda_0$ where λ_0 is the spatial wavelength of R_1.

For $\lambda_0 = \lambda_{crit}$ two subharmonic instabilities exist quite close to the point where R_1 connects to the base flow. The tertiary solution bifurcating close to Ra_{crit}, henceforth referred to as R_{1a}, continues to lower values of Ra. Compared to two copies of R_1, in the flow structure of R_{1a} one of the two upflow regions continuously becomes weaker with increasing distance to the bifurcation point. The solution can be tracked in Rayleigh number and it shows out that the turning point lies at much lower Rayleigh number than the one of R_1. A second tertiary solution bifurcates at $Ra \approx 15.5$. This equilibrium solution extends to higher Rayleigh numbers and differs from R_1 by a weakening of one of the two down-flow regions. In figure 11.3a a bifurcation diagram containing the two tertiary solutions R_{1a} and R_{1b} and the secondary solutions R_1 is shown. The insets show visualizations of the temperature fields of the tertiary solutions.

At $Ra = 8.63$, close to the turning point of R_1, a third tertiary solution (R_{1c}) bifurcates. This equilibrium solution that continues to higher values of Ra is characterized by a tilting of the two up-flow regions in opposite directions.

The upper branch of R_1 also shows subharmonic instabilities. When increasing the Rayleigh number, the first subharmonic instability is located at $Ra = 9.02$. The tertiary solution (R_{1d}) that is created in this bifurcation continues to higher values of Ra and is characterized by two different shaped up-flow regions. A bifurcation diagram containing the two tertiary solutions R_{1c} and R_{1d} and the secondary solutions R_1 is shown in figure 11.3b. The insets show visualizations of the temperature fields of the tertiary solutions.

To ensure that up to the point of bifurcation of R_{1d} all subharmonic disturbances involving two roll-pairs have been found, the eigenvalues of R_1 in a domain with width $2\lambda_0$ are calculated for different values of Ra. The real parts of the leading eigenvalues are shown as a function of Ra in figure 11.4a.

For the bifurcations creating the states R_{1a} and R_{1b} the dependence on the wavelength of the roll-solution R_1 is studied. The bifurcation curves are shown in figure 11.4b.

Localized solutions

If we allow for longer wavelengths, many more subharmonic instabilities can be found. Especially, it is possible to identify various two-dimensional equilibrium solutions that are localized

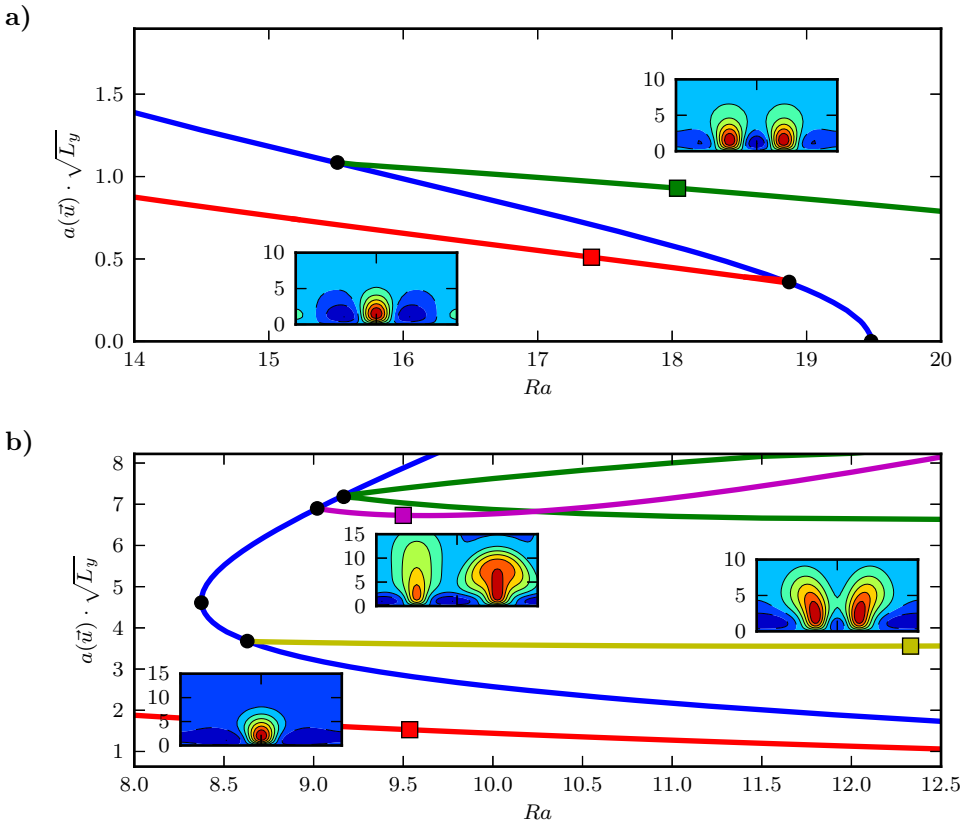

Figure 11.3: a) Bifurcation diagram for the tertiary solutions R_{1a} (red) and R_{1b} (green) bifurcating from the roll solutions R_1 (blue) with $\lambda_0 = \lambda_{crit}$. The tertiary solutions have a wavelength that is twice the wavelength λ_0 of the R_1 solution. The insets show visualizations of the temperature field for the states marked by the red and green square. The bifurcation diagram in b) contains the tertiary solutions R_{1a} (red), R_{1c} (yellow), R_{1d} (magenta) and PO_1 (green). For the states marked by the squares the temperature fields are visualized in the neighboring insets.

in one direction parallel to the plate. We will not study all of them but restrict ourselves to a family of localized equilibrium solutions that differ in the number of roll-pairs. In this subsection a domain with a width of $16\lambda_{crit}$ and a height of 40 is used. Since we are only interested in two-dimensional solutions, the length of the domain does not matter. The resolution is $N_x \times N_y \times N_z = 4 \times 49 \times 512$.

The simplest localized equilibrium that can be found consists of one single pair of convection rolls. This solution bifurcates from the spatially extended roll solution R_1 in a long-wavelength instability quite close to the point where R_1 bifurcates from the laminar state. The bifurcation that creates R_{loc1} is comparable to the one that creates PO_E in plane Poiseuille flow (see section 6.2). In figure 11.5 the genesis of this state, henceforth referred to as R_{loc1}, is illustrated by visualizations of the temperature field for different Rayleigh numbers. Close to the point where R_{loc1} bifurcates from R_1 it looks like R_1 with an overlaid modulation. With increasing distance to the bifurcation point the modulation becomes stronger and more and more convection rolls

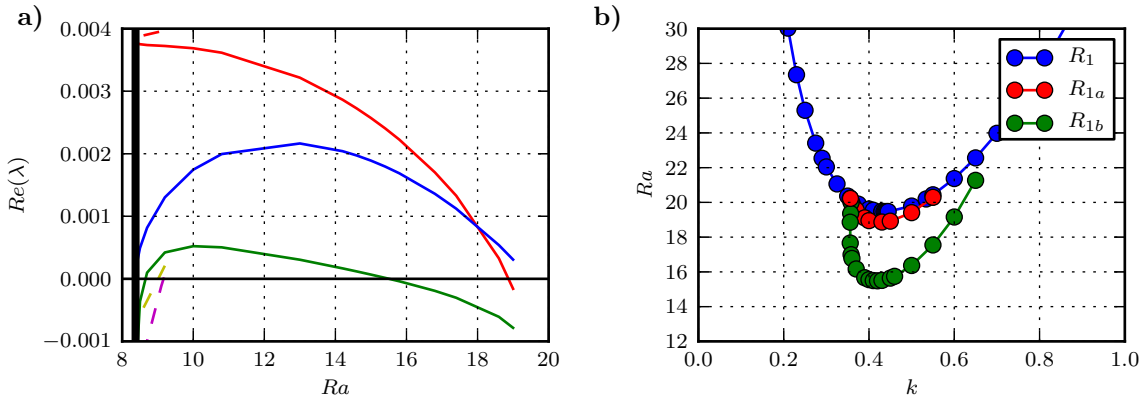

Figure 11.4: a) Eigenvalues of the lower branch of roll solution R_1 with wavelength λ_{crit} in a domain with a width of $2\lambda_{crit}$ for $Pr = 1$ and $Re = 0$. The thick black line marks the position of the turning point. Bifurcation points are marked by black circles. Solid lines and dashed lines are used for the eigenvalues of the lower and upper branch, respectively. Only eigenvalues that are unstable for some values of Ra are contained in the diagram. b) Bifurcation curve for tertiary solutions R_{1a} and R_{1b} bifurcating from the roll solutions R_1. The solutions have a spanwise wavelength that is twice the wavelength λ_0 of the R_1 solution.

disappear, until only one is left. The state R_{loc1} is tracked to lower Rayleigh numbers using a continuation method. It is found that its turning point lies at $Ra \approx 3.5$. The stability properties of R_{loc1} are remarkable. Down to its turning point it has one unstable direction and the upper branch is stable to two-dimensional disturbances at least for $Ra < 4.4$.

In addition to R_{loc1} further localized equilibrium solutions exist. Most easily they can be found using the window-functions proposed by Gibson and Brand (2014). The roll solution R_1 with wavelength λ_0 in a domain with a length that is an integer multiple of λ_0 is overlaid by the window-function

$$W_1(z) = \frac{1}{4}\left(1 + \tanh\left(\frac{6(a-z)}{b} + 3\right)\right)\left(1 + \tanh\left(\frac{6(a+z)}{b} + 3\right)\right). \tag{11.1}$$

The constructed flow fields are used in a Newton-search for an equilibrium solution as an initial guess. For appropriate choices of the parameters a, b and of the Rayleigh number the Newton-searches converge to localized exact solutions.

In figure 11.6 a family of equilibrium solutions obtained for $Ra = 18.04$ is visualized. The solutions differ in the number of pairs of convection rolls. Similar localized ECS of different size have been found for plane Couette flow by Schneider et al. (2010a), binary convection by Batiste et al. (2006), rotating convection (Beaume et al., 2013), doubly-diffusive convection (Bergeon and Knobloch, 2008) and magnetohydrodynamics convection (Lo Jacono et al., 2011).

The solution branches are tracked in the Rayleigh number and the resulting bifurcation diagram is shown in figure 11.7. The solution branches on which the states with four, six, and eight roll-pairs can be found do not connect as in the case of homoclinic snaking (for a comprehensive review see Knobloch, 2015).

Nevertheless, comparable to the snaking or pinning region in systems showing snaking a region in Rayleigh number can be identified where states with different numbers of rolls can

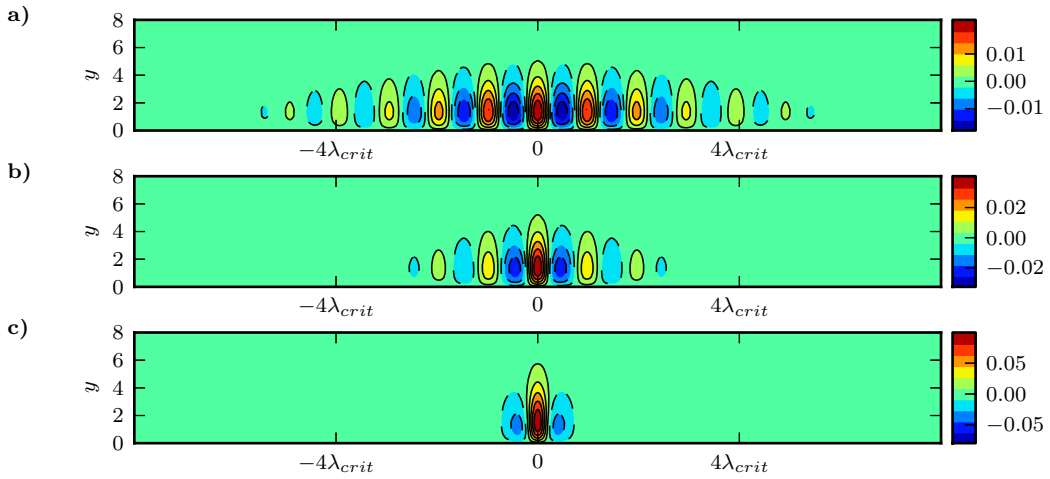

Figure 11.5: Genesis of localized equilibrium solution consisting of a single roll-pair. The Prandtl number is 1 and the Reynolds number is 0. The Rayleigh numbers for a), b) and c) are 19.35, 19.10 and 16.5, respectively. The plots show the color-coded temperature field of the exact solutions.

exist. For the studied set of parameters this region of coexistence is approximately between $Ra = 16.9$ and $Ra = 19.5$.

11.4 Plume-like motion along unstable directions

In the introduction in chapter 9 it was mentioned that the understanding of thermal plumes is of enormous importance for the understanding of thermal boundary layers. None of the time-dependent ECS that could be identified shows a dynamic that resembles a thermal plume. In particular, they only show a modulation or tilting of the convection rolls and nothing like an ejection of hot fluid out of the boundary layer. But as will be shown in this section, plume-like dynamic can be found on trajectories that depart from an exact solution along its unstable direction.

The lower branch of the roll solution R_{loc1} is localized in one direction parallel to the wall and only weakly unstable because it has only one unstable direction. A trajectory that starts at the slightly disturbed equilibrium remains in its vicinity for some time before it leaves and is attracted by the "turbulent" state. When the trajectory leaves the equilibrium a plume-like structure develops in its temperature field. Visualizations of the temperature field for various times are shown in figure 11.8. The time trace of the amplitude $a(\vec{u})$, where the positions of the temperature visualizations are marked, is shown in figure 11.9.

The mushroom-like plume grows quickly in height and width. The position of the top of the plume is also identifiable in the temperature profiles (base profile plus deviations) that are shown in figure 11.9b for different times. Using a threshold in the total temperature of 0.01 it is possible to define the top of a plume. The obtained positions of the tops are marked in the figure using red squares. Having a criterion to identify the top of the plume, it is feasible to quantify the growth of the plume. The temporal development of the plume height in shown in figure 11.9c for different values of Ra. The speed of the plume head depends on the Rayleigh number. For lower values of Ra it is lower than for higher ones.

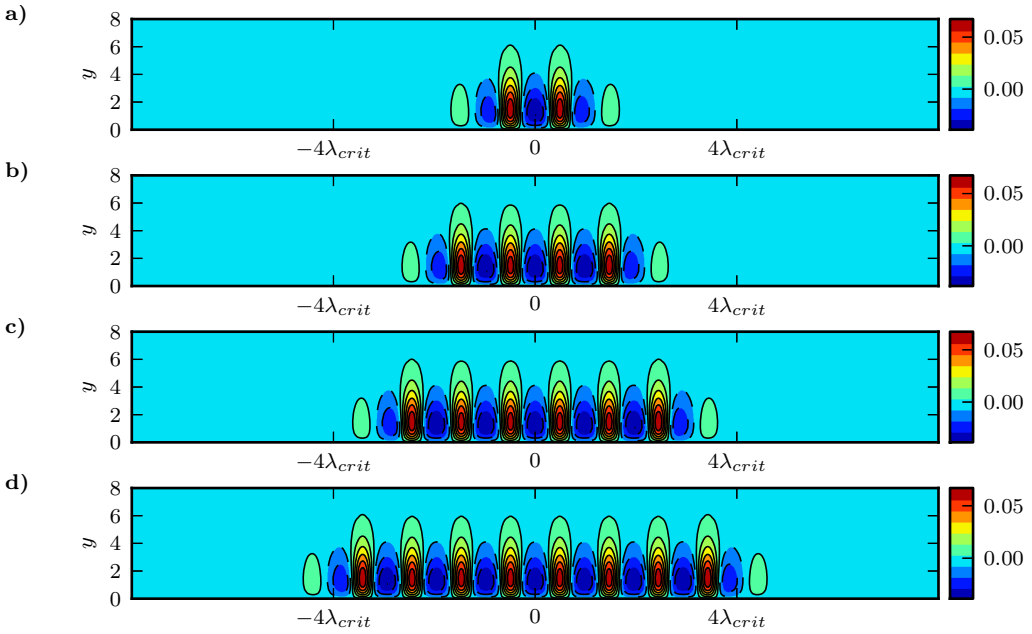

Figure 11.6: Visualizations of localized, two-dimensional equilibrium solutions for $Ra = 18.04$ and $Pr = 1$ with different numbers of roll-pairs. The plots show the color-coded temperature field of the exact solutions.

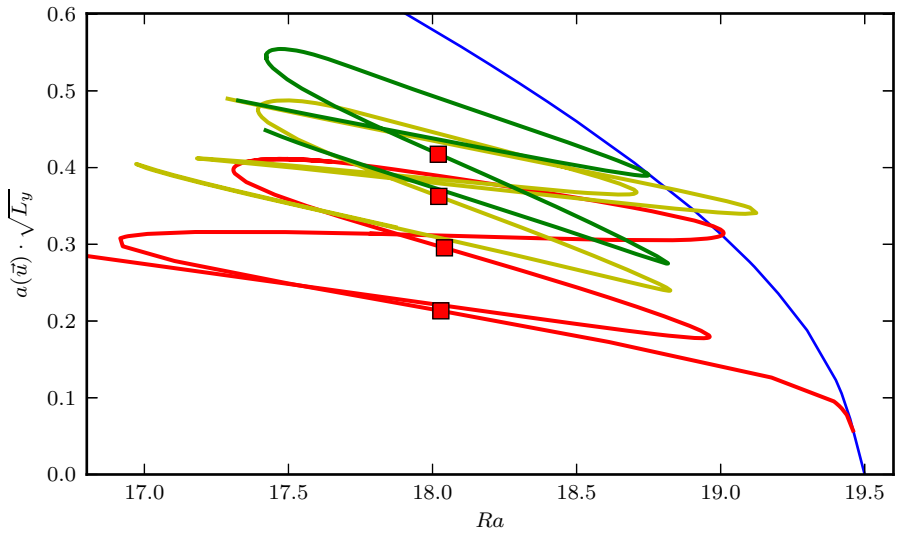

Figure 11.7: Bifurcation diagram in a wide computational domain with $L_z = 16\lambda_{crit}$. The states visualized in figure 11.6 are marked by squares. For the solution branches obtained by continuations starting at a state with eight, six and four rolls green, yellow and red lines are used. The light blue line shows the solution branch of the spatially extended roll-solution R_1 with a spatial wavelength $\lambda = \lambda_{crit}$

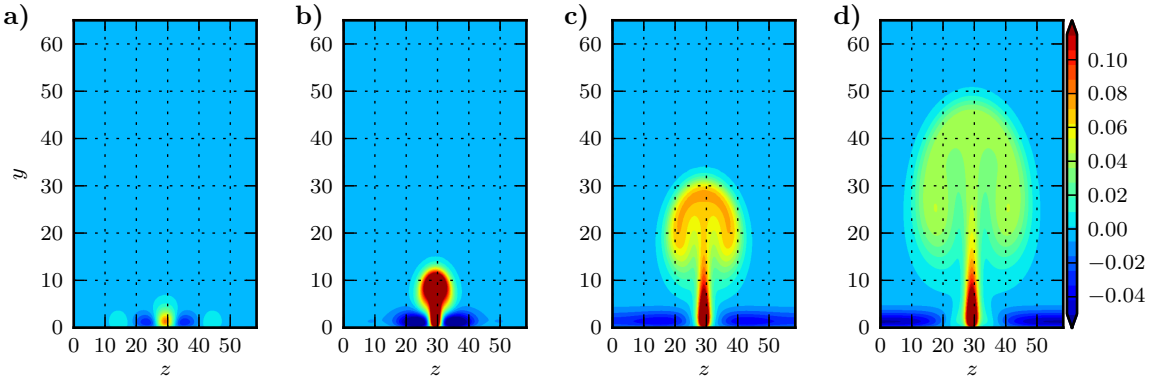

Figure 11.8: Instability of the secondary solution R_{loc1}. The Rayleigh number is 19 and therefore below Ra_{crit}. The panels a) - d) show the temperature field at different times. The positions of the visualization on a trajectory are marked in figure 11.9a).

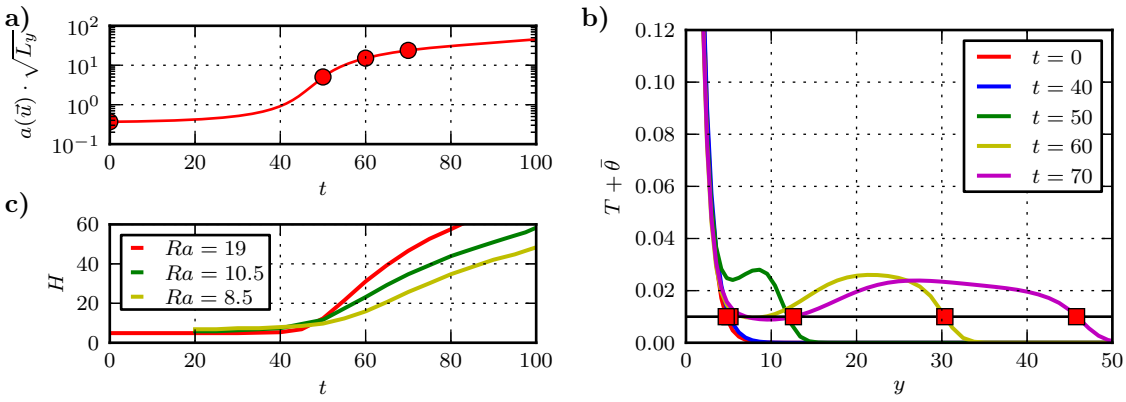

Figure 11.9: Panel a) shows the time evolution of $a(\vec{u}) \cdot \sqrt{L_y}$ of the velocity field for a trajectory starting at the disturbed equilibrium R_{loc1}. For the times marked by the red squares visualizations of the temperature field are given in figure 11.8. In panel b) the profiles of the temperature field for various positions on the trajectory are shown. The red squares mark the height of the plumes. In c) the height of the plume is shown as a function of the time for different Rayleigh numbers.

11.5 Fully localized solutions

In section 11.3 roll solutions localized in one direction parallel to the plate were identified that are bifurcations of the spatial extended roll solution R_1. Using this two-dimensional equilibrium solutions it is easily possible to construct initial guesses for three-dimensional, doubly-localized ECS.

In a computational domain with $L_x = L_z = 87.6$ we take the localized roll solution R_{loc1} consisting of one pair of rolls (figure 11.5c). We align one of the solutions along the x-axis and the other one along the z-axis. We add both solutions and multiply the resulting field with a function of form

$$W_2(x, y, z) = A \exp\left(-B(x^2 + z^2)\right) \tag{11.2}$$

where we choose a coordinate system with its origin in the center of the computational domain. The flow field obtained by the procedure, that is similar to the windowing method of Brand and Gibson (2014), is used as initial guess in a Newton-search for an equilibrium solution. For appropriately chosen values of A and B the Newton-method indeed converges to a doubly-localized equilibrium solution. The equilibrium solution is visualized in figure 11.10a for $Ra = 17$ using iso-surfaces of the wall-normal velocity v. The figure shows that the state is rotationally symmetric and has a strong up-flow region in its center. For such a simple localized convection state (also if only localized in one spatial direction) the term *convecton* has become widely spread (e.g. Blanchflower, 1999; Lo Jacono et al., 2011; Beaume et al., 2013). Adopting this notation, we will call the doubly-localized equilibrium a convecton and use the abbreviation C_1.

Tracking the equilibrium in Ra we can continue it to its bifurcation point and identify its upper branch. The resulting bifurcation diagram is shown in figure 11.10b. A stability analysis reveals that the lower branch has one unstable direction and the upper branch is, just as the solutions R_1 and R_{loc1}, stable right after the bifurcation point. But in contrast to these ECS, C_1 is stable in the full three-dimensional system. Therefore, it could actually be found in an experimental realization of TASBL. If the lower branch is tracked to higher values of Ra it connects to a spatially extended three-dimensional equilibrium solution. The plots of the wall-normal velocity in figure 11.10c illustrate how the convecton connects to the spatially extended pattern. The localized state discussed in the previous section and also those discussed in sections 6.2 and 6.5 are created in long-wavelength instabilities involving one spatial direction. For the spatially extended pattern at $Re = 0$ both directions parallel to the plate are equivalent, thus two long-wavelength instabilities involving both spatial directions can occur simultaneously and create the convecton. In figure 11.11 the energy densities of the three velocity components are shown for C_1 at $Ra = 17.4$. The plot reveals that all components decay exponentially over several orders of magnitude.

In addition to C_1 is is possible to find other doubly-localized solutions using Newton's method. Appropriate initial guesses for Newton-searches can be constructed using spatially extended solutions and the window function W_1 used by Gibson and Brand (2014) and given in equation 11.1 or the above defined function W_2, which is more appropriate for searching states with rotational symmetry. A third quite successful strategy is to use several convectons C_1 as building blocks to construct initial guesses.

Various flow patterns of equilibriums solutions are shown in the figures 11.12 and 11.13. All equilibrium solutions visualized in figure 11.12 are obtained with initial guesses that use the window function W_2. The state in 11.13d is obtained from an initial condition constructed

using the window function W_1. For all remaining states shown in figure 11.13 the initial guesses are constructed by combining multiple solutions of type C_1.

Although they might also exist in binary fluid convection or other hydrodynamic systems with subcritical instabilities, up to now there is only one investigation of doubly-localized patterns in a fluid system with two equivalent spatial directions[1]. The sole example of doubly-localized patterns in a fluid is described in a recent paper by Lloyd et al. (2015). For a polarizable fluid that undergoes the subcritical Rosenzweig instability, they study localized states that show two-dimensional snaking. The visualization of their states look qualitatively similar to the states found for TASBL. However, despite of the visual similarity the physical mechanism leading to the formation of the patterns is completely different since the Rosenzweig instability is related to the surface of the polarizable fluid.

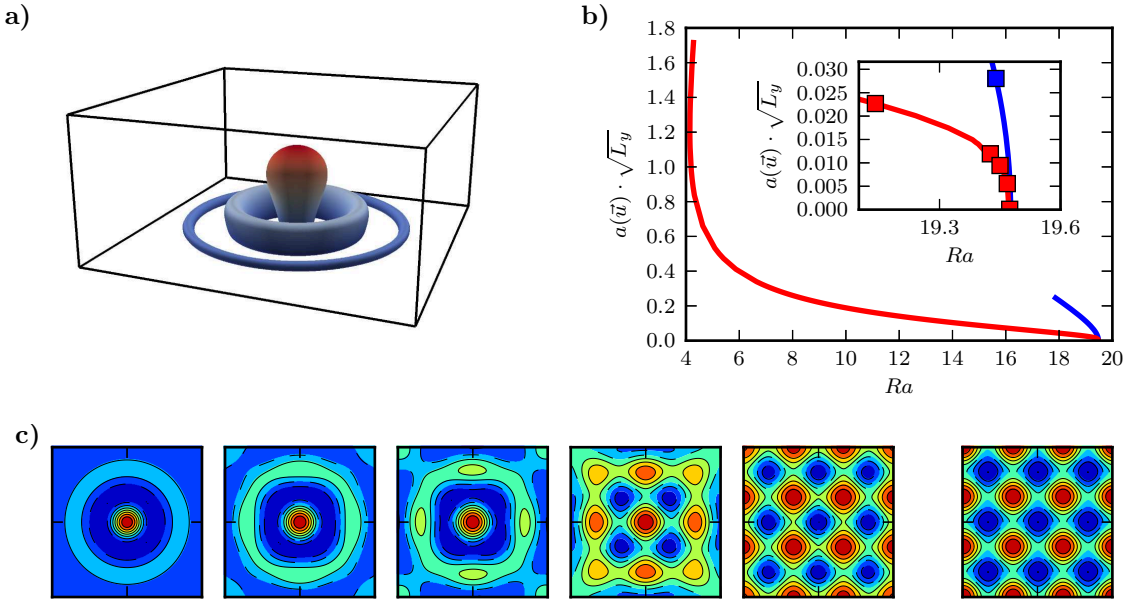

Figure 11.10: In panel a) the iso-surface $v = 0.0005$ is shown for the doubly-localized equilibrium at $Ra = 17.0$, $Re = 0$ and $Pr = 1$. The iso-surface is colored according to the distance to the plate from blue to red. Panel b) shows the bifurcation diagram for the doubly-localized equilibrium solution C_1 (red) and the spatially extended equilibrium (blue). The inset in b) shows the bifurcation diagram close to the point where C_1 connects to the spatially extended pattern. The states marked with the red squares in the insets are visualized in c). The plots show the wall-normal velocity v in a plane parallel to the plate in a distance of 1.5. The leftmost picture corresponds to the red square at the lowest Rayleigh number. The rightmost panel in c) shows the wall-normal velocity v for the state marked in b) by the blue square.

[1] Of course, there are doubly-localized ECS for plane Couette and plane Poiseuille, but in these flows spanwise and streamwise direction are not equivalent.

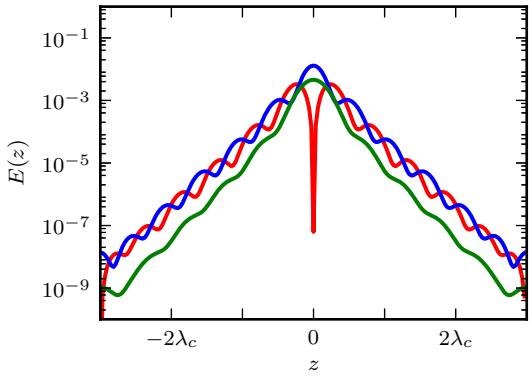

Figure 11.11: Energy densities for the streamwise (red), spanwise (green) and wall-normal velocity component for a convecton C_1 at $Ra = 17.4$. For all velocity components the decay is exponential.

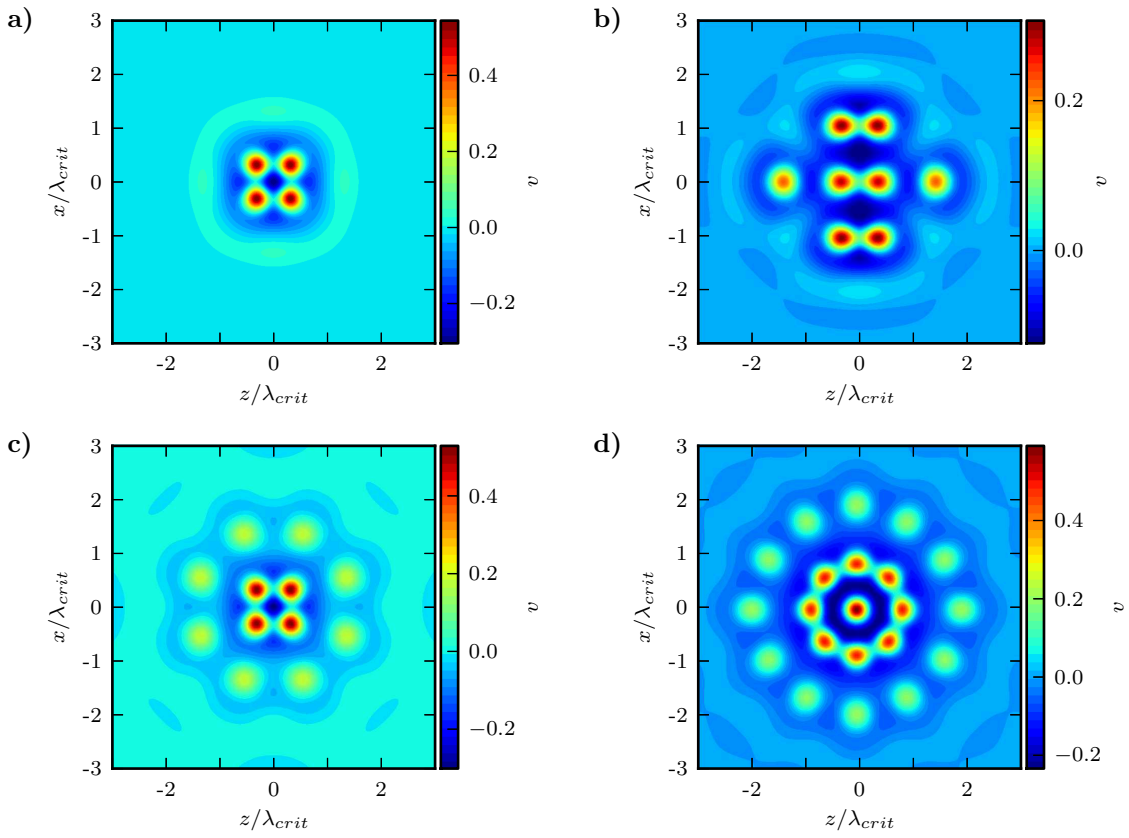

Figure 11.12: Doubly-localized solutions at $Ra = 17.8$. The Prandtl number is 1 and the Reynolds number is 0. The pictures show the wall normal velocity in a plane parallel to the lower plate at $y \approx 1.5$.

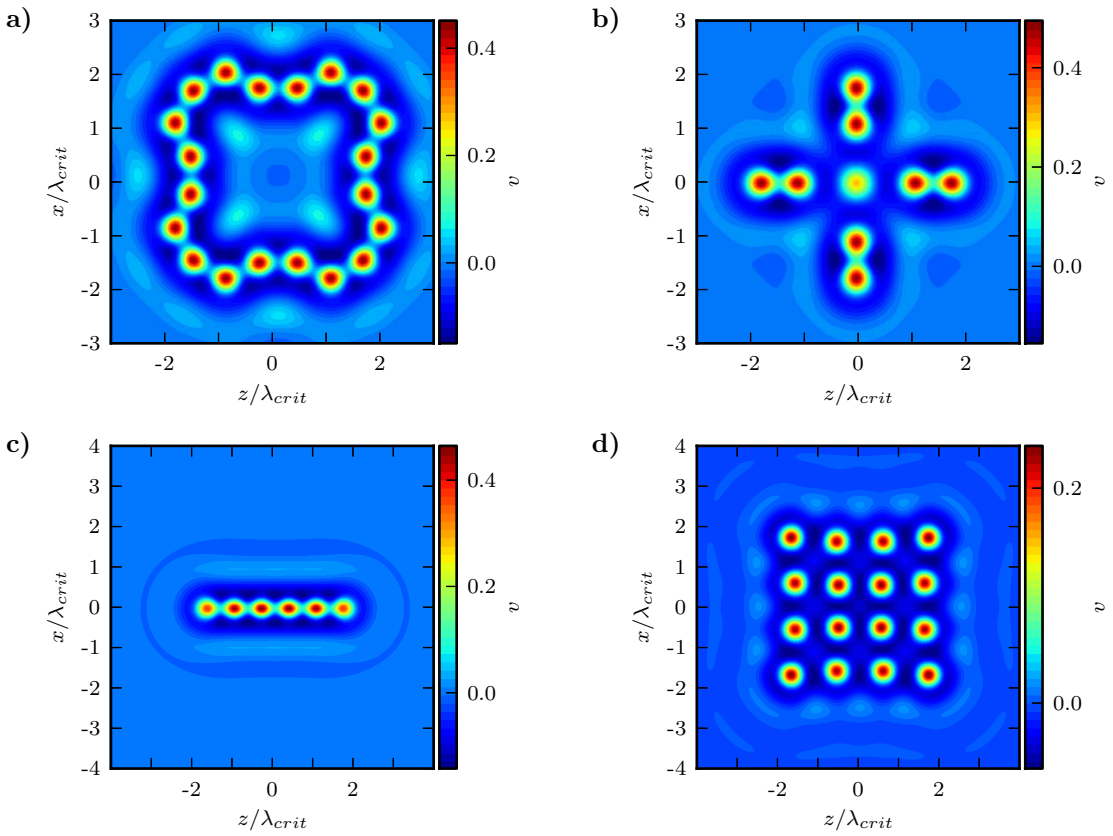

Figure 11.13: Doubly-localized solutions for $Re = 0$ and $Pr = 1$. The Rayleigh number is $Ra = 17.6$ for a) and $Ra = 17.5$ for b)-d). The pictures show the wall normal velocity in a plane parallel to the lower plate at $y \approx 1.5$.

11.6 Mean turbulent profiles

In this section the mean profiles of turbulent TASBL are studied. The focus is on two-dimensional TASBL. As sufficient approximation to two-dimensional TASBL, we simulate the three-dimensional flow with a small value of the spanwise extend L_z of the domain and only 4 modes in spanwise direction. In figure 11.14 the instantaneous streamwise vorticity is shown for turbulent states at different Rayleigh number and different length of the computational domain. For $Ra = 20$ and $L_x = 14.6$ (figure 11.14a) the dynamics is restricted to areas with $y < 20$. At a higher Rayleigh number of 40 (figure 11.14b) the flow extends to larger values of y and the complexity of the vorticity pattern increases. If the Rayleigh number is kept constant and the domain width is increased the flow does also extend to regions farer away from the plate. As figure 11.14c shows, a doubling of the domain length doubles the height of the flow structures. The observed increase of the height of the flow structures with increasing domains size was also observed by Schlatter and Örlü (2011) in their simulations of iso-thermal ASBL.

To quantify the dependence of turbulence in TASBL on Rayleigh number and domain size, mean profiles of the temperature are regarded. To obtain mean profiles, the turbulent profiles are sampled and averaged over several hundred viscous time units. Parameter values for the performed simulation are shown in table 11.1.

Examples of profiles of the total temperature are given in in figure 11.15a. In addition to mean profiles of turbulent states, the figure contains temperature profiles of the upper branch of R_1 for comparison. The mean profile for $Ra = 10$ in the subcritical range is generated by the stable chaotic state identified and discussed in section 11.2.

For small values of y all profiles show a steep decrease. Especially, for $y < 1$ all profiles are almost identical. They start to deviate for $y > 1$, where the steep decrease is replaced by a

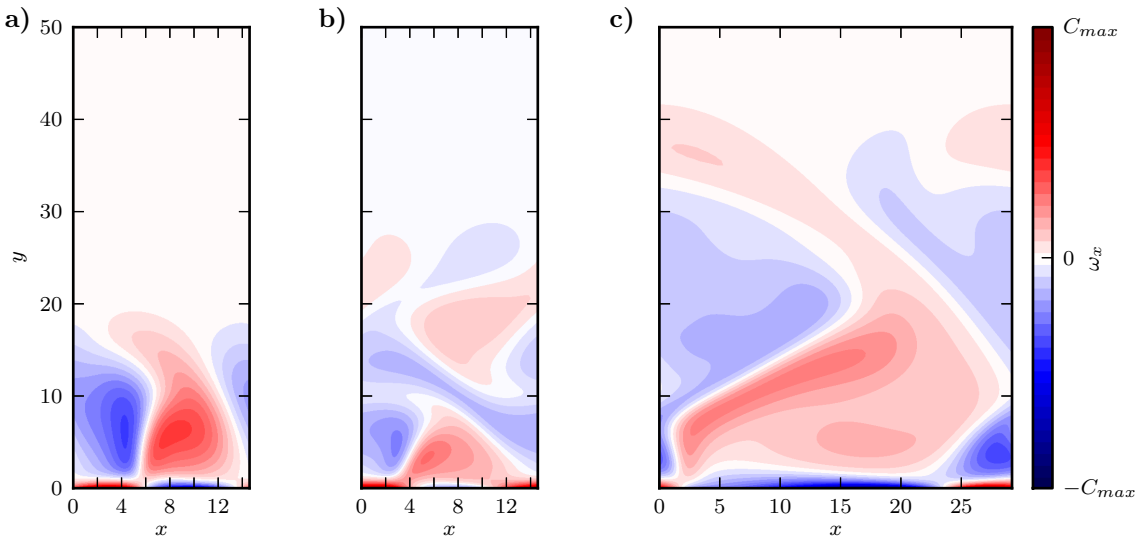

Figure 11.14: Instantaneous streamwise vorticity ω_x for the two-dimensional TASBL. The Reynolds number is 0 and the Prandtl number is 1.0. The Rayleigh numbers are 20.0 a), 40.0 b) and 20 c). The streamwise lengths of the computational domains are 14.6 for a) and b) and 29.2 for c) .

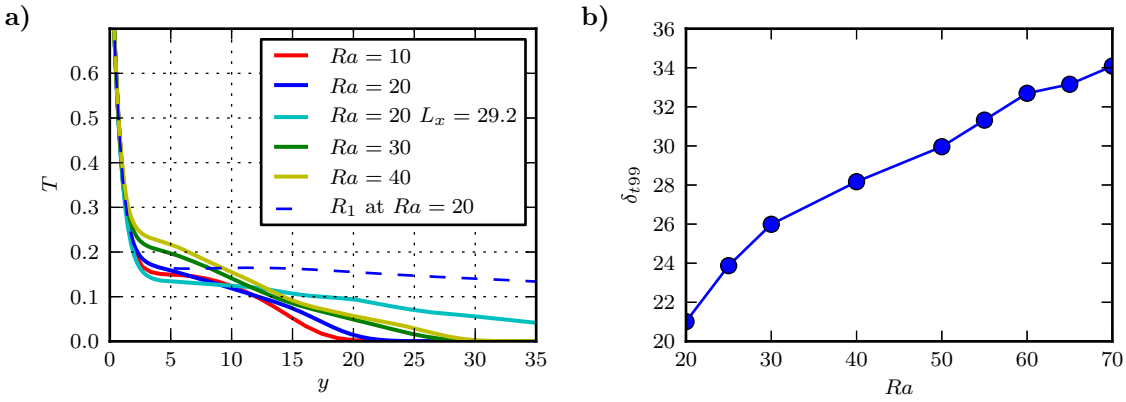

Figure 11.15: In a) mean turbulent temperature profiles for two-dimensional TASBL are shown for different values of Ra and L_x. In b) the dependence of δ_{t99} for $L_x = 14.6$ on the Rayleigh number is shown.

slower decrease that depends on Ra and the domain size.

Ra	Domain Size	Resolution	δ_{t99}
20	$14.6 \times 100 \times 0.1$	$96 \times 321 \times 4$	20.61
20	$29.2 \times 100 \times 0.1$	$192 \times 321 \times 4$	41.2102
25	$14.6 \times 100 \times 0.1$	$96 \times 321 \times 4$	23.89
30	$14.6 \times 100 \times 0.1$	$96 \times 321 \times 4$	25.9984
40	$14.6 \times 100 \times 0.1$	$96 \times 321 \times 4$	28.1795
50	$14.6 \times 100 \times 0.1$	$96 \times 321 \times 4$	29.9626
60	$14.6 \times 100 \times 0.1$	$96 \times 321 \times 4$	32.69
65	$14.6 \times 100 \times 0.1$	$96 \times 321 \times 4$	33.16
70	$14.6 \times 100 \times 0.1$	$96 \times 321 \times 4$	34.09

Table 11.1: Parameters for the simulations of turbulent two-dimensional TASBL.

As a measure for the height of the profile we use, as in section 11.4, the position where the temperature profile drops below 0.01 (one percent of the plate temperature). The obtained heights which we want to abbreviate δ_{t99} are given given in table 11.1 for the different simulation runs.

For $Ra = 20$ the calculated values of δ_{t99} double from 20.6 to 41.21 if the domain length is doubled, what confirms the visual impression from the vorticity plots.

As shown in figure 11.15b, δ_{t99} grows with increasing Rayleigh number. For all investigated values of Ra the value of δ_{t99} for the turbulent state lies below the value of δ_{t99} for the upper branch of the state R_1 for the same domain size. Thus, the strongly unstable upper branch solutions are of minor importance for turbulence in the thermal boundary layer.

11.7 The edge-of-chaos for finite *Re*

For the case of isothermal ASBL the attractors embedded within the laminar-turbulent boundary were extensively studied (Kreilos et al., 2013; Khapko et al., 2013, 2014). It was found that the attractor in the edge-of-chaos, the edge state, is a periodic orbit with a very large period. The edge state is characterized by long periods in that the shape of the state remains unchanged and short bursts that intermit the long quiet periods. Thus, they are dynamically very similar to the periodic orbits of PPF discussed in section 3.3.

For a computational domain with a streamwise wavelength $L_x = 4\pi$ and a spanwise wavelength $L_z = 2\pi$, which is the domain size used by Kreilos et al. (2013), we investigate the behavior of the edge state with increasing Rayleigh number. The edge state is continued in Ra using edge tracking. For a fixed Reynolds number of 400 an increase of the Rayleigh number causes an increase of the period of the edge state. Furthermore, the streamwise modulation of the state becomes weaker. The period diverges at $Ra \approx 28.7$ where a three-dimensional traveling wave appears in a saddle-node like bifurcation. If Ra is further increased the upper branch of the traveling wave becomes more two-dimensional and finally it connects to the two-dimensional roll solution R_1 originating form the thermal instability of the base flow.

In the bifurcation diagram in figure 11.16 the three states, the periodic state, the three-dimensional traveling wave, and the equilibrium R_1, are shown. The bifurcation creating the periodic state when the traveling wave disappears is a so-called SNIPER-bifurcation (Tuckerman and Barkley, 1988; Abshagen et al., 2005; Kreilos et al., 2013).

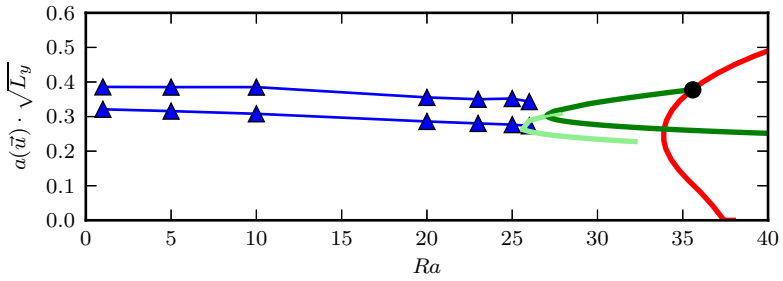

Figure 11.16: Bifurcation digram of edge state in dependence on the Rayleigh number. The Reynolds number is 400. For $Ra < 28.7$ the edge state is a relative periodic orbit. The minima and maxima values of $a(\vec{u}) \cdot \sqrt{L_y}$ are shown using blue triangles. The three-dimensional traveling wave that bifurcates from the roll-solution is shown for $Re = 400$ (green) and $Re = 1000$ (light green). The two-dimensional roll-solution is shown for $Re = 400$ using a solid red line.

When Re is increased the periodic state disappears at a lower value of Ra and the traveling wave extends down to lower values of Ra. As an examples, for the case $Re = 1000$ the solution curve of the traveling wave (light green) is shown in figure 11.16.

The results show that the edge state of iso-thermal ASBL can be connected to a bifurcation of the roll-solution originating from the thermal instability. For plane Couette flow the situation is quite similar. The edge state of iso-thermal plane Couette flow is the so-called NBC-solution (Schneider et al., 2008; Kreilos and Eckhardt, 2012) which was shown to connect to the thermal instability by Clever and Busse (1992).

Chapter 12

Summary of the results for the asymptotic suction boundary layer

At the end of this second part of my thesis the main findings are summarized and open questions as well as possible tasks for future work are pointed out.

Stability of the base flow and secondary solutions

The stability analysis of the base flow of the system revealed a subcritical instability at finite Rayleigh number. The critical Rayleigh number and wavelength depend on the Prandtl number. For a Prandtl number of 1.0 we obtain a critical Rayleigh number of 19.47. Increasing the Prandtl number increases this value, while decreasing it lowers the critical Rayleigh number. The critical Rayleigh numbers for the second unstable mode of the base flow are more than a factor of ten higher than for the first mode.

The secondary solutions that bifurcate from the base flow were tracked to their turning points and the upper branches were identified. While on the lower branch the wall-normal size of the flow structures is nearly constant, on the upper branch the states grow in height with increasing Rayleigh number.

In future studies the obtained critical wavelength and Rayleigh number could be compared to typical spacings of plumes in the thermal boundary layers that develop in Rayleigh-Bénard convection. Furthermore, the cloud-streets occurring in the atmospheric boundary layer are a possible real-life phenomenon the results could be compared to.

Tertiary solutions and subcritical turbulence

A stability analysis of the secondary solutions in a two-dimensional subspace revealed different superharmonic and subharmonic bifurcations. For the lower branch no superharmonic instabilities could be detected, but the upper branch shows several of them that create time periodic states. The further bifurcations of the periodic state bifurcating at lowest Rayleigh number were tracked and it was found that they create a chaotic attractor (attracting in small two-dimensional domains). Analogous to the case of PPF (see Zammert and Eckhardt, 2015b or

section 4.3), plane Couette flow (Kreilos and Eckhardt, 2012) and pipe flow (Avila et al., 2013), the attractor is transformed into a chaotic-saddle by a boundary crisis bifurcation which is a further evidence that this is the universal way how subcritical turbulence is generated.

Localized exact coherent states

The study of subharmonic bifurcations of the secondary roll solution R_1 for $Re = 0$ and $Pr = 1$ yielded several equilibrium solutions that are localized in one direction perpendicular to the plate. One of the localized states (R_{loc1}) that consists of a single roll-pair exists down to low values of Ra and has an upper branch that right after its appearance is stable to two-dimensional disturbances. Unfolding the further bifurcations of this upper branch and the possible creation of a spatially localized chaotic-saddle is not yet done because of the high computational costs.

In addition to the equilibrium state R_{loc1}, a class of localized two-dimensional states was found which differ in the number of roll-pairs and exist for a relatively narrow range in Rayleigh number. Comparable ECS in other fluid system, e.g. binary fluid convection (Batiste et al., 2006) or plane Couette flow (Schneider et al., 2010a), are connected by snaking bifurcations. At least for the set of parameters studied here, for ASBL over a heated plate the states are not connected by a proper snaking bifurcation. Future studies could address this family of localized states and study if snaking can be observed if the Prandtl or Reynolds number are changed or maybe if an upper wall is added. Furthermore, it could be checked if snaking exists if three-dimensional instead of two-dimensional states are regarded.

In addition to the two-dimensional localized solutions, some three-dimensional equilibrium solutions that are localized in both direction parallel to the plates were found. The simplest is rotational-symmetric and appears in a saddle node bifurcation at $Ra \approx 4.15$. For $Pr = 1$ and $Re = 0$ its upper branch is stable in the full three-dimensional space. As the state R_{loc1} and some ECS of PPF, this localized state bifurcates from a spatially extended equilibrium solution in a long-wavelength instability.

Plume-like dynamic

A motivation for the study of the ASBL over a heated plate is to use it as a model system for the dynamics inside of the boundary layers that occur e.g. in Rayleigh-Bénard convection. It was found that dynamics comparable to plumes can exist along unstable directions of ECS. Since the relevant ECS can be tracked easily to other values of Ra, these findings provide a systematic approach to study the dynamics of plumes in TASBL. The results show that the speed of the ejected hot fluid is approximately constant for some time and increases with the Rayleigh number. The influence of Prandtl and Reynolds number and of the domain size have not been studied yet and are an issue for future research.

Turbulent profiles

The turbulent states found in TASBL have a large extend in wall-normal direction. It was found that their height grows with the Rayleigh number and depends massively on the domain size. For all studied parameter sets the mean turbulent profile was less high than the upper branch of the roll solution. In general, the difference in height was enormous. Thus, the upper branch of the secondary roll-solution is of minor importance for turbulence in TASBL. Nevertheless, the bifurcating tertiary solutions are important for the generation of turbulence and thus for the profiles.

The influence of the Reynolds number on the turbulent profile has not bee studied yet and is an issue for further studies. Furthermore, up to now the sampling in Rayleigh number is rather coarse. A calculation of the height with a finer resolution in Ra could possibly reveal discontinuities that are caused by the appearance of further chaotic saddles.

Chapter 13

Comparison of the systems and concluding remarks

The two parts of this thesis show that, although the flows are quite different, plane Poiseuille flow and the asymptotic suction boundary layer over a heated plate have many features in common. The laminar states of both systems become unstable if a critical Reynolds or Rayleigh number is exceeded. In both systems, as in many others such as pipe or plane Couette flow, the Reynolds or Rayleigh numbers for the instability of the base flow do not coincide with those of the onset of turbulence which are considerably lower.

It was found that the occurrence of subcritical turbulence in both systems can be explained by a bifurcation cascade that starts at an exact coherent structure and forms a chaotic attractor. Eventually, the attractor is turned into a chaotic saddle by a boundary crisis bifurcation. In consideration of the fact that this scenario has also been found in plane Couette and pipe flow, it appears to be the generic mechanism to generate subcritical turbulence. However, up to now it was not possible to find evidences for this mechanism in experiments. The numerical simulations of the system without symmetry constraint in section 4.3 suggest that for plane Poiseuille flow it might be extremely difficult to identify the formation of the attractor and the crisis bifurcation in experiments. But the simulations of ASBL over a heated plate in section 11.5, in particular the identification of a stable localized solution in the full system, show a possible way to experimentally detect the formation of an attractor in an subcritical system.

For plane Poiseuille flow, the exact coherent structures forming the scaffold of the subcritical turbulence are dominated by streamwise vortices and are not connected to the laminar state. On the other hand, the base flow becomes unstable to spanwise rolls, the Tollmien-Schlichting waves. This discrepancy causes the presence of two different paths for the transition to turbulence. For the asymptotic suction boundary layer over a heated plate at $Re = 0$ the exact solutions related to subcritical turbulence are connected to the instability of the base flow. Thus, the subcritical edge state and the unstable mode of the base flow have a similar flow structure. With respect to varying Reynolds numbers, TASBL shows the same behavior as PPF because the base flow becomes unstable to transversal waves for high Reynolds numbers (see section 10.2 or e.g. Hocking 1975).

For plane Poiseuille as well as for TASBL it was possible to identify spatially localized exact solutions. Two different mechanisms for the emergence of localized states were observed. One mechanism is the spontaneous localization that occurs in PPF for the states TW_E and PO_E if they are continued in domain width. The mechanism was also reported by Chantry and Kerswell (2015) for a shear-flow model.

Another mechanism to generate localized exact solutions is by long-wavelength instabilities of spatially extended solutions (see also Melnikov et al., 2014). Examples for this mechanism are the creation of localized TS-waves and of the streamwise localized orbit PO_E in plane Poiseuille flow and the emergence of the localized roll solution R_1 in TASBL.

For both systems it was possible to find exact solutions localized in two directions parallel to the plates. The doubly-localized state in PPF (section 6.2 and 6.3) is generated by a combination of a long-wavelength instability in streamwise direction and spontaneous localization in spanwise direction. In TASBL the localized convection state C_1 (section 11.5) is created in two long-wavelength instabilities that occur simultaneously for both directions parallel to the plate.

In the tails of localized states, an exponential decay can be seen over some range. In the far tails of the doubly-localized state in PPF the decay follows a power-law due to the decay of the large-scale flow. For the doubly-localized states C_1 in TASBL the velocity components decay exponentially in all directions. In this case, since the Reynolds number is zero, there is no flow around the structure that leads to a formation of a large-scale flow. Because the large-scale flow is absent, for this doubly-localized structure only the exponential decay is visible.

In this thesis the occurrence of subcritical turbulence in both systems could be explained by the identification of a bifurcation cascade that leads to the formation of a chaotic saddle. It was also possible to identify localized exact solutions for both systems as well as the mechanism that creates such solutions. With the goal to understand the spatio-temporal character of turbulence close to its onset, the main task for future work is to investigate the formation of chaotic saddles starting from localized exact solutions and to study the interplay and possible mergings of different coexisting saddles in the state space.

Appendix A

Numerical methods

A.1 Channelflow and temperature

For the study of ASBL over a heated plate the Channelflow-code (Gibson, 2012) was adapted to integrate the following coupled equations:

$$\partial_t \vec{u}_{tot} + (\vec{u}_{tot} \cdot \nabla)\vec{u}_{tot} = -\nabla p_{tot} + \nu \Delta \vec{u}_{tot} + \beta g \vec{e}_2, \theta_{tot} \tag{A.1}$$

$$\nabla \cdot \vec{u}_{tot} = 0, \tag{A.2}$$

$$\partial_t \theta_{tot} + (\vec{u}_{tot} \cdot \nabla)\theta_{tot} = \kappa \Delta \theta_{tot}. \tag{A.3}$$

The velocity field is calculated as in the iso-thermal case. The coupling of the temperature field on the velocity field is incorporated in the nonlinear part that is treated explicitly in the code.

The time integration of the temperature field is analogous to that of the velocity field. The total velocity field $\vec{u}_{tot}$ as well as the total temperature θ_{tot} can be written as a sum of the base profile and deviations:

$$\theta_{tot}(\vec{x}) = \theta(\vec{x}) + T(y) \tag{A.4}$$

$$\vec{u}_{tot}(\vec{x}) = \vec{u}(\vec{x}) + U(y)\vec{e}_x \tag{A.5}$$

We plug this into equation A.3 and obtain:

$$\partial_t \theta + \underbrace{(\vec{u}_{tot} \cdot \nabla)\theta_{tot}}_{A(\vec{u},\theta)} = \underbrace{\kappa \Delta \theta}_{D\theta} + \underbrace{\kappa \partial_y^2 T(y)}_{C} \tag{A.6}$$

The time integration takes place in the Fourier-space. Therefore, it is necessary to Fourier transform equation A.6 which is denoted with a tilde.

$$\partial_t \tilde{\theta} + \tilde{A}(\vec{\tilde{u}}, \tilde{\theta}) = \tilde{D}\tilde{\theta} + \tilde{C} \tag{A.7}$$

Channelflow offers different time-integration schemes which were all adapted to work with the additional temperature field. Analogous to the isothermal case described in the *Channelflow* manual, I want to explain the time-stepping of the temperature field for the Crank-Nicolson/Adams-Bashforth scheme (CNAB2). We want to calculate $\tilde{\theta}^{n+1}$ which is the approximation of $\tilde{\theta}$ at time $n\Delta t$. Therefore, we first approximate the terms of equation A.7 as

follows:

$$\partial_t \tilde{\theta}^{n+1/2} = \frac{\tilde{\theta}^{n+1} - \tilde{\theta}^n}{2} + \mathcal{O}(\Delta t), \tag{A.8}$$

$$\tilde{D}\tilde{\theta}^{n+1/2} = \frac{1}{2}\tilde{D}\tilde{\theta}^{n+1} + \frac{1}{2}\tilde{D}\tilde{\theta}^n + \mathcal{O}(\Delta t), \tag{A.9}$$

$$\tilde{A}^{n+1/2} = \frac{3}{2}\tilde{A}^n - \frac{1}{2}\tilde{A}^{n-1} + \mathcal{O}(\Delta t), \tag{A.10}$$

$$\tilde{C}\tilde{\theta}^{n+1/2} = \frac{1}{2}\tilde{C}^n + \frac{1}{2}\tilde{C}^{n-1} + \mathcal{O}(\Delta t). \tag{A.11}$$

The approximations of D and A are called Crank-Nicolson and Adams-Bashforth, respectively. Substituting these approximations in equation A.7, we obtain:

$$\left[\frac{1}{\Delta t} - \frac{1}{2}\tilde{D}\right]\tilde{\theta}^{n+1} = \left[\frac{1}{\Delta t} + \frac{1}{2}\tilde{D}\right]\tilde{\theta}^n + \frac{3}{2}\tilde{A}^n - \frac{1}{2}\tilde{A}^{n-1}. \tag{A.12}$$

The right hand side of this equation can be calculated since only previous time steps contribute to it. Equation A.12 has the form of a Helmholtz-equation

$$\partial_y^2\tilde{\theta}^{n+1} - \lambda\tilde{\theta}^{n+1} = R, \tag{A.13}$$

where

$$\lambda = \frac{1}{\Delta t} + 4\pi^2\kappa\left(\frac{k_x^2}{L_x^2} + \frac{k_z^2}{L_z^2}\right), \tag{A.14}$$

$$R = \left[\frac{1}{\Delta t} + \frac{1}{2}D\right]\tilde{\theta}^n + \frac{3}{2}A^n - \frac{1}{2}A^{n-1} + \frac{1}{2}C^{n+1} + \frac{1}{2}C^n. \tag{A.15}$$

Therefore, to obtain the temperature at time $(n+1)\Delta t$, for each Fourier mode a Helmholtz-equation A.13 must be solved. Routines to solve these equation are included in the Channelflow-package because these equations have to be solved for the velocity fields, too.

In addition to CNAB2 the other time-steppers of Channelflow were adapted to handle an additional temperature field. In all cases, within one substep the temperature is first integrated forward. In the calculation of $A(\vec{u}, \theta)$ the velocity field of the previous substep is used. Afterwards the velocity field is integrated using a combination $(\theta^{n+1} + \theta^n)/2$ of the new and the old temperature fields.

Validation of the code

To test the implementation several qualitative and quantitative tests are performed. The critical Rayleigh number of Rayleigh-Bénard-convection is calculated and compared to the known values from literature $Ra = 1707.76$ (Busse, 1978). The relative error in critical Rayleigh number obtained with the code compared to the literature value is of order 10^{-5}. In figure A.1a the bifurcation diagram of the convection solution and a visualization of the temperature field of the convection solutions are shown.

The stability curve of isothermal ASBL at $Re = 0$ obtained by Fischer (2012) using an Orr-Sommerfeld stability analysis is compared to the stability curve obtained with the enhanced Channelflow-code. Both curves are shown for comparison in figure A.1b.

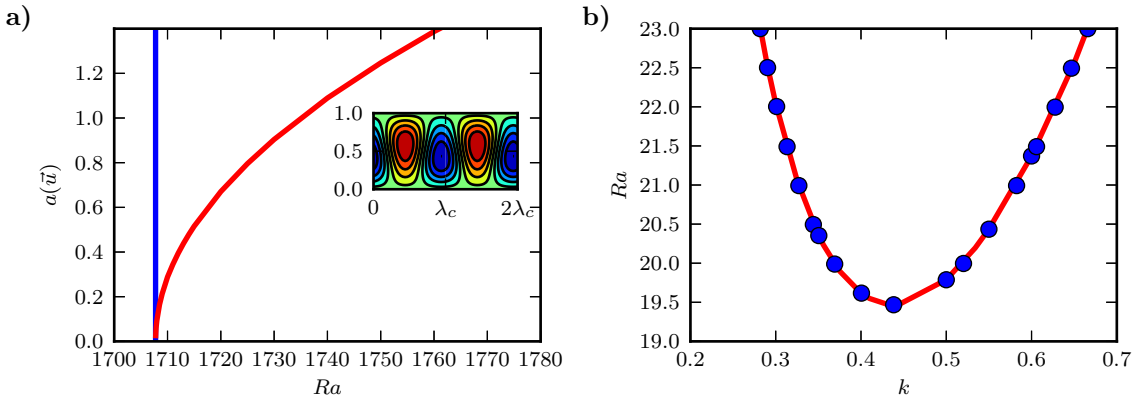

Figure A.1: a) Bifurcation diagram of the instability in Rayleigh-Bénard convetion. The blue line marks the position for the theoretical critical Rayleigh number. The inset shows the temperature field (deviation from conduction state) of the convection solutions at $Ra = 1880$. In b) stability curves of ASBL with heated plate at $Re = 0$ are shown. The red line was obtained using the modified Channeflow code, and the blue circles were obtained using an Orr-Sommerfeld stability analysis.

As a further (qualitative) test we consider sheared convection. The NBC-solution Clever and Busse (1992) of iso-thermal plane Couette flow is continued in Rayleigh number and shown to connect to the thermal instability.

Finkensieper (2013) enhanced the code to simulate rotating Rayleigh-Bénard-convection. The critical Rayleigh numbers he computed for different values of the Taylor number show a relative deviation from theoretical values of order 10^{-4}.

A.2 Stability analysis

In this section of the appendix it is briefly explained how the stability characteristics of an exact coherent structure can be calculated. We regard the time-integration map

$$F^T : \quad \vec{u}(t) \rightarrow \vec{u}(t+T) \tag{A.16}$$

that integrates a flow field a time T forward in time. Let us assume that $\vec{u}^*$ is a fixed point of F^T, i.e.,

$$F^T(\vec{u}^*) = \vec{u}^*. \tag{A.17}$$

The laminar states and all ECS in section 11.3 fulfill this requirement. Then, for a (small) deviation $d\vec{u}$ from $\vec{u}^*$, an operator $L(\vec{u}^*)(d\vec{u})$ can be defined by

$$L(\vec{u}^*)(d\vec{u}) \equiv L\ d\vec{u} := F^T(\vec{u}^* + du) - \vec{u}^* \tag{A.18}$$

The operator describes how small disturbances on top of the fixed point $\vec{u}^*$ develop and thus its eigenvalues can be used as a measure of the stability of an equilibrium solution. Instead of calculating the eigenvalues of L directly, which is computational very expensive because of the high number of dimensions of L, Krylov-subspace methods are applied. For a given matrix L and a starting vector q, the m-th Krylov-subspace $\mathcal{K}_m(R, q)$ is defined as

$$\mathcal{K}_m(L, q) := \{q, Lq, Lq^2, ..., Lq^m\}\ . \tag{A.19}$$

Using the so-called Arnoldi-iteration an orthogonal projection of L on the Krylov-subspace is calculated. For any given starting vector q, Arnoldi-iteration (e.g. Hanke-Bourgeois, 2013) starting with $d := q$ and $h_{1,0} = \|q\|_2$ works as follows:

$$\begin{aligned} &u^j := d/h_{j,j-1}, \\ &v := Lu^j, \quad h_{i,j} := v^T u^i,\ i = 1, ..., j, \\ &d := v - \sum_{i=1}^{j} u^i h_{i,j}, \quad h_{j+1,j} := \|d\|_2. \end{aligned} \tag{A.20}$$

The numbers $h_{i,j}$ are the entries of a matrix H_m. After m steps one ends up with an orthogonal projection H_m of L on the m-th Krylov-subspace. The eigenvalues of H_m approximate those of L and coincide if m is equal to the dimension of matrix L. To get an approximation of the eigenvalues of L, the eigenvalues of H_m are calculated (e.g. by QR-iteration). The big advantage of the Arnoldi-iteration is that the eigenvalues of H_m converge first to the eigenvalues of L with largest real part which are also the relevant eigenvalues for a stability analysis. Another important point is that only matrix vector products are used. Therefore, it is not necessary to calculate and save the matrix L.

The *arnoldi* function included in the *channelflow*-package uses the described method to calculate eigenvalues of a fixed points, travelling waves or (relative) periodic orbits. For travelling waves and periodic orbits a symmetry transformation s is needed, which is included in the calculation of L. A flow field of a fixed point, travelling wave or periodic orbit is delivered to the *arnoldi* function together with the necessary symmetry transformation. The *arnoldi* function of *channelflow* was originally designed for plane Couette flow and was adapted to work for PPF and also TASBL. To obtain appropriate choices of the adjustable variables (e.g. the number of iterations N and the strength of the disturbance $d\vec{u}$), for each flow and Reynolds number several calculations were performed.

A.3 Finding exact solutions

For the numerical procedure of finding exact solutions of the Navier-Stokes equation, it is appropriate to regard the operator

$$R(\vec{u}, T, \sigma)(d\vec{u}) = \sigma F^T(\vec{u}) - \vec{u}. \tag{A.21}$$

The arguments of this function are a velocity field $\vec{u}$, an integration time T and a symmetry operation σ. $F^T(\vec{u})$ denotes the map which integrates the flow field $\vec{u}$ forward for a time T.

Using this residual function, the basic idea of a Newton method for the identification of exact coherent structures is briefly described. For simplicity we will restrict ourselves to equilibrium solutions, as they are studied e.g. in section 10.

Let us assume that we have a flow field $\vec{u}^{(0)}$ for which the residual function $R(\vec{u}^{(0)}, T)$ is small. Such a flow field can be used as initial guess to search for a fixed point u^* that differs only slightly from $\vec{u}^{(0)}$, i.e $\vec{u}^* = \vec{u}^0 + d\vec{u}$. Then a Taylor expansion of the residual function around $\vec{u}^0$ gives:

$$0 = R(u^{(0)}) + DR(u^{(0)})du + \mathcal{O}(|du|^2). \tag{A.22}$$

Dropping higher order terms one obtains the Newton-equation:

$$0 = R(u^{(0)}) + DR(u^{(0)})d\vec{u}. \tag{A.23}$$

We can identify $DR(\vec{u}^{(0)})$ and the operator L defined in equation A.18 and obtain:

$$0 = R(u^{(0)}) + L(u^{(0)})d\vec{u}. \tag{A.24}$$

Thus, in principle $d\vec{u}$ can be calculated by

$$\vec{du} = L(u^{(0)})^{-1}R(u^{(0)}). \tag{A.25}$$

However, the calculation of the inverse matrix is inappropriate in most cases. Instead, the equation

$$-R(\vec{u}^{(0)}) = L(u^{(0)})d\vec{u} \tag{A.26}$$

is solved. Afterwards, we obtain a close approximation to the fixed point by

$$u^{(1)} = u^{(0)} + d\vec{u}. \tag{A.27}$$

Since we dropped higher order terms in A.22 we will in general not reach $\vec{u}^*$ within one iteration (one Newton step), but if the initial guess is sufficiently close to a fixed point within a few iterations we will converge to it.

To solve equation A.26 the Newton method included in the channeflow package uses a GMRES-method. This method minimizes the error $||L(\vec{u}^{(0)})d\vec{u} - R(\vec{u}^{(0)})||$ on condition that $d\vec{u} \in \mathcal{K}_m(L(u^{(0)}))$. For details of the GMRES-method see for example (Hanke-Bourgeois, 2013). To improve convergence of the Newton method the implementation in the channelfow package is a so-called Newton-hookstep method. The idea of this method is not to solve A.23 directly, but to minimize $||L(\vec{u}^{(0)})d\vec{u} - R(\vec{u}^{(0)})||$ subject to the condition $||d\vec{u}|| < \delta$, where δ in this constraint is called the trust radius. Additionally, the Newton step $d\vec{u}$ is constrained to lie in the Krylov-subspace $\mathcal{K}_m(L(u^{(0)}))$. For a detailed description see e.g. (Viswanath, 2007).

Bibliography

Abshagen, J., Lopez, J. M., Marques, F., and Pfister, G. (2005). Symmetry breaking via global bifurcations of modulated rotating waves in hydrodynamics. *Phys. Rev. Lett.*, 94:074501.

Ahlers, G., Grossmann, S., and Lohse, D. (2009). Heat transfer and large scale dynamics in turbulent Rayleigh-Bénard convection. *Rev. Mod. Phys.*, 81(2):503–537.

Aida, H., Tsukahara, T., and Kawaguchi, Y. (2014). Development of a turbulent spot into a stripe pattern in plane Poiseuille flow. arXiv:1410.0098.

Alavyoon, F., Henningson, D. S., and Alfredsson, P. H. (1986). Turbulent spots in plane Poiseuille flow - flow visualization. *Phys. Fluids*, 29(4):1328.

Allhoff, K. T. and Eckhardt, B. (2012). Directed percolation model for turbulence transition in shear flows. *Fluid Dyn. Res.*, 44:031201.

Altmeyer, S., Willis, A., and Hof, B. (2014). The role of periodic orbits and bubbles of chaos during the transition to turbulence. arXiv:1501.0198.

Avila, K., Moxey, D., de Lozar, A., Avila, M., Barkley, D., and Hof, B. (2011). The onset of turbulence in pipe flow. *Science*, 333(6039):192–6.

Avila, M. and Hof, B. (2013). Nature of laminar-turbulence intermittency in shear flows. *Phys. Rev. E*, 87(6):063012.

Avila, M., Mellibovsky, F., Roland, N., and Hof, B. (2013). Streamwise-Localized Solutions at the Onset of Turbulence in Pipe Flow. *Phys. Rev. Lett.*, 110:224502.

Avila, M., Willis, A. P., and Hof, B. (2010). On the transient nature of localized pipe flow turbulence. *J. Fluid Mech.*, 646:127.

Barkley, D. (2011). Simplifying the complexity of pipe flow. *Phys. Rev. E*, 84:016309.

Barkley, D. and Tuckerman, L. (2005). Computational Study of Turbulent Laminar Patterns in Couette Flow. *Phys. Rev. Lett.*, 94:014502.

Batiste, O., Knobloch, E., Alonso, A., and Mercader, I. (2006). Spatially localized binary-fluid convection. *J. Fluid Mech.*, 560:149.

Beaume, C., Bergeon, A., Kao, H.-C., and Knobloch, E. (2013). Convectons in a rotating fluid layer. *J. Fluid Mech.*, 717:417–448.

Bergé, P. and Dubois, M. (2006). Rayleigh-Bénard convection. *Contemp. Phys.*, 25(6):535–582.

Bergeon, a. and Knobloch, E. (2008). Spatially localized states in natural doubly diffusive convection. *Phys. Fluids*, 20(3):034102.

Biau, D. and Bottaro, A. (2009). An optimal path to transition in a duct. *Philos. Trans. A. Math. Phys. Eng. Sci.*, 367(1888):529–544.

Blanchflower, S. (1999). Magnetohydrodynamic convectons. *Phys. Lett. A*, 261:74–81.

Bottin, S. and Chate, H. (1998). Statistical analysis of the transition to turbulence in plane Couette flow. *Eur. Phys. J. E*, 155:143–155.

Brand, E. and Gibson, J. (2014). A doubly-localized equilibrium solution of plane Couette flow. *J. Fluid Mech.*, 750:R1.

Brethouwer, G., Duguet, Y., and Schlatter, P. (2012). Turbulent-laminar coexistence in wall flows with Coriolis, buoyancy or Lorentz forces. *J. Fluid Mech.*, 704:137–172.

Brosa, U. (1989). Turbulence without strange attractor. *J. Stat. Phys.*, 55(5-6):1303–1312.

Busse, F. H. (1978). Non-linear properties of thermal convection. *Rep. Prog. Phys.*, 41:1929–1967.

Carlson, D. R., Widnall, S. E., and Peeters, M. F. (1982). A flow-visualization study of transition in plane Poiseuille flow. *J. Fluid Mech.*, 121:487–505.

Chandler, G. J. and Kerswell, R. R. (2013). Invariant recurrent solutions embedded in a turbulent two-dimensional Kolmogorov flow. *J. Fluid Mech.*, 722:554–595.

Chantry, M. and Kerswell, R. R. (2015). Localization in a spanwise-extended model of plane Couette flow. *Phys. Rev. E*, 91:043005.

Chantry, M., Willis, A. P., and Kerswell, R. R. (2014). The genesis of streamwise-localized solutions from globally periodic travelling waves in pipe flow. *Phys. Rev. Lett.*, 112:164501.

Cherubini, S., De Palma, P., Robinet, J.-C., and Bottaro, A. (2011). Edge states in a boundary layer. *Phys. Fluids*, 23(5):051705.

Clever, R. M. and Busse, F. H. (1992). Three-dimensional convection in a horizontal fluid layer subjected to a constant shear. *J. Fluid Mech.*, 234:511–527.

Cvitanović, P. (2013). Recurrent flows: the clockwork behind turbulence. *J. Fluid Mech.*, 726:1–4.

Deguchi, K. and Hall, P. (2014). Free-stream coherent structures in parallel boundary-layer flows. *J. Fluid Mech.*, 752:602–625.

Deguchi, K., Meseguer, A., and Mellibovsky, F. (2014). Subcritical Equilibria in Taylor-Couette Flow. *Phys. Rev. Lett.*, 112:184502.

Del Álamo, J. C. and Jiménez, J. (2009). Estimation of turbulent convection velocities and corrections to Taylor's approximation. *J. Fluid Mech.*, 640:5–26.

Dijkstra, H., Wubs, F. W., Cliffe, A. K., Doedel, E., Dragomirescu, I. F., Eckhardt, B., Gelfgat, A. Y., Hazel, A. L., Lucarini, V., Salinger, A. G., Phipps, E. T., Sanchez-Umbria, J., Schuttelaars, H., Tuckerman, L. S., and Thiele, U. (2014). Numerical Bifurcation Methods and their Applicaton to Fluid Dynamics: Analysis beyond Simulation. *Commun. Comput. Phys.*, 15(1):1–45.

Drissi, A., Net, M., and Mercader, I. (1999). Subharmonic instabilities of Tollmien-Schlichting waves in two-dimensional Poiseuille flow. *Phys. Rev. E*, 60:1781.

Duguet, Y. and Schlatter, P. (2013). Oblique Laminar-Turbulent Interfaces in Plane Shear Flows. *Phys. Rev. Lett.*, 110:034502.

Duguet, Y., Schlatter, P., and Henningson, D. S. (2009). Localized edge states in plane Couette flow. *Phys. Fluids*, 21(11):111701.

Duguet, Y., Schlatter, P., and Henningson, D. S. (2010a). Formation of turbulent patterns near the onset of transition in plane Couette flow. *J. Fluid Mech.*, 650:119–129.

Duguet, Y., Schlatter, P., Henningson, D. S., and Eckhardt, B. (2012). Self-Sustained Localized Structures in a Boundary-Layer Flow. *Phys. Rev. Lett.*, 108:044501.

Duguet, Y., Willis, A. P., and Kerswell, R. R. (2008). Transition in pipe flow: the saddle structure on the boundary of turbulence. *J. Fluid Mech.*, 613:255–274.

Duguet, Y., Willis, A. P., and Kerswell, R. R. (2010b). Slug genesis in cylindrical pipe flow. *J. Fluid Mech.*, 663:180–208.

Eckert, M. (2010). The troublesome birth of hydrodynamic stability theory: Sommerfeld and the turbulence problem. *Eur. Phys. J. H*, 35(1):29–51.

Eckert, M. (2014). Fluid Mechanics in Sommerfeld's School. *Annu. Rev. Fluid Mech.*, 47(1):1–20.

Eckhardt, B. (2008). Turbulence transition in pipe flow: some open questions. *Nonlinearity*, 21:T1–T11.

Eckhardt, B. and Mersmann, A. (1999). Transition to turbulence in a shear flow. *Phys. Rev. E*, 60:509.

Eckmann, J. P. (1981). Roads to turbulence in dissipative dynamical systems. *Rev. Mod. Phys.*, 53(4):643–654.

Ehrenstein, U. and Koch, W. (1991). Three-dimensional wavelike equilibrium states in plane Poiseuille flow. *J. Fluid Mech.*, 228:111–148.

Etling, D. and Brown, R. (1993). Roll vortices in the planetary boundary layer: A review. *Boundary-Layer Meteorol.*, 65:215–248.

Faisst, H. and Eckhardt, B. (2003a). Sensitive dependence on initial conditions in transition to turbulence in pipe flow. *J. Fluid Mech.*, 504:343–352.

Faisst, H. and Eckhardt, B. (2003b). Traveling Waves in Pipe Flow. *Phys. Rev. Lett.*, 91:224502.

Faisst, H. and Eckhardt, B. (2004). Sensitive dependence on initial conditions in transition to turbulence in pipe flow. *J. Fluid Mech.*, 504:343–352.

Feigenbaum, M. J. (1978). Quantitative Universaility for a Class of Nonlinear Transformations. *J. Stat. Phys.*, 19(1):25–52.

Finkensieper, S. (2013). *Codimension 2 Bifurcations in Rotating Rayleigh - Benard - Convection.* Masters thesis, Philipps-Universität Marburg.

Fischer, N. (2012). *Linear Stability Theory For A Thermal Boundary Layer.* Diploma thesis, Philipps-Universität Marburg.

Fransson, J. H. M. and Alfredsson, P. H. (2003). On the disturbance growth in an asymptotic suction boundary layer. *J. Fluid Mech.*, 482:51–90.

Fransson, J. H. M., Matsubara, M., and Alfredsson, P. H. (2005). Transition induced by free-stream turbulence. *J. Fluid Mech.*, 527:1–25.

Gage, K. S. and Reid, W. H. (1968). The stability of thermally stratified plane Poiseuille flow. *J. Fluid Mech.*, 33(01):21–32.

Gibson, J. F. (2012). Channelflow: A spectral Navier-Stokes simulator in C++. Technical report, U. New Hampshire.

Gibson, J. F. and Brand, E. (2014). Spanwise-localized solutions of planar shear flows. *J. Fluid Mech.*, 745:25–61.

Gibson, J. F., Halcrow, J., and Cvitanović, P. (2008). Visualizing the geometry of state space in plane Couette flow. *J. Fluid Mech.*, 611:107–130.

Gibson, J. F., Halcrow, J., and Cvitanović, P. (2009). Equilibrium and travelling-wave solutions of plane Couette flow. *J. Fluid Mech.*, 638:243–266.

Grebogi, C., Ott, E., Romeiras, F., and Yorke, J. A. (1987). Critical exponents for crisis-induced intermittency. *Phys. Rev. A*, 36(11):5365.

Grebogi, C., Ott, E., and Yorke, J. A. (1982). Chaotic attractors in crisis. *Phys. Rev. Lett.*, 48:1507.

Grossmann, S. (2000). The onset of shear flow turbulence. *Rev. Mod. Phys.*, 72(2):603.

Grossmann, S. and Lohse, D. (2004). Fluctuations in turbulent Rayleigh-Bénard convection: The role of plumes. *Phys. Fluids*, 16:4462–4472.

Guennebaud, G., Jacon, B., and Others (2010). Eigen v3. Technical report, http://eigen.tuxfamily.org.

Halcrow, J., Gibson, J. F., Cvitanović, P., and Viswanath, D. (2009). Heteroclinic connections in plane Couette flow. *J. Fluid Mech.*, 621:365.

Hanke-Bourgeois, M. (2013). *Grundlagen der Numerischen Mathematik und des Wissenschaftlichen Rechnens*. Springer Berlin / Heidelberg.

Heisenberg, W. (1924). Über die Stablität und Turbulenz von Flüssigkeitsströmen. *Ann. Phys.*, 74(15).

Henningson, D., Lundblad, A., and Johansson, A. V. (1993). A mechanism for bypass transition from localized disturbances in wall-bounded shear flows. *J. Fluid Mech.*, 250:169–207.

Henningson, D., Spalart, P., and Kim, J. (1987). Numerical simulations of turbulent spots in plane Poiseuille and boundary-layer flow. *Phys. Fluids*, 30(10):2914.

Herbert, T. (1988). Secondary instability of boundary layers. *Annu. Rev. Fluid Mech.*, 20:487–526.

Hinrichsen, H. (2000). Nonequilibrium Critical Phenomena and Phase Transitions into Absorbing States. *Adv. Phys.*, 49(7):815–958, 0001070.

Hocking, L. (1975). Non-linear instability of the asymptotic suction velocity profile. *Q. Jnl. Mech. App. Maths.*, 28(3):341–353.

Hof, B., de Lozar, A., Kuik, D., and Westerweel, J. (2008). Repeller or Attractor? Selecting the Dynamical Model for the Onset of Turbulence in Pipe Flow. *Phys. Rev. Lett.*, 101(21):214501.

Hof, B., van Doorne, C. W. H., Westerweel, J., Nieuwstadt, F. T. M., Faisst, H., Eckhardt, B., Wedin, H., Kerswell, R. R., and Waleffe, F. (2004). Experimental Observation of Nonlinear Travelling Waves in Turbulent Pipe Flow. *Science*, 305(1594).

Hof, B., Westerweel, J., Schneider, T. M., and Eckhardt, B. (2006). Finite lifetime of turbulence in shear flows. *Nature*, 443(7107):59–62.

Itano, T., Akinaga, T., Generalis, S. C., and Sugihara-Seki, M. (2013). Transition of Planar Couette Flow at Infinite Reynolds Numbers. *Phys. Rev. Lett.*, 111:184502.

Itano, T. and Generalis, S. (2009). Hairpin Vortex Solution in Planar Couette Flow: A Tapestry of Knotted Vortices. *Phys. Rev. Lett.*, 102:114501.

Itano, T. and Toh, S. (2001). The dynamics of bursting process in wall turbulence. *J. Phys. Soc. Japan*, 70(3):703–716.

Jelli, E. (2014). *Kohärente Strukturen in einer abgesaugten Grenzschicht*. Bachelor thesis, Philipps-Universität Marburg.

Jeong, J. and Hussain, F. (1995). On the identification of a vortex. *J. Fluid Mech.*, 285:69–94.

Jiménez, J. (1990). Transition to turbulence in two-dimensional Poiseuille flow. *J. Fluid Mech.*, 218:265–297.

Kachanov, Y. (1994). Physical Mechanisms of Laminar Boundary-Layer Transition. *Annu. Rev. Fluid Mech.*, 26(1):411–482.

Kawahara, G. and Kida, S. (2001). Periodic motion embedded in plane Couette turbulence: regeneration cycle and burst. *J. Fluid Mech.*, 449:291–300.

Khapko, T. (2014). *Transition to turbulence in the asymptotic suction boundary layer*. Licentiate thesis, KTH Mechanics Stockholm, Stockholm.

Khapko, T., Duguet, Y., Kreilos, T., Schlatter, P., Eckhardt, B., and Henningson, D. S. (2014). Complexity of localised coherent structures in a boundary-layer flow. *Eur. Phys. J. E*, 37(32).

Khapko, T., Kreilos, T., Schlatter, P., Duguet, Y., Eckhardt, B., and Henningson, D. S. (2013). Localized edge states in the asymptotic suction boundary layer. *J. Fluid Mech.*, 717:R6.

Knobloch, E. (2015). Spatial Localization in Dissipative Systems. *Annu. Rev. Condens. Matter Phys.*, 6(1):325–359.

Kreilos, T. and Eckhardt, B. (2012). Periodic orbits near onset of chaos in plane Couette flow. *Chaos*, 22(4):047505.

Kreilos, T., Eckhardt, B., and Schneider, T. M. (2014a). Increasing Lifetimes and the Growing Saddles of Shear Flow Turbulence. *Phys. Rev. Lett.*, 112:044503.

Kreilos, T., Veble, G., Schneider, T. M., and Eckhardt, B. (2013). Edge states for the turbulence transition in the asymptotic suction boundary layer. *J. Fluid Mech.*, 726:100–122.

Kreilos, T., Zammert, S., and Eckhardt, B. (2014b). Comoving frames and symmetry-related motions in parallel shear flows. *J. Fluid Mech.*, 751:685–697.

Lagha, M. and Manneville, P. (2007). Modeling of plane Couette flow. I. Large scale flow around turbulent spots. *Phys. Fluids*, 19(9):094105.

Lai, Y.-C. and Tél, T. (2011). *Transient Chaos - Complex Dynamics on Finite Time Scales*. Springer Berlin / Heidelberg.

Landau, L. and Lifschitz, E. (1991). *Lehrbuch der Theoretischen Physik - Band 6: Hydrodynamik*. Harri Deutsch, Frankfurt, 5 edition.

Lemoult, G., Aider, J.-L., and Wesfreid, J. E. (2013). Turbulent spots in a channel: large-scale flow and self-sustainability. *J. Fluid Mech.*, 731:R1.

Lemoult, G., Gumowski, K., Aider, J.-L., and Wesfreid, J. E. (2014). Turbulent spots in channel : an experimental study Large-scale flow, inner structure and low order model. *Eur. Phys. J. E*, 37(25).

Lin, C. (1944). *On the development of turbulence*. Phd thesis, California Institute of Technology.

Lloyd, D. J. B., Gollwitzer, C., Rehberg, I., and Richter, R. (2015). Homoclinic snaking near the surface instability of a polarizable fluid. arXiv:1509.07317.

Lo Jacono, D., Bergeon, A., and Knobloch, E. (2011). Magnetohydrodynamic convectons. *J. Fluid Mech.*, 687:595–605.

Maslowe, S. (1986). Critical layers in shear flows. *Annu. Rev. Fluid Mech.*, 18:405–32.

Mellibovsky, F. and Eckhardt, B. (2012). From travelling waves to mild chaos: a supercritical bifurcation cascade in pipe flow. *J. Fluid Mech.*, 709:149–190.

Mellibovsky, F., Meseguer, A., Schneider, T., and Eckhardt, B. (2009). Transition in Localized Pipe Flow Turbulence. *Phys. Rev. Lett.*, 103(5):054502.

Melnikov, K., Kreilos, T., and Eckhardt, B. (2014). Long-wavelength instability of coherent structures in plane Couette flow. *Phys. Rev. E*, 89:043008.

Milinazzo, F. A. and Saffman, P. G. (1985). Finite-amplitude steady waves in plane viscous shear flows. *J. Fluid Mech.*, 160:281–295.

Moehlis, J., Eckhardt, B., and Faisst, H. (2004a). Fractal lifetimes in the transition to turbulence. *Chaos*, 14(4):11.

Moehlis, J., Faisst, H., and Eckhardt, B. (2004b). A low-dimensional model for turbulent shear flows. *New J. Phys.*, 6:56–56.

Montelli, R., Nolet, G., Dahlen, F. A., Masters, G., Engdahl, E. R., and Hung, S.-H. (2004). Finite-frequency tomography reveals a variety of plumes in the mantle. *Science*, 303:338–343.

Morkovin, M. V. (1969). On the Many Faces of Transition. In C. Sinclair Wells, editor, *Viscous Drag Reduct.*, pages 1–31. Springer US.

Moxey, D. and Barkley, D. (2010). Distinct large-scale turbulent-laminar states in transitional pipe flow. *Proc. Natl. Acad. Sci. U. S. A.*, 107(18):8091–8096.

Nagata, M. (1990). Three-dimensional finite-amplitude solutions in plane Couette flow: bifurcation from infinity. *J. Fluid Mech*, 217:519–527.

Nagata, M. and Deguchi, K. (2013). Mirror-symmetric exact coherent states in plane Poiseuille flow. *J. Fluid Mech*, 735:R4.

Nicolas, X., Luijkx, J., and Platten, J. (2000). Linear stability of mixed convection fows in horizontal rectangular channels of finite transversal extension heated from below. *Int. J. Heat Mass Transf.*, 43:589–610.

Nishi, M., Ünsal, B., Durst, F., and Biswas, G. (2008). Laminar-to-turbulent transition of pipe flows through puffs and slugs. *J. Fluid Mech.*, 614:425.

Noether, F. (1921). Das Turbulenzproblem. *Zeitschrift für Angew. Math. und Mech.*, 1(2):125–138.

Okino, S., Nagata, M., Wedin, H., and Bottaro, A. (2010). A new nonlinear vortex state in square-duct flow. *J. Fluid Mech.*, 657:413–429.

Orszag, S. A. (1971). Accurate solution of the Orr-Sommerfeld stability equation. *J. Fluid Mech.*, 50:689–703.

Pausch, M., Grossmann, F., Eckhardt, B., and Romanovski, V. G. (2014). Groebner Basis Methods for Stationary Solutions of a Low-Dimensional Model for a Shear Flow. *J. Nonlinear Sci.*, 24(5):935–948.

Peixinho, J. and Mullin, T. (2006). Decay of Turbulence in Pipe Flow. *Phys. Rev. Lett.*, 96(9):094501.

Pomeau, Y. (1986). Front motion, metastability and subcritical bifurcations in hydrodynamics. *Phys. D Nonlinear Phenom.*, 23:3–11.

Price, T., Brachet, M., and Pomeau, Y. (1993). Numerical characterization of localized solutions in plane Poiseuille flow. *Phys. Fluids A Fluid Dyn.*, 5(3):762.

Prigent, A., Grégoire, G., Chaté, H., and Dauchot, O. (2003). Long-wavelength modulation of turbulent shear flows. *Phys. D Nonlinear Phenom.*, 174:100–113.

Prigent, A., Grégoire, G., Chaté, H., Dauchot, O., and van Saarloos, W. (2002). Large-Scale Finite-Wavelength Modulation within Turbulent Shear Flows. *Phys. Rev. Lett.*, 89:014501.

Pringle, C. C. T., Duguet, Y., and Kerswell, R. R. (2009). Highly symmetric travelling waves in pipe flow. *Philos. Trans. A. Math. Phys. Eng. Sci.*, 367(1888):457–472.

Pringle, C. C. T. and Kerswell, R. R. (2007). Asymmetric, Helical, and Mirror-Symmetric Traveling Waves in Pipe Flow. *Phys. Rev. Lett.*, 99:074502.

Rawat, S., Cossu, C., and Rincon, F. (2014). Relative periodic orbits in plane Poiseuille flow. *Comptes Rendus Mécanique*, 342(8):485–489.

Reynolds, O. (1883). An Experimental Investigation of the Circumstances Which Determine Whether the Motion of Water Shall Be Direct or Sinuous, and of the Law of Resistance in Parallel Channels. *Philos. Trans. R. Soc. London*, 174:935–982.

Ruelle, D. and Takens, F. (1971). On the Nature of Turbulence. *Commun. Math. Phys.*, 20:167–192.

Saiki, E. M., Biringen, S., Danabasoglu, G., and Streett, C. L. (1993). Spatial simulation of secondary instability in plane channel flow: comparison of K- and H-type disturbances. *J. Fluid Mech.*, 253:485–507.

Sánchez, J. and Net, M. (2010). on the Multiple Shooting Continuation of Periodic Orbits By Newton - Krylov Methods. *Int. J. Bifurcat. Chaos*, 20(01):43–61.

Schlatter, P. and Örlü, R. (2011). Turbulent asymptotic suction boundary layers studied by simulation. *J. Phys. Conf. Ser.*, 318(2):022020.

Schlichting, H. and Gersten, K. (1997). *Grenzschicht-Theorie*. Springer Berlin / Heidelberg, 9. auflage edition.

Schmid, P. and Henningson, D. S. (2001). *Stability and transition in shear flow*. Springer Berlin / Heidelberg.

Schmiegel, A. (1999). *Transition to turbulence in linearly stable shear flows*. Phd thesis, Philipps-Universitität Marburg.

Schmiegel, A. and Eckhardt, B. (1997). Fractal Stability Border in Plane Couette Flow. *Phys. Rev. Lett.*, 79:5250.

Schneider, T. and Eckhardt, B. (2008). Lifetime statistics in transitional pipe flow. *Phys. Rev. E*, 78:046310.

Schneider, T. M., Eckhardt, B., and Yorke, J. (2007). Turbulence Transition and the Edge of Chaos in Pipe Flow. *Phys. Rev. Lett.*, 99:034502.

Schneider, T. M., Gibson, J. F., and Burke, J. (2010a). Snakes and Ladders: Localized Solutions of Plane Couette Flow. *Phys. Rev. Lett.*, 104:104501.

Schneider, T. M., Gibson, J. F., Lagha, M., De Lillo, F., and Eckhardt, B. (2008). Laminar-turbulent boundary in plane Couette flow. *Phys. Rev. E*, 78:037301.

Schneider, T. M., Marinc, D., and Eckhardt, B. (2010b). Localized edge states nucleate turbulence in extended plane Couette cells. *J. Fluid Mech.*, 646:441.

Schumacher, J. and Eckhardt, B. (2001). Evolution of turbulent spots in a parallel shear flow. *Phys. Rev. E*, 63:046307.

Shi, L., Avila, M., and Hof, B. (2015). The universality class of the transition to turbulence. arXiv:1504.03304.

Skufca, J., Yorke, J. A., and Eckhardt, B. (2006). Edge of Chaos in a Parallel Shear Flow. *Phys. Rev. Lett.*, 96:174101.

Song, B. (2014). *Direct Numerical Simulation of Transition to Turbulence and Turbulence Control in Pipe Flow.* Phd thesis, Georg-August-Universität Göttingen.

Thomas, L. (1953). The stability of plane Poiseuille flow. *Phys. Rev.*, 91:780–783.

Toh, S. and Itano, T. (2003). A periodic-like solution in channel flow. *J. Fluid Mech.*, 481:67–76.

Tuckerman, L. and Barkley, D. (1988). Global bifurcation to traveling waves in axisymmetric convection. *Phys. Rev. Lett.*, 61(4):408.

Tuckerman, L. S., Kreilos, T., Schrobsdorff, H., Schneider, T. M., and Gibson, J. F. (2014). Turbulent-laminar patterns in plane Poiseuille flow. *Phys. Fluids*, 26:114103.

van Doorne, C. W. H. and Westerweel, J. (2009). The flow structure of a puff. *Philos. Trans. A. Math. Phys. Eng. Sci.*, 367:489–507.

van Veen, L. and Kawahara, G. (2011). Homoclinic Tangle on the Edge of Shear Turbulence. *Phys. Rev. Lett.*, 107(11):114501.

Viswanath, D. (2007). Recurrent motions within plane Couette turbulence. *J. Fluid Mech.*, 580:339.

Waleffe, F. (1997). On a self-sustaining process in shear flows. *Phys. Fluids*, 9(4):883.

Waleffe, F. (2001). Exact coherent structures in channel flow. *J. Fluid Mech.*, 435:93–102.

Waleffe, F. (2003). Homotopy of exact coherent structures in plane shear flows. *Phys. Fluids*, 15(6):1517.

Wang, J., Gibson, J. F., and Waleffe, F. (2007). Lower Branch Coherent States in Shear Flows: Transition and Control. *Phys. Rev. Lett.*, 98:204501.

Wang, J., Li, Q., and E, W. (2015). Study of the instability of the Poiseuille flow using a thermodynamic formalism. *Proc. Natl. Acad. Sci. U.S.A.*, page 201501288.

Wedin, H., Bottaro, A., and Nagata, M. (2009). Three-dimensional traveling waves in a square duct. *Phys. Rev. E*, 79:065205(R).

Wedin, H. and Kerswell, R. R. (2004). Exact coherent structures in pipe flow: travelling wave solutions. *J. Fluid Mech.*, 508:333–371.

Willis, A. and Kerswell, R. (2007). Critical Behavior in the Relaminarization of Localized Turbulence in Pipe Flow. *Phys. Rev. Lett.*, 98(1):014501.

Wygnanski, I. and Champagne, F. (1973). On transition in a pipe. Part 1. The origin of puffs and slugs and the flow in a turbulent slug. *J. Fluid Mech.*, 59:281–335.

Wygnanski, I., Sokolov, M., and Friedman, D. (1975). On transition in a pipe. Part 2. The equilibrium puff. *J. Fluid Mech.*, 69:283–304.

Xiong, X., Tao, J., Chen, S., and Brandt, L. (2015). Turbulent bands in plane-Poiseuille flow at moderate Reynolds numbers. *Phys. Fluids*, 27(4):041702.

Yosuke, H., Quadrio, M., and Frohnapfel, B. (2014). Numerical simulation of turbulent duct flows with constant power input. *J. Fluid Mech.*, 750:191–209.

Zammert, S. (2011). *Turbulence transition in plane Couette and plane Poiseuille flow*. Diploma thesis, Philipps-Universität Marburg.

Zammert, S. and Eckhardt, B. (2014a). A spotlike edge state in plane Poiseuille flow. *Proc. Appl. Math. Mech.*, 14(1):591–592.

Zammert, S. and Eckhardt, B. (2014b). Periodically bursting edge states in plane Poiseuille flow. *Fluid Dyn. Res.*, 46:041419.

Zammert, S. and Eckhardt, B. (2014c). Streamwise and doubly-localised periodic orbits in plane Poiseuille flow. *J. Fluid Mech.*, 761:348–359.

Zammert, S. and Eckhardt, B. (2015a). Bypass transition and subcritical turbulence in plane Poiseuille flow. *Proc. TSFP-9*, arXiv:1506.04370.

Zammert, S. and Eckhardt, B. (2015b). Crisis bifurcations in plane Poiseuille flow. *Phys. Rev. E*, 91:041003(R).

Danksagungen

Mein Dank gilt Herrn Prof. Dr. Bruno Eckhardt für die Betreuung dieser Arbeit und seine zahlreichen Hinweise und Anregungen. Auch für den Freiraum bei der Gestaltung der Arbeit möchte ich mich bei Ihm bedanken.

Bei allen Mitgliedern der Arbeitsgruppe „Komplexe Systeme“ bedanke ich mich für das gute Arbeitsklima in den vergangenen Jahren. Insbesondere möchte ich Hannes Braukmann, Felix Schmidt und Tobias Kreilos danken, die die IT-Infrastruktur der Gruppe betreuen bzw. betreut haben.

Für das Korrekturlesen danke ich Marina Pausch, Kristof Beck, Michael Rath, Jens Pfeifer und Christian Mann, Robert Heinl und Lars Oliver Bernhammer.

Tobias Kreilos und Matthew Salewski danke ich für den regen Austausch über den verwendeten Channelflow-Code und der Hilfe bei dessen Weiterentwicklung.

John F. Gibson gilt mein Dank für die Entwicklung von *Channelflow* und dafür, dass er diese Software frei zugänglich gemacht hat. Außerdem möchte ich ihm für Diskussionen und hilfreiche Ideen zur Lokalisierung danken.

Vielen weiteren Kollegen, mit denen ich mich auf Tagungen und auf Treffen der DFG Forschergruppe 1182 „Wandnahe Transport- und Strukturbildungsprozesse in turbulenten Rayleigh-Bénard-, Taylor-Couette- und Rohrströmungen“ über meine Ergebnisse austauschen konnte, bin ich zu Dank verpflichtet. Insbesondere Dr. Yohann Duguet und Prof. Dr. Marc Avila möchte ich für zahlreiche Diskussionen, unter anderem über lokalisierte Zustände und Krisenbifurkationen, danken.

Meiner Familie und meiner Frau Sonja danke ich für die andauernde Unterstützung.